

THESE

Pour l'obtention du Grade de

**DOCTEUR DE L'ECOLE NATIONALE SUPERIEURE DE
MECANIQUE ET D'AEROTECHNIQUE**
(Diplôme National – Arrêté du 25 mai 2016)

Ecole Doctorale :
Sciences et Ingénierie en Matériaux, Mécanique, Energétique
Secteur de Recherche : Energétique, Thermique et Combustion

Présentée par :

Amal ZEAITER

**THERMAL MODELING AND COOLING OF ELECTRIC MOTORS.
APPLICATION TO THE PROPULSION OF HYBRID AIRCRAFT**

Directeurs de thèse :

Matthieu FÉNOT
Etienne VIDECOQ

Soutenue le 13 octobre 2020

devant la Commission d'Examen :

JURY

Présidente :

Eva DORIGNAC, Professeure des Universités, Université de Poitiers

Rapporteurs :

Julien PELLÉ, Professeur des Universités, ENSIAME, Valenciennes

Charbel HABCHI, Assistant Professor, Notre Dame University, Louaizé

Membres :

Xavier ROBOAM, Directeur de Recherche CNRS, ENSEEIHT, Toulouse

Matthieu FÉNOT, Maître de Conférences, ISAE-ENSMA de Poitiers

Etienne VIDECOQ, Maître de Conférences, ISAE-ENSMA de Poitiers

Time is way too long for us now... but it was too short with you.

You have given me the support, the encouragement, and everything I needed to begin the journey of my doctoral thesis, but you were not here when I've finished. Yet, your virtual presence is still inspiring me!

You deserve a lot more than the dedication of the present work to acknowledge your past existence in this life for all your sacrifices.

This one is for you...

I love you DAD <3

ACKNOWLEDGMENTS

En commençant la thèse, à part ce sentiment de fierté de pouvoir contribuer à l'avancement de la science ou du monde, on passe par une phase où l'on se projette dans le futur, au moment de la fin, mais on n'imagine pas le lot d'événements et de circonstances que l'on va traverser pendant ces quelques années. Je voudrais bien remercier de tout mon cœur toutes les personnes qui m'ont accompagnée, celles qui m'ont soutenue, et celles qui ont participé à la réalisation de la thèse jusqu'à la soutenance, voire au-delà.

Je tiens tout d'abord à présenter mes plus amples remerciements à **M. Matthieu FÉNOT**, qui a encadré ce travail de thèse, et à qui je suis profondément reconnaissante. Merci Matthieu pour tes conseils, ta confiance, tes recommandations judicieuses, mais surtout pour ta façon d'échanger sur les problématiques scientifiques. C'est avec beaucoup d'émotions que j'écris ces quelques lignes qui ne représentent que très peu de ce que j'ai à te dire pour te remercier encore, autant sur le niveau académique de la recherche que sur le niveau humain. J'ai eu la chance de te connaître et d'avoir effectué la thèse sous ta direction.

Je remercie profondément **M. Etienne VIDECOQ** tout d'abord pour son co-encadrement de thèse. Je suis consciente que tout le travail que nous avons effectué et les échanges scientifiques fructueux que nous avons eus m'ont permis d'avancer efficacement dans mon travail. Pourtant, si je tiens à te remercier, Etienne, c'est aussi pour avoir été présent durant la thèse surtout aux moments les plus délicats, pour avoir été patient mais toujours critique pour perfectionner le travail, et pour avoir donné les remarques pertinentes et suggestions scientifiques sincères et adaptées. Je te remercie également pour tout ce que j'ai appris de toi.

Merci Matthieu et Etienne d'être vous, parce que vous êtes des vrais encadrants, et je n'ai jamais arrêté d'apprendre de vous, de votre pédagogie, et surtout de l'intégrité scientifique et de l'esprit de progression pour le développement que vous portez en vous.

J'adresse mes remerciements aux rapporteurs de la thèse **M. Julien PELLÉ** et **M. Charbel HABCHI**. Je vous remercie d'avoir pris le temps d'évaluer le travail, de votre lecture très attentive du mémoire ainsi que de vos remarques précieuses. Je vous remercie également d'avoir participé au jury de soutenance. Grâce à cette participation, j'ai reçu des avis d'experts que j'apprécie infiniment et que je garderai dans mon esprit scientifique pour le futur.

Ce n'est pas toujours le cas dans un jury de soutenance d'avoir des chercheurs qui travaillent dans des domaines assez variés. Je remercie **Mme Eva DORIGNAC** et **M. Xavier ROBOAM** d'avoir participé à ce jury et d'être venus partager leurs avis, leurs connaissances et leurs

expertises sur différents points de vue : thermique, énergétique, électrotechnique et intégration de systèmes. Je remercie également **M. Yvan LEFEVRE** et **M. Jean-François ALLIAS** pour leur participation au jury en tant qu'invités.

Pour nos échanges collaboratifs, un grand merci à la famille du projet HASTECS, de l'institut Pprime, **M. Yves BERTIN**, **M. Vincent AYEL** et **M. Flavio ACCORINTI**, ainsi que du Laboratoire Laplace et d'Airbus. Particulièrement, à toi **Sarah**, je voudrais te dire plus qu'un merci... J'ai gagné une vraie amie et j'apprécie énormément cette amitié et tous les échanges que nous avons eus durant ces années de thèse.

Merci également à l'Union Européenne pour le financement de la thèse, à **l'ISAE-ENSMA** de m'avoir accueillie en tant que doctorante, ainsi que **l'Institut Pprime** et l'École Doctorale **SIMME**, membres, directions et personnel administratif. Merci aux membres de l'équipe de thermique de Pprime, ceux avec qui j'ai eu des discussions et j'ai partagé des moments conviviaux qui resteront gravés dans mon cœur.

Mes remerciements vont aux personnes charmantes que j'ai côtoyées et connues à Poitiers et qui m'ont accueillie à différents endroits dans cette ville assez originale et élégante : A l'ENSMA, **Mme Jocelyne BARDEAU**, cette dame attachante et aimable, et dans ma grande famille à l'ASPTT, **Mme Geneviève DELACHAUME** et **M. Gilles CATALOT**, ainsi que tous les membres et instructeurs de l'aéroclub. Merci à la Team Pilates pour votre accueil chaleureux et convivial, et pour les moments sportifs, spirituels et humains que nous avons partagés. Je remercie les amis que j'ai connus ici, pour tous les beaux souvenirs que nous avons créés. Merci surtout à celles et ceux qui réussissent toujours à avoir un esprit positif et à rehausser le moral, merci pour leur compréhension lorsque la situation était compliquée.

Un merci du fond du cœur va à ma petite famille, mes frères et ma sœur, et à mes amis, sans votre support je ne serais pas arrivée à tenir le coup, j'espère que vous êtes fiers aujourd'hui de cet aboutissement.

A ma maman que j'aime infiniment, je ne pourrai jamais te dire autant de 'merci' que tu le mérites. Merci pour m'avoir supportée et soutenue toujours dans les hauts et les bas, surtout ces deux dernières années.

Si je veux remercier la personne qui a eu le plus grand impact sur mon arrivée à ce stade de mon parcours académique, c'est sans doute toi papa. Ton absence me laisse sans mots, mais pour tous tes sacrifices et pour ton encouragement infini, je vais garder la force et la motivation que tu m'avais léguées pour avancer toujours.

CONTENTS

- ACKNOWLEDGMENTS iii
- CONTENTS v
- NOMENCLATURE ix
- CHAPTER 1 ELECTRIC MOTORS FOR AIRCRAFT PROPULSION 1
 - 1.1 Introduction 2
 - 1.2 HASTECS: The Project under CleanSky II 2
 - 1.3 Why Hybrid Aircraft? 5
 - 1.3.1 Environmental Issues, Reality or Myth? 5
 - 1.3.2 Towards Transportation Electrification and Hybridization 8
 - 1.4 Electric Motors for Vehicle Propulsion 10
 - 1.4.1 Overview of Electric Motors Types 12
 - 1.4.2 From Ground to Air Vehicles Examples 19
 - 1.4.3 Electric Motors, Suitable but? 24
 - 1.5 Thermal Issues in Electric Motors 25
 - 1.6 Purpose and Thesis Contents 25
- CHAPTER 2 E-MOTOR THERMAL MANAGEMENT STATE OF THE ART 27
 - 2.1 Introduction 28
 - 2.2 Heat Transfer in Electric Machinery 28
 - 2.2.1 Conduction Mode 29
 - 2.2.2 Convection Mode 33
 - 2.3 Electric Motor Cooling Methods 48
 - 2.3.1 External Cooling Methods 49
 - 2.3.2 Internal Cooling Methods 59
 - 2.4 Conclusion 73

CHAPTER 3	LUMPED PARAMETER THERMAL MODELING	75
3.1	Introduction	76
3.2	LPTM Approach.....	76
3.3	Electric Motor System Definition.....	80
3.3.1	E-Motor Geometry and Materials Properties	81
3.3.2	Boundary conditions	82
3.3.3	Electric Motor Losses (Heat Sources).....	82
3.3.4	Initial Conditions.....	87
3.4	Modeling Assumptions.....	87
3.4.1	Geometry.....	87
3.4.2	Symmetry and Periodicity for Model Reduction	88
3.4.3	Temperature-Independent Media Physical Properties	89
3.5	LPTM Construction.....	89
3.5.1	Thermal Conductance Matrix G	89
3.5.2	Thermal Capacity Matrix C	91
3.5.3	Heat Sources and Heat Sinks Vector Ψ	91
3.5.4	Space Discretization and Nodal Network	91
3.6	Thermal Properties of Components.....	95
3.6.1	Equivalent Properties of Heterogeneous Components.....	96
3.6.2	Contact Thermal Resistance.....	101
3.7	Validation with Experimental Results.....	103
3.8	Conclusion.....	106
CHAPTER 4	THERMAL MANAGEMENT OF DESIGNED E-MOTORS	107
4.1	Introduction	108
4.2	Electric Motor Design for 2025 (EM2025).....	108
4.2.1	Thermal Constraint Evaluation	109
4.2.2	Motor Design and Sizing.....	112

4.2.3	Thermal and Physical Properties	115
4.2.4	Dynamical Profile of Power	116
4.3	Cooling System.....	118
4.3.1	Thermal Resistance Analysis	119
4.3.2	Nodal Network	124
4.3.3	Cooling technology	126
4.3.4	Heat Exchanger of Cooling System	128
4.4	Thermal Behavior of the System	135
4.4.1	Thermohydraulic Parameters and Characteristics	136
4.4.2	Results and Analysis	138
4.4.3	Influence of Thermophysical Parameters Variation.....	147
4.4.4	Fluid Choice	150
4.4.5	Exchanger Surface and Coolant Flows	154
4.5	Case-studies	157
4.5.1	Influence of Flight Mission Scenarios	157
4.6	Electric Motor for 2035	158
4.6.1	Motor Cooling System Choice	159
4.6.2	First Motor Design and Results.....	161
4.6.3	Second Design for EM2035	165
4.7	Conclusion	171
CHAPTER 5 MODEL INVESTIGATION AND INVERSE METHOD		173
5.1	Introduction	174
5.2	Sensitivity of Motor Temperature to Losses	174
5.3	Losses Identification using an Inverse Method	178
5.3.1	Interest and Background.....	178
5.3.2	Heat Transfer Equation	179
5.3.3	State-Space Representation	179

5.3.4	Inverse Problem Solution	181
5.3.5	Results and Analysis	185
5.4	Conclusion	195
CHAPTER 6	CONCLUSIONS AND PERSPECTIVES	197
6.1	Conclusions	198
6.2	Perspectives	200
FUNDING ACKNOWLEDGMENT	203
CHAPTERS' SUMMARIES IN FRENCH	205
BIBLIOGRAPHY	213

NOMENCLATURE

Variables and Parameters

T	temperature	$^{\circ}\text{C}$
h	convection heat transfer coefficient	$\text{W}\cdot\text{m}^{-2}\cdot\text{K}^{-1}$
D	diameter	m or mm
c, c_p	specific heat	$\text{J}\cdot\text{K}^{-1}\cdot\text{kg}^{-1}$
g	gravitational acceleration	$\text{m}\cdot\text{s}^{-2}$
L or l	length	m
u	velocity	$\text{m}\cdot\text{s}^{-1}$
r	radius	m or mm
\dot{Q}_i	heat generation in motor system	W
V	volume	m^3
P	electric losses	W
H	hydraulic losses	m
S	surface	m^2
s	section	m^2
t	time	s
Δt	time step	s
q	flow rate	$\text{m}^3\cdot\text{s}^{-1}$
\dot{m}	mass flow rate	$\text{kg}\cdot\text{s}^{-1}$
A	linear surface current density	$\text{kA}\cdot\text{m}^{-1}$
J	current density	$\text{A}\cdot\text{mm}^{-2}$
R	thermal resistance	$\text{K}^{-1}\cdot\text{W}$
\mathcal{R}	electrical resistance	Ω
N	number of nodes	
\mathcal{C}	moment coefficient (for friction)	
nf	number of future times for specification function	
n_p	number of heat sources	
n_q	number of outputs	
nt	number of time steps	

Greek symbols

φ	heat flux density	$\text{W}\cdot\text{m}^{-2}$
λ	thermal conductivity	$\text{W}\cdot\text{m}^{-1}\cdot\text{K}^{-1}$
ω	rotational velocity	RPM
Φ	heat flux	W
μ	dynamic viscosity	$\text{kg}\cdot\text{m}^{-1}\cdot\text{s}^{-1}$
ρ	density	$\text{kg}\cdot\text{m}^{-3}$
ρ	electrical resistivity	$\Omega\cdot\text{m}$
ν	kinematic viscosity	$\text{m}^2\cdot\text{s}^{-1}$
β	coefficient of thermal expansion	K^{-1}
Γ	system boundary	

σ_U	mean quadratic error for U	W
σ_Y	main quadratic error for Y ,	$^{\circ}C$
χ	characteristic space function	
Ω	system domain	

Matrices and vectors

G	conductance matrix	$W \cdot K^{-1}$
ψ	heat sink vector	W
C	thermal capacity matrix	$J \cdot K^{-1}$
Ψ	vector representing heat generation term in the matrix form	W
$A (N,N)$	state matrix	
$B_c (N)$	command vector relative to environment	
$B_p (N,n_p)$	command matrix relative to heat sources	
$C_o (n_q,N)$	output matrix	
I	identity matrix	
P	heat source vector	W
U	vector of unknown heat sources	W
K	vector of known heat sources	W
V	vector of known inputs	
vol	volume	m^3
$Y (n_q)$	output vector	

Dimensionless numbers

Nu	Nusselt number
Pr	Prandtl number
Re	Reynolds number
Gr	Grashof number
Ra	Rayleigh number
Ta	Taylor number

Abbreviations

WP	Work-Package
EV	Electric Vehicle
HEV	Hybrid-Electric Vehicle
HASTECS	Hybrid Aircraft Academic reSearch on Thermal and Electrical Components Systems
MTOW	Maximum Take-Off Weight
MEW	Maximum Empty Weight
DC	Direct Current
AC	Alternating Current
PU	Per-Unit

NdFeB	Neodymium Iron Boron
Sm2Co17	Samarium Cobalt
LPTM	Lumped Parameter Thermal Model
PMSM	Permanent Magnet Synchronous Machine
SM	Surface Mounted
PCM	Phase Changing Material
EM2025	Electric Motor for year 2025
EM2035	Electric Motor for year 2035
FTS	Future Time Steps

Subscripts

<i>cv</i>	convective
<i>w</i>	wall
<i>ref</i>	reference
<i>h</i>	hydraulic
<i>p</i>	at constant pressure
<i>cr</i>	critical
<i>ext</i>	exterior
<i>k</i>	time index
<i>f</i>	for fluid at a surface
<i>rs</i>	rotor-stator
<i>r</i>	with respect to radius
<i>el</i>	for electrical
<i>ag</i> or <i>g</i>	for airgap
<i>ax</i>	for axial
<i>rad</i>	for radial direction
<i>ang</i>	for angular direction
<i>lam</i>	for laminations
<i>ins</i>	for insulation material
<i>cu</i>	for copper
<i>ch</i>	for channel

Superscripts

*	noisy temperature
^	estimated value
<i>T</i>	transposition sign
<i>-1</i>	inverse of a matrix
<i>cond</i>	for conduction
<i>conv</i>	for convection
<i>f</i>	for fluid
<i>radial</i>	for radial direction
<i>axial</i>	for axial direction
<i>eq</i>	for equivalent properties

CHAPTER 1 ELECTRIC MOTORS FOR AIRCRAFT PROPULSION

Synopsis:

A presentation of the subject area of the thesis and its problematics is developed in this chapter. Moreover, electric motors main characteristics and issues are summarized to focus on the topic of electric propulsion of aircrafts.

1.1 Introduction

Electric propulsion of vehicles is being increasingly investigated recently for a possible reduction in gas emissions and particulates. Besides the challenge of switching to a new architecture that goes with this goal, constraints relative to electric motors are defying the design of electric propulsion systems. Indeed, due to limited space and weight in vehicles, high-performance compact motors are strongly required. Fortunately, the technological advancements in materials and technologies have enabled the development of a new generation of high specific power motors (up to a few kW/kg). Generally in the transportation sector (ground, marine, and aeronautical applications) and specifically for cars, a turning point in the electric machinery domain has been registered during the last decade, highlighted by the rising interest in developing Electric Vehicles (EV) and Hybrid-Electric Vehicles (HEV). While propulsion electrification and hybridization are considered a promising solution for environmental pollution, electric motors in the aeronautical domain are constrained by several issues such as performance, weight, altitude, external conditions, safety, etc.

The objective of this chapter is to approach the thesis topic, by defining some important concepts and clarifying the basics in this subject area.

1.2 HASTECS: The Project under CleanSky II

This work is carried out within the framework of a project called **HASTECS** (*Figure 1.1*), standing for **H**ybrid **A**ircraft **A**cademic **r**e**S**earch on **T**hermal and **E**lectrical **C**omponents **S**ystems). This project kick-started in September 2016 and is currently running until 2021.



Figure 1.1 : HASTECS Project logo.

The hybrid-electric propulsion model consists of several inputs for electrical and thermal engines' systems (i.e. Mach number and altitude as a function of time) that contribute to determining the Maximum Take-Off Weight (MTOW) of the plane at each iteration in a global optimization process as depicted in *Figure 1.2*. The Maximum Empty Weight (MEW) is given by Airbus, and the loopback on this weight is performed using a simplified function, subject to specific constraints (for instance, the drag effect not taken into account). HASTECS project is located at the electric propulsion units' design and studies, aiming to reach the propulsion target in terms of weight.

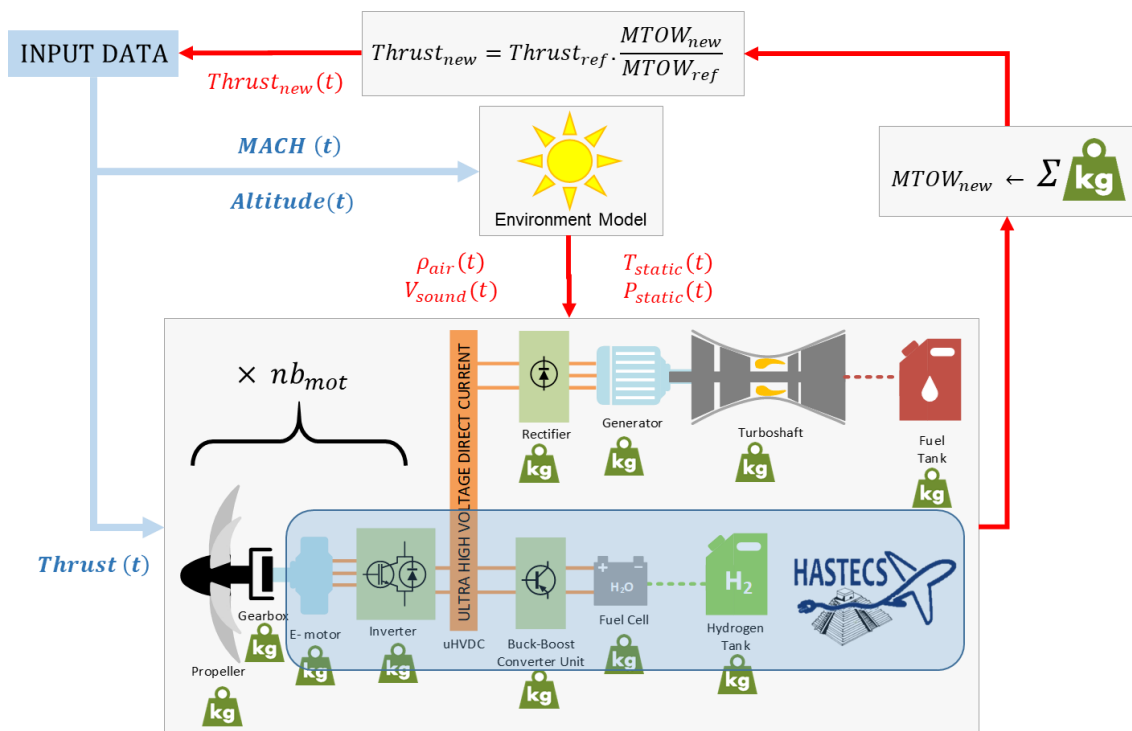


Figure 1.2 : Hybrid Aircraft power chain with HASTECS project-area [HASTECS Workshop October 2018].

The general objective of HASTECS project, indicated in the project proposal, is to support Hybrid Electric Aircraft propulsion demonstration by developing electro-thermal models and tools to assess the main benefits of different hybrid propulsion architectures and power management for short/medium-range aircraft.

These means will help to design propulsive electrical architectures for radical aircraft, by setting specific objectives for different Work-Packages (WPs). System-level integration of the assessments is the task assigned to the Work-Package 6 of the project (WP6) from main components design and analysis of the hybrid power chain (see *Figure 1.3*). This chain consists

of electric machine designs (WP1), associated cooling systems (WP3), power electronics and cables (WP2, 5), and associated thermal management (WP4). It considers the main environmental constraints, especially the partial discharges (WP5) due to high-power-ultra-high voltage new standards.

The project is funded by the CleanSky2 Joint Undertaking under the European Union's Horizon 2020 research and innovation program. For short and long-term targets, objectives have been fixed in terms of specific powers considering reasonable possible development in materials choices, and technologies. The specific power of electric machines is doubled from 5 kW/kg for 2025 to 10 kW/kg for 2035, while specific powers of converters must be increased from 15 kW/kg for 2025 to 25 kW/kg for 2035. For instance in electric machinery, the properties of new insulators, impregnation materials, and magnets, are currently being investigated in industries and research institutes to be applied in the long-term future, while it is confirmed for other promising materials that they will be available to use in electric machinery in the short-term future.

The current thesis is registered to work on WP3. The electric machines specialists of WP1 provide multiple designs of motors to match the short-term and long-term targets (2025 e-motor and 2035 e-motor). A strong interaction between our Work-Package (WP3) and WP1 has been developed during the project running time. Both workgroups have been collaborating to harmonize tools and models to meet the specific power density targets considering the electrical and thermal constraints and motor efficiencies.

To exceed the existing limits of motor specific power density, HASTECS electric machine and heat transfer specialists mutualized their electromagnetic and thermal investigations to find genuine technological solutions. From a thermal point of view, the interaction requires first a definition of some basic points: electric motor types, the specificity of electric motor for propulsion, the limiting constraints in terms of temperature and weight, origins of thermal problems in these motors, and possible configurations that could be suitable in this groundbreaking application.

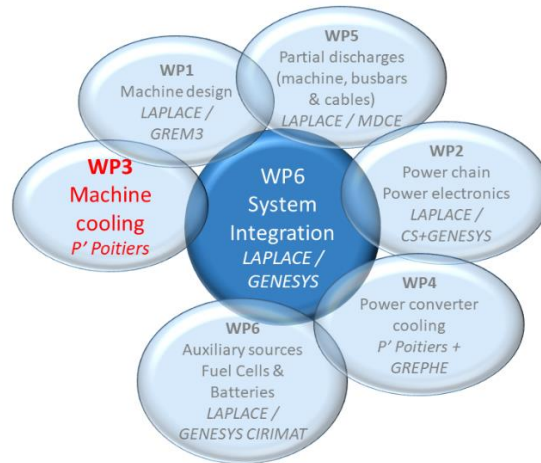


Figure 1.3 : HASTECS Project Work-Packages scheme for interactions.

In this framework, the objective of this thesis, concisely termed ‘Electric Motor Cooling’ or WP3, is to elaborate thermal models for super-high specific power electric motors, conceived in the project, and to configure suitable cooling systems. It aims to design and assess adequate techniques for the thermal management of such motors. With the existing technologies, the electric motors compactness and power are toughly limited by thermal constraints that should be respected. Also, with the high targets of global performance and specific power, motors for aeronautical propulsion should be investigated acutely from electro-technical as well as thermal points of view.

These points are the topic lead-ins of our study and will be developed successively in the thesis.

1.3 Why Hybrid Aircraft?

1.3.1 Environmental Issues, Reality or Myth?

The increased carbon footprint is challenging scientists, researchers, and environment specialists to raise interest and investigate other sustainable energy supply sources. The resulting anomaly is alarming with an increasing average land-sea temperature. This will change the global vital conditions on earth, together with higher frequency and intensity of heatwaves, hazardous fire weather, and drought conditions in multiple zones of the earth [1].

Many are the indicators of climate change and global warming, could it be the air temperature, ocean warming and sea-level rise, extreme weather events, or the changing rainfall patterns resulting from the changing global water cycle and intensifying with a warming climate. NASA [2] provided data on global temperature variations, as depicted in *Figure 1.4*. The rising temperature curves in the past decades prove that the warming effect on earth is rapidly growing. The climate models are developed, according to intermittent factors, to simulate and predict the responses of environment temperatures to all influencing factors [3]. Ignoring the alerting signs indicates that global surface warming will follow the trend line indicated in red in *Figure 1.5*.

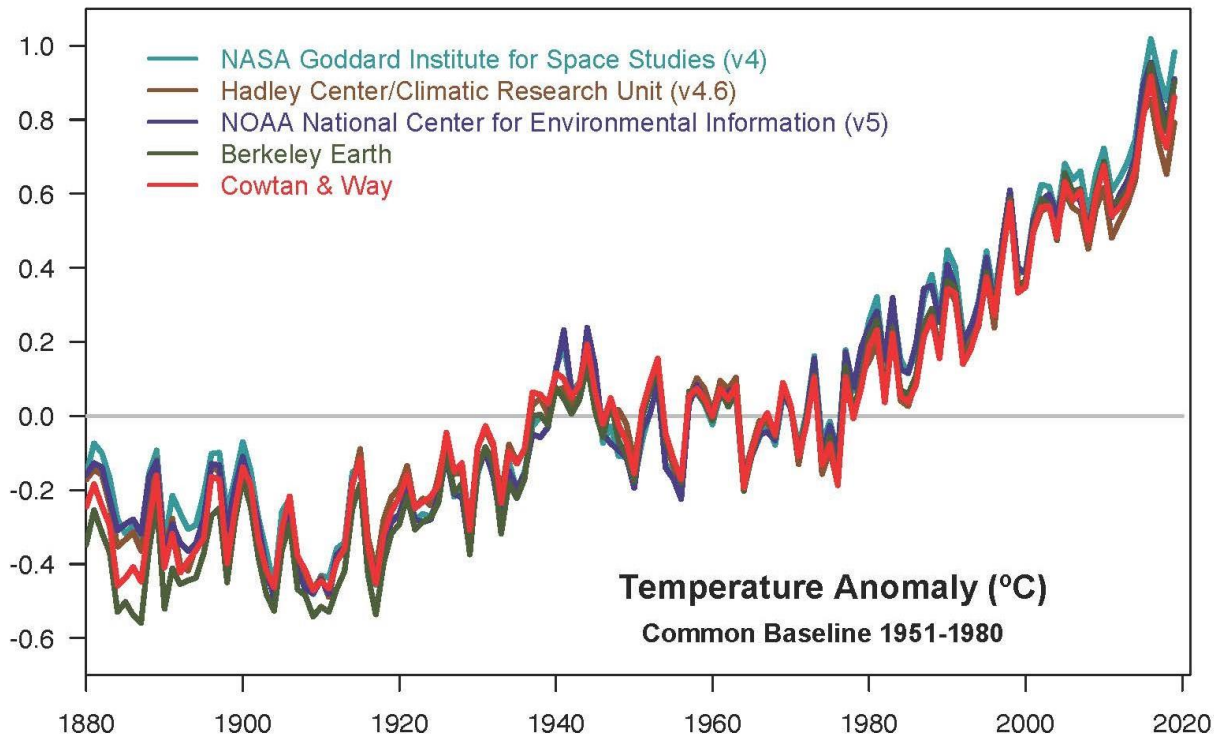


Figure 1.4 : Yearly temperature anomalies from 1880 to 2019 [2].

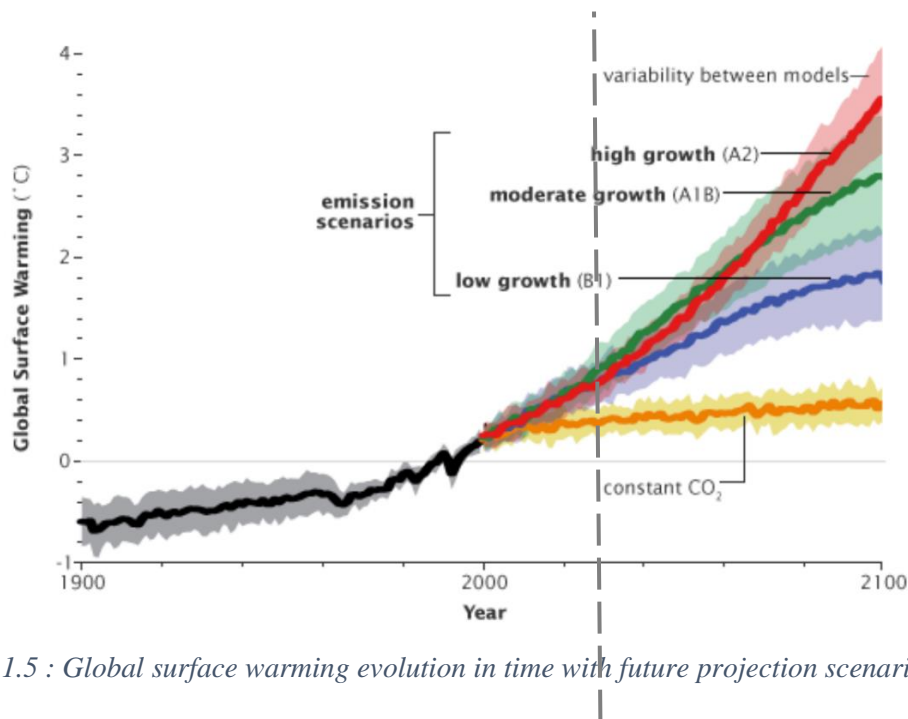


Figure 1.5 : Global surface warming evolution in time with future projection scenarios [3].

It is thought that if no concrete actions are adopted to reduce greenhouse gas emissions considering plausible emission scenarios, by the end of the current century, the average temperature could increase between 2 °C and 6 °C.

The European Union is committed to meet technical environmental goals set in the European Commission's Flightpath 2050 Vision for Aviation, which is to reduce by 75% CO₂ and by 90% NO_x emissions, and by 65% the noise. Data and statistics of the International Energy Agency 'IEA' [4] show that actually 'transport' sector accounts for around a quarter of global CO₂ emissions in the world, as seen in the diagram of *Figure 1.6*.

With that being said, the transportation sector, implying broad private companies and industries, is now seeking sustainability for propulsion power systems mainly, and for other deployments as well. One can cite, for instance, the CO₂ roadmap at Airbus. They, among other companies in this sector, are willing to achieve sustainable air travel soon, through greater decarbonization (a reduction of 50% of the net aviation carbon emissions by 2050 compared to what they were in 2005), by improving environmental performance and adopting sustainable supply chain, etc [5].

GLOBAL CO2 EMISSIONS BY SECTOR

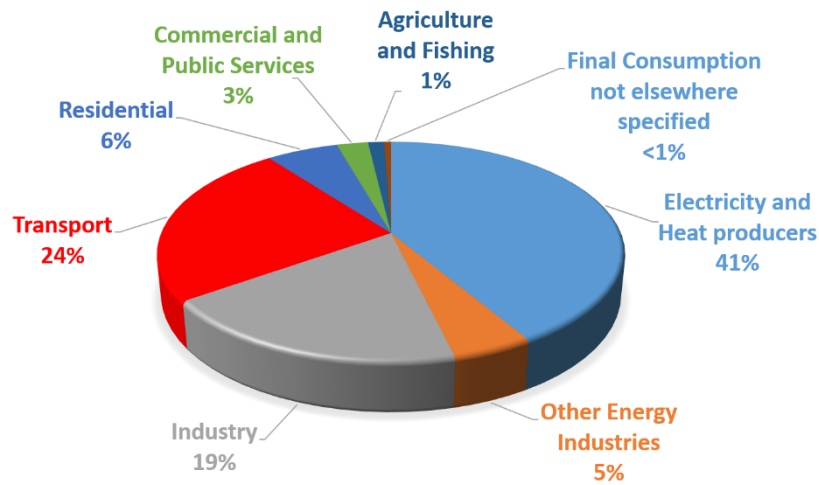


Figure 1.6 : Global CO2 emissions by sector in 2017 [4].

A key objective is to conceive and produce transportation means that consume less fuel or other « new » and cleaner energy sources and therefore reduce toxicity emission levels.

1.3.2 Towards Transportation Electrification and Hybridization

Vehicles have been powered, for a long time, predominantly by fuel of fossil - or biomass - origins that ignite in their heat engines emitting pollutant substances and gases. As for cars and ground vehicles, propulsion hybridization is thought to be an ecological solution for planes as well.

Aircraft hybridization (with solar power such as Sunseeker II [6] or electric power such as the Pipistrel Taurus Electro G2.5 [7]), and aircraft electrification (Siemens' electric aircraft designs [8] as an example) was recently investigated as a solution to enable achieving the aforementioned environmental goals. To accelerate electrification, Rolls Royce Company - in partnership with YASA electric motor and controller manufacturer and Electroflight aviation start-up - has started an initiative called ACCEL[9], within which an all-electric powered aircraft with zero-emissions was unveiled in late December 2019 in an Iron Bird test airframe as shown in *Figure 1.7*. This plane, characterized by its high speed (over 480 km/h), is scheduled to take off in 2020. On the other hand, the first flight of the largest commercial all-electric aircraft (flying testbed) took place on May 28, 2020, with a Cessna 208B Grand

Caravan from AeroTEC company [10]. With a propelling electric motor from MagniX of 560 kW power, the zero-emissions flight lasted 30 minutes at a maximum of 2500 ft.



Figure 1.7 : ACCEL Iron Bird test airframe [9].

These light aircraft units and prototypes showed the extent and the limits of using less-pollutant energy types for propulsion. However, the tough environmental objectives suggest taking firmer actions and pushing the boundaries as far as enabling hybridization of regional aircraft in the same standard. The aerospace companies and industries are investigating the use of electric power for hybrid-electric propulsion of commercial aircraft. Electricity is retained as a potential candidate for hybridization in the aeronautical transportation sector, with the lack of other powerful energy sources.

Receiving funds from the Boeing Company and the state of Washington, Zunum Aero [11] is working on the development of a hybrid electric private jet. NASA STARC-ABL [12] is the established concept of Single-Aisle Turboelectric Aircraft with an Aft-Boundary-Layer propulsor, to be more fuel-efficient than existing aircraft designs. With a large turbofan engine on the rear of the aircraft and generators added to wing-mounted turbofans supplying the back engine with generated electricity, this plane is designed to use 10% less fuel, promoting longer ranges of aircrafts for a long-term goal of two decades. NASA researchers are still carrying out tests on future turboelectric (and besides hybrid-electric) concepts of electrical components and systems (PEGASUS [13]). Airbus, Rolls Royce, and Siemens engaged to switch to hybrid electric propulsion of commercial air vehicles. Airbus company is thought to be a major player and enabler to reduce considerably the emissions of CO₂, NO_x, and particulate [14]. Their

E-Fan project aims to develop an e-system architecture and other related electrical propulsion technologies. Spotted with the launching of the E-Fan X hybrid-electric aircraft demonstrator [15] (see design in *Figure 1.8*), the year 2019 has also witnessed many transportation electrification events sponsored by the primary actors in the aircraft design industry (chiefly, but not limited to, Airbus and Boeing companies). Recently, the E-Fan X project was canceled during the COVID-19 pandemic.

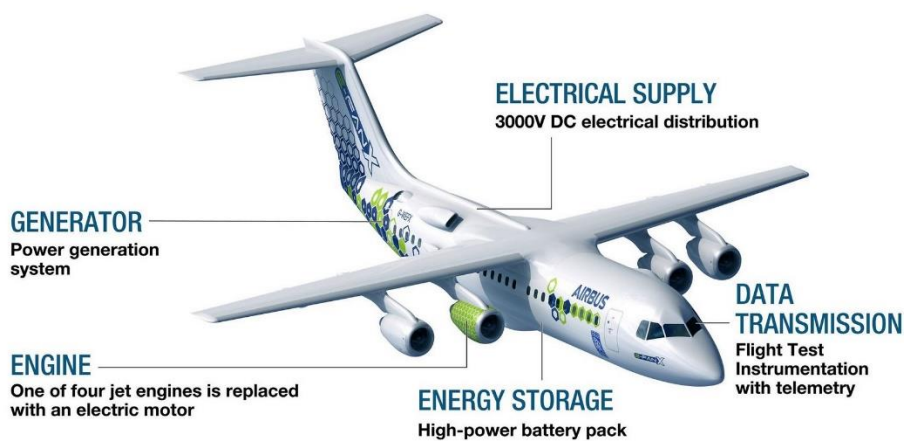


Figure 1.8 : E-Fan X demonstrator design [15].

Those major advancements in electrification and hybridization of commercial aviation are being led towards a less polluted environment and more sustainable actions in the air transportation sector.

Before getting through more details, let us comprehend the possibility of switching to electrical propulsion and its limitations, by getting through some general definitions and conventions.

1.4 Electric Motors for Vehicle Propulsion

In addition to their environmental benefits, electric motors have a proven advantage over gasoline engines, which is their higher specific torque. The curves from [16] in *Figure 1.9a* show the performance characteristics, in terms of torque and power, of two Internal Combustion Engine (ICE) that propel Renault Fluence 1.6 16V 110 and Renault Fluence dCi 105. The electric motor propelling the same vehicle model: Renault Fluence Z. E. battery electric vehicle,

is compared. Torque and power diagrams as function of speed are simultaneously depicted in *Figure 1.9b*. At certain conditions of grades, the performance of the EV is higher. Furthermore, *Figure 1.9a* and *Figure 1.9b* prove that at low speed the electric motor supplies a satisfactory torque for starting, which is not the case for thermal engines.

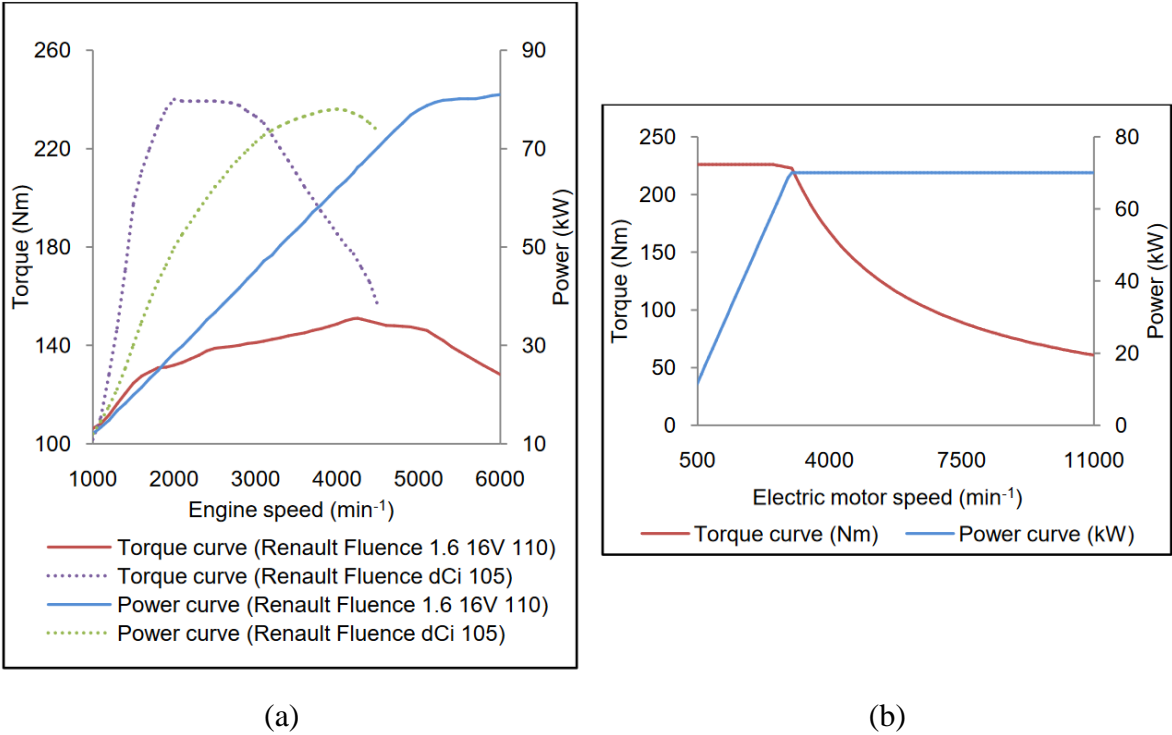


Figure 1.9 : Comparison between performance characteristics of (a) petrol ICE, diesel ICE, and (b) electric motor. Motors are used to propel the variants of the same vehicle model: Renault Fluence 1.6 16V 110, Renault Fluence dCi 105, and Renault fluence Z. E. respectively.

With the arising tendency to switch to electrified propulsion, the electric drive systems are one of the major components in the chain, provided that the electricity powering these drives is safely and continuously supplied. The development of these drives and motors belongs to the electric machinery and power systems industry. As the thesis concerns only the electric motor area, it is important to understand the topology of these machines. Herein, the first subsection overviews the main electric motor types, and the second subsection focuses on propulsion application types. Since technical information has not been published for air vehicles application, only electric motors developed for ground vehicles are presented. Besides, information is given on how these motor types can be derived for aircraft propulsion application.

1.4.1 Overview of Electric Motors Types

Back to the basics, electric motors are by definition devices that convert electrical energy into mechanical energy. This conversion is based on an electromagnetic process similar to a rectangular loop conductor placed in a magnetic field and through which a current passes. It will rotate due to the generated force applied to it, whose direction is determined based on Fleming's left-hand rule. Electric motors are classified as rotary electrical machines that require to be fed with electricity as input energy, and their application relies mainly on the resultant rotating motion as kinetic energy output. In their topology, a rotor and a stator are the main two parts of electric motors. Classically, the rotor is mounted on bearings so that the rotational motion is applied to a mechanical system (or load). The electrical energy supplying these motors can derive from Direct Current (DC) sources or Alternating Current (AC) sources.

From these statements, one can figure out that there are as many types of electric motors as there are operation principles and types of electrical energy sources. Two important categories depending on the electrical current type are presented hereafter which are the DC motors and AC motors. Other motor types are grouped in other electric motors' category, which are motors with special characteristics that cannot be included in any of the former two categories. Motors types are presented briefly and characterized accordingly. The differences between the presented motor types are clarified. Besides, some examples of applications are given.

1.4.1.1 *Direct Current Motors*

DC motors are electric motors that are supplied with direct current electrical energy. The working mechanism is based on Faraday's law of energy conservation from electrical to mechanical form. It is the first motor form working on the principle that when a voltage is applied to a conductor coil in a magnetic field, an electromagnetic force (Lorentz force) will be applied to the conductor driving it to rotate and producing a torque. There are different DC motors types: Shunt, separately excited, series, Permanent-Magnet DC, and compound.

The topology of these motors consists of the following parts: rotor, stator, airgap, winding, and brushed commutator. The airgap is the space that separates the rotor from the stator in which the magnetic field circulates. Winding is the coil made of wound conductors through which the current passes. The commutator in DC motors is the device that keeps switching the current direction in the rotor coil to ensure that the rotor will keep turning indefinitely in the static field,

i.e. the resulting force applied to the coil should change its direction every half rotation to lead to a rotating motion. Commutators consist of metallic segments and brushes mounted in a cylinder. Segments are connected by direct contact to rotor windings applying to them the electric current. Brushes are mounted on the commutator cylinder and are used to reverse the current direction.

The DC motors types are presented below:

❖ Shunt Motor

A shunt motor has its rotor and stator windings, respectively named armature and field windings, electrically connected in parallel. A DC shunt motor is characterized by maintaining a constant speed regardless of the applied load.

❖ Separately Excited Motor

The electrical energy supply is given from separate sources to field and armature windings. The DC voltage applied to the armature coil has a different source than the voltage source in the field winding. Coils are isolated from each other.

As for shunt motors, the electric current passing through the field coil in separately excited motors is constant and the field flux is also considered constant. However, with this latter type, it is possible to control the motor, compared to shunt motors where it is not possible.

Separately excited motors are used in industrial applications such as actuators.

❖ Series Motor

In series wound DC motor, armature, and field windings are connected in series and the current flowing through both windings is the same. The main difference between these motors and shunt motors is that for series motors the speed varies with load. The torque is proportional to the squared current value. Thus, they are characterized by the highest obtained torque among all other motor types for the same current ratio. Series motors can be applied as starter motors in the automotive sector and as elevators' motors.

❖ Permanent-Magnet DC Motor

Permanent-Magnet DC motors (PMDC) have winding in the rotor (armature winding) but have magnetized permanent magnets mounted on the inner side of the stator to produce the field flux instead of windings (no field windings). The required flux density provided by magnets will be therefore constant, and permanent magnets are chosen in the construction phase accordingly. Their advantage is mainly their smaller size compared to other types of DC motors; their disadvantage is their low applied torque.

❖ Compound Motor

In a compound wound DC motor, the connection between stator and rotor is a combination of connections of shunt and series excited DC motor windings. The field winding is connected both in parallel and in series to the armature winding. Two field coils are used for a compound working mechanism. These motors combine the efficient speed regulation property of shunt-wound motors and the high starting torque of series motors.

1.4.1.2 *Alternating Current Motors*

Alternating Current (AC) motors are electric motors supplied with AC voltage. There are two main types of AC motors: Induction (or asynchronous) motors and synchronous motors.

❖ Induction Motors (IM)

Induction motors or asynchronous motors are AC electric motors operating based on the principle that an induced current is created in a conductor (of the rotor) when placed in a rotating magnetic flux from the stator. The rotor induced current and stator current interact to produce a torque on the rotor.

Rotor part: The conductor is part of the rotor structure that is typically in the form of a squirrel cage with multiple conductor bars of aluminum or copper, connected cylindrically at both ends by rings (see *Figure 1.10a*). The bars are short-circuited by the rings, which allows the creation of the induced current. Inside the cage, steel laminations are stacked around the shaft. The rotating magnetic field from the stator and the induced current in the rotor drives this latter into rotation due to the generated force.

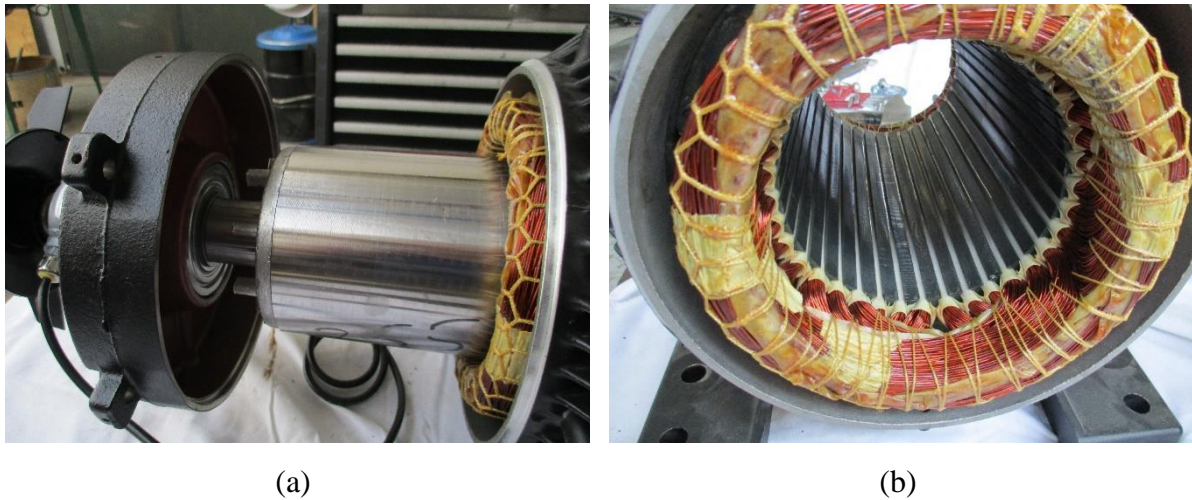


Figure 1.10 : Squirrel cage rotor (a) and stator (b) of an Induction Motor

Stator part: The construction of the induction motor stator, as depicted in *Figure 1.10b* verifies the role of this part in inducing the magnetic field that penetrates the rotor. Its main part is made up of a laminated core (stack of laminations sheets) and one or more windings depending on the number of phases. Windings are encapsulated in slots and they carry supply current.

When starting the motor, the rotor begins to rotate in the same direction and at the speed of the rotating magnetic field of the stator. To keep up its rotation, electrically wise, it is crucial to vary either the induced current in conductors or the magnetic flux. In AC induction motors, the latter one is changed. Since the rotation at synchronism speed will not produce torque at the rotor mechanical connection, there should be a ‘slip’ between rotor speed and synchronous speed i.e. the rotor operates at a slightly lower speed. When a load is applied, the motor will adapt its speed to the load torque. As a resulting drawback, slip losses are generated in the rotor and these losses reduce the efficiency and lifespan of motors [17].

This motor type is generally known to require low-maintenance, to be easily constructed, and to be robust. It can be coupled to variable frequency drive-in applications that require controlling a load velocity and displacement. The induction machine can be applied as both generator and motor.

❖ Synchronous Motors

In synchronous motors (SM), the rotor speed is equal to the stator current rotation speed. From an electromagnetic point of view, the rotor will be continuously lining up with the rotating magnetic field in the stator i.e. there is no slip between motor and stator current rotations.

The major difference between synchronous and induction motors is that synchronous motors have their rotors magnetized by external excitation (Wound-Rotor Synchronous Motor WRSM) or self-magnetization (Permanent-Magnet Synchronous Motor PMSM).

The stator of synchronous motors is structured similarly to that of an induction motor. The difference is in the rotor structure. There are two main SM rotor configurations: either with a wound rotor made with laminations and winding (also called electro-magnet) excited from a DC source or with permanent magnets within or at the surface of a laminated core.

They are used for devices of high precision positioning such as robots, as well as in powering elevators when coupled to variators. Their key advantages are their very high power factor (real power/apparent power ~ 1) and the constant motor speed regardless of the applied load. Permanent-Magnet motors support high overload current for fast kick-starting phase, while wound rotor synchronous motors are reversible electrical machine: they can operate as motors and as generators.

One of the drawbacks of synchronous machines is their operation failure in the case of overload torque.

1.4.1.3 Other Electric Motors

❖ Stepper Motor

A stepper motor is a DC motor that discretizes one rotation or revolution into multiple steps. Its stator is formed with a number of coils. Each winding group forms a phase. The steps are controlled by a computer, which gives them high precision characteristics in operation. There is a variety of stepper motors depending on the application requirement. Among these motors, one can site Permanent-Magnet or hybrid stepper motors, 2-phase bipolar or 4-phase unipolar.

❖ Brushless DC Motor

Brushless DC motors as their name suggests, are brush-free and their operation is owed to an integrated electronic controller. They achieve higher performance and efficiency levels. The electronic controller eliminates the friction losses of a brushed commutator. They can be better adapted to applications. Brushless DC motors have a smaller size than AC motors of similar performance. They have a higher torque-to-weight ratio than brushed motors.

❖ Hysteresis Motor

The hysteresis motor is a special synchronous self-starting electric motor without DC excitation. The stator rotating-field acts on the rotor as in induction motors. The hysteresis and eddy current induced in the rotor produce the torque. The stator of hysteresis motors is wound with coils similar to that of an induction motor. The rotor is made up of hardened steel laminations mounted on a nonmagnetic shaft [18]. The motor starts as in induction motors and runs as in synchronous motors. The motor has a smooth rotor with no teeth and no windings and operates soundlessly. The main drawbacks of this type are low efficiency and low output torque. It is generally used in sound equipment.

❖ Reluctance Motor

Reluctance Motors (RM) are electric motors that produce torque through magnetic reluctance. The magnetic reluctance quantifies the opposition or resistance of a magnetic circuit to magnetic field penetration. In this motor type, the rotor is made from soft magnetic material without windings. The stator has multiple projecting electromagnet poles (or salient poles). The rotor laminations have multiple projections that act as salient poles through reluctance. Their number is lower than the number of stator salient poles to allow the generation of torque. They can be either synchronous reluctance or variable (or switched) reluctance (which are a subtype of stepper motors). Reluctance motors can reach high power density; they have low cost and easy maintenance features and have various applications from computer hard disk drive to electric vehicle propulsion as in Tesla Model 3.

❖ Universal Motor

A universal motor is an electric motor that runs either on AC or DC source. Its stator consists of an electromagnet. Field and armature coils are connected in series. It has a wound rotor and a commutator with brushes. The motor structure is similar to the DC motors, but their stator and rotor are laminated to minimize eddy current losses. Universal motors are characterized by high starting torque similar to series DC motors. They can be found integrated into home appliances.

1.4.1.4 Summary of E-Motors Characteristics

In this subsection, *Table 1.1* sums up the main advantages and disadvantages of each electric motor type that is applied in electrified vehicle propulsion based on [19].

Motor type	Advantage	Disadvantage
Brushed DC Motor	+ Maximum torque at low speed	<ul style="list-style-type: none"> – Bulky structure – Low efficiency – Heat generation at brushes
Permanent Magnet Brushless DC Motor	<ul style="list-style-type: none"> + No rotor copper loss + More efficiency than induction motors + Lighter + Smaller + Better heat dissipation + More reliability + More torque density + More specific power 	<ul style="list-style-type: none"> – Short constant power range – Decreased torque with increase in speed – High cost because of PM
Permanent Magnet Synchronous Motor	<ul style="list-style-type: none"> + Operable in different speed ranges without using gear systems + Efficient + Compact + Suitable for in-wheel application + High torque even at very low speeds 	<ul style="list-style-type: none"> – Huge iron losses at high speeds during in-wheel operation
Induction Motor	<ul style="list-style-type: none"> + The most mature commutatorless motor drive system + Can be operated like a separately excited DC motor by employing orientation control 	<ul style="list-style-type: none"> – Very noisy – Low efficiency – Larger and heavier than PM machines – Complex design and control – Problems in controllability and manufacturing – Low power factor
Reluctance Motor	<ul style="list-style-type: none"> + Simple and robust construction + Low cost + High speed + Less chance of hazard + Long constant power range + High power density + Robust + Fault-tolerant + Efficient + Small 	–
PM assisted Synchronous Reluctance Motor	<ul style="list-style-type: none"> + Greater power factor than Synchronous Reluctance Motors + Free from demagnetizing problems observed in PM 	–

Table 1.1 : Advantages and disadvantages of electric motors according to their types [19].

1.4.2 From Ground to Air Vehicles Examples

The modern era has been marked by a substantially increased interest in Electric Vehicle (EV) and Hybrid-Electric Vehicle (HEV) concepts in the ground transportation sector. These concepts have been emerging for over a century now but have become recently a driving trend. Vehicles' propulsion electrification is shaping the future of the automotive industry with exponential development. Reviews of technologies used, benchmarking and an exhaustive database of these concepts are found in [20]–[24].

Vehicles' industries and manufacturers have been developing EV and HEV to reduce both, emissions and fuel consumption. Tesla Models (3, S and X), Jaguar I-Pace, General Motor EV1, BMW i3, Hyundai kona and ioniq, Audi e-tron, Nissan Leaf, Renault Zoe, Hybrid Toyota Camry and Prius, Hybrid Honda Accord are, among others, examples of EV and HEV. Actually, with this revolution over the combustion engines, and their replacement in part or total with batteries, the type of electric motor is one of the major choices to be made in this field of investigation. Indeed, with the wide variety of options, it has been proved – based on the diversity of the adopted types in existing electrified vehicles - that a suitable type depends on the technological targets aimed to be reached and some economic constraints (mainly motor construction cost).

Once an electric motor category and type seem to fit the specifications and requirements, researchers launch a process of design and optimization. This same procedure is conducted for air vehicles or planes as well. However, constraints and targets are quite different since external conditions and issues at altitudes are not similar, and objective loads are by far greater.

The typical types of electric machines used in traction applications are presented in *Figure 1.11* in assembled and exploded views. One can find that mainly the three presented types (Permanent-Magnet, Induction, and Switched-Reluctance machines) are the most suitable types for electrified powertrains allowing the engine to operate closer to its peak efficiency areas, lowering fuel consumption in hybrid vehicles [25].

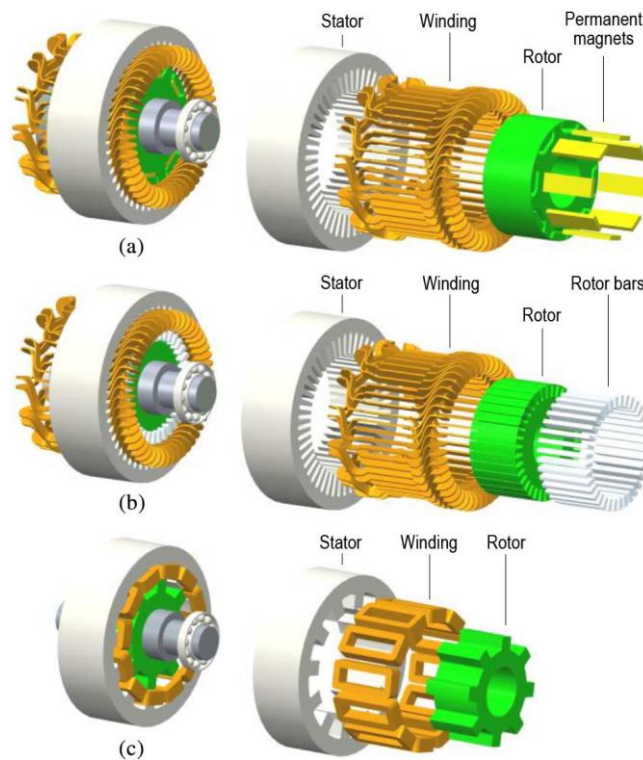


Figure 1.11 : Typical electric machines for traction applications, (a) PMSM (with interior magnets configuration), (b) IM, (c) SRM [25].

Statistics on electric motors technology for EV and HEV propulsion during the last twenty years are depicted in Figure 1.12.

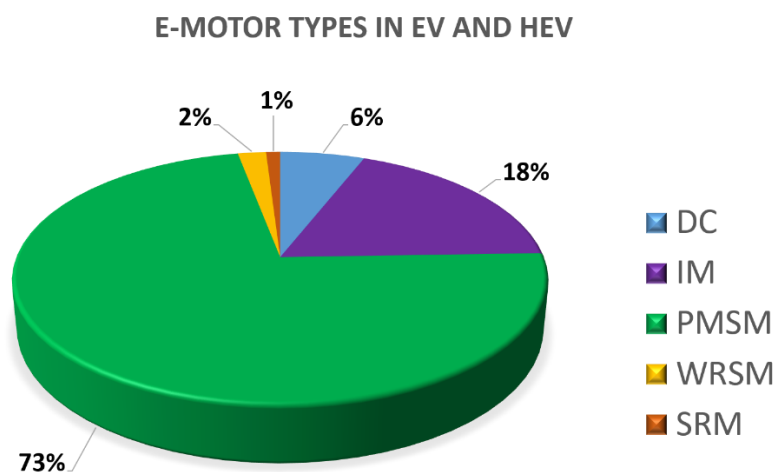


Figure 1.12 : The percentage distribution of electric machine technology in EV and HEV during the last twenty years, 'dc' (for DC), 'IM', 'PMSM', 'SRM', and 'WRSM' (Wound-Rotor Synchronous Machine) based on [22].

Data from [22] show that over the last twenty years, the PMSM type is widely used for electric propulsion vehicles (73% of vehicles with electrified propulsion). With the addition of 2% of wound-rotor SM type, Synchronous Machine type has globally 75% of the share. IM machines were selected for around 18% of EV and HEV. DC machines are less employed because of their maintenance requirements [21] (6%). SRM are used for 1% of the existing vehicles' electric propulsion. Their external control is more complex than equivalent induction and DC motors [26].

The e-motor types used commonly in electrified propulsion of ground vehicles existing in the automotive market so far are listed hereafter with examples of each:

- ❖ IM (Induction Motor): Tesla Model S 2012, Ford Think City 2008, and Honda Fit EV 2011, General Motors EV1 1996.
- ❖ PMSM (Permanent-Magnet Synchronous Motor): Lexus LS 600h 2008, Toyota Prius 2010, Toyota Camry Hybrid 2007, Hyundai Sonata 2011, Nissan Leaf 2012, Honda Jazz 2012.
- ❖ WRSM (Wound-Rotor Synchronous Motor): Renault ZOE 2011.
- ❖ PM assisted SynRM (Permanent-Magnet assisted Synchronous Reluctance Motor): BMW i3 2012 [19] (hybrid Synchronous Motor type).
- ❖ DC Motor: Peugeot Partner 1999 (Separately excited DC), Nice Mega City 2006.
- ❖ RM (Reluctance Motor): Tesla Model 3 2017 (Interior Permanent-Magnet Synchronous Reluctance), Holden ECommodore 2000 (Switched Reluctance).

PMSM type has been used increasingly for electric-propulsion vehicles in ongoing decades, because of the high machine performances in terms of torque-to-power ratio [28]. Common examples of EV and HEV with axial-field PMSM are Toyota Camry Hybrid 2007, Lexus LS 600h 2008, Toyota Prius 2010, Hyundai Sonata 2011, and Nissan Leaf 2012. Their stators' laminations are depicted in *Figure 1.13*.

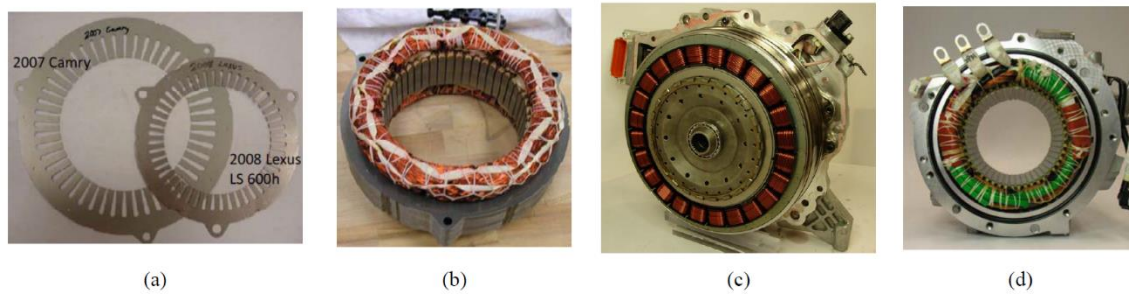


Figure 1.13 : Stator and stator laminations of (a) Camry and LS 600h, (b) Prius, (c) Sonata, (d) Leaf [28].

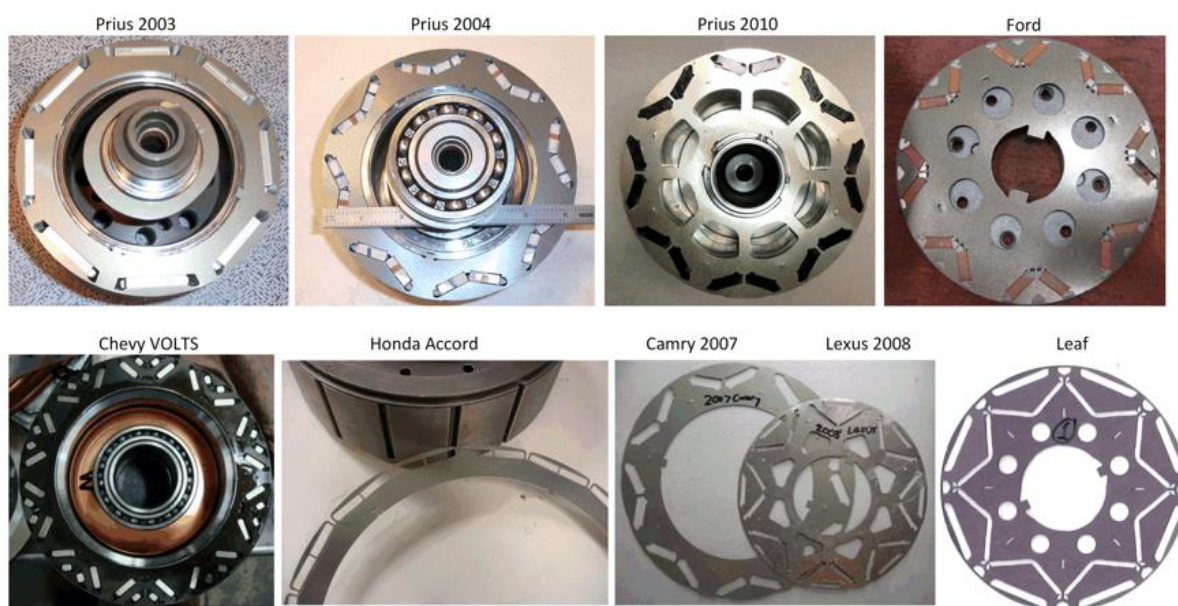


Figure 1.14 : Rotor laminations of different PM Machines in EV and HEV [23].

Rotor laminations and details of PM machines and other types used in vehicles' propulsion are found in the benchmarking of [23]. According to the authors, a trend is noticed in the use of electric motors with higher rotational speed. This is mainly due to the fact that with higher speeds, motors with less weight, and a lower volume of structure are needed, to achieve the same power targets.

Targets of powerful motors with less weight, existing in ground vehicles, are indicated by the specific power of the motor. For air vehicles, more attention is drawn to this indicator since higher values should be achieved. The existing motors in ground vehicles (mostly including the cooling system) have their specific power values grouped in *Table 1.2*.from [29]. Lexus LS 600h (2008) is equipped with one of the highest specific power motors of around 2.5 kW/kg [24].

Vehicle model	2012 Leaf	2012 Sonata HSG 23	2011 Sonata	2010 Prius	2008 Lexus LS600h	2007 Camry	2006 Honda Accord	2004 Prius
Power (kW)	80	8.5	30	60	110	70	12	50
Specific power (kW/kg)	1.4	1.9	1.1	1.6	2.5	1.7	0.5	1.1

Table 1.2 : Comparison between specific density of electric motor in EV and HEV based on [29].

Based on their multiple advantages in hybrid propulsion of vehicles, Permanent-Magnet Synchronous Motor type is considered suitable for our project’s application and targets (as a reminder: 5 kW/kg for the year 2025 and 10 kW/kg for the year 2035).

The selected motor for our project is of SM-PMSM type that is enclosed in a case. Laminations are made from soft-magnetic Co-Fe alloy. Materials are investigated and chosen at WP1 and some characteristics are extracted from catalogs. The rotor consists of laminated core and surface mounted Samarium-Cobalt magnets. NdFeB magnets could be an option for the machine unless simulations show that the temperature field in the magnet could exceed the maximum allowed value. The stator is made up of a laminated core with teeth-and-slots configuration and distributed windings in slots. The shaft consists of a steel rod. The motor frame is made of aluminum. In a modeling approach, a simplified motor section is depicted in *Figure 1.15*.

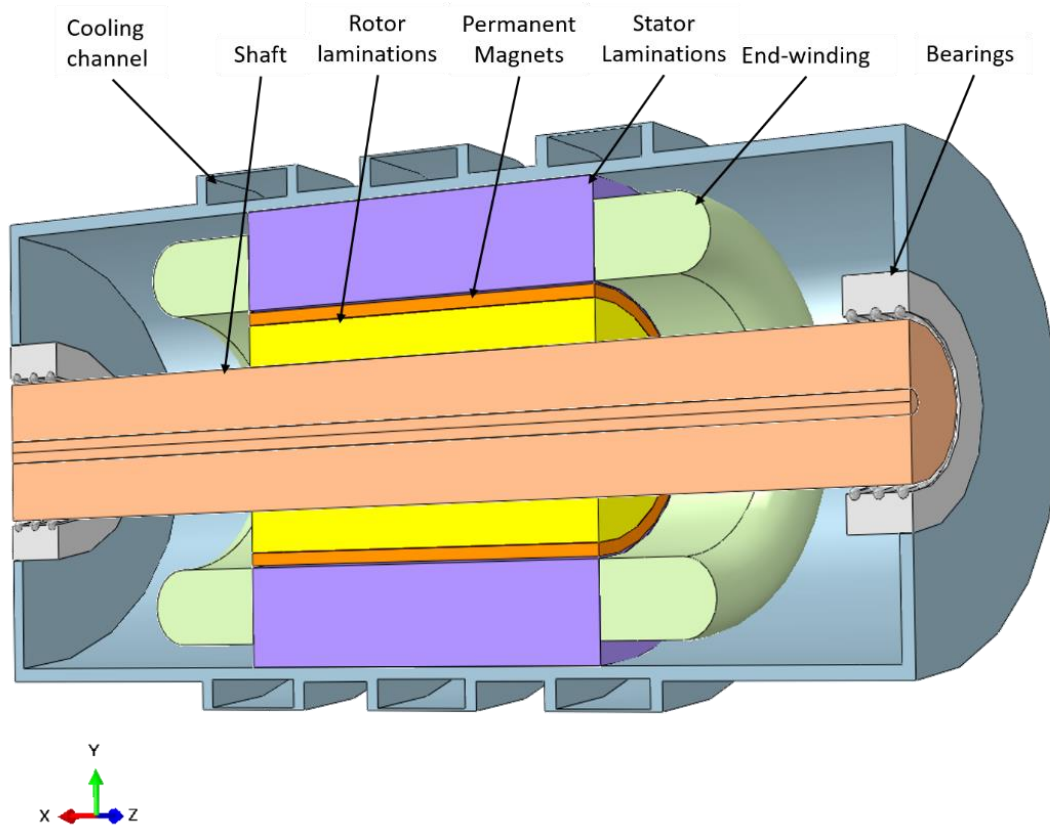


Figure 1.15 : Section of a simplified electric motor geometry for modeling.

1.4.3 Electric Motors, Suitable but?

One of the challenges met in e-motors with high performance, for power traction applications, for instance, is the thermal concern. When high performance is targeted, loads should be increased and the heat produced due to losses increases correspondingly as well. Since the heat flux in a system influences its thermal behavior, the e-motor temperature evolution depends on these losses. To reach high specific power values, required to maximize motor power and minimize its weight for propulsion application, loads should be increased wisely such that acceptable motor operating conditions are respected. Vice versa, loads are limited by motor thermal conditions, specifically, the maximum allowed temperature in winding insulation and the maximum operating temperature of permanent magnets. The excessive temperature increase may irreversibly demagnetize magnets [30] or could lead to shortening motor lifetime due to overheated electric insulation material [31]. Consequently, electrical machine cooling is becoming recently one of the biggest issues in the electrical machinery industry. The thermal issue in such high specific power density machines is brought back to the huge heat fluxes

generated in confined zones. The solution resides in a configuration where the produced heat is extracted from the motor core and simultaneously evacuated to a secondary cooling circuit. Extraction and evacuation of the heat through a cooling medium should be adapted efficiently so that the aforementioned limits are not exceeded, and no hot spot points are induced in motor sensitive parts.

1.5 Thermal Issues in Electric Motors

Stating that the emerging technologies aiming to increase specific power of motors and their efficiency and performance while economizing in production cost, has issued a serious thermal problem, researchers in electric machinery sector are concerned in finding suitable cooling solutions. To overcome the resulting thermal problem in electric motors and maintain acceptable temperatures in their critical components, some cooling techniques have been developed. In classical electric machines, traditional cooling methods managed to give satisfactory results in terms of temperature being maintained far below the limits. The machine cooling was handled sometimes with the simple natural convection as in Totally Enclosed Non-Ventilated (TENV) machines or with forced air-cooling through a fan as in Totally Enclosed Fan-Cooled (TEFC) type. These techniques rely on the machine ‘global cooling’ concept, which is adopted regardless of the heat generation location.

The developed e-motors, or prototypes being investigated, for the electrified vehicles’ propulsion, should have more sophisticated cooling than a global cooling concept, such as forced air or liquid cooling on specific areas. These techniques fall under the ‘specific and efficient cooling’ approach. During the design stage, motor cooling techniques and circuits must be accurately considered and integrated into thermal models to get reliable temperature results. This procedure requires sophisticated and detailed analysis and integration of coolant circuits’ to genuinely assessing the motor thermal behavior.

1.6 Purpose and Thesis Contents

The purpose of the present study is to thermally model specific motors designed in HASTECS project (Work-Package 1) for the propulsion of a hybrid aircraft and to find cooling solutions that could be integrated into this specific environment and context. To do so, we will start with

a presentation of the thermal characteristics and phenomena encountered in an electric motor in the following *Chapter 2*. Then, existing and future cooling solutions in electric machinery are reviewed and analyzed, to qualify their adaptability to our case-study motors.

Chapter 3 introduces the method that we will use for our model, which is the nodal network modeling method, also termed Lumped Parameter Thermal Modeling. Based on the general energy balance equation, the general matrix form of the numerical model is displayed, for application on electric motors. The bare model of the motor system is built and validated on an existing industrial motor, as close as possible to the studied motors.

In *Chapter 4*, the two target motors of the project are presented and investigated. Based on the provided electromagnetic design, the electric motor for 2025 is thermally assessed. A double liquid-cooling system in frame and shaft and an end-windings potting are adopted to maintain temperatures below the imposed limits. The resulting temperature evolutions in the motor are discussed. Besides, multiple studies are carried out on this motor to investigate the effect of some parameters and particular scenarios on the thermal behavior of the overall system. The weight of the motor with its cooling system is computed to ensure reaching the targeted value of specific power for this short-term. Whereas, for the long-term target (electric motor for 2035), several electric motor designs were assessed, and two of them are presented in this chapter for comparison purposes. The second design is adopted, and the cooling system is configured accordingly. It consists of the same cooling circuit as the electric motor for 2025, with an additional liquid cooling circuit in windings slots.

Finally, *Chapter 5* presents a study with slightly different objectives. The main goal of this chapter is to test and develop an inverse method based on the thermal model developed in *Chapter 3* and *Chapter 4* to predict motor losses using noisy temperatures. Indeed motor losses are generally difficult or impossible to measure directly. A thermal method allowing their identification would be a significant gain in the design and fabrication processes. A sensitivity study of motor temperatures to losses is conducted. It allowed determining the suitable locations of output data for each type of losses. Then, the sequential inverse method is presented. A regularization using Beck's function specification technique is applied to get losses dynamical profiles in real-time. Different cases of unknown losses are tested, and low-accessibility temperatures are predicted with high precision using the determined losses in the forward model. The method gives accurate results proving its reliability and efficiency in terms of computation time.

CHAPTER 2 E-MOTOR THERMAL MANAGEMENT STATE OF THE ART

Synopsis:

In this chapter, a literature review on the thesis topic is developed and a detailed theoretical background of the thermal management of e-machines is given.

2.1 Introduction

Conceiving the conceptual electric motors for aircraft propulsion with some tough specifications presented in *Chapter 1* comes out with multiple issues related to the thermal constraints and the cooling concepts. A detailed review of all existing techniques used for the thermal management of these motors is crucial to initiate the investigation of this topic. Great time investment was accorded to create a full state of the art on e-motor thermal management and apprehend the thermal phenomena inside the motor. In literature, suggestions can be found for global and specific cooling solutions to deal with the encountered problems. Classical approaches as well as recent advancements in thermal management are both reviewed to choose the most adapted technologies for the targeted motors. Since our motors to be conceived should have a super-high specific power, it is expected to have specific zones with hot spot temperatures. Therefore, particular attention to cooling methods of targeted parts of the machine should be drawn, particularly for zones where global cooling methods seem to be less effective, and where promising solutions are required.

The main physically dissociated parts of the electric motor are the rotor, the stator, and the frame. Hereby, a state of the art on heat transfer (conduction and convection modes) and heat extraction in electrical machines is detailed. The issue of radiation heat transfer will be discussed later in this thesis. This review consists of the following parts:

- i. Conduction heat transfer in the motor components
- ii. Convection phenomenon specifically in airgap and end windings
- iii. Renowned and groundbreaking cooling methods existing so far or being investigated for future application in electric machinery.

For simplification purposes, the symbols and letters used for variables in this chapter are not included in the Nomenclature section but are defined when mentioned.

2.2 Heat Transfer in Electric Machinery

Conduction and convection modes of heat transfer occurring in electric motors and their related issues are developed in this section. A general description of these modes and the definition of some important dimensionless numbers are presented.

2.2.1 Conduction Mode

The conduction mode of heat transfer is based on diffusion phenomena in a physical medium. Further information on the theory of heat transfer is found in [32], [33]. Studying the thermal conduction issue in an electric motor is related to assessing mainly the solid components of the motor. This assessment requires first specifying the adequate material for each component. Each material is chosen based on many criteria to meet the overall intended performance. The motor material composition and related conduction heat transfer occurring in the electric machines are known to be a complex and challenging problem that was investigated for decades. It is specifically challenging at some specific zones where hot spot temperatures, due to the low efficiency of conduction heat transfer, are encountered. When such problems occur at these levels, there will be no significant impact of optimizing other heat transfer modes (such as convection) on the thermal behavior of electric machines. Changing the materials, their ratios in heterogeneous elements, or even their dimensions would make a difference. However, any change in these characteristics will influence the loads of the machine and can affect its electrical performance. A trade-off decision is required between thermal and electromagnetic constraints.

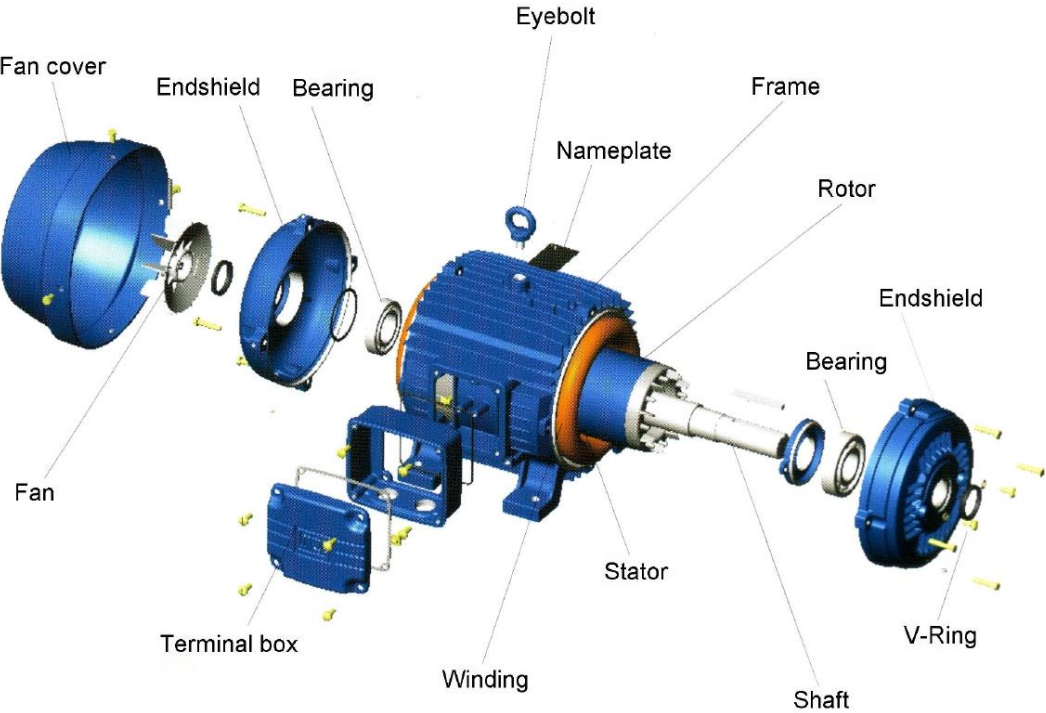


Figure 2.1 : Dissociated components of an electric motor [34].

The structure of the electrical machine consists of different parts as presented in *Figure 2.1*. In this configuration, the main machine components are the following: windings (made of coils), stator laminations, rotor laminations, motor housing (or frame), and eventually the magnets (in electrical machines with permanent magnets)

Each component will be described and studied from a thermal point of view. It will help to understand the element composition and structure and will allow figuring out the modeling of the conduction heat transfer in the motor.

2.2.1.1 Windings

The windings are formed with metallic coils covered by electrical insulation material(s), which can be generally a coat of insulator around the coil, traditionally a varnish, and lately, other constituents are added such as epoxy resin for impregnation. At the end-motor sides, the windings are coiled around the teeth, which creates a shape of wreaths that cover the stator at the cavities' sides. These wreaths are called end-windings.

According to [35], the impregnation material of the end windings and stator slots affects quite significantly the thermal behavior in electric machinery. Their experimental data show that around these two regions, the temperature reaches a serious peak value. In this same context, the authors explained that the hot spot temperature found in one of these two regions is essentially due to the low thermal conductivity of the impregnation material. The filling insulation material of the windings prohibits an efficient heat extraction from the conductors. What is practically occurring in these zones is that the heat produced due to Joule losses, hardly extracted from the metal, will result in temperature rise and will require more cooling effort. For this purpose, deep investigations of these two parts (the end winding and stator slots) are conducted. Materials are classified according to their characteristics and properties: electric properties (especially resistivity, which is directly related to electrical resistance), density, and thermal properties (mainly specific heat capacity and thermal conductivity).

Nategh et al. [36] used varnish and epoxy (named Epoxylite, which is a specific trademark of Elantas PDG, Inc., St. Louis, MO, USA) for winding impregnation in their studied motors. They presented a practical approach to model the thermal effects in directly-cooled electric machines. But later the authors in [35] studied the SbTCM, a silicone-based material, with higher thermal conductivity than epoxy and varnish ($3.2 \text{ W}\cdot\text{m}^{-1}\cdot\text{K}^{-1}$ compared to $0.85 \text{ W}\cdot\text{m}^{-1}\cdot\text{K}^{-1}$ for epoxy and $0.25 \text{ W}\cdot\text{m}^{-1}\cdot\text{K}^{-1}$ for varnish). They concluded that there is no change in thermal, mechanical, and electrical properties for the SbTCM under medium-term

tests (>1000 hours) at 150 °C. Table 2.1 groups the material characteristics considered for comparison. An evident reduction of the hot spot temperatures of electric machines was observed for the machines manufactured using SbTCM compared to those with varnish and epoxy.

Material	SbTCM	EpoxyLite	Varnish
Thermal conductivity ($W \cdot m^{-1} \cdot K^{-1}$)	3.2	0.85	0.25
Dielectric Strength ($kV \cdot mm$)	10	20	80
Price (PU)	4	2	1

Table 2.1 : Some characteristics of the materials used for impregnation [35].

This result can be justified by the relatively high thermal conductivity that SbTCM has. Despite the thermal gain obtained when using the SbTCM, this material is widely less reassuring from electric and economic sides, but deeper investigations proved that using materials with higher thermal conductivities, such as SbTCM, leads to increase torque densities, machine reliability, and machine efficiency (regardless of the impact of slot fill factor on the produced copper losses). This is the reason why the SbTCM can be considered as a promising solution for the thermal hot spots encountered in the end windings and stator slots in electric motors. The SbTCM was adopted in the work of [37] consisting of the cooling of traction electric motors.

2.2.1.2 Metallic Materials

Multiple parts of the electric machine, more specifically the synchronous electric motor, are made, totally or mostly, from metals. These parts are the housing (frame), the end-caps, the stator laminations, the conductors in windings, and the rotor. In general, for the stator laminations, the FeSi alloy is mostly used which is an iron-based alloy with silicone, in addition to other iron alloys that can be used. The winding conductors are commonly made of copper coils.

In an electric machine, there is a noticed interest in using aluminum (Al) in the structure of the housing, made classically of rolled-steel. Beginning with the mechanical features, Al metal gives high structural strength due to the stress and vibration resistance property of this material. Besides, Al frame motors are characterized by their lightweight compared to rolled-steel frame motors. On the other hand, from a thermal point of view, it is evident that Al has advantages over steel for the exceptional heat dissipation capacity and structural integrity of this metal that Siemens [38], one of the leading industry in motors, produced electric motors with aluminum coils.

Aluminum has a much better thermal conductivity than steel, but the former can be used at much higher temperatures than Al, which becomes soft above $400\text{ }^{\circ}\text{C}$ temperature.

In [39], the authors reviewed the modern heat extraction systems for electrical machines. In their work, they compared Al and Cu from a thermal viewpoint. This comparison of properties is reported in *Table 2.2* showing the higher specific heat and lower density of Aluminum against Copper.

Material	Copper	Aluminum 99.9%
Electric resistivity at $20\text{ }^{\circ}\text{C}$ ($\Omega\cdot\text{m}$)	1.724×10^{-8}	2.826×10^{-8}
Thermal conductivity ($\text{W}\cdot\text{m}^{-1}\cdot\text{K}^{-1}$)	386	205
Density ($\text{kg}\cdot\text{m}^{-3}$)	8890	2700
Specific heat ($\text{kJ}\cdot\text{kg}^{-1}\cdot\text{K}^{-1}$)	0.385	0.833

Table 2.2 : Copper and aluminum characteristics [39].

❖ Laminations

The stator of an electric motor consists of laminations of ferromagnetic material separated alternatively by insulator sheets. The stator laminations are usually made of magnetic alloys to reduce the induced Foucault currents. The iron is responsible for the low resistivity of the sheets while the added materials work on increasing this resistivity with a maintained level of polarization. Three main alloys were investigated in the literature [40]: Iron-Silicone (FeSi), Iron-Cobalt (FeCo), and Iron-Nickel (FeNi). The latter (FeNi) is the less dissipative. However, this alloy has relatively high permeability and average values of density and crack resistance. FeCo is the most dissipative alloy. As previously mentioned, FeSi is the alloy of preponderant use regarding the low resulting iron losses, the high resistivity, and its moderate density. However, those three alloys have many problems looking from economic and environmental sides.

The investigation of promising materials led to finding the Soft Magnetic Compound-(SMC), which is a kind of micro-dimensional granules or powder that deals with the technical and economic requirements. It was used in electric motors investigations such as in [41].

❖ Magnets

The rare-earth-based hard magnetic material Neodymium Iron Boron (NdFeB) is the most commonly used material for the permanent magnet of electric motors. Since Hybrid Electric Vehicles (HEV) have emerged, this material has offered the possibility to get higher performance of machines. The motor technology that uses NdFeB has allowed the development

of compact electric traction motors with higher torque and higher power density [42]. Besides, the demagnetization of magnets is a possible failure mechanism in the electric motor. The demagnetization curve has a strong dependence on magnets' temperature. Sm2Co17 (Samarium-Cobalt) magnets are also used in electric machinery. They show a relatively high resistivity to temperature compared to NdFeB, which makes them appropriate for use in high specific power synchronous machines where high temperatures may be easily attained.

2.2.2 Convection Mode

In this paragraph, we are interested in presenting the numerical and experimental models (and resulting reliable correlations) elaborated by authors for setting the thermal parameters for convection heat transfer in the machine internal cavities. These cavities refer to the internal spaces between the rotor-stator configuration and the motor housing (black areas in *Figure 2.2*).

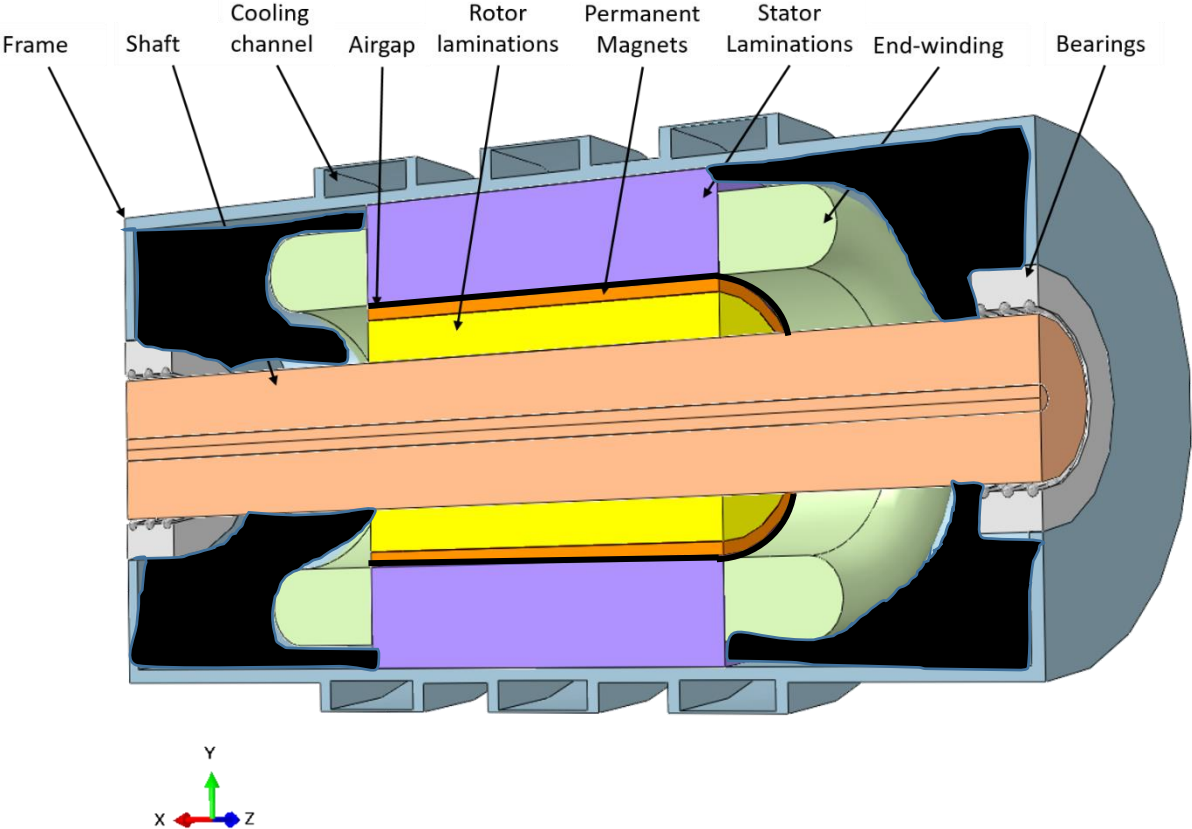


Figure 2.2 : 3-D section of a permanent magnet synchronous e-motor showing in black color the air spaces inside the machine.

The convection transfer inside the motor is divided into three main regions of convection in the motor:

- iv. The airgap between rotor and stator,
- v. The rotor end-disk,
- vi. The end-space regions (mainly the end-windings and the frame inner surfaces at both motor sides).

Let us begin with general definitions in this field. Essentially, convection is the heat transfer mode where a fluid interacts with a surface such that the fluid and the surface exchange thermal energy. Three types of convection exist: natural, forced, and mixed convection types. In natural convection, the fluid motion is due entirely to the buoyancy forces arising from density variations in the fluid, while in a forced convection system, an external force causes the fluid motion. Mixed convection is when both phenomena occur simultaneously and comparably (i.e. a density variation accompanied with imposed velocity).

In the electric motor, we distinguish external convection at the motor external surfaces, and the internal convection, which often takes place in a confined area (the closed area not connected to the atmosphere and where specific conditions are imposed), for example in the airgap [43]. The heat transfer law of convection (Newton's law) is defined by:

$$\varphi_{cv} = h(T_w - T_{ref}) \quad (2.1)$$

Where φ_{cv} is the heat flux, h is the convection heat transfer coefficient, T_w is the surface temperature, and T_{ref} is fluid reference temperature. Kreith et al. [44] presented the range of values generally reached by h , depending on the fluid nature, its physical state, and the convection type and characteristics (see *Table 2.3*).

Fluid	Convection Heat Transfer Coefficient	
	W/m ² K	Btu/h ft ² °F
Air, free convection	6–30	1–5
Superheated steam or air, forced convection	30–300	5–50
Oil, forced convection	60–1,800	10–300
Water, forced convection	300–18,000	50–3,000
Water, boiling	3,000–60,000	500–10,000
Steam, condensing	6,000–120,000	1,000–20,000

Table 2.3 : Order of magnitude of the convection heat transfer coefficient [44].

Some dimensionless numbers are used to characterize the convection phenomenon according to its type. Above all, the Nusselt number allows the determination of the convection coefficient and is defined by:

$$Nu = \frac{hL_{ref}}{\lambda_f} \quad (2.2)$$

Where L_{ref} is the characteristic length of the surface of heat exchange, also called hydraulic diameter D_h , and λ_f is the fluid thermal conductivity. When a circular channel is the fluid domain, the D_h is the channel diameter, in other cases, D_h is computed as: $D_h = 4 \times \text{channel section/wetted perimeter}$.

Other dimensionless numbers are often used in convection defined by:

$$\text{Prandtl number } Pr = \frac{c_p \mu}{\lambda}$$

- Forced and mixed convections:

$$\text{Axial Reynolds number } Re_{L_{ref}} = \frac{\rho u L_{ref}}{\mu}$$

$$\text{Rotational Reynolds number (mainly for rotational flows): } Re_{\omega} = \frac{\omega r_i L_{ref}}{\nu}$$

- Natural and mixed Convections:

$$\text{Grashof number } Gr = \frac{\beta g \Delta T \rho^2 L_{ref}^3}{\mu^2}$$

$$\text{Rayleigh number } Ra = Gr Pr$$

Where:

μ is the fluid dynamic viscosity,

ρ is the fluid density,

c_p is the fluid specific heat capacity,

u is the fluid velocity,

ΔT is the temperature difference between surface and fluid,

L_{ref} is the length,

ω is the rotational velocity,

ν is the kinematic viscosity,

r_i is the outer radius of the inner cylinder (rotor)

β is the fluid coefficient of thermal expansion, equals to $1/(273+T_{Fluid}^{\circ C})$ for perfect gases,

g is the gravitational acceleration.

Through literature, the calculation of convection coefficient is mainly based on the empirical formulations, as stated by [45], and convection correlations from [32], [33], specifically for common geometries. Nowadays, due to the complexity of the flow dynamics and the geometries investigated, the coefficient h is often determined through numerical (CFD) and/or experimental methods. In our study, we were based on correlations from literature to compute these coefficients.

2.2.2.1 *Stator-Rotor Airgap Convection*

The stator-rotor airgap in an electric machine is the space between the rotor external surface and the stator inner surface. The geometry in the electric machine could be assimilated to two coaxial cylinders where the inner one is in rotation while the outer one is fixed. The space between rotor and stator in an electric motor is relatively thin and the thermal effects are generally critical on windings and magnets. This region creates a radial heat path between stator and rotor and could have either a negative impact on hot spot temperature (when a significant heat flux is dissipated due to friction in this area) or a positive impact by a possible air-cooling axial flow (mainly in the case of open-motor configuration). The flow dynamics analysis in this region is crucial for obtaining temperature gradients. It helps in finding the heat transfer coefficient h . Some authors studied the airgap convection specifically in rotating electrical machines for annular case ([46] and [47]) and non-annular (or slotted) case ([48]). Other authors reviewed both annular and non-annular airgap cases ([43], [49]). Since in our case, the PMSM has surface-mounted magnets that cover the whole rotor surface to form a cylindrical shape, only an annular airgap flow case is considered, and the corresponding heat transfer studies are presented.

The governing flow in a closed machine is the Taylor-Couette flow, while in an open machine, where there is an additional axial cross flow, it is rather the Taylor-Couette-Poiseuille flow. The distinction between the two cases is that for the former, there is only the effect of the rotor rotation while for the latter there is also the external force of the axial flow acting on the fluid. As the motor is applied in specific environmental conditions, a closed configuration is maintained for this aeronautical application and a brief review of the annular airgap case without axial flow is presented.

This current study concerns the Taylor-Couette flow (normally with no or slight axial flow), for which a dimensionless number characterizes the importance of centrifugal forces, which is the Taylor number Ta , defined by:

$$Ta = \frac{\omega^2 (r_e - r_i)^3 r_i}{\nu^2} \quad (2.3)$$

Where r_e and r_i are respectively the inner stator diameter and outer rotor diameter.

Bertin et al. [47], Fasquelle [43] and Fénot et al. [49] adopted a slightly different correlation for a modified Taylor number Ta_m as follows:

$$Ta_m = \frac{\omega^2 (r_e - r_i)^3 r_m}{\nu^2 F_g} \quad (2.4)$$

where $r_m = (r_e - r_i) / \ln(r_e / r_i)$, and F_g is the geometrical factor that has many definitions depending on the airgap type and form (annular, slotted, with or without axial flow [50]) and is around the value of 1 for a narrow airgap. In [47], the authors suggested the computation of this factor as follows:

$$F_g = \left(\frac{\pi^4}{1697 P_g} \right) \left(\frac{r_e + r_i}{2r_i} \right) \quad (2.5)$$

Where P_g is calculated as a function of e and r_i based on the following:

$$P_g = 0.0571 \left[1 - 0.652 \left(\frac{e}{r_i} \right) \right] + 0.00056 \left[1 - 0.652 \left(\frac{e}{r_i} \right) \right]^{-1} \quad (2.6)$$

Fénot et al. [49] unified the formulations of the three parameters: Taylor number, the characteristic length, and Nusselt number, to compare results from different authors' works. The dynamical property that defines the flow regime, in this case, is the rotor speed (referred to as the inner cylinder rotational velocity) ω . Besides, the channel performance coefficient (also called aspect ratio of the radial cylindrical gap) is defined by: $\eta = \frac{r_i}{r_e}$. Based on [51], for low rotor speeds, the flow is steady and laminar (Couette flow). There is a critical Taylor number Ta_{cr} corresponding to a critical speed ω_{cr} , for which the torque transmitted to the fluid begins to increase faster, as the rotational speed increases [49]. Above this value, the flow is a Taylor vortex flow and vortices (called Taylor vortices) appear as can be seen in *Figure 2.3*. These vortices are in an axially centered disk form. Coles et al. [52] described that when further increasing the velocity and exceeding the critical Taylor number to reach a ratio of $Ta/Ta_{cr} =$

1.2 with a narrow gap ($\eta = 0.95$), a wavy mode appears (*Figure 2.3*) with azimuth waves [53]. Then the number of waves increases with velocity to reach a constant maximum for a range of values of the ratio: $4.5 < Ta/Ta_{cr} < 25$. The critical Taylor number in the case of two co-axial cylinders is determined by [51] as: $Ta_{cr} = 1700$.

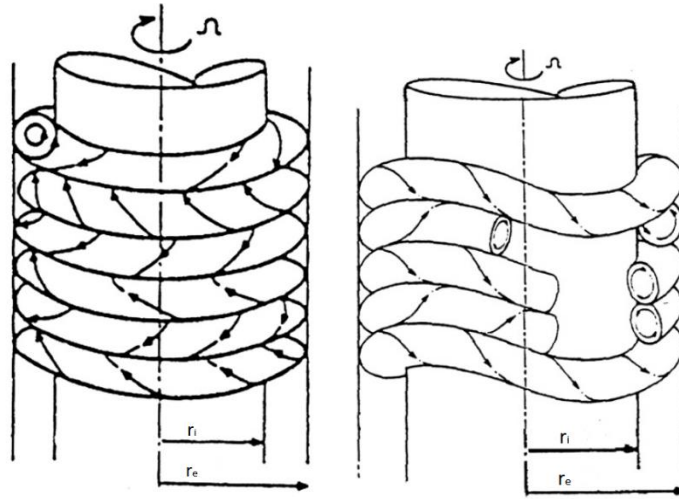


Figure 2.3 : Taylor Vortices (left) and Azimuth waves (right) [53].

In a Taylor-Couette flow, [49] focused on three types of flows: Couette, Taylor vortex, and turbulent flows, and provided heat transfer correlations to well define the heat transfer phenomena happening between two co-axial cylinders. For a closed annulus system with a rotating inner cylinder in both laminar and turbulent flow modes without axial flow, [53] proposed the following expression of the global Nusselt number:

$$Nu_{D_h} = \frac{D_h h_{rs}}{\lambda_{air}} \quad (2.7)$$

Where the characteristic length is D_h is the hydraulic diameter of the airgap, λ_{air} is the thermal conductivity of the air, and h_{rs} is the heat transfer coefficient between rotor and stator defined by:

$$h_{rs} = \frac{\Phi_{rs}}{S_m (T_r - T_s)} \quad (2.8)$$

Where S_m is the average surface between rotor and stator ($S_m = \frac{S_{rotor} + S_{stator}}{2}$), T_r and T_s are respectively the rotor and stator temperatures, Φ_{rs} is average flux density between the rotor and stator. The hydraulic diameter D_h is defined as:

$$D_h = 4s_{ag}/P_{gm}$$

Where s_{ag} is the airgap section and P_m is the wetted perimeter of the airgap area.

Herein, the thermophysical properties of the fluid are calculated at the average air-film temperature T_f :

$$T_f = \frac{T_w + T_\infty}{2} \quad (2.9)$$

Where T_w is the wall (surface) temperature and T_∞ is the air temperature in airgap.

Below the critical Ta number, heat transfer across the gap is quasi-conductive. In this same strategy, and for the Couette flow part ($Ta < 1700$), the constant value of the Nusselt number found by some authors ([54]) was: $Nu = 1$. Becker et al. [55], Gazley et al. [53] and Bjorklund et al. [56] determined a value of Nusselt number of 2, when a laminar and stable flow type is considered. This specific value corresponds obviously to the radial conduction phenomenon in the air driven into rotation in the annular space between the rotor and stator.

When Taylor number is increased with increasing the rotational speed until reaching Taylor vortex flow and then turbulent flows, it was concluded from previous studies that Nu increases with Ta , which means a higher heat transfer. Authors in [55], [57]–[59] described another transition at $Ta = 10^4$ corresponding to a minimum of wavelength. Fénot et al. [49] explained that the lack of information about this second transition in some authors' results is due to two possible factors: either the difference in experimental settings or the relatively small range of Ta values before the transition. Tachibana et al. [54], [60] observed one additional transition for $Ta = 10^8$ when working with relatively high Taylor numbers. *Figure 2.4* depicts the comparison between different authors correlations from [49] according to a common definition for Nusselt number calculation. In this comparative graph, variation in line slope is observed for the high Ta region.

As previously presented, there are general forms of empirical formulations (elaborated from experiments) of the Nusselt number as a function of the Ta reported to be: $Nu = K_b Ta^{n_b}$

Where K_b and n_b are constants depending on the values of a geometrical factor (radial cylindrical gap aspect ratio).

Nusselt number expressions for Taylor vortex flows are used by several authors ([43], [53], [56]), based on Taylor [61]. It is expressed according to Taylor number ranges as in equation (2.10).

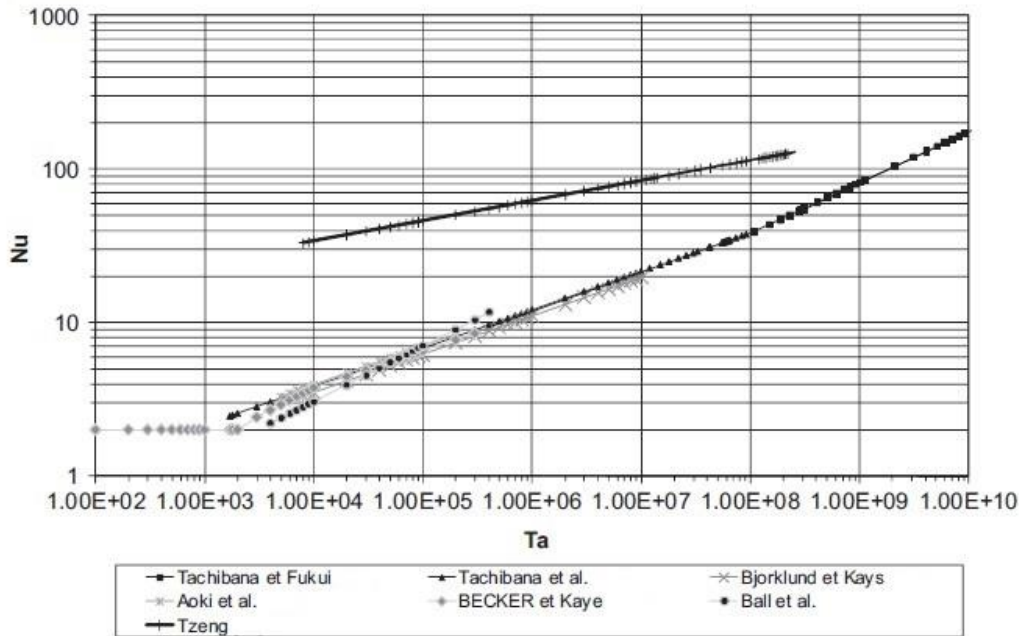


Figure 2.4 : Comparison of the evolution curves of Nusselt number (modifying its definition to have coincidence between authors' results) with respect to Taylor number [49].

$$Nu = 0.128 Ta^{0.365} \text{ for } 1700 < Ta < 10^4$$

$$Nu = 0.409 Ta^{0.241} \text{ for } 10^4 < Ta < 10^7$$
(2.10)

2.2.2.2 Rotor End-Disk Convection

The convection heat transfer issue at the rotor end-caps in each side of the motor facing the lateral frame surfaces can be solved using a simple modeling approach. The configuration is thought to be comparable to the geometry of a rotating disk in an air domain. For the electric machine, the disk is enclosed in an air cavity of thickness ϵ (see *Figure 2.5*). The determination of the corresponding coefficient should be performed according to the case of a rotating disk in a closed space [47].

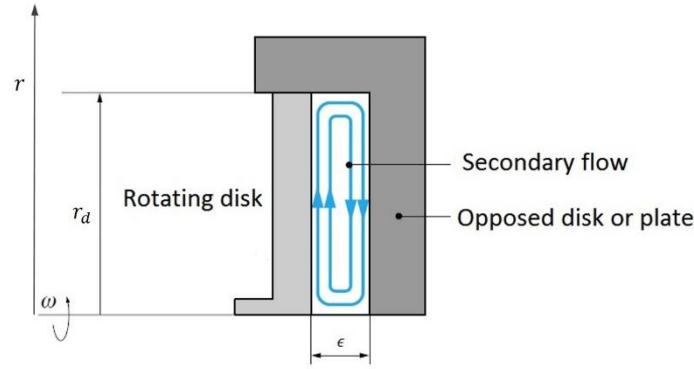


Figure 2.5 : Lateral view of the enclosed rotating disk [47].

For the rotating disk, a local Reynolds number and a global Reynolds number, Re_r and Re_ω respectively, are defined as follows:

$$Re_r = \frac{\omega r^2}{\nu} \quad (2.11)$$

$$Re_\omega = \frac{\omega r_d^2}{\nu} \quad (2.12)$$

Where r is the radial coordinate and r_d is the disk radius.

The authors of [46], [47], [62] reviewed the configuration of a disk in closed space (shroud cylinder covering it). Critical Reynolds numbers were ranged in [63] for the flow transition (from laminar to turbulent) according to literature, between 1.8×10^5 and 3.6×10^5 . From the authors' works, there are general correlations forms for the local and average Nusselt numbers respectively as follows:

$$Nu_r = c_1 \times Re_r^{d_1} \quad (2.13)$$

$$\overline{Nu_{r_d}} = c_2 \times Re_\omega^{d_2} \quad (2.14)$$

where the indices r and r_d are relative to the radial coordinate and the radius of the disk, respectively. As explained in [62], coefficients c_1 and c_2 depend on the flow regime, Prandtl number Pr , and radial temperature distribution on the disk; for laminar and turbulent flows they are highly affected by the temperature profile. Whereas d_1 and d_2 are only influenced by the flow regime (Re number). For laminar flows and isothermal disk surface, $d_1 = d_2 = 0.5$, and $c_1 = c_2 = 0.28$ to 0.38 ; for transient (laminar to turbulent) flows, coefficients are grouped in Table 2.4 from [64]–[66]. Finally for turbulent flows and isothermal surface, $d_1 = d_2 = 0.8$, $c_1 = 0.0179$ to 0.0197 , and $c_2 = 0.015$ (evaluation of all constants is for $Pr = 0.72$).

Authors	Correlation	Lowest Re	Highest Re
Popiel et al.[64]	$Nu_r = 10 \times 10^{-20} Re_r^4$	1.95×10^5	2.5×10^5
Elkins et al. [65]	$Nu_r = 2.65 \times 10^{-20} Re_r^4$	2.9×10^5	3.6×10^5
Cardone et al. [66]	$Nu_r = 8.01 \times 10^{-14} Re_r^{2.8}$	2.6×10^5	3.5×10^5

Table 2.4 : Local Nusselt numbers over a rotating disk for transitional flows [62].

Kreith et al. [67] found, from the experimental data obtained, a correlation for Nusselt number of a rotating disk in a closed space (Nu) compared to that in a free space (Nu_∞). Bertin et al. [47] reported the equation of the free space case and its corresponding coefficients (Table 2.5); this equation is as follows:

$$Nu_\infty = \frac{4a}{2b_1 + 1} Re_\omega^{b_1} Pr^{b_2} \quad (2.15)$$

Application Domain	Wall conditions	a	b_1	b_2	Flow regime
$Re < 1.8 \times 10^5$	-	0.41	0.5	0.44	Laminar
$Re < 2.5 \times 10^5$	uniform T	0.024	0.8	0.6	Turbulent
	uniform φ	0.031	0.8	0.6	

Table 2.5 : Coefficients of the correlation equation (3.26) of Nu_∞ depending on the flow type [67].

In Figure 2.6 the ratio Nu/Nu_∞ is represented as a function of the aspect ratio of the cavity G (ratio of the cavity thickness to the disk radius: ϵ/r_d). It is evident that when this geometrical coefficient is above the value $\epsilon/r_d = 0.2$, the Nusselt number is equal to Nu_∞ .

In [44], the Nusselt number is evaluated with respect to the disk radius $r_d = r_0$ and a critical value r_c of the radial coordinate (indicating the radial limit between flow regions: laminar and turbulent) as follows:

$$\overline{Nu}_{r_0} = 0.36 \left(\frac{\omega r_0^2}{\nu} \right)^{0.5} \left(\frac{r_c}{r_0} \right)^2 + 0.015 \left(\frac{\omega r_0^2}{\nu} \right)^{0.8} \left(1 - \left(\frac{r_c}{r_0} \right)^{2.6} \right) \quad (2.16)$$

They described the different flows and transition radii as well as the different boundary layers for each flow type as presented in Figure 2.7.

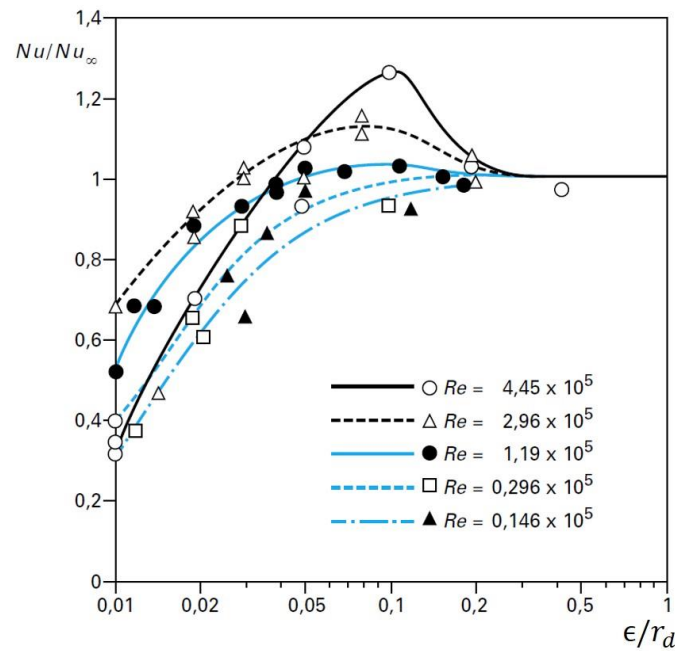
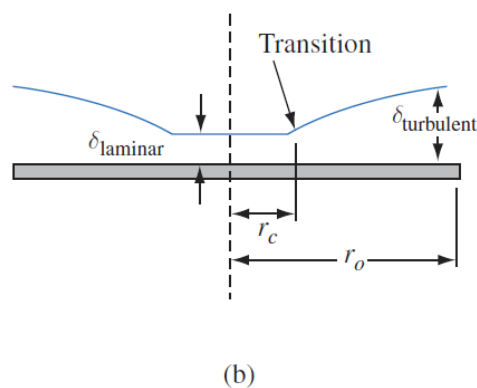


Figure 2.6 : Nu/Nu_{∞} as function of geometric ratio ϵ/r_d and Re [67].



(b)

Figure 2.7 : The rotating disk velocities' profiles and transition radii and their impact on boundary layer thickness δ [44].

Four flow regimes are deduced in [68] from their experimental and theoretical study of an enclosed rotor-stator. The graph of *Figure 2.8* represents the four different flow regimes as regions, separated by the partition curves and governed by the two parameters $G_c = \epsilon/r_d$ and Re number. They reported the moment coefficient (\mathcal{C}_M) correlations based on the torque measurement. Moreover in [69], the authors evaluated Nusselt number (Nu) according to the region to which the flow belongs (*Table 2.6*).

Regions	ζ_M from Daily [68]	Nu from Vasilescu [69]
I	$\pi G_c^{-1} Re_\omega^{-1}$	$0.6119 G_c^{-1}$
II	$1.85 G_c^{0.1} Re_\omega^{-0.5}$	$0.2195 G_c^{0.1} Re_\omega^{0.5}$
III	$0.04 G_c^{-0.167} Re_\omega^{-0.25}$	$0.00823 G_c^{-1/6} Re_\omega^{0.75}$
IV	$0.051 G_c^{0.1} Re_\omega^{-0.2}$	$0.0092 G_c^{0.1} Re_\omega^{0.8}$

Table 2.6 : Torque and Nusselt number correlations according to the flow regions.

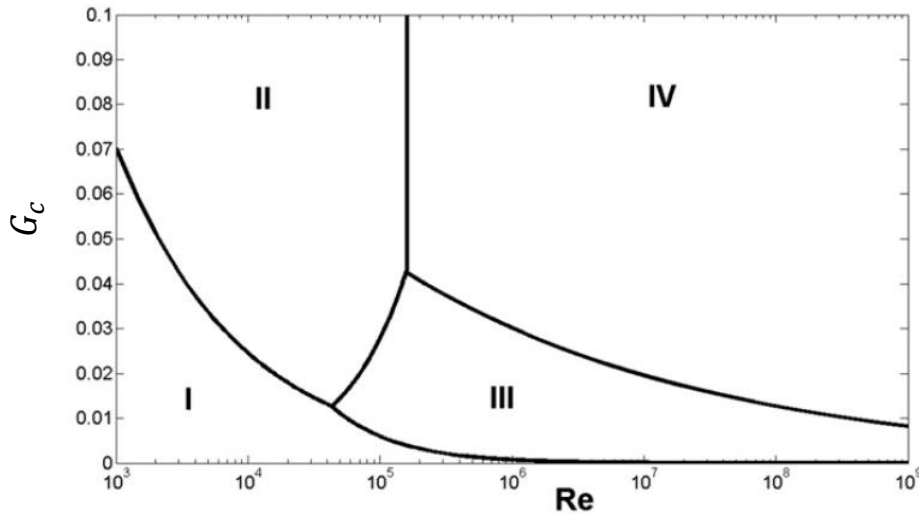


Figure 2.8 : Flow regions in an enclosed stator-rotor cavity according to G and Re (rotational). I --> laminar merged boundary, II --> laminar unmerged boundary, III --> turbulent merged boundary, and IV --> turbulent unmerged boundary [68].

In our motor application, depending on G_c value, the corresponding correlation is adopted to evaluate the convection coefficient in rotor end-disk. The aspect ratio G_c depends on the geometry of the machine, subject to multiple variations throughout the thesis.

2.2.2.3 End-Space Regions Convection

The correlations for the coefficient of convective heat transfer in the end-space regions of an electric machine (especially end windings and cavities' internal surfaces) and the thermal problems related to these regions are elaborated through some bibliographical reviews and publications. Generally, several authors ([44], [45], [70]–[72]) based their electric motors studies on the following correlation, for the convection phenomenon at the end-space region:

$$h = k_1[1 + k_2 u^{k_3}] \quad (2.17)$$

Where k_1 , k_2 , and k_3 are curve fit coefficients and u is the average air velocity.

❖ *End Windings*

In [47], the authors studied forced convection around the end-windings and suggested the correlation of Nusselt number found by [73] for the cooling of end-windings of small electrical machines in different geometrical forms as a function of the end windings Reynolds number (Re_{ew}):

$$Nu = K_1 Re_{ew}^{0.8} \quad \text{for } 25000 < Re_{ew} < 125000 \text{ and } 0.031 < K_1 < 0.04 \quad (2.18)$$

In the thesis of [74], they investigated experimentally and numerically the heat transfer coefficients at the end-winding surface according to each end-winding part. They grouped their results from experiments and simulations for thick and thin end-windings (*Figure 2.9*), and it is concluded from these results that at the far end of the end-windings (the zone where coils are folded), there are the lowest heat transfer coefficients. Pickering and their co-authors [75]–[78] worked on the heat transfer in different end winding configurations. In [79], they investigated the heat transfer in a high-voltage strip-wound 4-pole induction motor ventilated with a fan mounted on the motor rear end (air outlet end). They found that the overall heat transfer coefficient in the fan side of the end windings was much higher than that at the air inlet end. Furthermore, they studied the effect of removing the wafers (which is an additional device mounted on the rotor used for changing the airflow inside the motor) on this coefficient and obtained the results in *Figure 2.10*. These results show an unexpected effect of wafers removal on the overall heat transfer coefficients at the fan end where a strong circulation of the flow is developed. The authors concluded that the wafers are thermally beneficial at the inlet end but they affect negatively the heat transfer at the motor end to fan side where the convection coefficient increases thoroughly when removing them, especially on the outer surfaces of the end-windings.

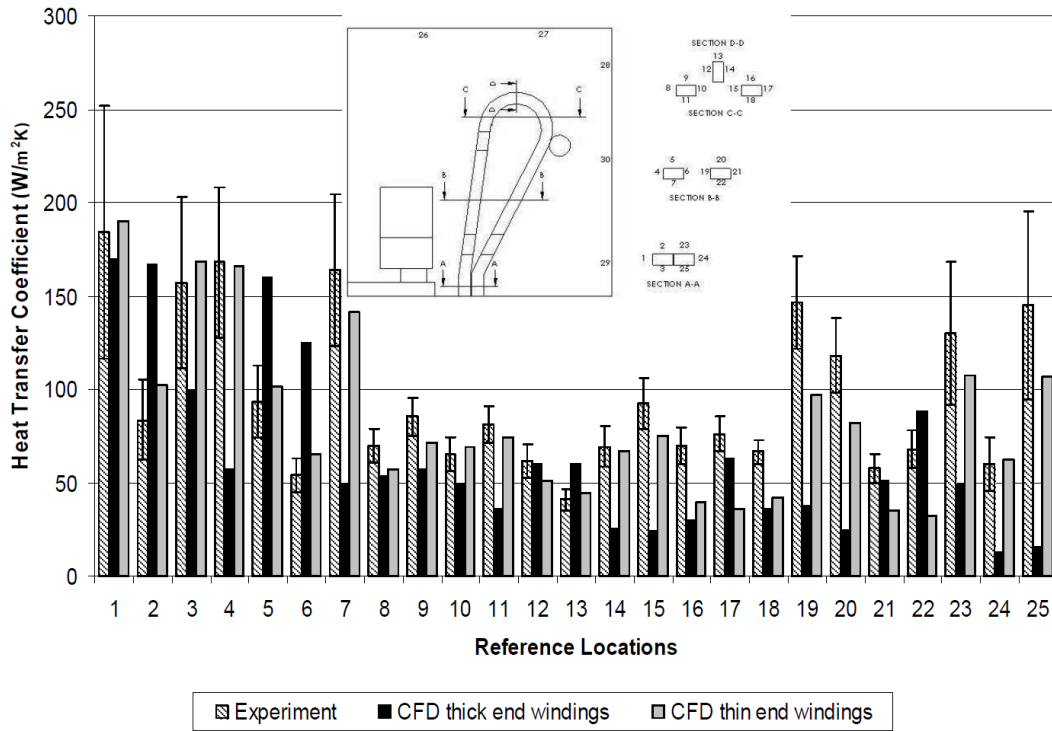


Figure 2.9 : Resulting heat transfer coefficient according to location, at the end-winding region [74].

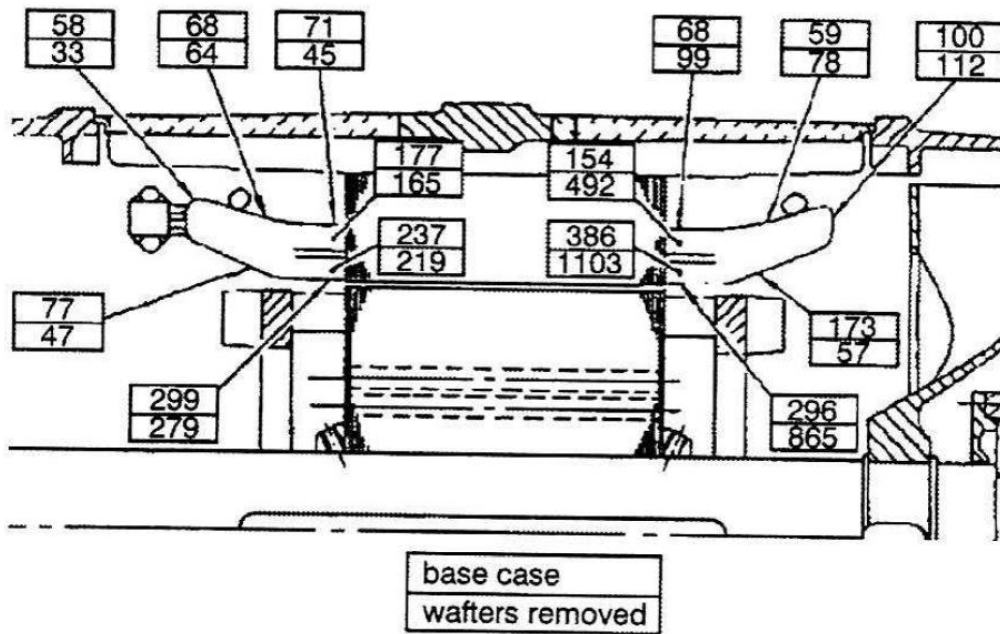


Figure 2.10 : End-winding heat transfer coefficients found by [79].

In our case, there are no wafers at the rotor surfaces and an estimated average value from the results of [74] between the lower bound of $50 \text{ W}\cdot\text{m}^{-2}\cdot\text{K}^{-1}$ and the upper bound $170 \text{ W}\cdot\text{m}^{-2}\cdot\text{K}^{-1}$, is considered for the whole end-winding.

❖ *Frame Inner Surface*

As shown in *Figure 2.11* from [45], the frame lateral inner surfaces are part of the circumferential surfaces of the e-motor air cavities (white spaces). For the convection in the frame internal static surfaces, the authors in [69] used the same correlations of the heat transfer coefficient as those of the rotor end-disk.

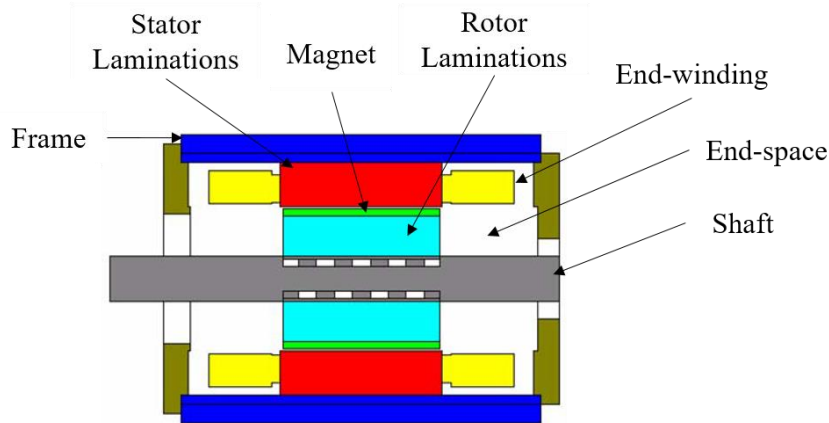


Figure 2.11 : Electric motor axial view [45].

Based on the work in [68], the authors of [80] assumed that the rotor acts as a fan, and the airflow in this end-space is turbulent due to rotor speed. They analyzed the motor thermal behavior by evaluating the Nusselt number as follows:

$$\begin{cases} Nu = \frac{3.87}{2\pi} Re_{\omega}^{0.5} Pr & Re_{\omega} < 3 \times 10^5 \\ Nu = \frac{0.146}{2\pi} Re_{\omega}^{0.8} Pr & Re_{\omega} \geq 3 \times 10^5 \end{cases} \quad (2.19)$$

$$h_{cavity} = \frac{\lambda_{air}}{r} Nu \quad (2.20)$$

λ_{air} is the air thermal conductivity, r is the rotor radius.

The authors in [70] studied also the convection coefficient at the bearing level of enclosed asynchronous machines to determine the convection coefficient: $h = 20 (1 + 0.0425 u^{0.7})$

Later, in [72], the study of the electric motor design was improved to find out a more accurate form of the correlation as follows:

$$h_{cavity} = 40 (1 + 0.1 u) \quad (2.21)$$

In [50], the authors assimilated the geometry of the cavity in electric machines to the space between two vertical or horizontal disks where one disk is heated. They used the correlations of [44] for the Nusselt number relative to the cavity's thickness (as the characteristic length).

2.3 Electric Motor Cooling Methods

The thermal study and cooling of an electric machine designed to achieve promising electrical objectives have a critical influence on its performance. We can cite from [81]: 'The analysis of heat transfer and fluid flow in electric machines is actually more complex, more nonlinear, and more difficult than the electromagnetic behavior. Bertin [82] has studied the main heat evacuation possibilities and issues in electric machines.

Nowadays the importance of finding modern solutions for acceptable maximum temperatures in the machine and uppermost heat dissipation to surrounding areas is rising. In fact, these machines are required to provide high-efficiency and huge power values specifically when applied for propulsion in the aeronautical domain, compared to what was designed in the previous decades. Similarly, automotive motors main constraint is the high specific power density. The works of researchers in this domain are studied in [83]. They have set out, explained, and evaluated different cooling schemes and methods for automotive traction motors.

Two possible strategies can be adopted to solve the thermal problems encountered. The first strategy consists of finding critical physical parameters that influence the heat transfer (for instance, it could be the structure materials used in motor construction, geometrical factors, or properties of cooling fluids, etc.), and working on optimizing them to fit with the adequate machine thermal design (passive cooling). The other strategy is to focus on developing cooling techniques allowing the highest heat dissipation (active cooling). Through literature, it is remarked that authors essentially worked on one of the two strategies for possible improvement in heat extraction methods and few of them studied both. Some parts of the machine that are classically cooled must be accurately studied in different electrical and environmental

conditions, such that their cooling will be adapted to the electrical performance of the machine and will enhance its overall efficiency. Those parts are mainly the stator, the frame, and the rotor. In this section, we will be interested in reviewing the motor cooling methods, separated into two categories: external cooling without inflowing to the motor structure and internal cooling methods when cooling media are directly cooling the inside of the motor core.

2.3.1 External Cooling Methods

The external cooling allows cooling the motor skin (the frame in this case) by creating areas of heat exchange or equipment for thermal energy release. These cooling methods do not require, in most of the cases, modifications inside the motor. They are easily mounted outside the motor but are consequently far from hot spot zones. The heat flux must get through the different parts of the motor to reach the heat sink. However, they are still used widely in electric machinery to evacuate heat through the frame. Several techniques are employed, mainly convective air-cooling through fins and liquid-cooling with water jackets.

2.3.1.1 External Cooling through Fins

The frame of an electric machine, or directly its stator sometimes, can be equipped with fins that are mounted to increase the surface of air convection of the motor stator and to improve the heat transfer (by creating a flow with forced convection for instance). Many authors raised interest in studying the effect of motor cooling through fins and their optimization as in [31], [84], [85].

On the other hand, through literature, a great number of research investigations focused on the heat transfer through fins depending on their configurations. Deployed in multiple applications (turbines, fans, heat exchangers...), numerous fins' designs can be conceived. Optimization of their shapes is proposed for finned-tube heat exchangers in [86].

Generally, the efficiency of fins depends, among other factors, on the flow nature around the stator. Both natural and forced convection types around motor finned frame are reviewed.

❖ Natural Convection with Fins

Natural Convection is one of the less expensive cooling methods since no extra components neither further consideration of the cooling system design are needed. However, an important drawback of this system is the small rate of heat transfer achieved, as detailed in heat transfer

books [32], [44]. Based on these books and other advancements in this field, the authors of [71] proposed the use of the following general correlation for natural convection in the case of electric motor application:

$$Nu = a(GrPr)^b \quad (2.22)$$

Where Gr is Grashof number calculated as follows: $Gr = \frac{\beta g \Delta T \rho^2 L_{ref}^3}{\mu^2}$, and Pr is Prandtl number determined as follows: $Pr = \frac{c_p \mu}{\lambda_f}$, a and b are given constants depending essentially on the nature of the flow and the surface shape.

Natural convection through the housing surface is mainly a function of the temperature difference between the structure and the fluid.

The total enclosed non ventilated electric machine (TENV) housing thermal behavior depends on surface characteristics. According to [45], a few examples of housings types are designed and they are usually smooth. However, the housing can be designed with fins to increase the convection surface but in a well-oriented design suitable for optimal convection cooling (i.e. without disturbing natural airflow). As suggested by [45], radial fins are suitable for vertical mounted TENV motors.

❖ Forced Convection with Fins

Improvement of heat transfer can be provided by mounting a fan on the motor shaft that induces turbulent airflow in the longitudinal direction of the motor housing. The total enclosed fan-cooled (TEFC) motor has sometimes a smooth housing, for which the Nusselt number can be obtained in terms of axial Reynolds (Re_a) and Prandtl numbers with well-known correlations for a configuration of flow over flat plate [32], [33], as follows:

- Laminar flow ($Re_a < 5 \times 10^5$ and $0.6 < Pr < 50$):

$$Nu = 0.664 Re_a^{0.5} Pr^{0.33} \quad (2.23)$$

- Turbulent flow ($Re_a > 5 \times 10^5$):

$$Nu = (0.037 Re_a^{0.8} - 871) Pr^{0.33} \quad (2.24)$$

However, motor housing is generally finned, and geometries vary according to requirements and constraints to get optimized convection cooling.

The authors of [31] studied experimentally the effect of finned casing modifications on the thermal behavior of the motor when its external surface is subjected to a flow. The authors compared commercial and prototype motors' thermal behavior and deduced that a considerable reduction in temperature due to the improvement of geometry and flow characteristics. According to [87] who conducted tests on finned induction motors and considered a turbulent flow due to existing fans and cowlings, the convection heat transfer coefficient h for semi-open channels made with axial fins is given by:

$$h = \frac{\rho c_p D_h u_a}{4 L_a} (1 - e^{-m}) \quad (2.25)$$

And m is calculated as follows:

$$m = 0.1448 \frac{L_a^{0.946}}{D_h^{1.16}} \left(\frac{\lambda_a}{\rho c_p u_a} \right)^{0.214} \quad (2.26)$$

Where L_a is the axial length of the finned frame, u_a is the airflow velocity, D_h is the hydraulic diameter of the channel; , c_p , and λ_a are respectively the density, the specific heat capacity, and the thermal conductivity of the air at the average air temperature in each channel.

Based on these correlations, the finned housing of a TEFC electric machine was recently investigated by [85]. In this work, the authors were concerned in optimizing the cooling fin design by elaborating a conjugate heat transfer model validated by CFD results and used then to evaluate whether a fine or a coarse engineering tolerance is required for the casting of motor housing. In *Figure 2.12*, the geometry shape of the studied finned motor housing is depicted.

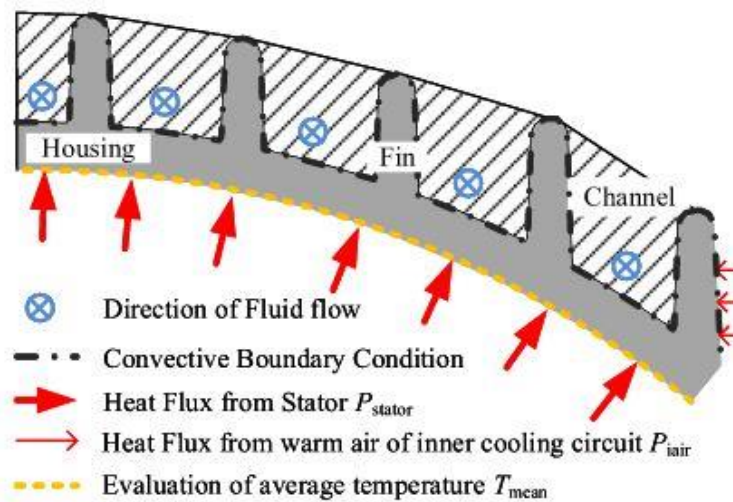


Figure 2.12 : Heat and fluid flow conditions for motor finned housing [85].

Their method consists of evaluating many possible designs of fins using a novel algorithm that allows a great reduction of candidate geometries for CFD simulations.

2.3.1.2 Frame Channels and Pipes

Intending to bring cooling closer to the heat sources in the stator, some authors propose to create a fluid circulation through stator channels. Examples are found in [36], [45], [47], [88]–[90]. Some authors investigated the fluid flow in multiple geometries of the cooling channels [47], [91]. In this latter research, the authors simulated motor behavior with different duct sections (*Figure 2.13*) and, based on this study, they recommended an oval shape for a traction motor application in a hybrid electric vehicle or zero-emission vehicle. In most cases, water is used as a coolant fluid and the technique is commonly known as water jacket cooling. Channels are classified into two groups: smooth channels and channels with perturbations (ribs). In [92] (evaluation of the 2008 Lexus LS 600H hybrid synergy drive system), oil is used as a coolant in the cooling channels of the motor, and ethylene glycol/water for heat exchanger. Cooling channels are made with Aluminum. Based on the works of [93], the authors of [89] developed a model simulating the thermal behavior of a TEFC induction machine with empirical direct lamination cooling (where cooling tubes are implemented within the frame).

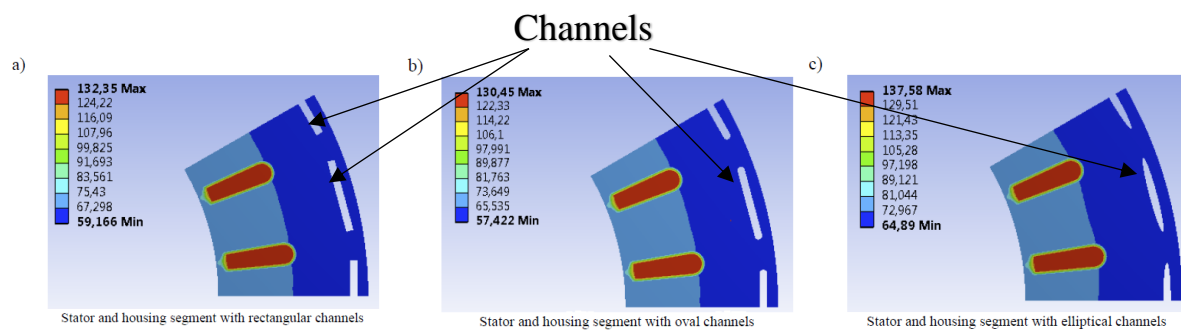


Figure 2.13 : Different geometries of channels simulated in CFD [91].

The frame or stator channels of electric machines have generally a specific geometry (curved duct). Throughout literature, flow in stator channel geometry has not been widely studied analytically, while numerous correlations concern another panel of duct geometries. [88] proposed the simplified rectangular form as in *Figure 2.14*, which shows the actual curved channel form (with respective internal and external diameters R_i and R_e) and the rectangular duct representation (with height H and width W). Physical parameters for hydraulic and thermal calculations for this geometry are defined in *Table 2.7*.

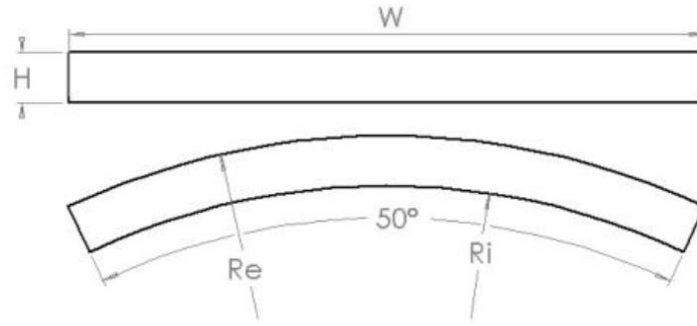


Figure 2.14 : Rectangular section of the cooling channel compared to its effective form [88].

Parameter	Expression
Channel length	L_{ch}
Hydraulic Diameter	$D_h = 4WH/2(W + H)$
Channel aspect ratio	W/H
Channel length to hydraulic diameter ratio	L_{ch}/D_h

Table 2.7 : Geometrical parameters of the stator channel [88].

❖ Smooth Channels

The study is divided into two parts according to the flow type: laminar or turbulent.

For laminar flow ($Re_{D_h} < 2000$): In dynamic developing, and based on correlation from [94], the ratio of the dynamic development length (L_m) to the hydraulic diameter is given by:

$$\frac{L_m}{D_h} = 0.0575 Re_{D_h} \quad (2.27)$$

According to [47], for a circular channel of isothermal wall, where the flow is dynamically fully developed and for which temperature and velocity profiles are developing, the thermal developing length L_{th} can be expressed by:

$$\frac{L_{th}}{D_h Re_{D_h} Pr} = 0.05 \quad (2.28)$$

When $L_{ch} < L_{th}$, Nusselt number :

$$Nu_{D_h}(x) = 1.86 [Re_{D_h} Pr / (x/D_h)]^{1/3} \quad (2.29)$$

Different correlations of Nusselt number are provided by [32] depending on channel shape.

For a circular channel:

$$Nu_{D_h} = 3.66 + \frac{0.065 Re Pr D_h/L_{ch}}{1 + \left[0.04 \left(\frac{Re Pr D_h}{L_{ch}}\right)^{2/3}\right]} \quad (2.30)$$

For concentric cylinders:

$$Nu_{D_h} = 7.54 + \frac{0.03 Re_{D_h} Pr D_h/L_{ch}}{1 + \left[0.016 \left(\frac{Re_{D_h} Pr D_h}{L_{ch}}\right)^{2/3}\right]} \quad (2.31)$$

For turbulent flow: In their thesis [88], where the author adopted an effective channel section, as in *Figure 2.14*, they considered for airflow in channels that in stator channels the flow typically found is turbulent developed corresponding to a Reynolds number between 2×10^4 and 2.5×10^4 . Bertin et al. [47] distinguished between two possible cases, relatively to the ratio of the channel length to the hydraulic diameter (L_{ch}/D_h), around the critical value of 60.

For $\frac{L_{ch}}{D_h} > 60$, Dittus-Boelter correlation is used consequently for a circular channel's section as follows:

If $0.7 < Pr < 100$ and $Re_{D_h} > 2000$

$$Nu_{D_h} = A_n Re_{D_h}^{0.8} Pr^{n_{pr}} \quad (2.32)$$

$A_n = 0.024$ and $n_{pr} = 0.4$ for heating, $A_n = 0.026$ and $n_{pr} = 0.3$ for cooling.

For liquids, the temperature effect is taken into account in the correlation of Sieder and Tate [95]:

$$Nu_{D_h} = 0.027 Re_{D_h}^{4/5} Pr^{1/3} \left(\frac{\mu_m}{\mu_p}\right)^{0.14} \quad (2.33)$$

The corrected form, that considers the length of the channel, is:

$$Nu_{D_h} = 0.0243 Re_{D_h}^{0.8} Pr^{0.4} (1 + k D_h/L_{ch}) \quad \text{with } k = 0.067 Re_{D_h}^{0.25} \quad (2.34)$$

Mc Adams [96] gives a general form of the correlation for cooling and heating:

$$Nu_{D_h} = 0.023 Re_{D_h}^{0.8} Pr^{0.4} \quad (2.35)$$

For $\frac{L_{ch}}{D_h} < 60$, [47] proposed the computation of Nusselt number using another equation that considers the channel length:

$$Nu_{D_h}(L_{ch}) = 0.036 Re_{D_h}^{0.8} Pr^{n_{pr}} \left(\frac{D_h}{L_{ch}} \right)^{1/18} \quad (2.36)$$

Where $n_{pr} = 0.4$ for heated gas, $n_{pr} = 0.3$ for cooled gas and $n_{pr} = 0.5$ for water.

The authors of [97] used a modified equation of Dittus-Boelter in their studies:

$$Nu = 0.023 Re_{D_h}^{0.8} Pr^{0.4} \left(\frac{2R_{av}}{D_e} \right)^{-0.2} \quad (2.37)$$

Where $\left(\frac{2R_{av}}{D_e} \right) = \left(\frac{1.156 + \frac{w}{H} - 1}{\frac{H}{W}} \right)$ for $2500 \leq Re_{D_h} \leq 1.24 \times 10^5$

Gnielinski correlation used to find the Nusselt number takes into consideration the average temperatures of the fluid and the solid surfaces, respectively T_{fm} and T_{pm} . It is noted that this correlation slightly underestimates the convection heat transfer and is stated as follows:

$$Nu = 0.0214 (Re^{0.8} - 100) \left\{ 1 + \left(\frac{D_h}{L_{ch}} \right)^{0.66} \right\} \left(\frac{T_{fm}}{T_{pm}} \right)^{0.45} Pr^{0.4} \quad \text{for } 2300 \leq Re \leq 10^6 \quad (2.38)$$

The author in [88] noted that the Nusselt number depends on the ratio of the heated length along the channel to the hydraulic diameter L_{ch}/D_h , which explains the difference between authors.

In [32], [33], [45], researchers calculated analytically the Nusselt number for fully developed flow, considering the friction coefficient f (detailed subsequently) even for a smooth channel wall, as follows:

$$Nu = \frac{\left(\frac{f}{8} \right) (Re - 1000) Pr}{1 + 12.7 \left(\frac{f}{8} \right)^{\frac{1}{2}} \left(Pr^{\frac{2}{3}} - 1 \right)} \quad \text{for } 3000 < Re < 10^6 \quad (2.39)$$

Where $f = [0.79 \ln(Re) - 1.64]^{-2}$

❖ Friction coefficient

In any channel configuration, it is important to determine the friction coefficient function f . The expression of this coefficient relates the fluid flow to the thermal behavior and differs throughout literature. In general, the researchers in this field ([98]–[100]) used the modified Blasius expression function of Reynolds number which is supposed to underestimate the friction coefficient for low Reynolds number (compared to experimental results of [99]); The friction coefficient is defined by:

$$f = 0.085 Re^{-0.25} \quad (2.40)$$

Bhatti and Shah Correlation fits better with the experimental results, covering a larger domain of Reynolds number; the friction coefficient is determined with respect to the Reynolds number criterion, and the friction coefficient of a circular section channels f_c :

$$f = \left(1.0875 - 0.1125 \frac{H}{W} \right) f_c \quad (2.41)$$

f_c is defined in terms of Reynolds number as follows:

$$\begin{aligned} f_c &= 0.0054 + 2.3 \times 10^{-8} Re^{1.5} && \text{for } 2300 \leq Re \leq 4000 \\ f_c &= 1.28 \times 10^{-3} + 0.1143 Re^{-0.311} && \text{for } 4000 \leq Re \leq 10^7 \end{aligned} \quad (2.42)$$

Karwa et al. [101] suggested the following correlation:

$$f = 0.0791 Re^{-0.25} \quad \text{for } 4000 \leq Re \leq 10^5 \quad (2.43)$$

While the authors in [102] used for the entire domain:

$$f = 0.046 Re^{-0.2} \quad (2.44)$$

In reference [88], they found that generally, the friction coefficient decreases when the Reynolds number increases, except for $2300 \leq Re \leq 4000$ in the Bhatti and Shah correlation, and that this decrease becomes less rigorous for high Reynolds numbers.

❖ Channels with Perturbations

It is commonly known that the use of disruptive elements or ribs at the flow surfaces of heated channels (as in *Figure 2.15*) increases the convection phenomenon in these regions. Perturbations in the cooling system channels are used to increase the thermal efficiency of the system by increasing the coefficient of heat transfer.

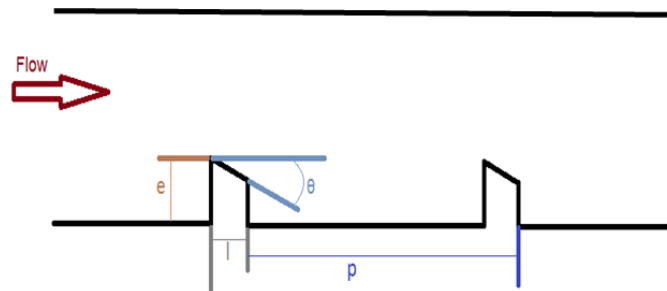


Figure 2.15 : ribs geometrical parameters in a rectangular channel.

However, adding ribs to the channel will also affect the fluid flow mechanics by increasing the friction and thus the coefficient of hydraulic losses specifically for liquid cooling. This will require more pumping power for the operation of the system. In [88], the author was interested specifically in air-cooling through channels. They investigated different configurations of perturbations in channels and provided a detailed literature review from which we can sum up some correlations of Reynolds number computation according to roughness function Rg .

$$Rg = \sqrt{\frac{2}{f}} + 2.5 \ln\left(\frac{e}{D_h}\right) + E \quad (2.45)$$

Where E is a geometrical constant depending on the channel configuration.

2.3.1.3 External Heat Pipes and Two-Phase Loop

❖ Heat Pipes

A heat pipe is a cooling device that is based on phase-changing to transfer heat between two interface structures. Heat pipes are solid structures relatively static to their environment and are composed of three parts: the evaporator at one side, the condenser at the other side, and the adiabatic part at the center. The working principle relies on the temperature difference between the two ends of the pipe. When one end is heated, the working fluid inside the pipe at that end evaporates and increases the vapor pressure inside the cavity of the heat pipe. The latent heat of evaporation absorbed by the vaporization of the working fluid reduces the temperature at the hot end of the pipe (*Figure 2.16*). At the other end of the pipe, the cold sink (namely the condenser) absorbs the heat by the condensation of the vapor. The working fluid flows back to the hot end due to temperature differences. A typical heat pipe consists of a sealed pipe or tube made of a material that is compatible with the working fluid such as copper for water heat pipes, or aluminum for ammonia heat pipes. They are used in many engineering applications (spacecraft, computer systems, ventilation heat recovery...); a wealth of studies were conducted on their operation and performance. Chen et al.[103] stated that Heat Pipes are characterized by a high thermal conductivity, a high efficiency (with no electric energy consumed), and a suitable working temperature for electric devices.

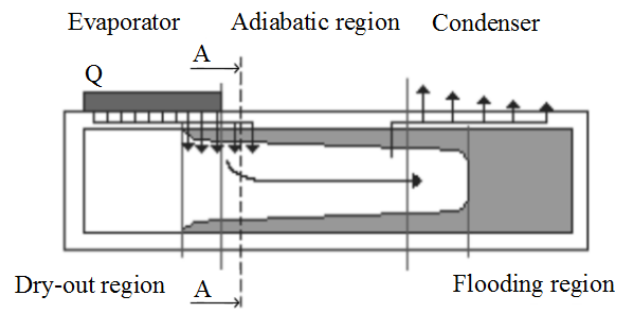


Figure 2.16 : Heat Pipe axial section showing the different regions [103].

Some authors were interested in studying the electric motors cooling using heat pipes [104]–[107]. Recently, authors of [108] investigated a new design of L-shaped heat pipes placed at the surface of the motor housing. Their objective was to determine experimentally the performance of the electric motor. In the design, heat sinks are mounted to each condenser side to increase heat transfer to the ambient air as in *Figure 2.17*.

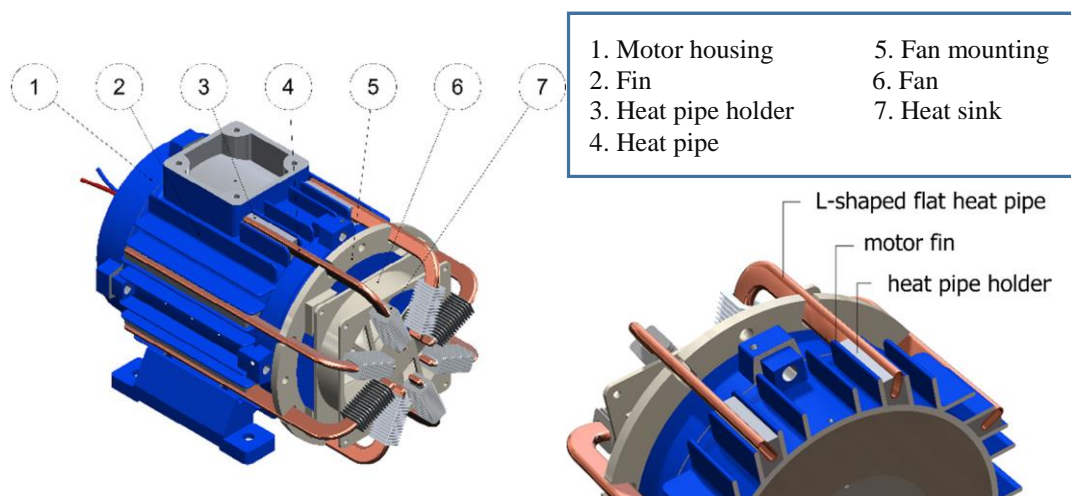


Figure 2.17 : Electric motor prototype cooled with L-shaped heat pipes [108].

Putra et al. [108] reported that the use of heat pipes was capable of reducing the motor housing temperature less than the classical solutions (water jackets, hollow shaft), but the authors mentioned that the surface of heat exchange with ambient air in the studied motor is smaller.

Two-phase loop cooling technologies are based on the same principle as heat pipes, but with liquid and vapor phases circulating in different areas of the circuit. Though, these systems can dissipate greater heat flux densities. Among these cooling technologies, one can cite Loop Heat

Pipe, Looped Pulsating Heat Pipes, and Capillary Pumped Loop. Recently, many authors investigated these systems [109]–[115] and their industrial applications in gas turbines, energy savings applications, solar power (photovoltaic) applications, reactors, and others. Besides, they are widely applied in electronics cooling. The possibility of applying these techniques in electric machinery has not been yet explored. However, their efficacy in evacuating heat fluxes incites to investigate their possible deployment in high specific power electric motors for promising cooling results.

It is nevertheless important to consider the geometrical characteristics of the heated system, specifically lengths since they are one of the main factors that define the operation of heat pipes and two-phase loops.

2.3.2 Internal Cooling Methods

In internal cooling, the components where hot spot temperatures are encountered inside the motor are directly cooled. Actually, in this review cooling is performed by different means: through convection in a single-phase (air: jet impinging or flowing, liquid: jet impinging or spraying), eventually two-phase (internal heat pipes), or another physical phenomenon (phase-changing materials).

2.3.2.1 End-Space Potting

Motor potting has been recently investigated in the electric machines industry as a solution to improve heat evacuation in electric motors [116], [117]. This technique consists of adding a high thermally conductive potting material such as epoxy resin with $3.5 \text{ W}\cdot\text{m}^{-1}\cdot\text{K}^{-1}$ of thermal conductivity or silicone with $3.2 \text{ W}\cdot\text{m}^{-1}\cdot\text{K}^{-1}$ to connect hot spot zones, more specifically the end-winding, to the frame. According to [116] a reduction in winding temperature of a potted motor goes up to $50 \text{ }^\circ\text{C}$ at a given power, while at a given temperature, an increase in power output by 15-25% has been shown. In their study, they described the potting process, beginning with motor sealing, hardener, and resin mixing then degassing, applying the potting mixed material to the end winding (*Figure 2.18*), and the final product after curing. Machines were potted with two materials of different thermal conductivities ($1.1 \text{ W}\cdot\text{m}^{-1}\cdot\text{K}^{-1}$ and $3.5 \text{ W}\cdot\text{m}^{-1}\cdot\text{K}^{-1}$). Temperature decrease between potted and unpotted machines is found sensitive to the machine active length as shown in *Figure 2.19*.



Figure 2.18 : Potting technique processing [116].

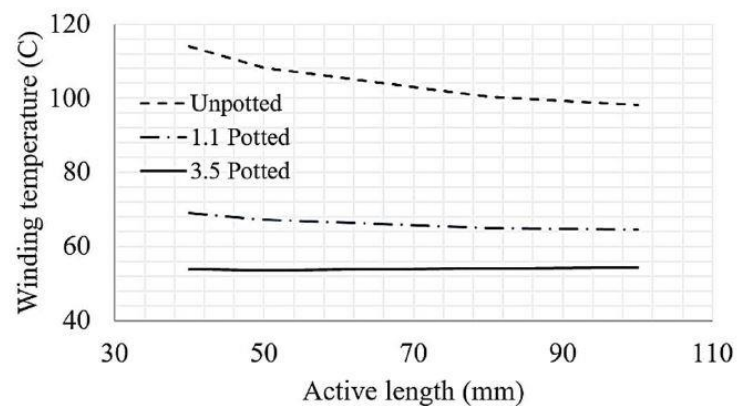


Figure 2.19 : Comparison of motor winding temperature for unpotted and potted (with different types of epoxy) motor end-space [116].

Besides, other potential advantages characterize potting: more uniform distribution of the temperature throughout the windings and lower overheating risk.

2.3.2.2 Metallic Bars

The complexity of heat extraction from electrical machines motivated researchers to find some original and advanced cooling techniques. Pyrhönen et al. [117] proposed some heat transfer improvement methods in an axial-flux permanent magnet synchronous machine by introducing copper bars in stator teeth transferring heat to a “liquid cooling pool”. Using a 1-copper-bar per tooth, the authors noticed that end windings temperature diminishes by 15 °C. In their study, they also used potting of end-windings (as illustrated in *Figure 2.20*) and liquid jackets around the machine.

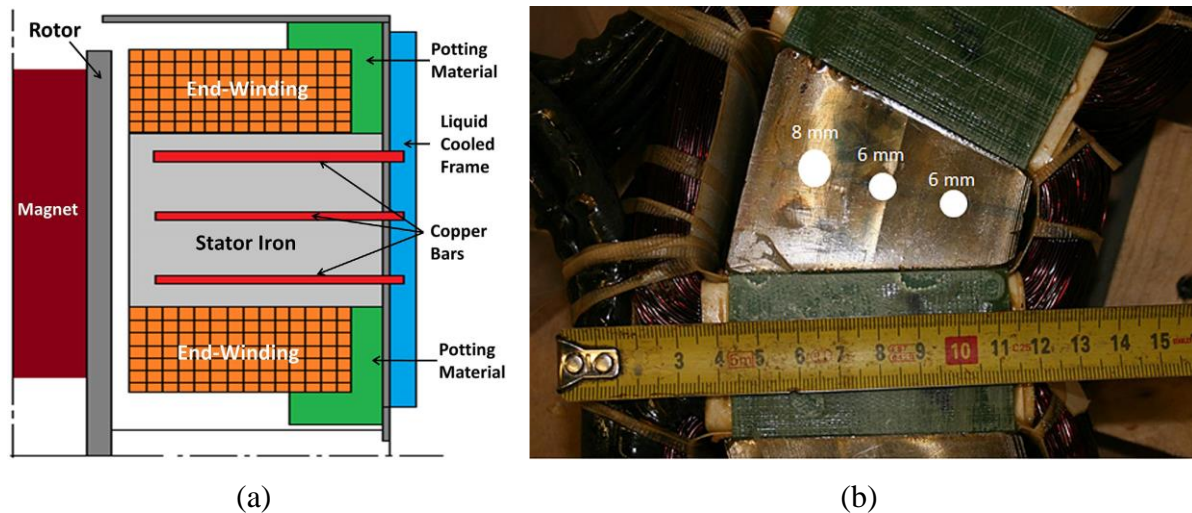


Figure 2.20 : Improved e-motor cooling from [117] using copper bars, potting, and frame liquid cooling (a) schematic e-motor radial section and (b) photo view section.

For 3-copper-bars with end winding potting, a further reduction of the end-winding temperature by approximately $10\text{ }^{\circ}\text{C}$ with respect to the 1-copper-bar case. The results showed that both improved internal cooling techniques are efficient in decreasing hot spot temperatures provided that the machine has liquid jacket cooling.

2.3.2.3 Phase-Changing Materials (PCM) Cooling

The investigation of Belletre et al. [118] is one of the rare works on the use of Phase-Changing Materials (PCM) in the cooling of electric machines. In their design, they considered a low power auto-synchronous machine with eighteen slots. Two models were considered in the simulation procedures: the first model with one side of the end-windings covered with PCM (*Figure 2.21a*) and the second is when the material covers the whole end-windings surfaces (*Figure 2.21b*). The authors remarked that when radiation heat transfer is considered, the hot spot and conductor temperatures decrease. Their study shows that the hot spot temperature decreases when the PCM thermal conductivity, its thermal inertia, and its latent heat of melting increase and when its melting temperature decreases.

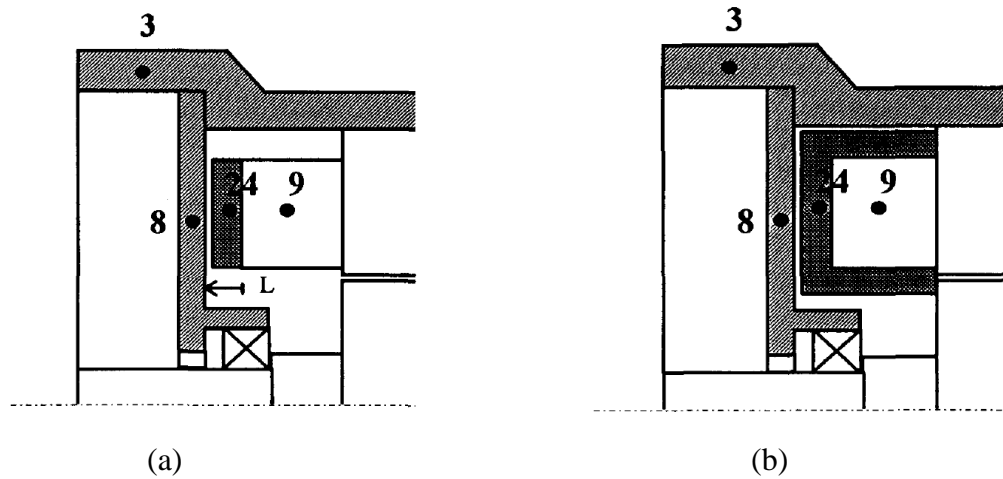


Figure 2.21 : PCM in solid-state node 24 (a) in one end-winding side (b) covering the whole end-windings cavity [118].

As reported in the work, the modeling considers four stages of PCM cooling which are described herein:

The first stage is the pre-melting where the interface temperature is calculated. The second stage is for the melting phenomenon when the heat flows at a constant temperature and the liquid-solid phase temperatures are determined by solving corresponding equations. The melted mass is assumed based on the heat flux difference at the solid-liquid interface.

Rayleigh number (Ra) is calculated at each step ($Ra = Gr Pr$, characterizing natural convection) until reaching a certain value in terms of a geometrical parameter. Reaching this value indicates the beginning of the third stage where natural convection starts. The corresponding heat transfer coefficient is computed according to Seki correlation:

$$h = 0.096 Pr^{0.051} Ra^{0.3} \quad (2.46)$$

Finally, a fourth and last stage takes place where a post-melting of PCM is noticed. It is similar to the first stage but with a PCM in a liquid state.

Depending on PCM properties, the end-windings temperature is reduced by either increasing conductivities, thermal inertia, and latent heat of melting or decreasing melting temperature. End-winding cooling can be achieved also by increasing the stator thermal inertia (15% is equivalent to 69 K cooling with gallium PCM or 14 K with P116 paraffin PCM).

2.3.2.4 Air Cooling

Despite the development and application of multiple fluid cooling technologies aiming to dissipate the increasing heat fluxes in electronic and electrical industries, air-cooling is still

used significantly and on a large scale as a classical cooling solution in electrical machines. Different configurations are used for air cooling of the electric motors and can be separated into two categories according to motor type: closed motor and open motor.

The closed motor refers to the electric machine implemented in a confined area where no environmental flow circulates in any of the machine's internal spaces (*Figure 2.22a*). It is complex to determine the convection inside the motor, and consequently, its global thermal behavior and the level of temperatures reached; it is due to many factors that affect the fluid flow inside the machine (surface finish of the rotor end sections, turbulence effect due to the rotational speed, wafers..) [45]. Usually, different types of heat dissipation can be added passively to the rotor movement providing an improved heat transfer between solid components and spaces. For example, wafers can be added to the rotor giving a fanning effect useful for end-space cooling, i.e. improving heat transfer by creating turbulent effects and therefore increasing the heat transfer coefficient. It is worth mentioning that inside the closed motor, the flow is Taylor-Couette and correlations correspond to natural convection.

In an open motor, fluid flows (usually air) through the machine, where cooling channels may exist (or simply through open space: airgap, end-space..), and the cooling process is well-improved by convection heat transfer (*Figure 2.22b*). The flow is Taylor-Couette-Poiseuille (see *subsection 2.2.2.1*).

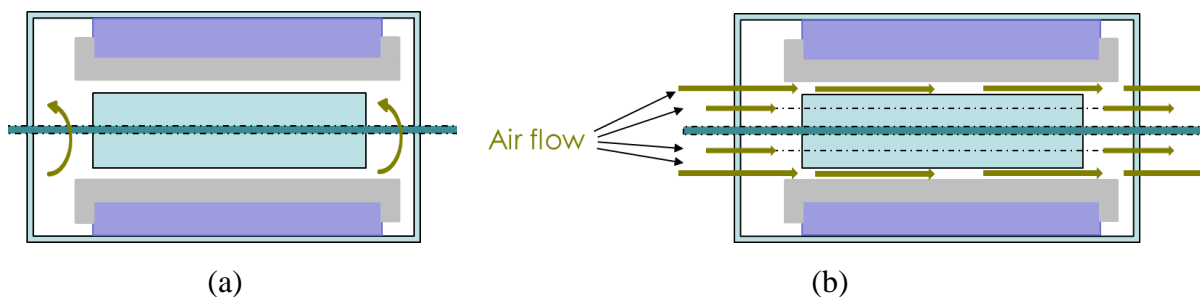


Figure 2.22 : Schematic representation of an axial section of (a) a closed electric motor and (b) an open electric motor.

At the stator level, the authors in [90] proposed the vortex tube (also known as Ranque-Hilsch vortex tube) cooling method to be used in cooling the stator with an air flowing at $-40\text{ }^{\circ}\text{C}$. It is based on the temperature separation phenomenon and consists of converting normal pressurized gas, injected into a swirl chamber through a nozzle, into two gas streams: hot gas and cold gas, with a specific nozzle geometry allowing the transfer of energy between the two gas streams. As described in their work, the technique needs no coolant, is made of a compact and lightweight system, has a low cost of application, does not need maintenance, and presents no

spark or explosion hazard. Compared to a water-cooled machine, this method provides, in transient-state and at low speeds (~up to 3000 RPM), a reduction in stator temperature up to 60 °C, but on the other hand, there is no reduction noted at the windings level (Table 2.8).

	Water Cooling		Vortex Cooling	
	3000 rpm	8000 rpm	3000 rpm	8000 rpm
Temp_Slot (°C)	121,55	140,26	113,15	170,55
Temp_Teeth (°C)	77,51	95,65	83,29	144,84
Temp_Teeth_2 (°C)	69,02	86,37	57,94	111,94
Temp_Yoke (°C)	48,38	57,90	41,49	90,73

Table 2.8 : Comparison of vortex cooled machine with the water-cooled machine [90].

❖ Air Jet Impingement

Martin [119] provided a literature review on air submerged jets. In [120], theoretical studies on air-jet impingements were conducted. Single and multiple impinging air jets are widely used in many industrial applications because of the high heat and mass transfer coefficients which are developed in the impingement region. Generally, they are either circular (or axisymmetric jets), or slotted (or two-dimensional jets). Jet configuration and influencing factors on heat transfer coefficient (mainly Reynolds number, nozzle-to-surface distance...) are currently under investigation. Recently authors of [62], [121], [122] investigated the air impingement cooling on different parts that are similar to some specific motor parts.

❖ Air Jet Impingement on Rotating Disk

The adequate cooling of the rotor end-disks will enhance the reduction of rotor temperature. Hamdan et al. [62] reviewed the case of the geometry of a rotating disk facing a stationary one, with an air jet. They focused on the case where a confined (closed surrounding space) round jet impinged onto the rotating disk from the center of the stationary one, at a flow rate q_j and through a diameter D_j , which is expected to improve the heat transfer process. Since the same fluid is impinged through the cavity then this is a submerged jet (Figure 2.23). They found that only few groups of researchers focused on the study of the rotating disk with jet impingement. In [123], the authors studied experimentally shrouded parallel disks with both rotation and

coolant through-flow and visualized the flow and the heat transfer for the different values of the following parameters: Gr , Re_ω and $Cw = q_j/(v_j r_d)$ (flow rate coefficient) in *Table 2.9*.

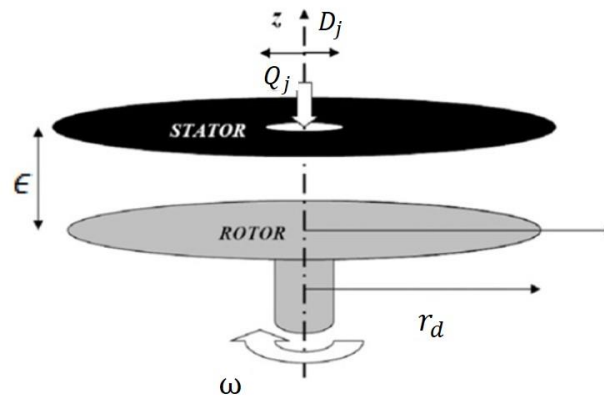


Figure 2.23 : Configuration of a disk rotating at ω and facing stationary one with impinging jet [62].

Parameter	Value		
G_c	4/9	8/9	2
Re_ω	1.8×10^5	5.4×10^5	1.1×10^6
Cw	23560	37700	73830

Table 2.9 : Parametric study values for Re_Ω and Cw [123].

Nusselt number is found to be increasing with the rotation rate as well as with the flow-rate but decreasing with G_c . Otherwise, in the laminar flow regime, Nu is not influenced by the variation of Cw . Haynes et al. [124] extended the investigation adding other values of the parameters of the previous study: the shroud clearance ($G_c = \epsilon_c/r$, ϵ_c is the axial clearance between the shroud cylinder and the rotor), with two values $G_c = 0.0033$ and $G_c = 0.0067$.

$$Cw_{min} = 0.61G_cRe_\omega \quad (2.47)$$

It was deduced that the average Nusselt number and the axial clearance are inversely related and that for small rotational Reynolds number, the rotational speed rate seems to not affect the results, while for large values the case is similar to that of a free disk. For a range of rotational Reynolds number Re_ω and jet Reynolds numbers ($Re_j = u_j D_j / \nu_j$ respectively, where u_j is the jet velocity, D_j is the jet diameter and ν_j is the kinematic viscosity of the jet fluid, which is the air in this case), the correlations of the average Nusselt number at the rotor surface \overline{Nu}_{r_d} , proposed by [121] for different aspect ratio values, can be grouped in *Table 2.10*. Harmand et al. [62] considered also the multiple jets solution for the cooling study of this component, considering two possible interactions: the first between every two successive jets and the second

between the impinging jets and the flow formed by the fluid of the neighboring jets. They deduced that the correlations obtained for a single jet based on the dimensionless numbers are not enough for the case of multiple jets.

G	[0.01; 0.02]	[0.04; 0.08]	0.16
Re_j	$\leq 4.17 \times 10^4$		
Re_ω	[2×10^4 ; 5.16×10^5]		
\overline{Nu}_{rd}	$0.08G^{-0.07} Re_j^{0.5} Re_\omega^{0.25}$	$0.006G^{-0.07} Re_j^{0.5} Re_\omega^{0.5}$	$0.006Re_j^{0.25} Re_\omega^{0.25}$

Table 2.10 : Average Nusselt number in the rotor for different aspect ratio according to Re_ω and Re_j [121].

Lallave et al. [125] suggested the following correlation for averaged Nusselt number of rotating disk under confined jet impingement cooling:

$$\overline{Nu}_{rd} = 1.97619 \left(\frac{t_{noz}}{D_j} \right)^{0.0909} \left(\frac{4Q_j}{\pi v_j D_j} \right)^{0.75} \left(\frac{v_j}{4\omega r_d^2} \right)^{-0.1111} \left(\frac{\lambda_s}{\lambda_f} \right)^{-0.9} \quad (2.48)$$

Where t_{noz} is the distance from the rotor disk to the nozzle, λ_s and λ_f are the thermal conductivities of the solid and the fluid respectively.

❖ Air Jet Impingement on Windings

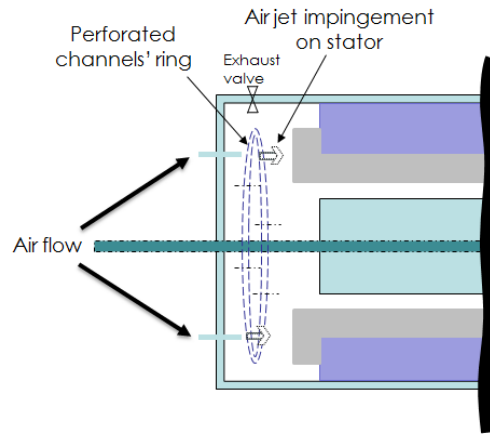


Figure 2.24 : Schematic representation of an open electric motor jet impingements on stator windings.

A possible air jet cooling technique applied at the surface of the end-windings is depicted in Figure 2.24. This technique aims mainly to improve the convection coefficient in this area and to create a circulation of fresh air arriving at the surface of these hot spot zones. These two factors will significantly help to extract heat from the motor windings efficiently (see subsection 2.2.2.3 for end-windings end-space convection).

2.3.2.5 Liquid Cooling

Many authors investigated liquid cooling in electrical machines as water jackets around the stator [80], [126] or refrigerant cooling of the stator [127], [128]. Liquid cooling can be applied to rotor [83] or both stator and rotor [107].

❖ Internal Flow Liquid Cooling

Electric motor cooling through channels has been the subject of many patents [129]–[132].

Most of the concerned authors suggested using oil as a coolant in internal liquid channels for electric safety reasons. To improve the performance at low speed and high torque of a 43 kW induction motor (TEFC machine with turbine fitted on the external part of the shaft and housing fins), Assaad et al. [133] proposed to integrate an oil cooling circuit in a hollow shaft having three holes inside the motor. These holes are used for oil injection directly on motor active parts and are illustrated in *Figure 2.25*.

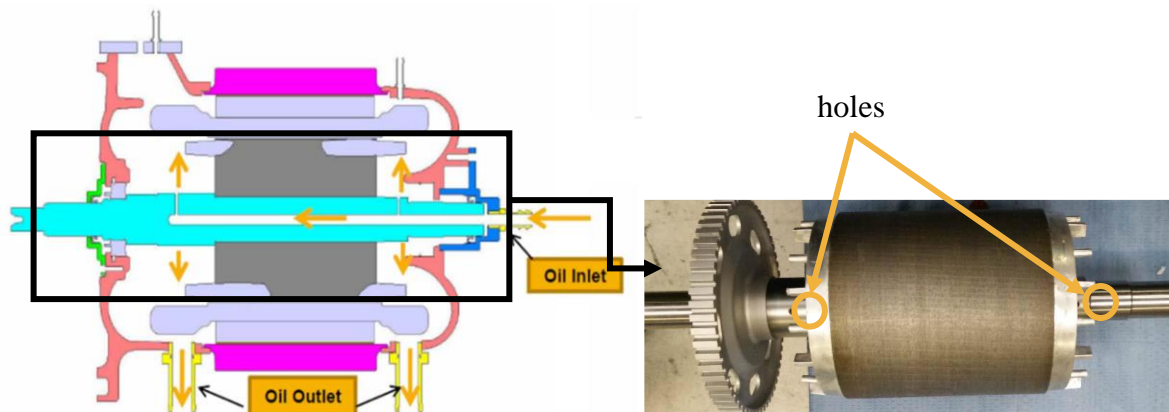


Figure 2.25 : Motor oil cooling, (left) circuit illustration, (right) with rotor and shaft with holes [133].

Nategh et al. [36] proposed oil jackets used for both stator and end-windings cooling. They simulated and tested experimentally two machines made respectively with two different impregnation materials (varnish and epoxy) and under different cooling conditions and losses levels. In their system, after flowing in the stator channels, the oil drops off on the outer surface of the end winding body and is then collected at the bottom side of the housing. The collected oil is emptied using two outlets mounted in both end shields. Based on [32], [33], they used the following correlation for Nusselt number calculation in the model (considering laminar flow and rectangular channel of *Figure 2.14*):

Heat transfer from stator back to the oil of thermal conductivity k_{oil} :

$$Nu_{D_h} = 7.49 - 17.02 \left(\frac{H}{W}\right) + 22.43 \left(\frac{H}{W}\right)^2 - 9.94 \left(\frac{H}{W}\right)^3 + \frac{0.065 Re_{D_h} Pr_{D_h} / L_{Ch}}{1 + \left[0.04 \left(\frac{Re_{D_h} Pr_{D_h}}{L_{Ch}}\right)^{2/3}\right]} \quad (2.49)$$

Where L_{Ch} is the length of each cooling channel.

Heat transfer from the end-winding surface to the oil (laminar flow in a flat surface):

$$Nu_{D_h} = 0.664 Re_{D_h}^{0.5} Pr^{1/3} \quad (2.50)$$

$$h = Nu k_{oil} / D_h$$

❖ Liquid Jets and Sprays

From a general point of view, liquids provide a better heat transfer coefficient than air, therefore some electric motor designers and researchers have focused recently on studying liquid cooling methods. In some works [134], [135], the authors compared jet and spray cooling using water, and found that the same global heat transfer is achieved by spray at a lower flow rate. Other authors [136]–[138] investigated oil jets and sprays for electric machine cooling and searched for improving heat transfer by modifying corresponding parameters. In their theses, [43], [139] studied the oil cooling of the motor airgap. Besides, patents were granted to some original works in this area, such as those in [140], [141].

❖ Liquid Jets

Jet impingements offer a good solution for surface cooling. Impingement cooling schemes may be classified according to whether they involve unconfined or semi-confined jets, crossflow effects associated with neighboring jets, circular or rectangular (slot) jets, and free-surface or submerged jets. Unconfined free surface and submerged jets are shown in *Figure 2.26* [142]. Depending on these conditions and properties, correlations for Nusselt number are presented to study convection heat transfer by jet cooling.

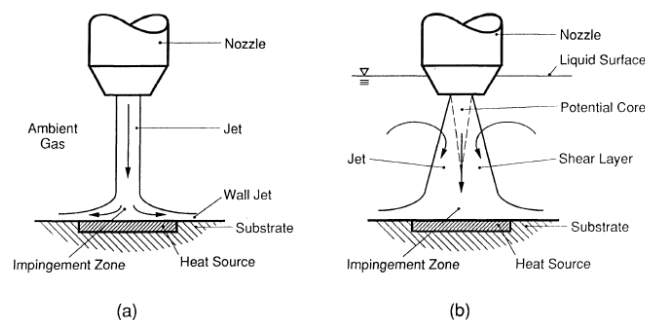


Figure 2.26 : Schematic representation of unconfined (a) free surface and (b) submerged jets impinging on a discrete heat source [142].

Zheng and his co-authors [143]–[145] conducted their studies on submerged and free jets using different liquids (transformer oil, ethylene glycol) and compared results of measurements or prediction of heat transfer coefficient. Jet impingements are recently used in the cooling of electric traction drive machines in some vehicles and the cooling is accomplished by impinging automatic transmission fluid (ATF) directly onto the copper windings [92]. According to [138] the dielectric property of the ATF makes it a good choice for removing heat by direct cooling but no major studies are available regarding direct cooling of end-windings by ATF. The authors approached concentrated ATF jets for a temperature T ranging between $50\text{ }^{\circ}\text{C}$ and $90\text{ }^{\circ}\text{C}$. They tested jet impingements with different surface features with sandpaper polished baseline and other samples are made with wire bundles with radii corresponding to American wire gauge AWG. Highlighting the effect of the surface topology, they found a coefficient of heat transfer, depending on the jet velocity ranging between $1000\text{ W}\cdot\text{m}^{-2}\cdot\text{K}^{-1}$ and $10000\text{ W}\cdot\text{m}^{-2}\cdot\text{K}^{-1}$ for a jet velocity from $0.5\text{ m}\cdot\text{s}^{-1}$ up to $10\text{ m}\cdot\text{s}^{-1}$. They concluded also that the pressure drop across the nozzle was found to be decreasing with increasing fluid temperature (lower viscosity values). According to [146] and based on [147], the average Nusselt number for an unconfined circular free jet on a surface equivalent diameter (D_s much larger than nozzle diameter (d_n) (i.e. $D_s/d_n \gg 1$), is correlated as follows:

$$\text{For } 2.2 \times 10^3 \leq Re_{d_n} \leq 1.4 \times 10^5, 3 \leq Pr \leq 150, 1.75 \leq \frac{D_s}{d_n} \leq 25.1, 1 \leq \frac{d_s}{d_n} \leq 3$$

$$\overline{Nu}_{D_s} = 2.74(Re_{d_n})^{0.348}(Pr)^{0.487}\left(\frac{D_s}{d_n}\right)^{-0.774}\left(\frac{\mu_s}{\mu_{\infty}}\right)^{-0.37} \quad (2.51)$$

Where d_s is the surface to nozzle distance, μ is the dynamic viscosity, subscripts s and ∞ correspond respectively to the surface and the free-stream condition.

❖ Liquid Sprays

Since it was first applied in electronic system technology and despite being based on a complex phenomenon, spray cooling (*Figure 2.27*) was able to provide a great balance of high heat flux removal capability, iso-thermal property, and fluid inventory, compared to other liquid cooling methods [148]. Some works focused on spray cooling under multiple conditions. Mudawar and their co-authors [149]–[153] and more recently Wang and their co-authors [154]–[156] examined spray cooling in different modes and under different conditions (single-phase convection, which is found to be the primary heat transfer mechanism and two-phase convection, beyond and within critical heat flux (CHT)..). Wang et al. [154] studied the effect of varying the orifice-to-surface distance and the spray inclination, on the performance of the

cooling, in a non-boiling regime. They found the optimum distance between orifice and test square surface for the best heat transfer efficiency (6 mm, 3.5 mm, and 2.1 mm) corresponding to each spray inclination angle adopted for optimum results (28°, 42°, and 49°). Besides, they developed in this work an empirical correlation for the Nusselt number based on the experimental study (equation (2.52)).

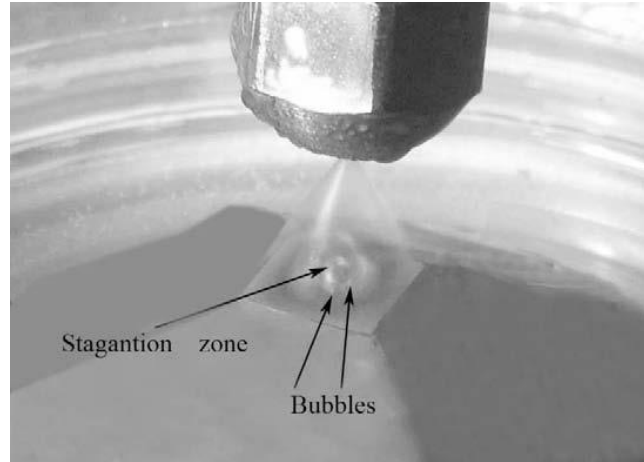


Figure 2.27 : Spray cooling over a square test surface in stagnation at 0° angle inclination and 8.66 mm standoff distance [154].

This correlation is a function of Reynolds number and the non-dimensional temperature $\xi = \frac{T_s}{T_{boiling} - T_e}$ where T_s is the surface temperature, $T_{boiling}$ is the liquid boiling temperature and T_e is the environment temperature. The authors also provided correlations of the Reynolds number and the average heat flux with taking into account inclination that produces elliptical spray area.

$$Nu = 7.144 Re^{0.438} \xi^{0.9016} \quad (2.52)$$

The authors in [148], [157], in combination with data from [153], adopted the following correlation (2.53) for Nusselt number on the targeted surface of sprays in single-phase regime for the PF-5052 coolant, which is an ozone-depleting substance:

$$Nu_{d_{32}} = 4.7 Re_{d_{32}}^{0.61} Pr_f^{0.32} \quad (2.53)$$

With:

$$Nu_{d_{32}} = \frac{q''}{T_s - T_i} \frac{d_{32}}{k_l} \quad (2.54)$$

And:

$$Re_{d_{32}} = \frac{\rho_l \bar{Q}'' d_{32}}{\mu_l} \quad (2.55)$$

Where \bar{Q}'' is the average volumetric flux, k_l , ρ_l and μ_l are respectively the thermal conductivity, density, and viscosity of the liquid, d_{32} is the Sauter mean diameter which is the droplet diameter with the same volume to surface ratio as the entire spray, expressed by:

$$d_{32} = \frac{\sum n_i d_i^3}{\sum n_i d_i^2} \quad 0.6 \times 10^{-3} < Q'' < 9.96 \times 10^{-3} \quad (2.56)$$

These expressions are defined for surface temperatures below 400°C.

Few authors examined spray cooling in the electric machine case. The interesting work of Lim et al. [158] in this area concerns a 35 kW in-wheel electric motor oil cooling. Based on their numerical analysis and experiments, they found that oil spray cooling injected from a hollow shaft to coil/stator core, bearings, and reduction gear (as shown in *Figure 2.28*), has better thermal performance compared to conventional models where oil stagnates in the lower end of the machine.

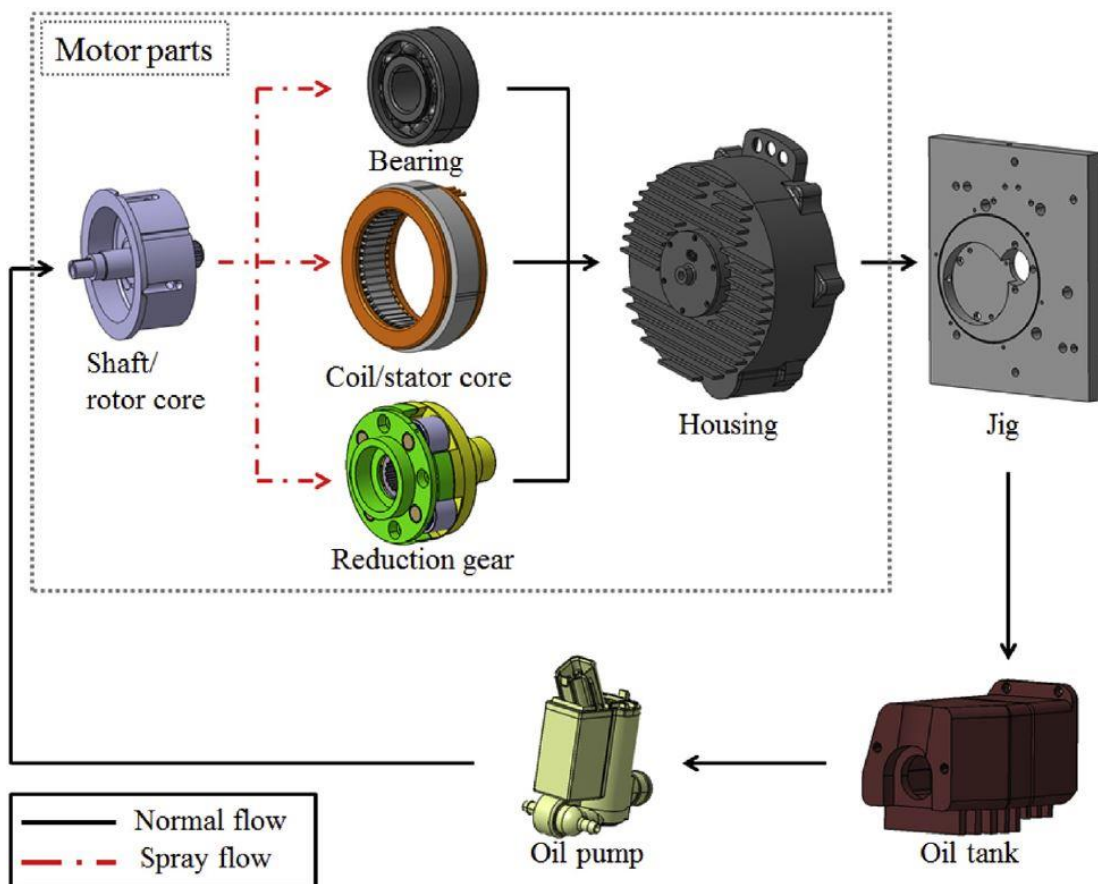


Figure 2.28 : Flow circuit of an in-wheel motor cooling system [158].

They deduced that the windings temperature is reduced and that this cooling technique demonstrates a more uniform inner temperature distribution.

2.3.2.6 *Internal Heat Pipes and Two-Phase Loop*

Heat Pipes and Two-Phase Loops technology integrated to electric motors has been recently the object of many patents (approved or under revision), yet very few studies investigated two-phase cooling in this configuration. In 2009, research on Heat Pipes has led to initiate and incite investigations of these cooling devices and their installation inside the motor. The aim is to cool directly the machine's internal part with a more efficient and more compact system. Through the patent [104] with publication number US 7569955 B2 entitled: "Electric Motor with Heat Pipes", the authors were based on using straight heat pipes and placing the evaporator part in the stator laminated core, and the condenser in a cooling chamber containing a coolant circulating using a pump (*Figure 2.29a*). In this conception, there are many difficulties to mention. First, the risk of leakage of heat pipes inside the motor, second the possible maintenance that is difficult to perform, and finally the power supply required to circulate the coolant. Later on, the invention of [105] has been granted a patent in this field with publication number US 8368265 B2, entitled: "Electric Motor Having Heat Pipes" also using straight heat pipes. The heat pipes are placed around the motor shaft while the condenser is on the impeller. In this technique, the disadvantage is that any leakage in the heat pipes will risk damaging the motor in addition to the difficulty of repairing eventual damage. The work of [106] has been granted a patent for the invention entitled: "Cooling of an Electric Motor via Heat Pipes", patent with publication number US 9561716 B2 in which straight heat pipes were used. The evaporator section was installed in the motor housing and the condenser in the cooling tank. Also, [107] considered another model for electric motor cooling with heat pipes under patent number US 9331552 B2 entitled: "Rotor Assembly with Heat Pipe Cooling System". It was based on putting the evaporator in the shaft and the condenser equipped with cooling fins outside the motor (*Figure 2.29b*). Here also, the drawback is that any leak in heat pipes may cause damage to the motor construction since they are put inside the shaft and a special design is required.

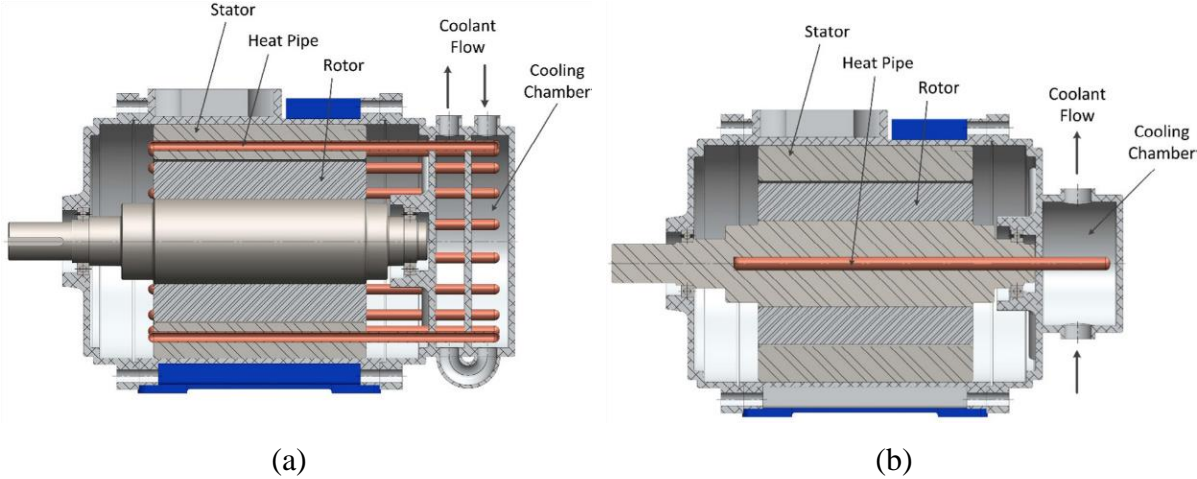


Figure 2.29 : Electric motor internal Heat Pipes: (a) Electric Motor with Heat Pipes [104]
(b) Rotor Assembly with Heat Pipe Cooling System [105].

2.4 Conclusion

A review of the existing methods for e-motor thermal management was presented based on the literature. In this review, the basics of heat transfer phenomena in electric machines are assessed and the existing cooling solutions are presented with corresponding descriptions and information. Efficient techniques are relative to the motor design, but the major conclusion is that liquid cooling provides higher heat extraction for high specific power machines. An important point as well is that critical temperature found in end windings of these machines encouraged researchers to bring cooling techniques closer to these zones, which helped to reach higher performance through windings direct cooling.

CHAPTER 3 LUMPED PARAMETER THERMAL MODELING

Synopsis:

Given the general notions and characteristics of a permanent-magnet synchronous electric motor, the numerical thermal model of the system is constructed using nodal modeling method. Elaboration of the main model components and details on the construction procedure are presented hereafter.

3.1 Introduction

Based on the literature [93], [159], among many thermal modeling techniques, the Lumped Parameter Thermal Modeling (LPTM) is considered an interesting method to assess electric motor thermal behavior. This method can be applied to solve steady-state and transient thermal problems and their relative equations for the whole machine. It is often used in electrical problems as well as in thermal and heat transfer problems thanks to the analogy between electrical and thermal quantities.

In addition to the time-based efficiency of this technique (compared to other solutions such as Finite Element Modeling or Computational Fluid Dynamics), for e-motor application, this technique is also characterized by other features. The main feature of LPTM is the possibility to model components of multiple dimensions. Moreover, the model can be integrated into other systems and/or aspects i.e. the electromagnetic and mechanical models, the simple fluid dynamics, connection to system control, and others. LPTM is also a multiscale modeling technique that allows considering thermal resistance for structures of different scales from micro-scale (contact resistance) to a higher one (conduction along rotor axis).

3.2 LPTM Approach

The lumped parameter analysis is a modeling method that consists of discretizing a distributed system to apprehend its behavior. It will be applied to the electric motor system to investigate its thermal behavior and proceed with its thermal management. Also called Nodal Network Modeling, this technique is based on certain assumptions reducing the system and presented thereafter. Being a nodal network, the main components in the thermal nodal network are the thermal conductance between two nodes that defines the heat transfer between them, the thermal capacity of each node for transient analyses, and the heat sources or heat sinks at each node. To address the determination of these components, a direct approach to heat transfer modes and principles to proceed with LPTM is presented. Further description of the LPTM method, as well as thermal modeling theories and equations, can be found in [160].

The heat transfer in LPTM is modeled based on the thermal energy balance. The equation governing heat diffusion in a domain Ω , including the mass transport term, is written as follows:

$$\rho c_p \left[\frac{\partial T}{\partial t} + \vec{u} \cdot \vec{\nabla} T \right] = \vec{\nabla} \cdot (\lambda \vec{\nabla} T) + \dot{q} \quad (3.1)$$

Where $\vec{u} \cdot \vec{\nabla} T$ is the mass transport term, $\vec{\nabla} \cdot (\lambda \vec{\nabla} T)$ is the diffusion term, \dot{q} is the heat production density. T is the temperature at a point in the domain, ρ is the density, c_p is the specific heat, λ is the thermal conductivity, and \vec{u} is the velocity field. This latter equation is associated with the following general boundary condition at the boundary Γ of domain Ω , and initial condition respectively:

$$\lambda \vec{\nabla} T \cdot \vec{n} = h(T_{ref} - T) + \varepsilon \sigma (T_p^4 - T^4) \quad (3.2)$$

$$T(t = 0) = T_{init} \quad (3.3)$$

The term $h(T_{ref} - T)$ is the heat flux density exchanged through convection mode, where h denotes the convection coefficient and T_{ref} is the reference temperature of the fluid media. The term $\varepsilon \sigma (T_p^4 - T^4)$ is the heat flux density relative to radiation heat transfer mode, where ε is the emissivity of the surface, σ is the constant of Stefan-Boltzmann, and T_p is the temperature of the body surface with which the surface Γ exchanges heat by radiation.

To proceed with LPTM, a discretization of the domain into N finite volumes V_i must be performed. Each volume is represented by a node i at its center, to which a temperature T_i , a thermal capacity $C_i = (\rho c_p)_i V_i$, and a heat source \dot{Q}_i representing the generated heat through this volume, are assigned. Assuming that each finite volume is homogeneous and isothermal and that the heat is produced uniformly through that volume, the equation of thermal energy balance can be expressed as follows:

$$\begin{aligned} (\rho c_p)_i V_i \frac{dT_i}{dt} = & \sum_k \Phi_{ik, conduction} + \sum_l \Phi_{il, convection} + \sum_m \Phi_{im, radiation} \\ & + \sum_p \Phi_{ip, mass transport} + \dot{Q} \end{aligned} \quad (3.4)$$

Where the sums $\sum_k \Phi_{ik, conduction}$, $\sum_l \Phi_{il, convection}$, $\sum_m \Phi_{im, radiation}$, and $\sum_p \Phi_{ip, mass transport}$ are the sums of exchanged heat fluxes through conduction, convection, radiation, and mass transport modes respectively between node i and its surroundings.

If radiation phenomenon is to be considered directly in the nodal network model, problem linearization is needed, since a nonlinear equation characterizes this heat transfer mode. In

numerical models, this requires some specific considerations and assumptions (view factors, surface properties, and grey or black bodies hypotheses) and many iterative procedures.

According to [161], radiation heat transfer for e-motors could be negligible when forced cooling is occurring. In our case, radiation is assumed negligible during the first-time simulation, and then the obtained temperatures in end-windings and surrounding surfaces are extracted to evaluate the probable radiation heat flux. This flux will be compared to the preeminent heat flux in this area - mainly convection heat flux - and the assumption of neglecting this phenomenon is either maintained or rejected in the subsequent simulations.

Therefore, a system of N Ordinary Differential Equation (ODE) is obtained, and equation (3.4) is expressed for each node as follows:

$$C_i \frac{dT_i}{dt} = \sum_{j, i \neq j} G_{ij} (T_j - T_i) + \dot{Q}_i \quad \text{for } j: 1 \dots N \quad (3.5)$$

Where G_{ij} is the thermal conductance characterizing the heat transfer in both solid and fluid regions between volumes of nodes i and j (index j corresponds to the adjacent node connected to node i). For diffusion and convection processes, heat transfer is reciprocal, hence: $G_{ji} = G_{ij}$.

It can be more convenient in a nodal representation to formulate the previous equation without exhibiting the temperature difference $T_j - T_i$, as follows:

$$C_i \frac{dT_i}{dt} = \left(- \sum_{j, i \neq j} G_{ij} \right) T_i + \sum_{j, i \neq j} G_{ij} T_j + \dot{Q}_i \quad (3.6)$$

When i is connected to reference temperature T_{ref} , a corresponding conductance appears $G_{i,ref}$, and an additional heat sink term for the evacuation of heat ($\psi_{i,ext} = G_{i,ref} T_{ref}$) is added to the equation as follows:

$$C_i \frac{dT_i}{dt} = \left(-G_{i,ref} - \sum_{j, i \neq j} G_{ij} \right) T_i + \sum_{j, i \neq j} G_{ij} T_j + \dot{Q}_i + \psi_{i,ext} \quad (3.7)$$

\dot{Q}_i and $\psi_{i,ext}$ stand respectively for heat sources (motor losses in our case) and heat sinks (coming out from boundary conditions for heat evacuation by convection). To solve the first-order linear differential equation of temperature, they can be summed in one term: $\Psi_i = \psi_{i,ext} + \dot{Q}_i$.

As it was evoked, fluidic connections by mass transport can also be represented in the model, for which the appropriate expression of conductance between two fluid nodes i and j depends on the flow and its direction. There is no reciprocal relation in thermal conductance when both nodes are fluidic.

This allows writing a matrix form of the thermal balance equation of the overall domain discretized into N nodes as follows:

$$C \frac{dT}{dt} = G T + \Psi \quad (3.8)$$

Where C and G are $N \times N$ matrices representing capacity and conductance matrices, and T and Ψ are vectors (of dimension N) representing temperature and heat generation vectors in the system. These matrices and vectors are structured as follows:

$$C = \begin{pmatrix} \cdot & & & 0 \\ & \cdot & & \\ & & \cdot & \\ & & & C_i \\ & & & & \cdot \\ & 0 & & & & \cdot \end{pmatrix},$$

$$G = \begin{pmatrix} \cdot & & & & & & \\ & \cdot & & & & & \\ & & \cdot & & & & \\ & & & \cdot & & & \\ G_{i1} & \cdot & \cdot & -G_{i,ref} - \sum_{\substack{j=1 \\ j \neq i}}^n G_{ij} & \cdot & \cdot & G_{in} \\ & & & & \cdot & & \\ & & & & & \cdot & \\ & & & & & & \cdot \end{pmatrix}$$

$$T = \begin{pmatrix} \cdot \\ \cdot \\ \cdot \\ T_i \\ \cdot \\ \cdot \\ \cdot \end{pmatrix} \quad \text{and} \quad \Psi = \begin{pmatrix} \cdot \\ \cdot \\ \cdot \\ \dot{Q}_i + \psi_{i,ext} \\ \cdot \\ \cdot \\ \cdot \end{pmatrix}$$

An implicit Euler time-scheme will be used to solve Equation (3.8) in the transient regime. Whereas the steady-state temperature vector T can be obtained by inverting the matrix G : $T = -G^{-1} \Psi$. The heat flux Φ_{ij} between nodes i and j is computed using the following equation:

$$\Phi_{ij} = G_{ij}(T_j - T_i) \quad (3.9)$$

In both transient regime and steady-state, the thermal conductance matrix G and the heat generation vector Ψ should be defined according to the geometry structure and the system characteristics. The thermal capacity matrix C is only defined to solve transient regimes, allowing the prediction of temperature evolution as a function of time. LPTM of the motor system requires specific input parameters, which are extracted from the motor geometry, materials and their properties, initial and boundary conditions, and machine losses generating the heat inside the motor. The following section points out the definition of electric motor system composition.

3.3 Electric Motor System Definition

The case-study system consists mainly of the electric motor structure and its subsystems including cooling techniques, heat generation, etc... These parts should be defined to proceed with LPTM configuration and simulation based on Equation (3.8). Therefore, this requires the definition of many parameters and conditions to enable system modeling and get representative results of the thermal analysis: determination of motor temperatures, detection of thermal problems, finding appropriate cooling solutions, and others.

These parameters and conditions include:

- Geometry and relative data
- Structure materials and properties
- Fluid properties (namely air and liquid coolant if applied)
- Initial and boundary conditions, such as surrounding temperature
- Heat sources distribution, location, and values

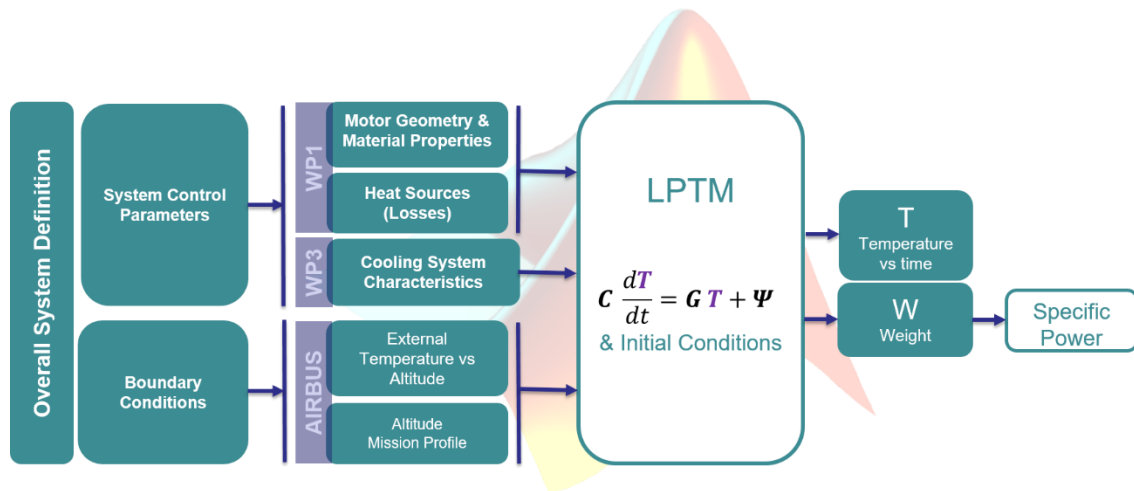


Figure 3.1 : Overall system definition of e-motor LPTM.

The overall system definition of e-motor LPTM is suggested as in *Figure 3.1*. The system control parameters defined at WP1 and WP3 are related to electric machine design and cooling and can be modified upon the given specifications and targets. Boundary conditions are provided by our industrial partner Airbus to represent the outside motor operating conditions and can be modified accordingly. The outputs of the model are mainly the temperatures of the components. On the other hand, in the specific context of the present study (electric motor for the propulsion of transportation means and more specifically in the aeronautical sector), the system weight has major importance. Consequently, the results of our model (called *AThEM*) will include the system weight calculation, particularly the cooling system weight (taking into account the cooling fluid weight and the pipe weight for instance). The system definition and outputs are detailed in the following subsections.

3.3.1 E-Motor Geometry and Materials Properties

For the motor system discretization into finite volumes, it is crucial to define a geometry design that includes all data on motor components and their dimensions, materials properties, and some mechanical and electrical data. Depending on these electro-technical design data, the cooling system design can be proposed and modeled. Several questions may be asked to help to define the possible cooling type consequently, for instance: is the motor open or close? In other words, is it directly connected to the outside medium or totally enclosed? is it possible to integrate an external flow inside the machine? Actually, on one hand, the motor type, design, and geometry

determine the electro-magnetic and mechanical phenomena (that take place in the e-motor to allow converting electrical energy into other energy forms) and define by this way the generated heat fluxes of the motor system. On the other hand, the motor geometry influences the cooling techniques that could be selected for thermal management. Materials' physical properties should be defined to determine conduction thermal conductances and thermal capacities. When recalling the geometry of the case-study motor type: SM-PMSM (Surface Mounted-Permanent Magnet Synchronous Motor) presented earlier in *Chapter 1*, it is revealed that motor parts are made up of many materials with various physical properties. Some motor components are heterogeneous and made out of multiple micro-structures (up to hundreds of copper wires in the winding for example), whose geometries are generally not accurately known (e.g. precise position and configuration of wires in the winding slot). For time-optimization reasons, these components are better considered homogeneous with equivalent properties. Therefore, all motor components geometry, dimensions, and materials must be defined to solve the motor model and find suitable cooling solutions, and in an advanced step, optimize the motor thermal management.

3.3.2 Boundary conditions

Boundary conditions are defined as boundary temperatures (termed reference temperatures T_{ref}) and convection Heat Transfer Coefficients (HTC) for external nodes connected to some system nodes. In general, the electric motor heat sinks depend on cooling solutions. It could be one or more heat exchangers (to which reference temperatures and heat convection coefficients are set), with or without forced air convection. Along with the adapted modeling of the motor, the location and type of these boundary conditions are determined.

The value of HTC between the motor structure and its surroundings depends on the motor environment and can be determined based on [32], [33], [61], [74] as detailed in the previous *Chapter 2*.

3.3.3 Electric Motor Losses (Heat Sources)

The high heat dissipation inside the electric motor is due to the losses resulting from electro-magnetic phenomena and aerothermal effects due to high rotational speed. Generally, these

losses are categorized for the PMSM type as follows: **Joule Losses** (in windings), **Magnetic Losses** (Iron Losses and Permanent-Magnets Losses), and **Mechanical Losses** due to friction (Windage Losses in Airgap and Rotor End-caps, and Bearings Losses). Magnetic losses in the rotor are neglected based on electro-technical data (iron losses in the rotor are neglected to assume the hypothesis of first harmonic). Windage or aerothermal losses in rotor result from friction between air and rotor surfaces. They can be quite significant in the case of high-speed rotation. They are located mainly in airgap and rotor end-caps and are estimated based on correlations.

It is commonly known in PMSM machinery that stator losses are highly significant and lead to serious thermal problems that can end up with real damage to the motor if heat dissipation is not well treated.

In the rotor, thermal constraints on magnets can be critical even when losses in this motor area are relatively low. Due to the relatively low allowed maximum temperature in magnets ($100\text{--}150\text{ }^{\circ}\text{C}$ against $200\text{ }^{\circ}\text{C}$ for other motor parts).

Since the heat sources in the system correspond to these losses, it is important that an accurate distribution and allocation of the thermal input sources could be defined in the thermal model. In the nodal network, these heat sources are injected into nodes according to where losses occur. Surface losses are assigned to surface nodes, particularly at the extremities while volume losses are correspondingly allocated to volume nodes. Moreover, due to the dynamical change of required power during the flight mission losses have resultant profiles in terms of time. This aspect will be considered in the electric motor design (WP1 expertise area- see *Chapter 1*) and in the cooling system definition and sizing in the present work. In the thermal model, losses variation in terms of flight time will be taken into account instantly to take advantage of the thermal inertia of some motor components. This transient effect may help to reduce the increase in temperature in the motor core and consequently decreasing the required cooling effort.

Let us first briefly define the PMSM losses and the physical phenomena behind them. For each type of losses, the corresponding definition, determination, and distribution of heat production in the motor model are presented.

3.3.3.1 Joule Losses

Joule losses (or winding losses in our case-study motor) are located in copper conductors and can also be called copper losses. As their name reveals, they result from Joule effect and are produced due to current circulation in windings resulting from the electrical potential difference between each of the stator ends. Since these losses are the main reason behind temperature rise in windings, they are considered as the primary threat to windings damage and thus the operation failure of motors of PMSM type. Motor Joule losses resulting from an electrical current I_{el} in the winding coils having an electrical resistance \mathcal{R}_{el} , are calculated in terms of the number of phases n_{ph} as follows:

$$P_{Joule} = n_{ph} \mathcal{R}_{el} I_{el}^2 \quad (3.10)$$

Electrical resistance is calculated, considering Direct Current (DC) circulation, as a function of the conductor temperature T_{cu} as follows: $\mathcal{R}_{el} = \rho_{cu, T_0} (1 + \alpha_{el} (T_{cu} - T_0)) l_c / S_c$, where ρ_{cu, T_0} is the electrical resistivity of copper at 20°C , α_{el} is the temperature coefficient resistance ($\alpha_{el} = 3.93 \times 10^{-3} \text{ K}^{-1}$), l_c is the conductor length and S_c is the conductor cross-section.

An existing effect in conductors called skin effect results from the circulation of Alternating Current (AC) in windings once surrounded by the magnetic field (in the stator, in airgap...) and will lead to additional Joule losses. Due to the magnetic field in a conductor, the proximity effect occurs as well in the other neighboring conductors. The calculation of Joule losses of a PMSM with alternating current circulation should take into consideration skin and proximity effects. Estimation of these losses depends on the AC electrical resistance \mathcal{R}_{AC} . In this case $\mathcal{R}_{el} = \mathcal{R}_{AC}$ is used in the previous equation (3.10) to determine Joule losses. This resistance is defined by its ratio to the DC electrical resistance: $\mathcal{R}_{AC} / \mathcal{R}_{DC}$. This ratio is function of many parameters and is roughly estimated by the analytical approach since it strongly depends on the effective configuration of coils in the slots. These parameters are mainly geometrical depending on the slot dimensions, number of conductors in the slot, their height and width for rectangular copper wires, and the spacing of conductors. There are also physical factors mainly copper electrical conductivity and current frequency. These effects can be neglected in some configuration cases (Litz wires or ultra-thin insulator conductors are examples of these cases).

In the PMSM Thermal model, these losses are injected into stator slots enclosing the windings and to end-winding parts at each motor side (front and rear).

3.3.3.2 Iron Losses

Iron losses are produced in ferromagnetic materials. In PMSM, they are found in laminations and can be sometimes more significant in value than Joule losses, and can be estimated according to their category (Hysteresis, eddy current resulting from Faraday's law, and excess losses) based on [162] as follows:

$$P_{Iron} = k_h f_{el} B_m^2 + k_c f_{el}^2 B_m^2 + k_e f_{el}^{3/2} B_m^{3/2} \quad (3.11)$$

Where B_m is the maximum magnetic flux density, f_{el} is the frequency, k_h is the hysteresis loss coefficient, k_c is the eddy loss coefficient and k_e is the excess loss coefficient.

Iron losses are very important to consider in the thermal management of e-motors. Based on the aforementioned assumptions (neglecting the rotor laminations losses), they are mainly located in the stator laminations and are considered uniformly distributed between teeth and other areas.

3.3.3.3 Airgap Losses

Windage losses in airgap are relative to rotor movement creating tangential velocity components. The friction of rotating air to surfaces and between its fluid layers, creates significant heat dissipation, These losses are estimated according to [163] based on [164] by:

$$P_{Airgap} = k_r \Phi_{M,airgap} \pi \rho_{air} \omega^3 r_{rotor}^4 L_{airgap} \quad (3.12)$$

Where k_r is the roughness coefficient. According to [163]: $1 < k_r < 4$, depending on rotation speed and surface smoothness. To estimate these losses WP1 of the project used the value $k_r=1$ considering smooth rotor and stator surfaces. $\Phi_{M,airgap}$ is the friction coefficient in airgap depending on flow characteristics. It is defined at WP1 by:

$$\Phi_{M,airgap} = 0.515 \frac{(e_g/r_{rotor})^{0.3}}{Re_{ag}^{0.5}} \text{ for } 500 < Re_{ag} < 10^4 \quad (3.13)$$

$$\Phi_{M,airgap} = 0.325 \frac{(e_g/r_{rotor})^{0.3}}{Re_{ag}^{0.2}} \text{ for } Re_{ag} > 10^4 \quad (3.14)$$

Where e_g is the airgap thickness and Re_{ag} is the rotational Reynolds number relative to airgap considering rotor speed ω defined by: $Re_{ag} = \frac{\rho_{air} r_{rotor} e_g \omega}{\mu_{air}}$

3.3.3.4 Rotor End-caps Losses

At the end-caps of the rotor, there are windage losses at each side due to friction between these rotating ends and the surrounding air layer in motor cavities. These losses are estimated by [163] as in equation (3.15):

$$P_{Rotor} = \frac{1}{2} \zeta_{M,rotor} \pi \rho_{air} \omega^3 (r_{rotor}^5 - r_{shaft}^5) \quad (3.15)$$

$\zeta_{M,rotor}$ is the friction coefficient at the rotor end-caps deduced from the coefficient of moment relative to torque presented earlier in *Chapter 2*. WP1 used the following correlations to compute the friction coefficient:

$$\zeta_{M,rotor} = \frac{3.87}{Re_{\omega}^{0.5}} \text{ for } 500 < Re_{\omega} < 10^4 \quad (3.16)$$

$$\zeta_{M,rotor} = \frac{0.146}{Re_{\omega}^{0.2}} \text{ for } Re_{\omega} > 10^4 \quad (3.17)$$

Re_{ω} is the rotational Reynolds number relative to rotor radius defined in *Chapter 2*.

3.3.3.5 Bearings Losses

Bearings of high specific power electric motors are subject to high loads in different directions (radial, thrust). Due to the loads applied to bearings along with their rotation motion, friction losses occur at this level. In addition to loads factor, other factors such as the solids' friction coming out from surface contact between bearings elements and the adjacent elements (cage, raceways, and other rolling elements) will influence these losses. These non-negligible losses produce heat dissipation in the bearings ending up increasing their temperature above their operating limits. Heat may also be transferred through diffusion or convection to the motor rotor, frame, or even end-windings. This might raise the temperature of some degrees in the motor.

$$P_{Bearing} = \frac{1}{2} \mathfrak{C}_{M,bearing} F_d d_b \omega \quad (3.18)$$

Where $\mathfrak{C}_{M,bearing}$ is the bearings friction coefficient whose value depends on the bearing type, F_d is the equivalent dynamic bearing load, d_b is the bearing bore diameter, and ω is the rotation speed.

3.3.4 Initial Conditions

Solving the system equation in transient regime provides the temperature evolution during the flight mission considering the thermal capacity matrix of the motor system, and any variation in input data such as the external temperature and power profile (generating motor losses profiles). An initial condition, in terms of system variables, has to be set to solve the LPTM equation system in transient regime. For the aeronautical application of the motor, this condition corresponds to the initial temperature of the motor environment (or simply the motor temperature at time=0).

3.4 Modeling Assumptions

The numerical model based on the LPTM method is a low-order reduced model. To exhibit the motor thermal behavior in an efficient representative way, the corresponding calculations should be executed in the fastest yet accurate possible procedure. Thus, some modeling assumptions could be considered based on the motor and cooling system configurations.

3.4.1 Geometry

In *Chapter 1*, a global geometry of motor chosen for our application was depicted (see *Figure 3.2*). It is a Surface Mounted – Permanent-Magnet Synchronous Motor (SM-PMSM) characterized by its rotor geometry, compared to other AC motor types. The rotor is made of iron laminations tightly packed with permanent magnets mounted at the surface.

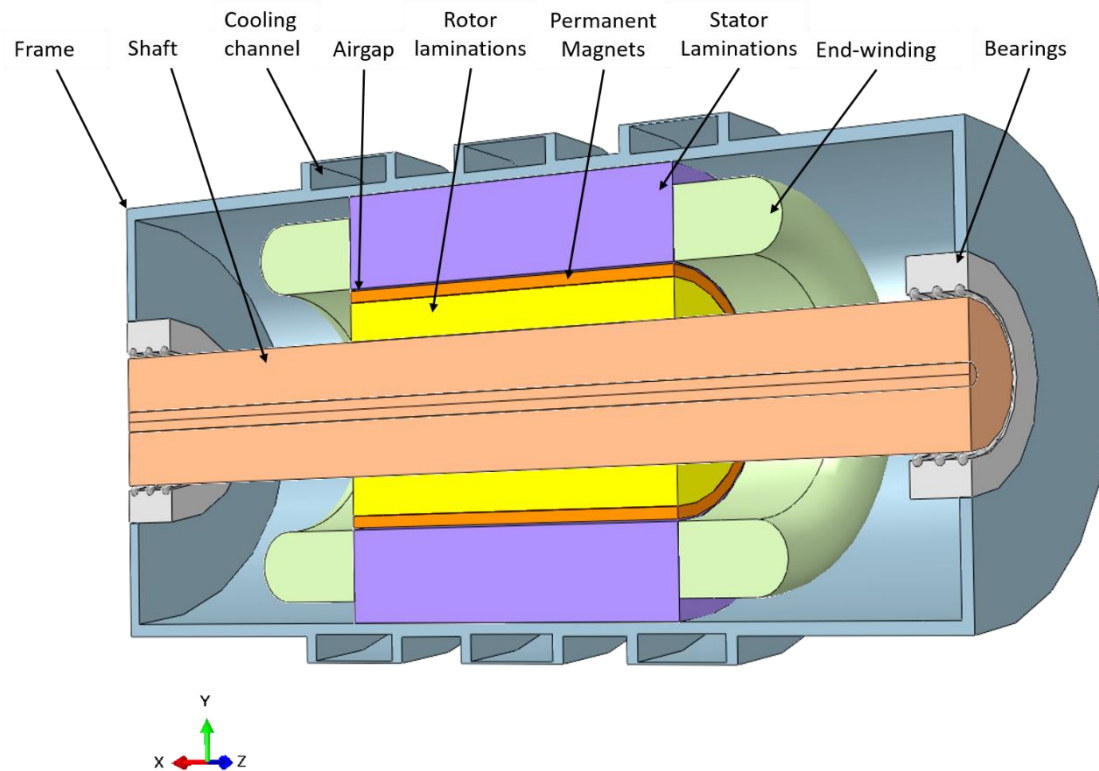


Figure 3.2 : An example of a simplified geometry design of SM-PMSM used for numerical modeling.

As in other motors, the stator has windings inserted into the slots of an iron structure of ferromagnetic laminations. Since the motor has a cylindrical geometry, it is convenient to consider cylindrical coordinates and sections.

3.4.2 Symmetry and Periodicity for Model Reduction

The solid configuration of the SM-PMSM machine adopted for the thermal model is homogeneous in an axisymmetric rotor section since the rotor consists of one type of material for each radial dimension. In the stator, a periodicity is considered due to the alternation of winding slots and teeth. This is depicted in a real stator geometry (see stator of AC motors in *Chapter 1*), as well as in the modeled e-motors designs. The core motor structure is axially symmetric with respect to the middle section of the motor.

3.4.3 Temperature-Independent Media Physical Properties

The system's thermophysical properties are considered temperature-independent. These properties refer particularly to thermal conductivity, specific heat capacity, density, viscosity, and electrical resistivity of copper conductors. Sensitivity studies are carried out and, in a further approach, some media properties are varied in terms of the temperature evolution of each medium.

3.5 LPTM Construction

To solve the problem and get temperature results, the differential equation system (equation (3.8)) should be elaborated. For this purpose matrices G and C , and vector Ψ should be constructed for the motor model.

3.5.1 Thermal Conductance Matrix G

Based on the thermal conductivities of materials, and the boundary conditions, the conductance matrix G can be evaluated. To sum up, *Table 3.1* gathers the expressions of the thermal conductance for each heat transfer mode.

Conduction connections are referred to two configurations: axial and radial, since our electric motor can be represented in cylindrical coordinate system for which components' volumes are connected radially, while volumes of the same component are connected considering axial conductance expressions.

Considering temperature-independent conductivities for each element, in the case study electric motor, the anisotropic property of the material and the cylindrical configurations of the motor structure and main parts motivated us to use a 3D representation of the equation of conduction heat transfer with constant conductivities in each direction (radial (r), angular (θ) and axial (x)).

Heat Transfer Mode	Heat Flux Expression	Conductance
Conduction (axial and ortho-radial)	$\frac{\lambda S_{ij}}{L_{ij}} (T_j - T_i)$	$G_{ij}^{cond,axial} = \frac{\lambda S_{ij}}{L_{ij}}$
Conduction (radial)	$\frac{2\pi \lambda H}{\ln(r_j/r_i)} (T_j - T_i)$	$G_{ij}^{cond,radial} = \frac{2\pi \lambda H}{\ln(r_j/r_i)}$
Convection	$h S_i (T_f - T_i)$	$G_{S_i}^{conv} = h S_i$
Fluidic Flow	$\dot{m} c_p (T_j - T_i)$	$G_{ij}^f = \dot{m} c_p$

S_{ij} is the surface of heat transfer between volumes represented by nodes i and j

S_i is the surface of V_i exposed to convection heat transfer

T_f is the average temperature of the fluid surrounding surface S_i

L_{ij} is the distance between nodes i and j

H is the height of the cylindrical object

\dot{m} is the fluid flow rate

r_i is the radius of node i from motor axis

$r_j > r_i$ (radii)

Table 3.1 : Flux and conductance expressions for each heat transfer mode.

Where:

$G_{ij}^{cond,axial}$ and $G_{ij}^{cond,radial}$ are respectively axial and radial conduction conductances in cylindrical systems between two volumes represented by nodes i and j

$G_{S_i}^{conv}$ is the convection conductance between surface S_i of node i and the fluid surrounding this surface.

G_{ij}^f is the fluidic conductance which represents the energy transfer through mass transport between two fluid elements from node j to node i .

As one can see in *subsection 3.2*, additional elements of matrix G are assigned for boundary nodes connected to the cold media of heat evacuation.

3.5.2 Thermal Capacity Matrix C

The heat capacity C of a volume is the product of the average mass m of the volume and specific heat capacity c_p^1 of the material of which the volume is made: $C = m c_p = \rho V c_p$, where ρ is the material density. Matrix C is diagonal and contains the C_{ii} elements of the heat capacity of each V_i of node i , calculated based on the physical property of the volume.

3.5.3 Heat Sources and Heat Sinks Vector Ψ

The vector Ψ of heat sources and heat sinks consists of adding heat production vector to heat evacuation thanks to boundary conditions heat exchange as explained in *paragraph 3.2* of LPTM approach. \dot{Q} vector is integrated using the values of different losses injected to nodes correspondingly. Heat sinks correspond to the values of the extracted heat through the cold plate or heat exchanger. Therefore, they are injected to heat exchanger nodes.

3.5.4 Space Discretization and Nodal Network

To assess thermally the complete front-to-rear motor structure, it is important to consider several sections along the motor shaft axis, specifically when a coolant flow is integrated, which may create a temperature gradient between the two motor ends. This probable temperature difference suggests using many radial sections all motor long.

In our model, the nodal network created according to the assumptions, with nodes locations, is displayed in *Figure 4.5*.

¹ For solids, the specific heat capacity is not a pressure-constant property, since the pressure is not an influencing parameter. However, the “ p ” subscript is maintained for text uniformity reasons.

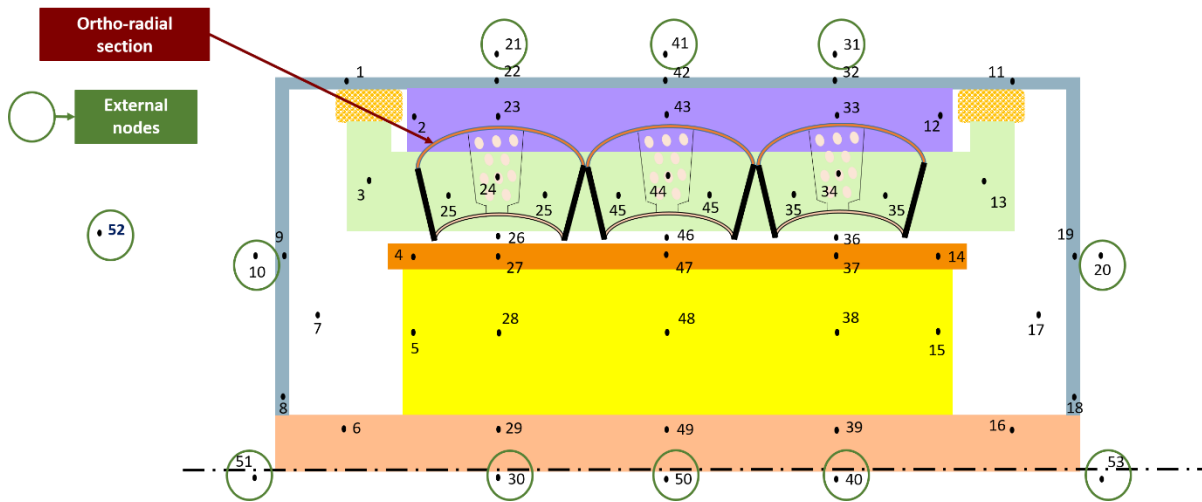


Figure 3.3 : Electric motor axial section showing nodes' location for nodal network model.

To represent the motor block, three sections along the axial direction at three different positions, symmetrically to the middle of the motor core, are considered (front side: nodes 22 to 29, middle section: nodes 42 to 49, and rear side: nodes 32 to 39). In addition to those three sections, each extremity (front and rear) of each motor component is assigned one node (nodes 1 to 6 and nodes 11 to 16), which connect motor parts to air cavities' nodes.

Due to the periodicity of the slots in the stator and to ortho-radial homogeneity in other motor parts, ortho-radial sections of the motor instead of radial ones consisting of one tooth-step are adopted. Consequently, the model is reduced radially to an angle $\alpha = 2\pi/(\text{slots' number})$. In each section, each motor part is represented by at least one node. The conductance connections in the ortho-radial section (front side) are shown in *Figure 3.4(a)*.

Each of the three tooth-nodes (25, 45, and 35) is relative to the teeth adjacent to each corresponding slot volume. Due to symmetry and periodicity in the stator, we assumed that this node is at the same temperature on each side. Hence, it is considered as one node, and the connection between these nodes and the winding nodes is computed based on this assumption with parallel conductances.

Axial and extremity connections of a quarter motor section are depicted in *Figure 3.4(b)*.

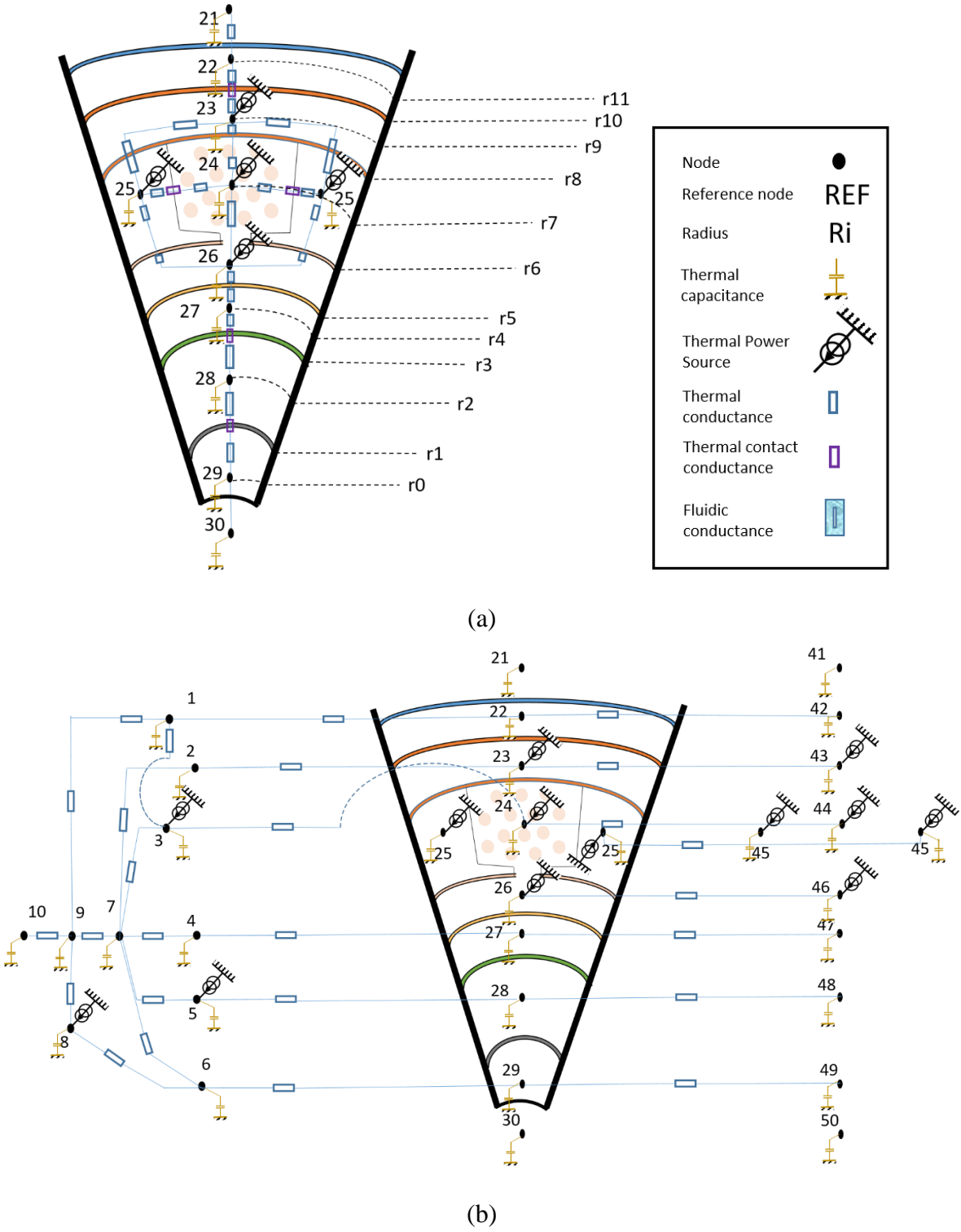


Figure 3.4 : Conductance connections of the motor nodal network. (a) Radial and ortho-radial connections of ortho-radial section. (b) Axial and Extremity connections of a quarter of the motor.

The nodes in each of the three motor axial sections are repeated for each component as follows:

Shaft nodes 29, 49, and 39;

Rotor laminations nodes 28, 48, and 38;

Magnets nodes 27, 47, and 37;

Airgap nodes 26, 46, and 36

Teeth nodes 25, 45, and 35;

Windings nodes 24, 44, and 34;

Stator laminations nodes 23, 43, and 33;

Frames nodes 22, 42, and 32.

Extremities' nodes are important in the lumped circuit for two main reasons. On one hand, they represent the convection heat transfer occurring in end-space regions with air in each cavity. Indeed, all extremities' nodes, at the front and rear sides, are connected to the air node in the cavity correspondingly. On the other hand, some of these nodes receive surface heat sources such as aerothermal losses due to friction (mainly found at rotor end-caps). Normally, these surface nodes should have a tiny axial dimension. The air in each cavity is considered homogeneous in terms of properties and temperature (which is generally the case due to the mixing process produced by the rotation) and is thus assigned one node at each motor end (nodes 7 and 17).

Bearings at each side are assigned nodes 8 and 18 connecting them to the frame lateral sides and shaft.

The frame, in the radial direction, takes part of the three sections (nodes 22, 32, and 42). It has also extremities' nodes (nodes 1 and 11). Both lateral frame surfaces are represented each by one node (node 9 for front side and node 19 for rear side) connected to air cavities' nodes and to radial frame nodes.

The complete nodal network of the motor with axial and extremity connections and external nodes is presented in *Figure 3.5*.

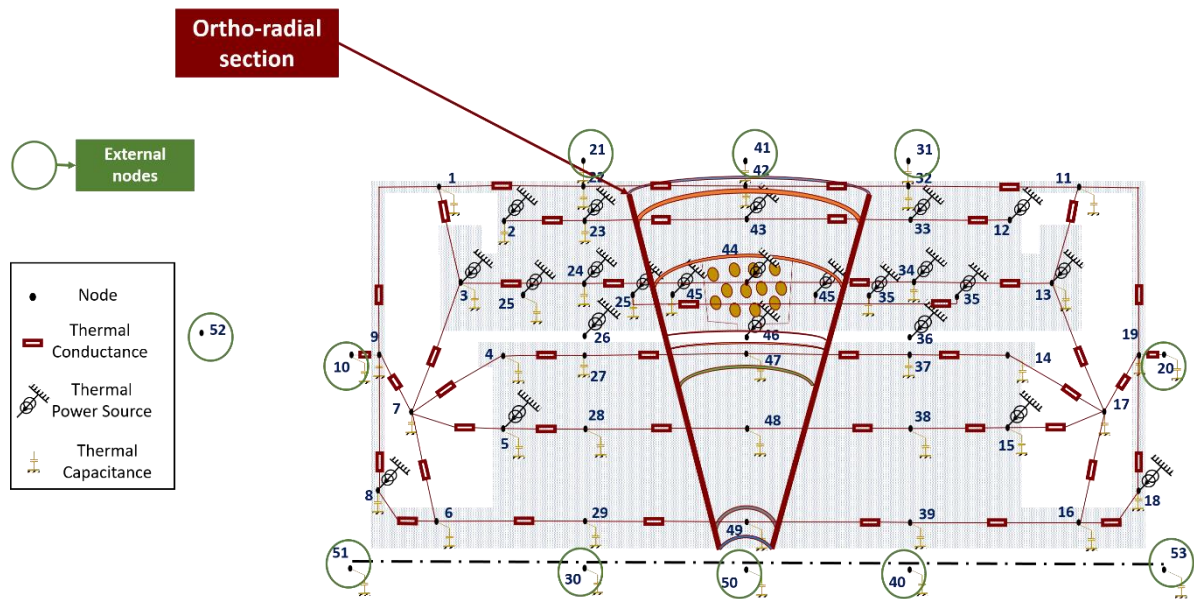


Figure 3.5 : Nodal network of e-motor with axial and extremity connections including the external nodes.

External nodes are added to the model to represent the surrounding environment of the motor: in the shaft, there are nodes 30, 40, and 50 (hollow shaft case), and around the motor frame, there are nodes 10 and 20 and nodes 51 to 53.

3.6 Thermal Properties of Components

Before going further in lumped model construction, we have to define the thermophysical properties of motor components implied in the system. In the model, materials are defined in terms of their properties; namely: thermal conductivities, densities, and specific heat capacities.

As described for the motor type applied, windings are mainly made of copper wires impregnated in an epoxy resin and wrapped with a polyimide film insulator. The motor stator has slots, wound with distributed windings. Rotor and stator iron cores are made of axially stacked ferromagnetic sheets alternatively with insulator disks. Permanent Magnets are made from rare-earth magnetic alloys. The shaft and frame are made of metallic materials or alloys.

As one can remark, some components of the motor are not homogeneous and have their structure made of two or more materials, such as the windings and laminated core of both rotor and stator. One of the advantages of LPTM is that multi-scale components can be modeled in

the same system. However, when detailed and delicate modeling requires longer computation time, which normally lowers the time-based efficiency of solving and may not be needed, it is more convenient to optimize the solution by determining and setting equivalent properties for these assemblies. The thermal and physical properties of both homogeneous and heterogeneous elements have to be defined in the nodal network model.

3.6.1 Equivalent Properties of Heterogeneous Components

In this section, methods for the determination of equivalent properties of the heterogeneous e-motor parts are elaborated. The two main heterogeneous components in the e-motor are the windings and the laminations.

3.6.1.1 Windings Equivalent Properties

The high heat dissipation existing in slots (spaces between every two consecutive teeth of stator filled with wound coils) and end-windings, due to Joule losses, and the confined character of these components encapsulated in low-conductivity materials, explain why this motor part in the motor reaches the high temperatures. The maximum allowed winding temperature depends on the impregnation thermal class. A non-uniform heat dissipation characterizes this part since it is made of multiple dissipative and non-dissipative materials. It is then crucial to find an accurate thermal model that takes into account the equivalent properties of winding coils.

❖ Equivalent Thermal Conductivity

The first approach is to determine the thermal conductivity of these elements based on the thermal conductivities of the constituents and the slot fill factor. The axial conductivity (along the motor shaft direction) of the windings is much greater than the radial one (relative to the radial direction in the motor). The coils are wound around the teeth parallel to the motor axis with a copper fill factor. In the axial direction, thermal resistances of copper wires and resin layers are parallel, while in the radial direction they are in series. When the copper thermal conductivity is hundreds of times greater than that of impregnation material, the approximate equivalent thermal conductivity of a series-set of equal proportions is closer to that of the more

resistant material. Thus, the heat flux propagation is limited mainly by the thermal conductivity of the impregnation material.

For the radial and ortho-radial thermal conductivities, some authors evaluated this conductivity for a two-material component $\lambda_{rad}^{eq,2}$ using homogenization formula from the work of Milton [165] (consisting of studying two-material composite structure properties). It was assumed a two-material microstructure, with cylindrical fibers (copper coils), distributed in an isotropic way in a matrix material (resin in this case). Then another computation from Mori [166] is adopted to evaluate the three-material slot thermal conductivity $\lambda_{rad}^{eq,3}$ (addition of varnish). These configuration approaches are respectively expressed in equations (3.19) and (3.20).

$$\lambda_{rad}^{eq,2} = \lambda_{res} \frac{(1 + \tau)\lambda_{cu} + (1 - \tau)\lambda_{res}}{(1 - \tau)\lambda_{cu} + (1 + \tau)\lambda_{res}} \quad (3.19)$$

$$\lambda_{rad}^{eq,3} = \lambda_{res} \frac{(2\lambda_{res} + \lambda_{cu})(\tau_2(2\lambda_{res} + \lambda_{var} + 3\tau_3\lambda_{var}) + 3\tau_1\lambda_{cu}(2\lambda_{res} + \lambda_{var}))}{\tau_2(2\lambda_{res} + \lambda_{cu})(2\lambda_{res} + \lambda_{var}) + 3\lambda_{res}(\tau_1(2\lambda_{res} + \lambda_{var}) + \tau_3(2\lambda_{res} + \lambda_{cu}))} \quad (3.20)$$

Where λ_{res} , λ_{cu} and λ_{var} are the resin, copper, and varnish conductivities respectively, τ is the slot fill factor of copper in the case of a two-material slot (τ =ratio of copper volume in the slot to total slot volume). τ_1 , τ_2 and τ_3 are the ratios of the volume of each material (respectively copper, resin, and varnish) in the slot to the total volume of the slot (can be the section ratios in an axis-orthogonal section). The thickness of the insulator layer (varnish here) used to cover each coil is generally set to be around $0.25 \mu m$ as an approximation.

To determine the axial equivalent conductivity of the slots λ_{ax}^{eq} , Lutun [167] used a simple approach. It consists of the linear combination in the following equation:

$$\lambda_{ax}^{eq} = s_{cu} \lambda_{cu} + s_{var} \lambda_{var} + s_{res} \lambda_{res} \quad (3.21)$$

Where s_{cu} , s_{var} and s_{res} are the volume percentages of copper, varnish, and resin respectively.

Two nomographs from General Electric [168] and Rohsenow [169] consisting of heterogeneous materials as a function of the slot fill factor (*Figure 3.6* and *Figure 3.7*) are generally used. The assumptions to determine the radial and ortho-radial conductivities of the windings for their case were: steady-state (or permanent regime), homogeneous impregnation material, highly conductive conductors, thermal flux along the winding axis, and negligible boundary effects. In these nomographs, λ_e is the winding equivalent thermal conductivity and λ_i is the resin thermal conductivity.

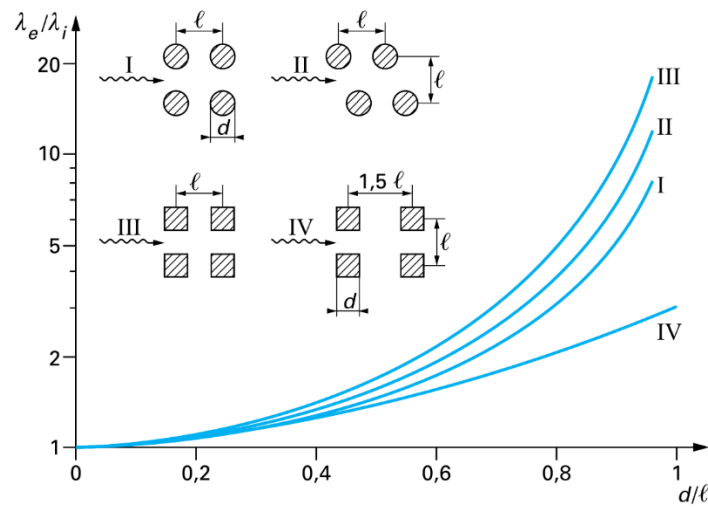


Figure 3.6 : Rohsenow nomograph [169] for equivalent thermal conductivity in heterogeneous materials with different configurations from [47].

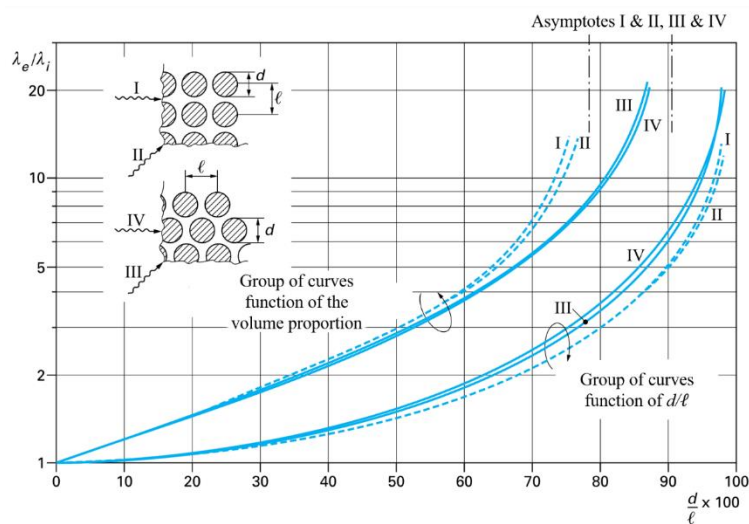


Figure 3.7 : General Electric nomograph for the thermal equivalent conductivity in heterogeneous materials with different configurations [47].

Renard [170] maintained the value of the equivalent winding conductivity in the radial direction from the linear regression for 8 circular coils ($0.42 \text{ W} \cdot \text{m}^{-1} \cdot \text{K}^{-1}$), with a slot, fill factor of 54.8% for windings and 65.1% for wreaths (end-windings). While for transverse (angular) and axial conductivities for a slot fill factor of 38%, the values are obtained from Finite Element (FE) model simulation on I-DEAS software considering that the heat is produced only in copper wires. Based on the numerical FEM simulation, they found for the adopted configuration case the following values: $\lambda_{ang} = 0.33 \text{ W} \cdot \text{m}^{-1} \cdot \text{K}^{-1}$ and $\lambda_{ax} = 203 \text{ W} \cdot \text{m}^{-1} \cdot \text{K}^{-1}$.

Subsequently, based on the sensitivity analysis to thermal parameters [171] conducted in our work, the accurate thermal conductivity of the slot in the radial plan is considered an important parameter. Therefore, it has been determined through FE analysis corresponding to heat production inside the slot. A complete parametric two-dimensional study of the thermal conductivity of winding in radial and ortho-radial directions has been conducted during the thesis. This study takes into account the dissipative character of coils impregnated in the resin and wrapped with an insulator sheet. Multiple parameters were considered in this analysis. Based on wide ranges of possible parameters values and options, correlations were elaborated to estimate more accurately this conductivity in each direction. The full study [172] was presented at the 2018 International Conference on Electrical Machines. We have extracted a polynomial correlation with two different sets of coefficients respectively to the two mentioned directions as in equation (3.22) with coefficients in *Table 3.2*.

$$\lambda_{rad,ang}^{eq} = A^{eq} + B^{eq}\lambda_{res} + C^{eq}\tau + D^{eq}\tau\lambda_{res} + E^{eq}\tau^2 \quad (3.22)$$

Coefficient	A^{eq}	B^{eq}	C^{eq}	D^{eq}	E^{eq}
Radial direction: λ_{rad}^{eq}	2.05	0	-12.14	4.39	17.4
Angular direction: λ_{ang}^{eq}	0.23	1.17	0.94	0.56	-0.57

Table 3.2 : Coefficients for winding thermal conductivity expression in equation (3.22).

❖ *Equivalent Density*

Similarly to thermal conductivity, considering that the variation of physical properties with temperature is negligible, the equivalent density of the winding, ρ_{wind} is calculated, based on the densities of copper and resin (ρ_{cu} and ρ_{res}) and the fill factor, as in the following equation:

$$\rho_{wind} = [\rho_{cu}\tau + \rho_{res}(1 - \tau)] \quad (3.23)$$

❖ *Equivalent Specific Heat Capacity*

Considering the temperature-independent property of the motor constituents, the heat (or thermal) capacity of volume V_i in the system is the product of the average weight of V_i and the

specific heat capacity of the material. In the electric motor, the equivalent heat capacity of the overall winding, c_{wind} , is related to its two main elements: coil and impregnation material. It is determined, based on specific heat capacities of copper and resin (c_{cu} and c_{res}) and the fill factor, as follows:

$$c_{wind} = c_{cu}\tau \frac{\rho_{cu}}{\rho_{wind}} + c_{res}(1 - \tau) \frac{\rho_{res}}{\rho_{wind}} \quad (3.24)$$

Where ρ_{cu} and ρ_{res} are respectively the copper and resin densities, ρ_{wind} is the winding equivalent density and τ is the slot fill factor.

3.6.1.2 Laminations Equivalent Thermal Conductivity

The equivalent thermal conductivity is calculated for the stator and rotor laminations in terms of the conductance of lamination and insulators sheets, as parallel in the angular and radial directions, or in series in the axial direction. For the sheets' plane direction, the conductivity is close to that of the ferromagnetic sheets since in parallel, the equivalent conductance is the sum of all conductances, and for the same dimensions, the total thickness of insulator sheets is negligible compared to the thickness of ferromagnetic sheets. In the direction of the sheets' thickness, the conductivity is a function of the interface connection and its thermal contact resistance [47]. In [170], the authors considered that the radial and angular conductivities are similar. They used equation (3.25) to evaluate these thermal conductivities for the stator and rotor laminations of an electric motor made up of ferromagnetic sheets with 0.65 mm thickness of FeSi (Iron-Silicon material) and insulator sheets of $1 \text{ }\mu\text{m}$ thickness each. These equivalent conductivities are computed as the sum of the thermal conductivities of all components considered in parallel. Besides, the axial thermal conductivity is evaluated using a series approach between the insulator and ferromagnetic sheets' conductivities as in equation (3.26):

$$\lambda_{rad} = \lambda_{ang} = \frac{\ell_{ins} \cdot \lambda_{ins} + \ell_{lam} \cdot \lambda_{lam}}{\ell} = 41.9 \text{ W} \cdot \text{m}^{-1} \cdot \text{K}^{-1} \quad (3.25)$$

$$\lambda_{ax} = \frac{\ell \cdot \lambda_{ins} \cdot \lambda_{lam}}{\ell_{ins} \cdot \lambda_{lam} + \ell_{lam} \cdot \lambda_{ins}} = 25.6 \text{ W} \cdot \text{m}^{-1} \cdot \text{K}^{-1} \quad (3.26)$$

Where ℓ denotes the total thickness of all insulator sheets and laminations, λ is the thermal conductivity property, ℓ_{ins} and ℓ_{lam} are the thicknesses of insulator sheets and laminations respectively.

3.6.2 Contact Thermal Resistance

It is important to note that the equivalent lumped model of any system depends strongly on physical factors, one of which is the nature of the connection between different elements. In particular, the complex nature of the interface region between two different elements (presence of residual impurities, air...) influences the thermal behavior of the electric motor at some locations in the stator (*Figure 3.8*) as well as in rotor (for instance, between magnets and rotor core). For an imperfect surface contact, calculating the total conductance between machine elements consists of adding directly or indirectly a contact thermal conductance representing the interface.

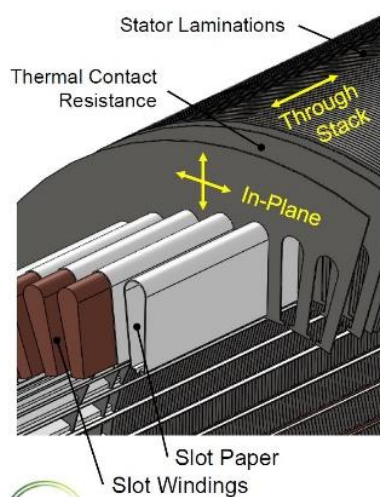


Figure 3.8 : Electric motor stator geometry showing slot coils and papers and thermal contact resistance of laminations [138].

Bertin [47] suggested some values of the contact conductance at some locations for different electric motor types, depending on the pressure applied to the contact region, surface roughness, materials properties, and connection type and technique. For each region, the contact conductance is reported in the following subsections.

3.6.2.1 *Between Coil and Slot Walls*

An insulator sheet separates the contact region between coils and the slot surface to protect the conductors. This contact region between the sheet and the coils is not fully adherent, and the connection problem is modeled as a thermal conductance existing between each slot surface and the corresponding coils. Bennion [138] found a surface contact conductance between slot liner paper and the coil of around $555 \text{ W}\cdot\text{m}^{-2}\cdot\text{K}^{-1}$, which is equal or smaller than the paper same property alone ($597 \text{ W}\cdot\text{m}^{-2}\cdot\text{K}^{-1}$). Bertin [160] found experimentally a value of $333 \text{ W}\cdot\text{m}^{-2}\cdot\text{K}^{-1}$, lately adopted by Thieblin [173], which is equivalent to an insulator sheet of 0.67 mm of thickness. This value of the surface contact conductance will be used in our case to account for the contact effect in radial and angular directions according to contact surfaces.

3.6.2.2 *Between Stator Laminations and Frame*

Renard [170] considered a value of $1500 \text{ W}\cdot\text{m}^{-2}\cdot\text{K}^{-1}$ for the surface contact conductance between stator and frame. In their application, an alerno-starter consists of a closed compact machine for which the model was recalibrated according to the contact thermal conductances and to ambient temperature. Due to aluminum and iron dilatation, a value of $5000 \text{ W}\cdot\text{m}^{-2}\cdot\text{K}^{-1}$ is found more adequate at an ambient temperature of $35 \text{ }^\circ\text{C}$ and $2000 \text{ W}\cdot\text{m}^{-2}\cdot\text{K}^{-1}$ at an ambient temperature of $70 \text{ }^\circ\text{C}$.

3.6.2.3 *Between Magnet and Rotor Laminations*

Permanent magnets of the rotor are directly bonded to the rotor laminations. Thieblin [173] considered a 0.05 mm adhesive thickness assuming a perfect contact of adhesion. Depending on the temperature difference value and sign between laminations and magnets in the rotor assembly of the motor, this contact property is classified to be a major or minor, positive or negative factor, or even insignificant.

However, in this thesis a contact conductance is added and is extracted from the value range found in [170], stating that for rough contact with undulations, the surface thermal resistance value is located between $10^{-3} \text{ m}^2\cdot\text{K}\cdot\text{W}^{-1}$ to $10^{-4} \text{ m}^2\cdot\text{K}\cdot\text{W}^{-1}$, and for simply rough contact, the

value ranges between $2 \times 10^{-4} \text{ m}^2 \cdot \text{K} \cdot \text{W}^{-1}$ to $10^{-5} \text{ m}^2 \cdot \text{K} \cdot \text{W}^{-1}$. In our case, an average value of $10^{-4} \text{ m}^2 \cdot \text{K} \cdot \text{W}^{-1}$ is adopted considering a rough surface contact.

3.6.2.4 *Between Rotor Laminations and shaft*

According to [170], and according to the range of values mentioned in subsection 3.6.2.3 for rough contact type, we have decided to use a penalizing value of $10^{-3} \text{ m}^2 \cdot \text{K} \cdot \text{W}^{-1}$ to consider the surface contact resistance between rotor laminations and shaft. This will affect the heat flux path from the rotor to the shaft.

3.7 Validation with Experimental Results

Before sizing the high specific power electric motor cooling system, it is crucial to validate the thermal model core (inner motor thermal model). An electric motor of the same type as the one to be conceived has been chosen. It is a permanent magnet synchronous machine designed for automotive propulsion designed and optimized for a hybrid-electric vehicle [174]. Experiments are conducted on the machine, and results were used to validate the elaborated small thermal network (eight-node model), which was used for sensitivity analysis in [52] as well.

The experimental PMSM is liquid-cooled in the stator, with water jackets and a coolant flow temperature of $16 \text{ }^\circ\text{C}$. Stator, rotor, and frame structural materials are listed in *Table 3.3*. Motor power data and losses distribution are grouped in *Table 3.4*. Motor characteristics and dimensions are found in *Table 3.5*.

The experimental temperatures are given at an operating point with 6000 RPM speed corresponding to an output power of the motor of 50 kW . The total losses are around 2.3 kW .

Motor part	Structural material	Density ($kg \cdot m^{-3}$)	Thermal conductivity ($W \cdot m^{-1} \cdot K^{-1}$)	Specific heat capacity ($J \cdot kg^{-1} \cdot K^{-1}$)
Lamination	EBG, NO20	7600	38	460
Coil	Copper (Cu)	8900	395	385
Frame	Aluminum (Al)	2705	230	900
Shaft	Steel	7800	51	460
Magnets	NdFeB	7500	9	-
Winding impregnation	Unsaturated polyester	1350	0.2	1700
Slot insulation	Mylar film	-	0.2	-

Table 3.3 : Experimental PMSM structural material data used in the model[174].

Size	Value	Unit
Shaft power	49	kW
Maximum speed	6021	RPM
Terminal current	170	A
Supply frequency	201	Hz
Winding losses	822	W
End-winding losses	513	W
Stator yoke losses	464	W
Stator teeth losses	387	W
Rotor losses	22	W
Friction losses	90	W
Total losses	2.298	kW

Table 3.4 : Experimental PMSM power data and losses [174].

The specific power of the motor with the cooling is around 1 kW/kg , which is less than the targeted motor in the current project but can be considered for motor model comparison.

The motor design is applied to the thermal model and steady-state results have been compared against the measured temperatures in the stator.

This comparison shows a strong agreement of the simulated and measured data (the relative errors considering the coolant temperature are around 3.2% for the end-windings and 1.2% for the coils). The results of this comparison are presented in *Table 3.6*.

Motor type	PMSM	
Cooling type	Water cooling of stator frame	
Application	Hybrid Electric Vehicle	
Dimension	Value	Unit
Stator core length	231	mm
Lamination filling factor	0.965	mm
Stator inner diameter	110	mm
Stator outer diameter	189	mm
Number of stator slots	48	-
Yoke thickness	16.4	mm
Tooth width	3.5	mm
Tooth height	20.4	mm
Slot area	89.8	mm ²
Number of pole pairs	2	-
Slot filling factor	0.45	-
Mechanical airgap	0.3	mm
Magnet thickness	5	mm
Rotor core outer diameter	107.1	mm
Rotor core inner diameter	64.6	mm
Retaining sleeve thickness	0.75	mm

Table 3.5 : Experimental PMSM characteristics and dimensions [174].

Temperature Node	Measured [174] (°C)	Computed (Nodal Network) (°C)
End-windings	72	70.2
Coil Sides	51	51.7
Coolant inlet	16	16

Table 3.6 : Comparison between experimental and numerical resulting temperature.

Consequently, the developed thermal model could reasonably be considered for a high specific power permanent magnet motor.

3.8 Conclusion

The basics of the LPTM technique and its application to our study were addressed. The structure and general characteristics of the electric motor system (PMSM type) are described and detailed to elaborate a global thermal model network. Compared against experimental data, the developed motor model core is stated valid for subsequent investigations. Hence, the model can be used in different context studies for the same motor type. In the following chapter, the motor designs provided by WP1 are simulated. A description of the electric machine and the configuration of the associated thermal model considerations and cooling system are discussed, and thermal results are analyzed and processed.

CHAPTER 4 THERMAL MANAGEMENT OF DESIGNED E-MOTORS

Synopsis:

After elaborating the model of the e-motor core, the cooling systems of e-motors are integrated to the numerical model. Simulation results are displayed and analyzed. Then, sensitivity studies and investigations on the motor thermal behavior are carried out. Considering the thermal constraints, a final design for each e-motor is selected, with electromagnetic and thermal data. The designs of the e-motor fulfill the conditions and project targets, mainly the specific power values.

4.1 Introduction

In HASTECS project, several configurations of the propulsion of the hybrid aircraft have been investigated. In particular, two configurations were specifically investigated with high specific power motors, inducing complex electrical and thermal problems. For each of the project targets (Target 1 for 2025 and Target 2 for 2035), a sizing point of the propeller power is adopted to which a suitable electric motor design is elaborated and verified according to the required mechanical power. The objective is to find a suitable cooling configuration for each motor design. The motors should have high specific power densities of at least 5 kW/kg for Target 1 and 10 kW/kg for Target 2. Electric motors designed in this framework are thermally assessed to deal with hot spot temperatures through cooling techniques. A global design procedure of high specific power electric motors based on an equivalent thermal constraint value is presented.

Based on the model presented in the previous chapter, cooling techniques and circuits are simulated for each machine design correspondingly. The targeted specific power of each motor takes into consideration the weight of the motor with the cooling installed in the system. Temperature limits are the main constraints of the numerical model.

To find the most efficient and light cooling technology that maintains motor temperatures below the maximum allowed values, several strategies and investigations are conducted for each of the two electric motor targets.

4.2 Electric Motor Design for 2025 (EM2025)

The first objective of the current work is to manage the thermal behavior of the future electric motor for the first target of the project. The electromagnetic design calculations are performed by WP1 and the provided data needed for thermal management design are integrated into the thermal model (LPTM).

4.2.1 Thermal Constraint Evaluation

The issue of reaching high specific power targets for electric motors of hybrid propulsion requires a complex procedure. With that being added to several constraints, both the electric motor and its cooling system are subject to investigation and mutual effort in the design phase. For this purpose, in collaboration with the WP1 team, a sizing approach using electro-thermal models is proposed and defined. This study is detailed in [176]. Although all electromagnetic design parameters are provided by WP1, some interesting criteria related to thermal management have to be taken into account.

A thermal constraint has been introduced in the design process by the joint work of WP1 and WP3 of the project to make sure motor temperatures could be maintained below the limits. This constraint is equivalent to a current density product called Aj , which is a parameter that depends only on the effectiveness of the cooling system (Aj expressed in $[A^2 \cdot m^{-3}]$). It is the product of the linear surface current density (A or A_{rms} [$kA \cdot m^{-1}$]) by the current density (j or j_{rms} [$A \cdot mm^{-2}$]). It reflects the allowed values of electromagnetic loads and their limits according to the cooling technology. Each electric motor type has specifically permitted values of the electromagnetic loads depending on the cooling technology used [177]. In the case of direct water cooling, Aj attains essentially higher values. *Table 4.1* categorizes the value ranges of these two loads parameters (A and j) and their product, according to the machine cooling technique for low rotational speed non-salient synchronous machine. Knowing that this product considers only Joule losses and intending to find a global thermal constraint that takes into account all losses [176], an equivalent product Aj_{eq} [$A^2 \cdot m^{-3}$] (defined as the thermal constraint for the electromagnetic design of our motors) is evaluated as follows:

$$\langle Aj_{eq} \rangle = \frac{\sum \text{Motor Losses}}{2\pi R_{stator} L_m \rho_{cu}(T) k_{tb}} \quad (4.1)$$

Where R_{stator} is the inner stator radius, L_m is the active length, $\rho_{cu}(T)$ is the copper electrical resistivity as a function of winding temperature, and k_{tb} is the end-windings coefficient (equals to the ratio of machine total length to machine active length).

Electric loads	Indirect cooling		Direct water cooling
	Air	Hydrogen	
$j_{rms} (A \cdot mm^{-2})$	3-5	4-6	7-10
$A_{rms} (kA \cdot m^{-1})$	30-80	90-110	150-200
$A_{rms} j_{rms} (A^2 \cdot m^{-3})$	$10.5-40 \times 10^{10}$	$36-66 \times 10^{10}$	$1.05-2 \times 10^{12}$

Table 4.1 : Permitted values of electromagnetic loads for non-salient synchronous machines according to cooling technology [177].

The organigram in *Figure 4.1* models the interaction between the electromagnetic and thermal models developed by WP1 and WP3.

The design procedure consists of six steps enumerated below:

Step 1: assess the electric motor technologies required using WP1 model called Target Setting Tool (TST) for high specific power electric motor design.

Step 2: size the surface-mounted permanent magnet synchronous motor using WP1 tool called SM-PMSM for this electric motor type.

Step 3: check the value of the thermal constraint according to the cooling method chosen in step 1.

Step 4: determine the electric motor temperatures and verify that no motor parts are overheated.

Step 5: get the sizing of the cooling system.

Step 6: compute the total weight and verify that the specific power target is obtained.

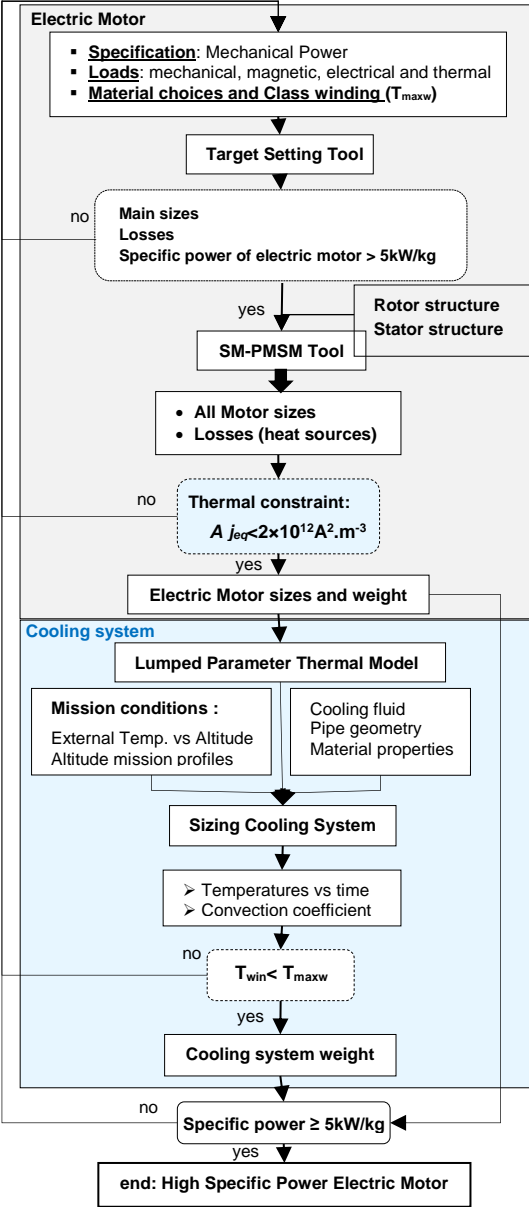


Figure 4.1 : Interaction between electro-thermal models for sizing high specific electric motors with their cooling system [176].

This joint work of both Work-Packages allowed the determination of a maximum value of this equivalent thermal constraint according to cooling configurations to design high-specific motors (EM2025 and EM2035). The proposed cooling for EM2025 and EM2035 respectively enabled the design of a high specific power electric motor with $2 \times 10^{12} A^2 \cdot m^{-3}$ and $5 \times 10^{12} A^2 \cdot m^{-3}$ as thermal constraint values.

4.2.2 Motor Design and Sizing

A three-dimensional (3D) section of the Electric Motor for 2025 (EM2025) designed for the first target provided by WP1 is depicted in *Figure 4.2*. The electric motor design is of SM-PMSM type with distributed windings forming a wreath at each extremity.

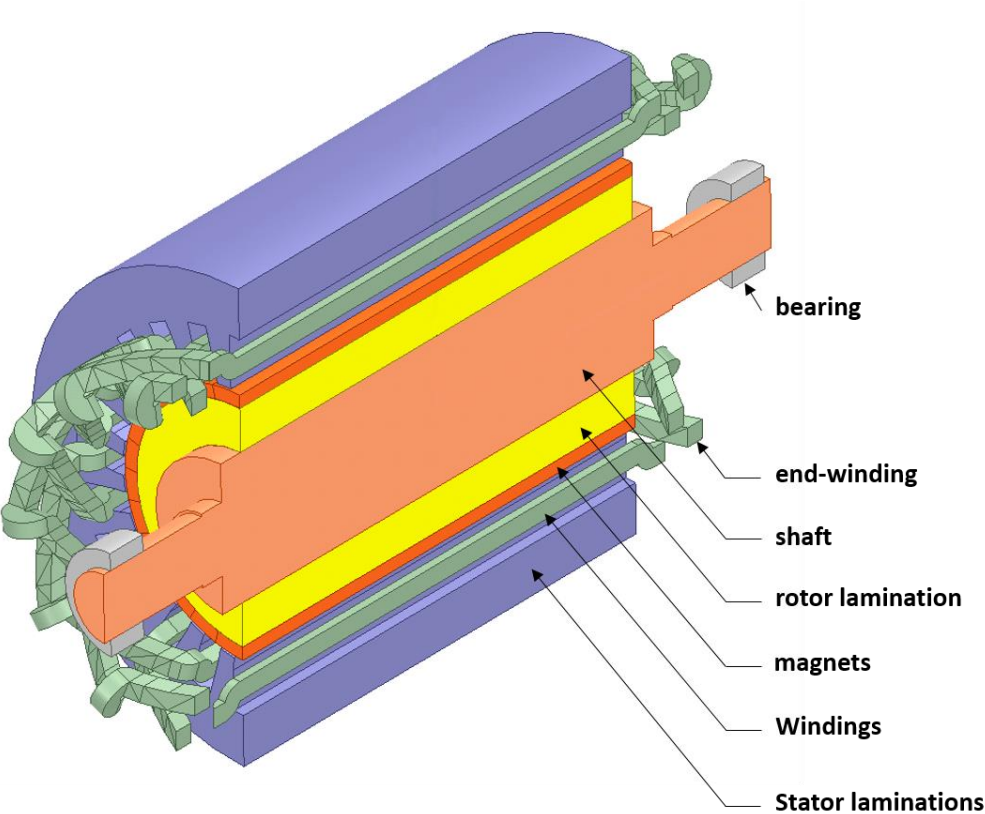


Figure 4.2 : Electric Motor 3D section view (from WP1).

The motor section shows the core geometry of the e-motor with its components. E-motor data are presented thereafter.

4.2.2.1 Electric Motor Characteristics

Developed by the WP1 group, the electrical design of the motor and corresponding data with their maximum values are gathered in *Table 5.1*.

The losses values in *Table 5.1* are the maximum level of heat sources in the thermal model. For a steady-state simulation, they can be used to estimate a continuous full-power operating motor. A dynamical profile for each losses type is presented thereafter.

The machine geometrical dimensions are grouped in *Table 4.3*. With a motor power around *1.5 MW*, tens of *kW* of losses are estimated at a full power operation of the machine.

The EM2025 is characterized by a high rotation rate. It should have a minimum specific power of *5 kW/kg* which is the ratio of the power to the weight. The overall weight of the bare motor without the frame is kept confidential. These weights are optimized to achieve the specific power target. Confidential values of losses are expressed in Per-Unit (PU) with respect to motor total losses (equal to 1 PU).

Characteristic	Unit	Value
Mechanical speed	RPM	15696
Number of phases	-	3
Number of slots	-	24
Winding losses	PU	0.25
End-winding losses	PU	0.18
Stator yoke losses	PU	0.30
Stator teeth losses	PU	0.13
Windage losses	PU	0.10
Friction losses	PU	0.04

Table 4.2 : PMSM Power Data and losses from WP1.

Main size	Unit	Value
External stator radius	mm	162.87
Inner stator radius	mm	92.47
Stator yoke height	mm	34.29
Slot height	mm	36.11
Tooth width	mm	10.58
Slot width	mm	13.48
Airgap thickness	mm	1.53
Permanent magnet thickness	mm	9.00
Rotor yoke height	mm	29.72
Shaft radius	mm	50.98
Active length	mm	317.33
Motor length	mm	538.6

Table 4.3 : Main dimensions of the electric motor without cooling system [176].

4.2.2.2 Specific Characteristics (Maximum Temperatures)

The maximum temperatures in the motor are set as constraints for our machine. They are mainly due to the operation conditions of the windings and permanent magnets. These two components are particularly sensitive to temperature, once exceeding a certain maximum allowed level, they can undergo serious electrical and magnetic malfunctioning. Through repeated cycles of reaching these maximum temperatures, this malfunctioning leads to total motor failure. The temperature constraint is defined according to the material properties constituting these components. For windings, each degree above the allowed maximum temperature will shorten the motor lifetime exponentially. Permanent magnets are subject to demagnetization in the case of temperature overshoot. This specificity must be taken into consideration when defining the motor and cooling system design.

For EM2025, the temperature limits are given in *Table 4.4*. The adopted winding thermal class defining the insulation material's maximum temperature is class 220 °C, which allows reaching 180 °C considering the safety margin set by WP1. The permanent magnet used in the motor is the Samarium-Cobalt alloy with a maximum limit of the temperature of 150 °C, which practically gives 135 °C depending on materials, with a safety margin according to WP1.

Component	Temperature limit for Target 1
Windings	180 °C
Permanent magnet	135 °C

Table 4.4 : Temperature limits for EM2025 critical components.

4.2.3 Thermal and Physical Properties

Thermal and physical properties of media should be defined to run the model simulation. They are determined based on the components' materials. Rotor and stator laminations are made of a soft magnetic material: cobalt iron alloy. Permanent magnets are samarium-cobalt rare earth magnets. The shaft is made of steel and finally, the frame is made of aluminum. Properties of different materials of the e-motor are grouped in Table 4.5. They are assumed constant relatively to the changing component temperature in this numerical study.

Material		Properties			Data Source
		Density ($kg \cdot m^{-3}$)	Thermal conductivity ($W \cdot m^{-1} \cdot K^{-1}$)	Specific Heat Capacity ($J \cdot kg^{-1} \cdot K^{-1}$)	
Winding	Copper	8920	360-400	390	WP1/WP5
	Resin	1500	1	1700	
Stator/Rotor Laminations	Soft Magnetic Alloy Co-Fe	8120	Axial: 25 Radial: 46 Angular: 42	460	Material choice: WP1. Properties' definition: literature [170], [174]
Permanent Magnets	Sm2Co17	8400	10	370	WP1
Shaft	Steel	8100	45	502	WP1
Frame	Aluminum	2700	200	900	Set by WP3
Bearings	Steel	8100 (70% filled)	45	502	Set by WP3

Table 4.5 : Material properties of EM2025 at ambient temperature.

The thermal conductivity of resin applied for impregnation of windings is $1 W \cdot m^{-1} \cdot K^{-1}$ for EM2025. As a perspective for the year 2025, these materials will be available for application.

Based on the study presented in *Chapter 3*, the resulting winding thermal conductivities are $2.53 \text{ W}\cdot\text{m}^{-1}\cdot\text{K}^{-1}$ and $2 \text{ W}\cdot\text{m}^{-1}\cdot\text{K}^{-1}$ respectively in radial and angular directions. After defining these parameters, the thermal model can be configured for the electric motor EM2025. These properties' values are used as constants then a sensitivity study is conducted to determine whether their variation due to temperature could change significantly the resulting maximum temperature in each motor part (see *subsection 4.4.3*).

4.2.4 Dynamical Profile of Power

4.2.4.1 Mission Profile

Based on hybrid chain studies of the aircraft propulsion system analyzed and investigated by our project partners, a mission profile of the power required at the shaft level for one propeller has been delivered by Airbus. This dynamical profile is depicted in *Figure 4.3*.

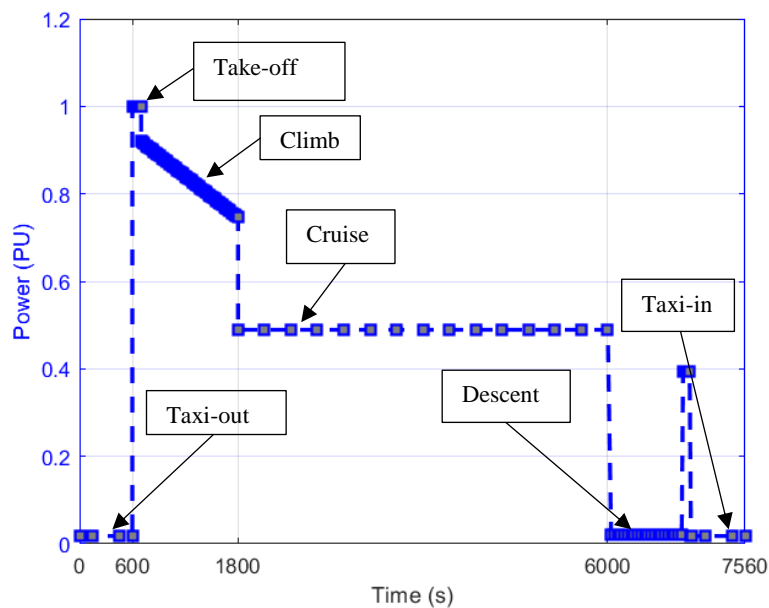


Figure 4.3 : Mission profile provided by Airbus.

During the first and last phases of taxiing, a low level of power is needed, while full power is required for the take-off phase. After this short phase, a decreasing power level is depicted in this profile during the climb phase reaching around its half at the beginning of the following

phased of the cruise. A constant value is applied during the whole cruise phase until the descent phase where a decreasing profile of power is required.

4.2.4.2 Losses Profiles

In this work, losses profiles dissipated in the designed electric motor are obtained from electrical, magnetic, and mechanical equations based on power profile at maximum torque. These losses – equivalent to heat sources - are provided by WP1 as a function of the flight mission, and the resulting graph is depicted in *Figure 4.4* accordingly. The plot gives the dynamical profiles of losses according to their types (total of 5) in percentages (%), with respect to the total losses value at full power.

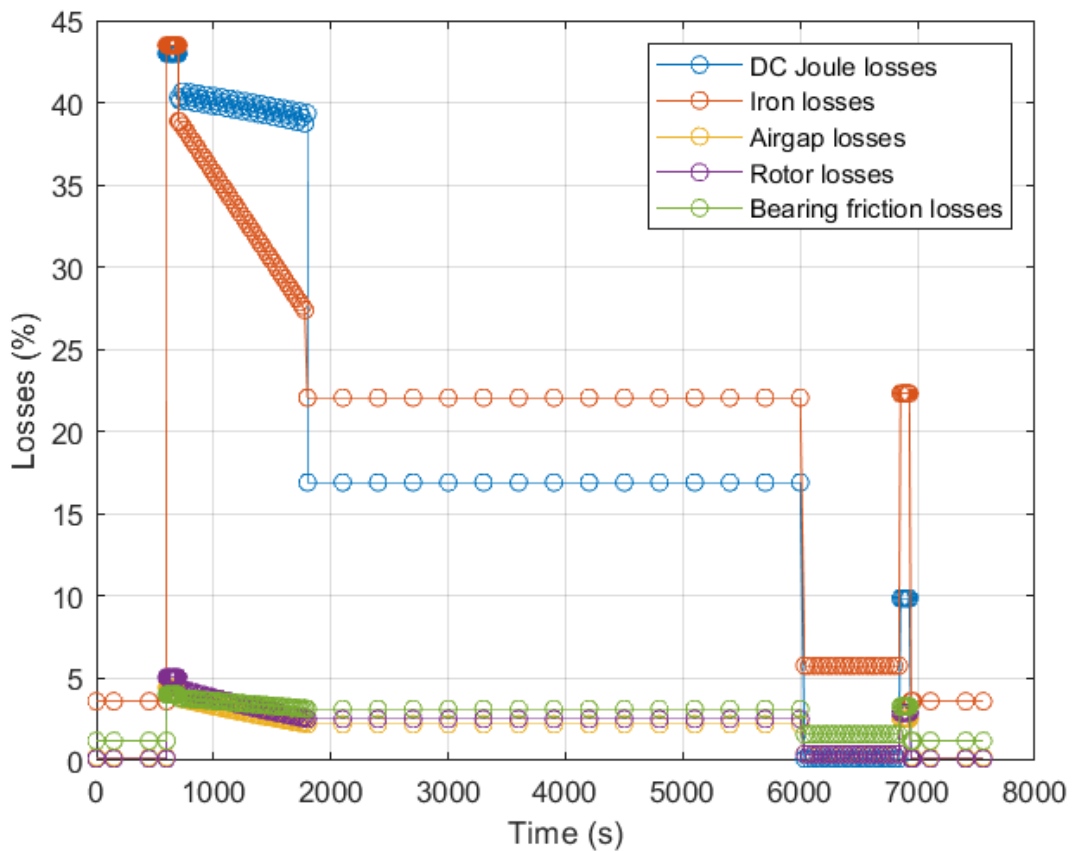


Figure 4.4 : Losses profile of EM2025 in % with respect to maximum total value from WP1.

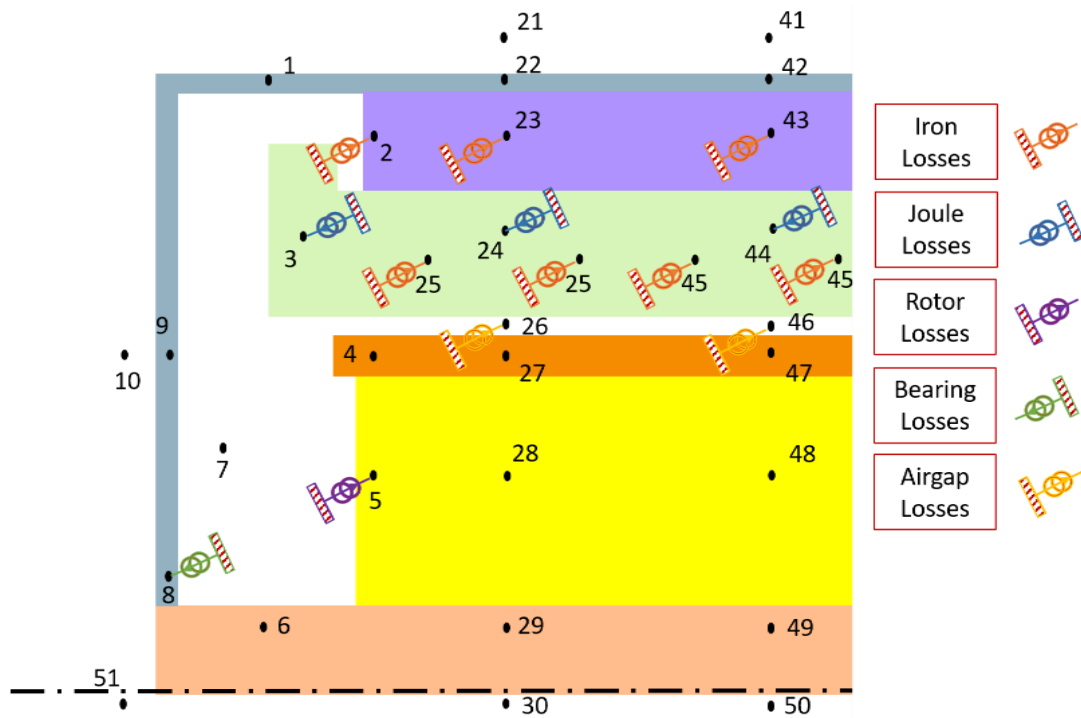


Figure 4.5 : losses location in a quarter e-motor axial section.

Figure 4.5 shows the location of generated losses. Losses are injected uniformly between the different nodes of a given motor part. Due to symmetry in the electric motor structure, half of the axial section is represented in this figure. In the model, Joule losses are injected into windings nodes in both the slot parts and the end-windings. Iron losses are computed for the stator iron part since rotor iron losses are neglected. Mechanical losses due to friction are considered as follows: airgap losses in the airgap, rotor windage losses at the rotor endcaps (surface heat sources), and bearing friction losses injected into both front and rear bearings.

4.3 Cooling System

Cooling technology choice is a matter of the required effort to reduce the temperature of each critical part. This effort should be proportional to temperature rise during the motor operating process. The objective is always to maintain temperature and weight below the limits. Therefore, excessive cooling penalizes the weight and hence it decreases the specific power that should be at least equal to 5 kW/kg . Investigations and analyses concern mainly the heat paths towards the outside environment. Based on the heat transfer equation, these heat paths depend on the thermal resistance values between the elements and the heat sink or more

specifically the specific cooling media. Consequently, possible cooling solutions and techniques are drawn from these analyses.

4.3.1 Thermal Resistance Analysis

To determine suitable cooling methods, a preliminary analytical study of thermal global resistances helped us choosing the cooling techniques for specific motor zones by analyzing heat fluxes paths. It is based on steady-state heat transfer calculations oriented towards eliminating some inefficient methods.

The main thermal constraint of the electric motor is in the windings, which are limited by their maximum acceptable temperature. Moreover, the windings generate the highest heat dissipation in the motor. Their conductors are isolated from the surrounding parts with an insulation material of low thermal conductivity (impregnation material). Permanent magnets have also a constraint related to their maximum allowed temperature. All of these facts lead us to investigate finding an optimum way to extract heat through cooling. Windings and rotor parts are the main studied areas.

Our LPTM consists of considering one-twenty-fourth (one over the slots number) of the motor. Volumes, surfaces, and heat sources, are required to calculate the temperature rise in the motor core

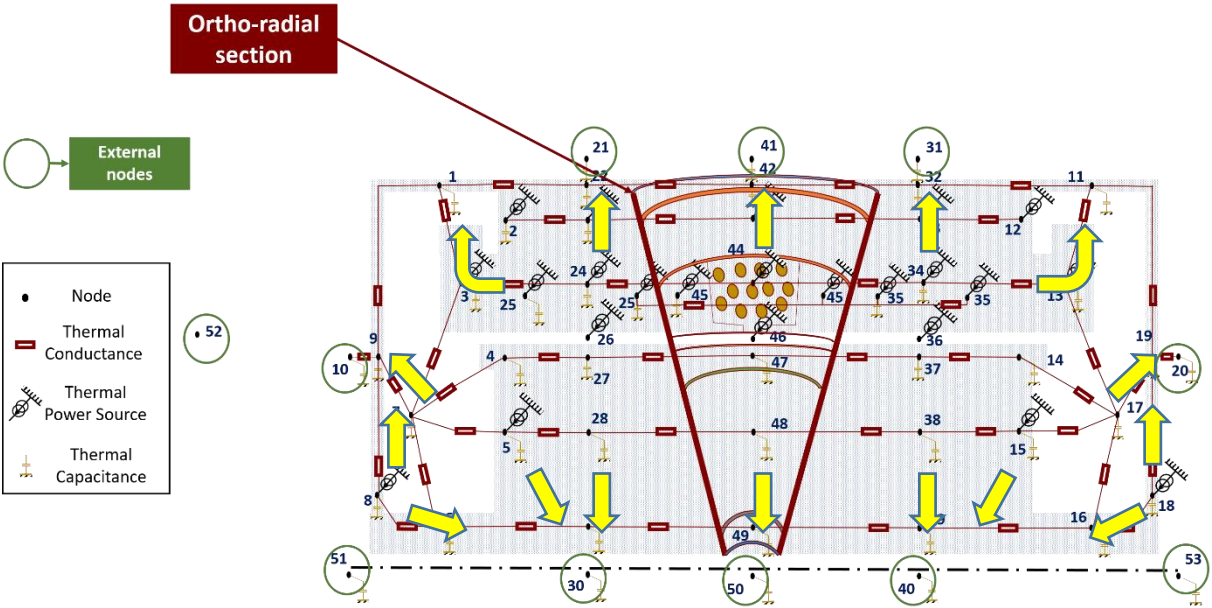


Figure 4.6 : Nodal network of the electric motor with emphasis on heat paths (yellow arrows) through external nodes connections.

For this purpose, the analysis based on the nodal network and heat path connections with external nodes (*Figure 4.6*) is conducted for the main critical hot spot zones: windings and rotor magnets. The total value of maximum heat dissipations is considered for steady-state temperatures.

4.3.1.1 Analysis for Winding Case

Before analyzing heat paths and resistances in windings material, it seems practical to separate motor windings into two main parts: slot part representing the windings inside slots and end-windings or winding wreaths at each of the motor sides.

On external nodes (in green in *Figure 4.6*), heat transfer coefficients have been imposed assuming forced air cooling ($200 \text{ W}\cdot\text{m}^{-2}\cdot\text{K}^{-1}$) or forced liquid cooling ($2000 \text{ W}\cdot\text{m}^{-2}\cdot\text{K}^{-1}$). The windings in the slot and the end-windings are studied, based on a simplified network depicted in *Figure 4.7*.

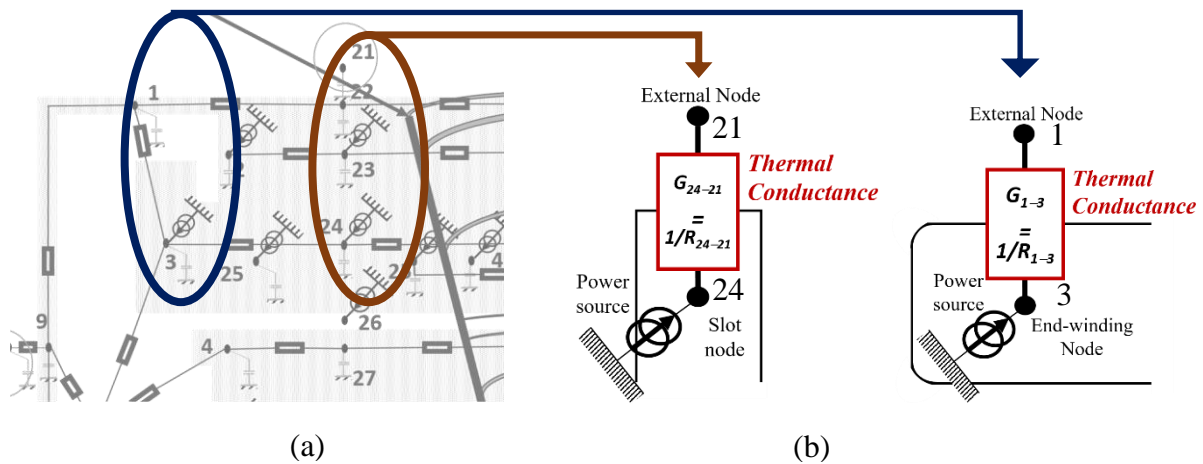


Figure 4.7 : (a) Nodal network near the stator zone at front motor side. (b) Thermal resistances between external nodes and slot node (left) and end-winding node (right).

For slot node 24 in our LPTM, we have considered connecting the central winding node, to the external node representing the cooling medium (air in the case of air cooling). The total heat path through a corresponding thermal resistance in permanent full power regime results in heating the windings to a maximum temperature that we will call: $T_{w,max}$.

The simplest way for the generated heat to evacuate from windings to the outside is through the housing radial part depicted in *Figure 4.7b (left)*. The thermal resistances are calculated for two possible cases: air cooling and liquid cooling. Knowing that the difference is mainly in the convection coefficient, the thermal conduction resistance remains the same for both cases. This resistance is calculated between slot node 24 and frame node 22 in the studied ortho-radial section for the corresponding volumes. It corresponds to two series resistances R_{24-23} (of $5.435 K \cdot W^{-1}$) and R_{23-22} (of $0.095 K \cdot W^{-1}$). The estimation gives the equivalent resistance of these two series resistances: $R_{24-22} = 5.53 K \cdot W^{-1}$, which is close to the slot-to-laminations resistance value due to the low thermal conductivity of windings compared to other high-conductivity materials.

The remaining thermal resistance in the path corresponding to cooling, which stands in series with the previous resistance, is R_{22-21} connecting node 22 to external node 21. A total thermal resistance called $R_{slot-ext}$ corresponding to R_{24-21} is calculated for each coolant option.

In the case of air at a temperature of $38 \text{ }^\circ\text{C}$ (the ground temperature at ISA+23), with $200 W \cdot m^{-2} \cdot K^{-1}$ of convection coefficient, $R_{22-21} = 0.633 K \cdot W^{-1}$, and $R_{slot-ext} = 6.163 K \cdot W^{-1}$. In this case a temperature $T_{w,max} = 403 \text{ }^\circ\text{C}$ is found.

For liquid cooling with water-glycol jackets providing around ten times the previous coefficient of convection heat transfer ($\sim 2000 W \cdot m^{-2} \cdot K^{-1}$), the resistance between nodes 22 and 21 is reduced by nearly the same ratio and $R_{22-21} = 0.085 K \cdot W^{-1}$. The total resistance between the slot node and the external node is $R_{slot-ext} = 5.61 K \cdot W^{-1}$, which can reduce the winding temperature by at least $30 \text{ }^\circ\text{C}$ ($T_{w,max} = 370 \text{ }^\circ\text{C}$). This temperature difference of $30 \text{ }^\circ\text{C}$ is significant with respect to the maximum allowed temperatures in the motor. Thus, the liquid cooling solution with a jacket around the stator will be privileged.

The same calculation methodology is applied for the end-winding zone (also generating heat). The value of thermal resistance R_{ew-ext} between end-winding and the external node is analyzed. In the case of air convection at the end-winding end-space, this resistance is approximated as $R_{ew-ext} = 8.6 K \cdot W^{-1}$ with a convection coefficient of $110 W \cdot m^{-2} \cdot K^{-1}$. It leads to an end-winding steady-state temperature $T_{ew,max} = 571 \text{ }^\circ\text{C}$. A novel technique detailed in literature consists of potting the end-windings with highly conductive material (see *Chapter 2*). Thanks to this

technique the thermal resistance is reduced to $R_{ew-ext}=7.1 \text{ K}\cdot\text{W}^{-1}$ (since thermal conduction, in this case, is more significant than air-convection). This results in a temperature decrease of around $100 \text{ }^\circ\text{C}$. Obviously, in this motor design, potting is more efficient than air cooling in the case of winding wreaths with high heat dissipation.

As might be expected, the level of $T_{w,max}$ and $T_{ew,max}$ is very high in steady-state. As can be seen in *Figure 4.4*, the maximum losses are imposed during a very short time. Moreover, during this phase (take-off), the outside air temperature decreases rapidly due to the plane climb phase. Consequently, we decided to get profit from the system inertia to maintain the temperatures below the limits with an optimized cooling configuration.

4.3.1.2 Analysis for Rotor Case

The critical temperature in the rotor is that of magnets. The thermal resistance between rotor and external node (or nodes), $R_{rotor-ext}$, depends on the heat paths to outside as depicted in *Figure 4.8*.

For the front motor side, near the rotor, a focused network scheme is depicted in *Figure 4.8a*.

Two ways of heat extraction are possible according to the nodal network in this area. It can be either the heat path through the air cavity node (through node 7 to external node 10 in the lateral side of the frame) or the shaft and along the channel (towards node 30, the cooling node in the hollow shaft).

As for stator channels, two cooling techniques are evaluated for the rotor, which are liquid cooling and air cooling with similar heat transfer coefficient values: $200 \text{ W}\cdot\text{m}^{-2}\cdot\text{K}^{-1}$ for air case and $2600 \text{ W}\cdot\text{m}^{-2}\cdot\text{K}^{-1}$ for the liquid case. With forced liquid cooling (with water-glycol for instance), a high convection coefficient can be obtained, and thus the dominant heat path is through the shaft axial channel.

The simplified connections network is depicted in *Figure 4.8b* between rotor node 5 and the external nodes 10 and 30.

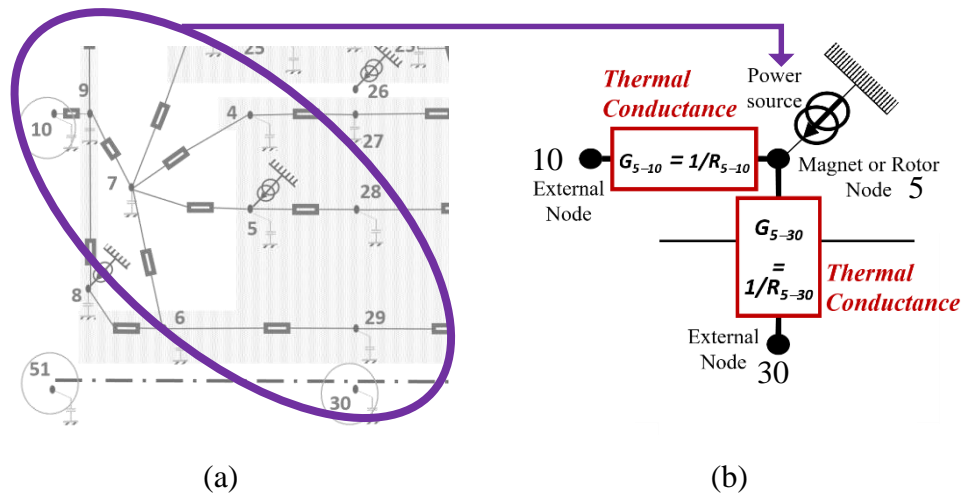


Figure 4.8 : (a) Nodal network near the rotor zone at front motor side. (b) Thermal resistances between external nodes and rotor or magnet node for the evacuation of heat.

The heat dissipation from windage losses at the rotor end-caps is assigned to the rotor laminations surface since magnets have a relatively low thickness in radial direction compared to the rotor radial surface. This results in approximately the same temperature levels in these elements since there is a low conduction resistance from laminations to magnets.

For air-cooling, $R_{5-30} = R_{rotor-ext,1} = 24.43 \text{ K}\cdot\text{W}^{-1}$.

Liquid cooling gives $R_{5-30} = R_{rotor-ext} = 5.14 \text{ K}\cdot\text{W}^{-1}$ for the corresponding volumes in the ortho-radial section.

The other thermal resistance through the air cavity is $R_{5-10} = R_{rotor-ext,2} = 15.52 \text{ K}\cdot\text{W}^{-1}$.

In this steady-state analysis and considering the maximum losses, the average estimated maximum temperature reaches $360 \text{ }^\circ\text{C}$ with air cooling, while in the same conditions it reaches $210 \text{ }^\circ\text{C}$ with liquid cooling. This result means that a temperature decrease of around $150 \text{ }^\circ\text{C}$ is possible.

The liquid cooling technology provides a significant improvement in thermal results with a high-temperature reduction. Therefore, this solution will be adopted for motor cooling and the LPTM will be extended accordingly.

4.3.2 Nodal Network

Liquid cooling of the motor requires that a model that takes into account the temperature increase of the liquid in the axial direction of the motor, be developed. Moreover, a heat sink or exchanger allows transferring the extracted heat from the motor to the environment (outside air). This model is particularly important with regards to the significance of time and inertia factors in our application. As stated previously, the maximum losses occur during a short period. Thus, the optimization of the cooling system has to consider the liquid temperature variation during the mission.

In the nodal network of the motor core, the three radial sections along the e-motor shaft axis, allow taking into account the variation of coolant temperature when flowing from front side to rear one. Between the inlet and the outlet, the fluid temperature increases and influences the temperature of each radial section connected to each fluid node.

An illustration of the complete LPTM nodes' locations is depicted in *Figure 4.9*. This schematic representation shows half of the axial section of the motor.

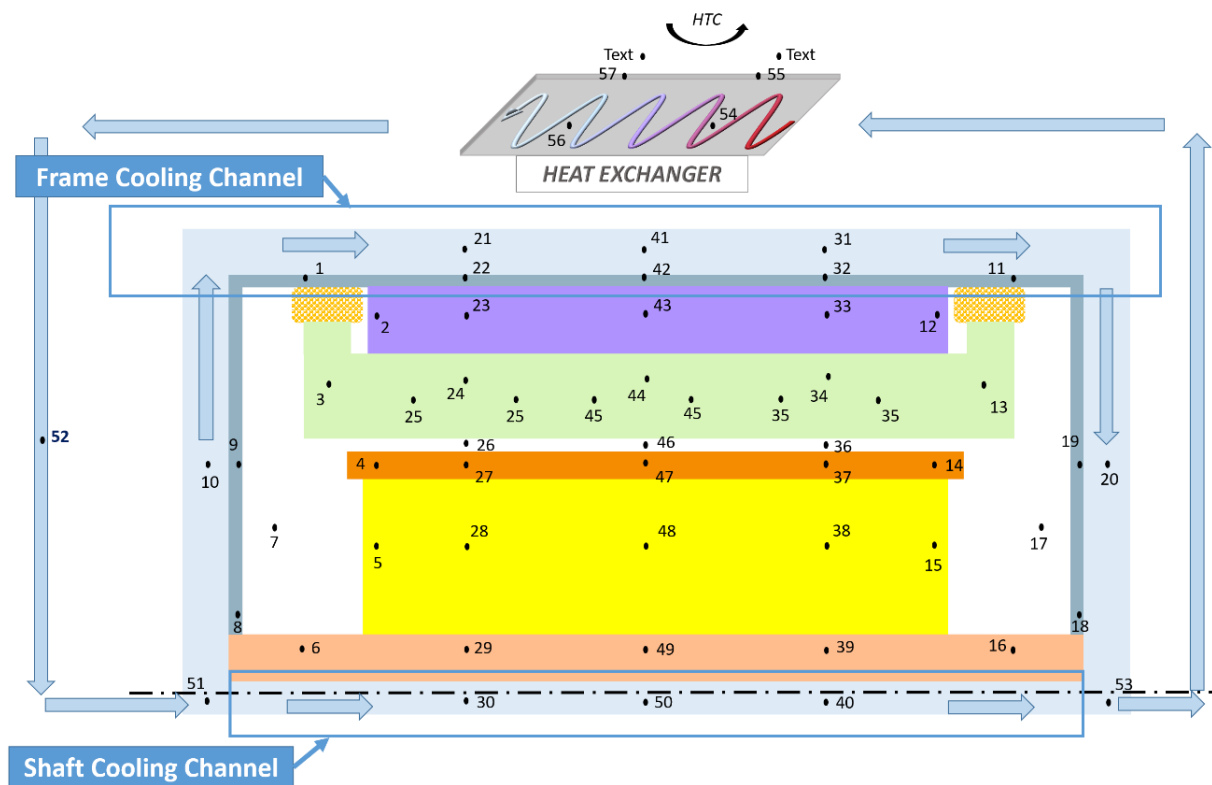


Figure 4.9 : LPTM nodes of the motor and its heat exchanger and the end-windings potting.

A connected heat exchanger plate is represented regardless of the actual shape and design used in our application. The full connections and nodes characteristics are set to the LPTM. *Figure 4.10* shows radial and ortho-radial connections and *Figure 4.11* shows the axial and end-space connections.

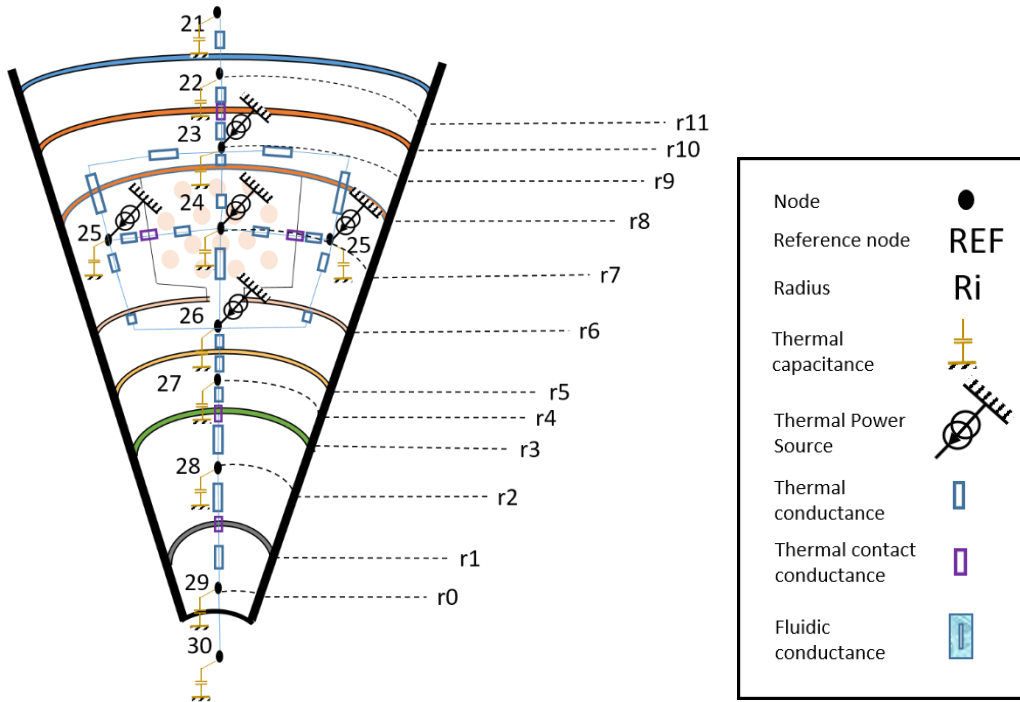


Figure 4.10 : Radial and ortho-radial connections of the motor nodal network.

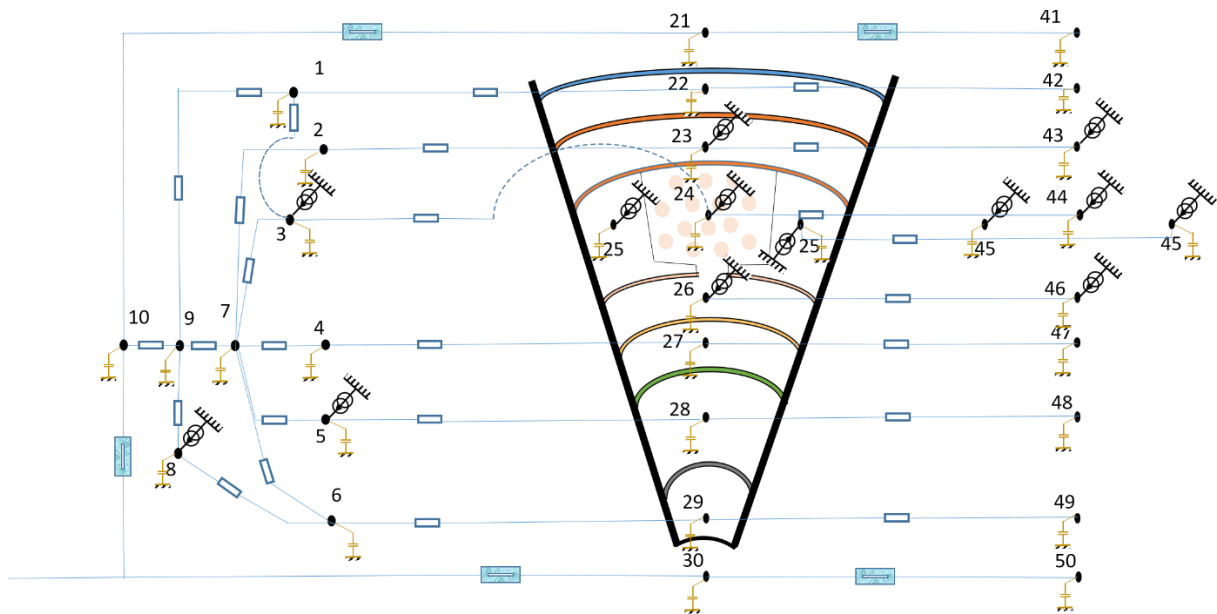


Figure 4.11 : Axial and extremity connections of the motor nodal network.

The model is simulated on MATLAB software and can be adapted to the motor dimensions to give temperature evolution. The cooling circuit, the heat exchanger, and the connections will be specifically described in the following subsections.

4.3.3 Cooling technology

The thermal issue and cooling solutions are defined based on the analytical study in subsection 4.3.1. To maintain the motor temperatures below the limits, the cooling system focuses on frame liquid cooling with liquid jackets around the motor core, a possible rotor liquid cooling through the motor shaft, and end-windings potting.

❖ Cooling Channels in Motor

The coolant circulation in motor channels is illustrated in *Figure 4.12*. A cooling circuit has been chosen consisting of a water-glycol jacket with the internal liquid flow around the motor and possibly a liquid flow inside the shaft (examples of such technology is found in [178], [179]).

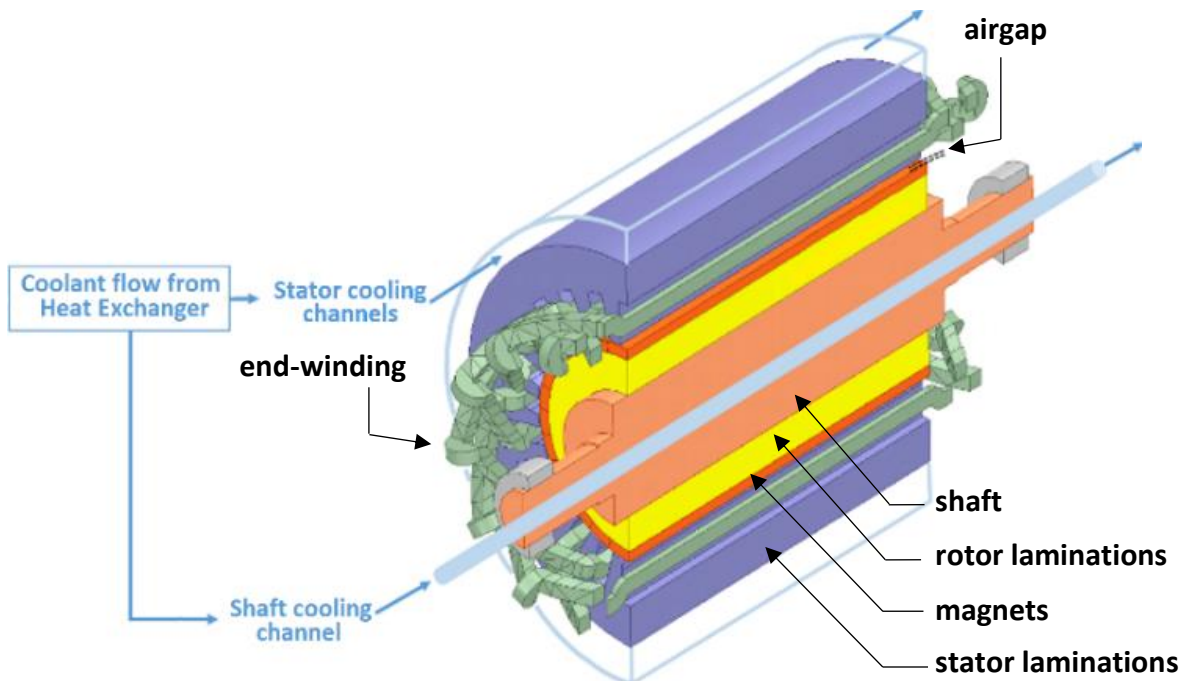


Figure 4.12 : Illustration of an electric motor 3-D section with cooling system channels.

Through these liquid channels, the coolant will flow to absorb the thermal flux, and the outside environment acts as a heat evacuation medium to dissipate the absorbed heat. DOWTHERM SR-1 Fluid at 50% Ethylene Glycol has been chosen as a coolant in the circuit for multiple properties and in particular its low solidification temperature. Even if cases with low outside temperatures will not be tested, the aircraft could encounter such environment.

In the stator channel, the liquid flows axially from the front to the rear sides of the motor. The frame structure, in which the channel is located, has a total thickness equal to 5% of the stator outer diameter. The channel has hence an annular shape whose height is equal to 3% of this latter diameter.

From one motor end to the other, we have considered three coolant nodes in the radial plans numbered 21, 41, and 31. The liquid in the channel gets in and out through the frame lateral surfaces at the front and rear sides respectively nodes 51 and 53. This improves the heat transfer from motor cavities to the coolant directly through these latter surfaces. The corresponding coolant nodes in the network are numbered 10 and 20 respectively. An annular shape channel is not structurally realistic but corresponds to a less advantageous case than a multi-channel configuration from a thermal point of view.

In the rotor, the possible cooling channel has a circular section with a diameter D_{rot-ch} of 5% of shaft diameter. As in the stator channel, the considered flow is axial along the motor rotation axis from the front side to the rear side of the motor. Three corresponding nodes in the shaft are numbered as follows: 30, 50, and 40.

The coolant pipe from the exchanger is connected to the motor channels at the inlet node 51 and outlet node 53 for thermal behavior evaluation in simulations.

❖ Potting

End-winding potting is adopted to lower the temperature in the end-winding critical zone. Thus, a solid connection between end-windings and the frame is made out of highly conductive epoxy resin (with $3.5 \text{ W}\cdot\text{m}^{-1}\cdot\text{K}^{-1}$ of thermal conductivity) allowing efficient conduction of heat through the potting material. As a reminder of *Chapter 2* review, this technique is investigated in [116].

Since this technique is applied to create a heat path to the frame, only the upper surface of each end-winding is encapsulated with potting material. The annular potting has a length equal to that of end-windings, an internal radius R_8 in *Figure 4.10*, and external radius equal to stator outer radius.

Finally, the heat flux extracted through liquid cooling should be evacuated to the outside environment. This job is accomplished using an efficient heat exchanger designed for this purpose.

4.3.4 Heat Exchanger of Cooling System

For the targeted hybrid aircraft, the nacelle is used to hold, cover, and protect the propulsion power units and components; it offers also an aerodynamical shape to these systems. Nacelle dimensions are defined by the project industrial partner Airbus as seen in *Figure 4.13*. It has a cylindrical revolved form of 532 mm central diameter and a total of 1382 mm length. It will enclose the propulsion components and could be used for other purposes in the design process of the hybrid propulsion chain for aeronautical application.

In the current study, the nacelle of the propulsion system will be employed as a heat sink plate to help to design a heat exchanger at minimum weight. For this purpose, a pipe is wound to the internal surface of this nacelle. A sketch is depicted in *Figure 4.14*.

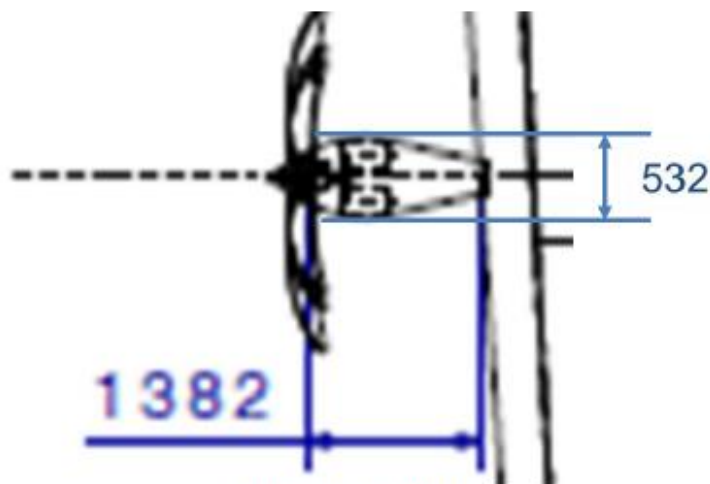


Figure 4.13 : Nacelle size with dimensions in mm from Airbus deliverable.

The calculations must include convection heat transfer and hydraulic calculations that are crucial to simulate our thermal model. In the model, the external dynamical conditions are considered to get accurate results and design a reduced cooling system with an optimum size.

The transient effects in power command during the mission enable us to conceive the cooling system with adapted size. Besides, the outside temperature variation of the environment air around the nacelle T_{env} should be considered during the flight mission time. The dynamical model should consider as well the inertia of the overall system to guaranty an optimized cooling system weight along with the safety of the motor operation.

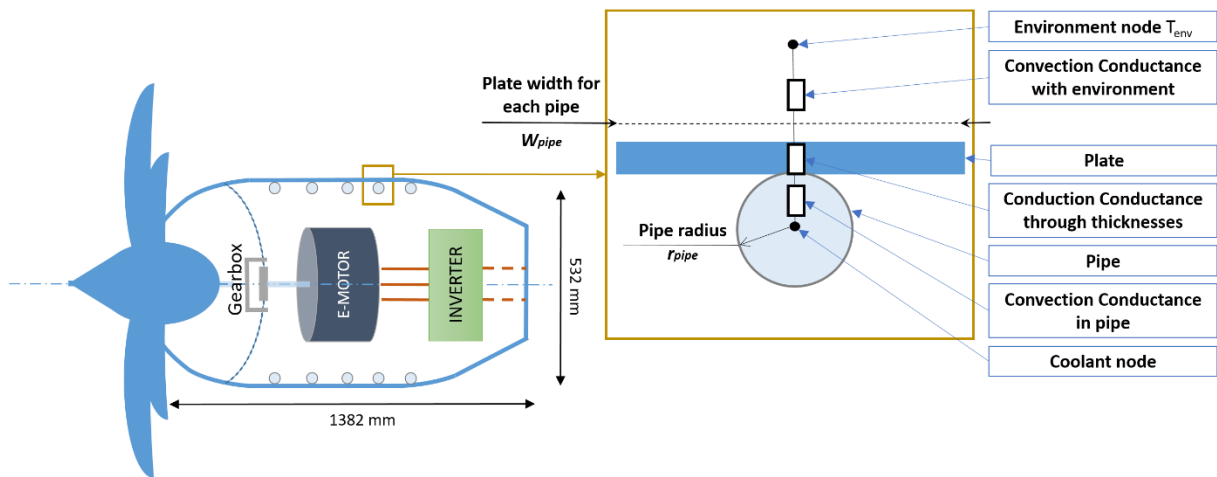


Figure 4.14 : Nacelle sketching view with radial sections used as heat exchanger cold plate.

Therefore, *AthEM* model is developed to integrate in addition to the core motor system and design, the cooling system and hydraulic circuits and components required in thermal simulations and weight computation. The heat exchanger and cooling circuit integration in the model will be displayed subsequently.

4.3.4.1 Characteristics

During the flight, the motor conditions of temperature and pressure depend on the surrounding conditions (internal and external conditions of the nacelle behind the propeller).

The project industrial partner, Airbus, defines the conditions of the flight mission. Their specifications on the flight include the aircraft mission profile and the external conditions of the atmosphere during the flight.

This allows determining the temperature dynamical evolution during the complete aircraft mission from taxi-out to taxi-in. *Figure 4.15* shows the altitude profile during the flight mission. *Figure 4.16* gives the temperature as a function of altitude. Temperature conditions are considered at the ISA+23 °C Norm level according to Airbus. The ISA is the International Standard Atmosphere: 15 °C temperature and 1013 hPa pressure, whose level is displayed with a red line in *Figure 4.16*. The resulting temperature dynamical profile during the considered flight is depicted in *Figure 4.17*.

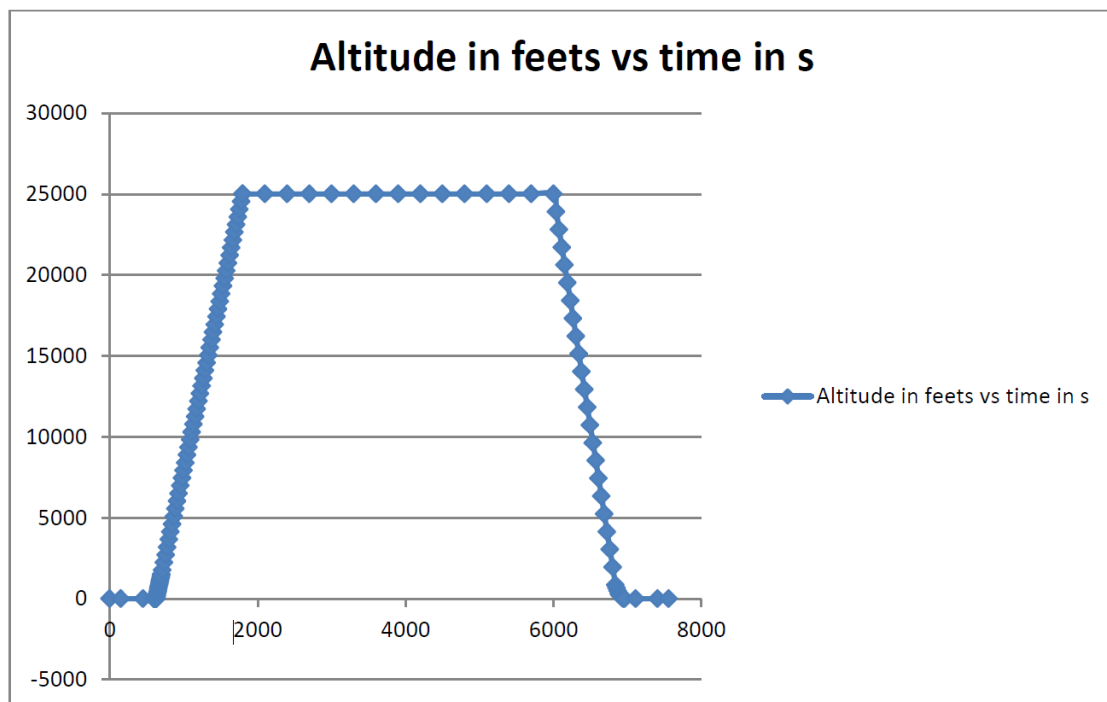


Figure 4.15 : Altitude (ft.) vs time (s) for a flight mission according to Airbus specifications.

Based on the ISA+23 °C level, ground temperature around the nacelle is equal to 38 °C, and the atmospheric air temperature T_{ext} decreases with altitude reaching -12 °C at the end of the climb phase.

The coolant circulating in the pipe transfers the heat to the ambient air through the nacelle wall at the rate of the external air convection Heat Transfer Coefficient HTC.

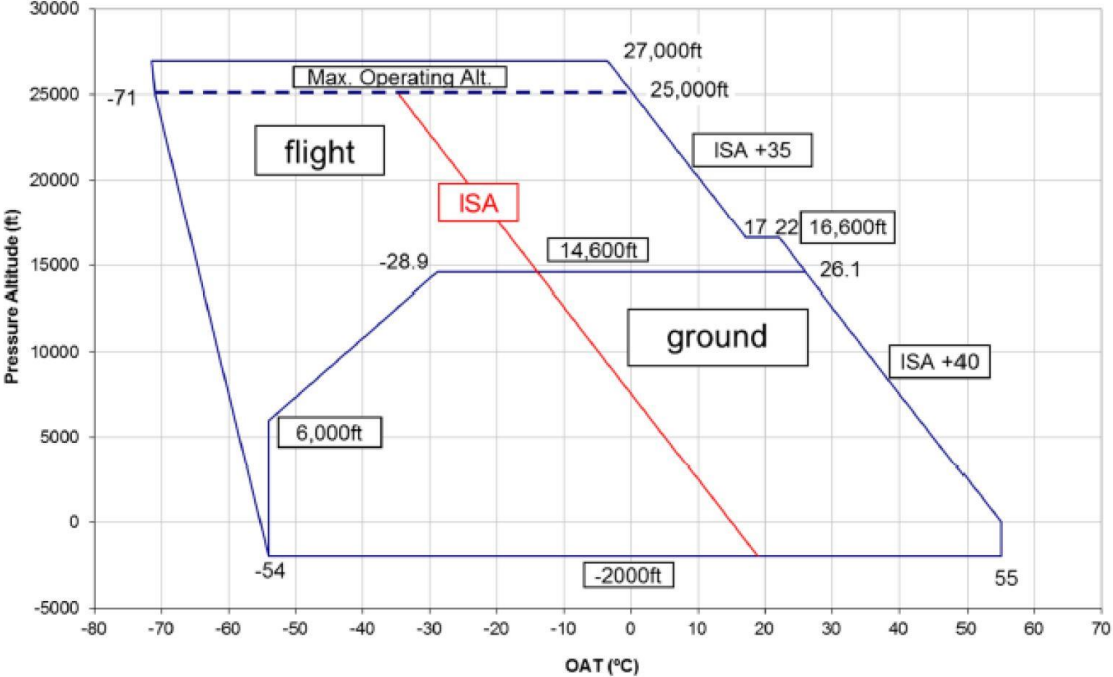


Figure 4.16 : External conditions of pressure altitude and temperature from Airbus deliverable.

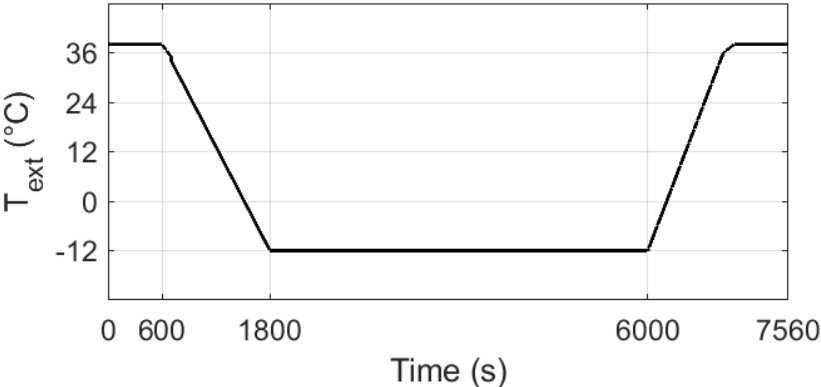


Figure 4.17 : Outside temperature’s profile during aircraft mission.

The evacuation of the extracted heat from the motor is consequently limited by the nacelle surface, the HTC as well as the cooling circuit characteristics (coolant, flow rate, pipe geometry).

❖ Nodal Network at Exchanger Level

The nodal connection in *Figure 4.14* depicts three thermal conductances associated with three heat transfer phenomena: convection inside the exchanger pipe, conduction through the pipe, and plate thicknesses (t_{pipe} and t_{plate} respectively), and outside air convection at the exchanger plate surface.

The convection inside the pipe depends mainly on the coefficient of convection deduced from coolant flow type and properties and on pipe diameter ($d_{pipe}=2 r_{pipe}$) and length (l_{pipe}).

The conduction through the structure thickness depends on two characteristics: the thermal conductivity of the material and the thickness value. It is also a matter of how wide is the portion of the exchanger surface allocated to dissipate heat along the pipe length. Since the thickness value could be relatively low and the thermal conductivity is high ($200 W \cdot m^{-1} \cdot K^{-1}$), the conduction conductance has less impact on thermal data than the other ones.

The last conductance concerns the heat transfer with external air through the total surface of the heat exchanger, which is the nacelle surface $S_{nacelle}$ with a total available surface of $2.3 m^2$.

For pipe diameter, the thermal conductance depends on a percentage $S_{nac-pipe}$ of this surface such that: $S_{nac-pipe}=W_{pipe} l_{pipe}$, and on the external Heat Transfer Coefficient (HTC) with the plate. This coefficient determines how the process of evacuation of thermal flux to the surrounding atmosphere occurs. Behind the propeller, HTC depends on the airflow velocity and characteristics. With the poorly known velocity profile around the nacelle behind the propeller, an intermediate value of this coefficient, of $140 W \cdot m^{-2} \cdot K^{-1}$, has been used. It falls between the two values: $135 W \cdot m^{-2} \cdot K^{-1}$ from empirical flat plate correlation (in turbulent regime based on from *Chapter 2* with an approximate take-off velocity) and $185 W \cdot m^{-2} \cdot K^{-1}$ from the literature [180]. Finally, for W_{pipe} we have assumed that the heat will be evacuated from the coolant in the pipe through the corresponding width as follows: $W_{pipe}=\pi \times d_{pipe}$. The pipe length in the exchanger l_{pipe} required for motor cooling is deduced from the surface of the exchanger plate and the fixed distance between adjacent pipes (equal to W_{pipe}).

The thermophysical properties of exchanger components are also integrated into the model according to the values found in *Table 4.6*. Aluminum is chosen for pipes and plates based on the attractive properties it has thermally and physically compared to other materials (high thermal conductivity, corrosion resistance, lightness, a strength-to-weight ratio higher than steel.).

Material Property \ Component	Pipe	Plate
		Aluminum
Density ρ	2699 kg·m ⁻³	
Thermal conductivity λ	200 W·m ⁻¹ ·K ⁻¹	
Specific heat c_p	900 J·kg ⁻¹ ·K ⁻¹	
Thickness t	2 mm	3 mm

Table 4.6 : Pipe and plate properties.

These values are based on classical data existing in the market. Some considerations are taken into account for this specific aeronautical application such as lightness (weight), aerodynamics (shape), and thermal performance.

4.3.4.2 Thermal and Hydraulic Formulas

❖ Pipe Internal Convection Heat Transfer Coefficient

According to the theoretical and bibliographical correlations, the cooling channels' Nusselt number (Nu) expression (based on Prandtl and Reynolds numbers, respectively Pr and Re) is used to determine the coefficient of convection heat transfer in each pipe or channel (correlations in *Chapter 2*). Reynolds number is computed based on the flow dynamic characteristics which are the flow velocity u (determined by $u = \text{volumetric flow rate} / \text{channel section}$) and the coolant dynamic viscosity μ , in addition to coolant density ρ and the hydraulic diameter D_h . In the case of the non-circular channel section, the hydraulic diameter used in computation is defined by $4 \times \text{channel cross-section} / \text{wetted perimeter}$; otherwise, the real diameter of the channel is used.

Fluid connections can be represented as a one-way flow-pass that permits a heat flux transfer through the mass transport phenomenon. In *Chapter 3*, the fluidic connection between fluid nodes is detailed. Thus, a heat path is created in the coolant flow, which will define the temperature level in the coolant medium and consequently in the motor.

❖ Hydraulic Losses, Pump Power, and Weight Calculations

The adopted cooling system consisting of the exchanger, the pipes, and the pump, is evaluated according to hydraulic equations and motor specifications. Mainly, the exchanger pipe and plate are determined respecting surface and volume constraints in the application.

The total flow rate of the coolant circulating in the system and the properties of this latter are used to determine the hydraulic losses and consequently the pump power, according to equations (4.2) to (5.1). The total value of hydraulic losses is the sum of dynamic and static losses. Dynamic losses are the sum of major losses (which are linear losses along the circuit) and minor losses (which characterizes the singular losses occurring at specific points).

Major losses H_M are obtained based on the following equation:

$$H_M = \frac{K_{pipe} u^2}{2g} \quad (4.2)$$

Where K_{pipe} is the major losses coefficient computed as follows:

$$K_{pipe} = \frac{f_{pipe} L_{pipe}}{d_{pipe,int}} \quad (4.3)$$

Detailed explanation, nomographs, and numerous correlations corresponding to hydraulic specifications and properties related to minor losses H_m are found in [181]. Since specifications on positions and configuration of hydraulic components (such as Tees, valves, elbows,...) are not fixed, an approximation of the minor losses by half of the major losses value is adopted.

❖ Friction Coefficient and Pump Head

Friction coefficient f and pump head H_{pump} are calculated as in the following equations respectively:

$$f = \frac{1}{\left(\ln \left(\frac{k}{3.7 d_{pipe,int}} \right) + \left(\frac{5.74}{Re_{pipe}} \right)^{0.9} \right)^2} \quad (4.4)$$

$$H_{pump} = H_{dynamic} + H_{static} \quad (4.5)$$

The dynamic head $H_{dynamic}$ is the sum of the major and minor heads (or losses). In our application, static head H_{static} is considered negligible assuming that there is no significant difference in horizontal levels of the hydraulic components.

$$H_{dynamic} = H_m + H_M \tag{4.6}$$

$$H_{static} = 0 \tag{4.7}$$

Finally, the pump power P_{pump} is computed as follows:

$$P_{pump} = \frac{\dot{m} H_{pump} g}{\eta_{pump}} \tag{4.8}$$

Classically, the pump efficiency η_{pump} is considered around 60% and the roughness coefficient of the channel is $k=3 \times 10^{-4} m$. The gravity acceleration is considered constant at the ground level $g = 9.81 m \cdot s^{-2}$. Pump weight is evaluated according to its power P_{pump} mass flow rate \dot{m} in $kg \cdot s^{-1}$, and hydraulic losses (pump head) H_{pump} .

4.4 Thermal Behavior of the System

The model of our motor system can simulate the thermal behavior of the motor considering the dynamical profile of boundary conditions (see Figure 4.18). Therefore, steady-state analysis is far from being realistic when a full power use of the motor is required only during the take-off phase lasting a hundred seconds. Actually, during the longest phase, which is the cruise phase, less than half of this power is involved. Besides, during the aircraft mission (specifically climb and cruise phases), the outside air temperature change is significant (see Figure 4.17).

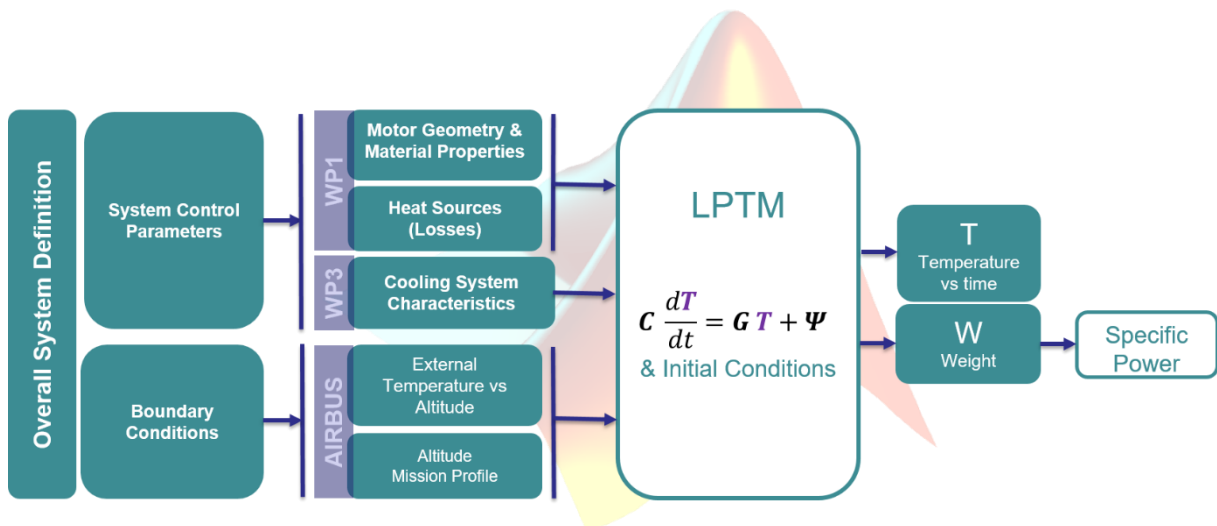


Figure 4.18 : Overall system definition of e-motor LPTM.

It influences the peak temperatures results in the motor since it affects the cooling system exchanger. The LPTM of the EM2025 is simulated using *AthEM* model and the results are progressively displayed and analyzed.

4.4.1 Thermohydraulic Parameters and Characteristics

The parameters of the overall system of EM2025 are categorized into control parameters and boundary conditions.

Now that the motor is designed and that aircraft mission and boundary conditions have been presented, the missing characteristics of the cooling system will be filled out. The applied cooling system is defined by some control parameters that affect the temperature in the motor. They are mainly related to the hydraulic circuit in the motor and are prone to variation in the sizing process. They concern the coolant properties, channels and pipes dimensions in motor and exchanger, and flow rates in channels. The resultant characteristics coming out are mainly the convection coefficients, the pipe length in exchanger, and the hydraulic losses in order to compute pump head and power.

In our motor application, a water-glycol mixture (DOWTHERM SR-1 Fluid) is chosen as a coolant. Water-glycol mixtures present some interesting features over other possible fluids, mainly high specific heat. Moreover, this coolant can stand a wider range of temperatures than other liquids (such as pure water) before phase changing. Its liquid state belongs to a wider temperature interval ($[-33\text{ }^{\circ}\text{C}$ to $107\text{ }^{\circ}\text{C}$] for the chosen mixture at 50% water to ethylene-glycol). Actually, with the outside air temperature dropping down to $-12\text{ }^{\circ}\text{C}$ during the cruise phase, the coolant temperature will be directly impacted and could run a risk of falling to a negative level. Besides, high temperatures in motor stator due to high heat dissipations (up to $180\text{ }^{\circ}\text{C}$ allowed in windings for EM2025) with the thermal resistances between stator nodes and jackets are deemed able to raise significantly the coolant temperature. That being said, other possible choices of liquids will be investigated later in this chapter to test their efficiency given the dynamical profiles during the mission.

The properties of the selected solution of water-glycol at $40\text{ }^{\circ}\text{C}$ are grouped in *Table 4.7*.

Coolant Property	Unit	Value for water-glycol
Density ρ	$\text{kg}\cdot\text{m}^{-3}$	1065
Thermal conductivity λ_{fluid}	$\text{W}\cdot\text{m}^{-1}\cdot\text{K}^{-1}$	0.3937
Specific heat c_p	$\text{J}\cdot\text{kg}^{-1}\cdot\text{K}^{-1}$	3361
Dynamic viscosity μ	$\text{kg}\cdot\text{m}^{-1}\cdot\text{s}^{-1}$	2.2564×10^{-3}

Table 4.7 : Properties of water-glycol coolant at 40 °C.

In the following study, these properties will be considered constant with respect to temperature.

Hydraulic diameters, coolant flow rates, and channels or pipe lengths characterize the stator and shaft channels on one hand and the heat exchanger on the other hand. The resultant convection coefficients are computed according to these characteristics based on the presented thermal and hydraulic correlations. The stator convection coefficient value is applied to corresponding conductances connected to nodes: 10, 20, 21, 31, and 41. For the shaft, the convection coefficient value is used in the convection conductances connected to nodes 30, 40, and 50. Finally, the exchanger convection coefficient characterizes the convection in the pipe nodes 54 and 56.

In Table 4.8, the values of the hydraulic diameters, the flow rates, the channel lengths, and the convection coefficients h are grouped for each corresponding zone. The total flow rate of coolant in the exchanger channel is $q_{exch} = 4.1 \times 10^{-3} \text{ m}^3 \cdot \text{s}^{-1}$. The following results of temperatures are obtained considering that 65% of the nacelle surface is engaged. Later on, an advanced study on the effect of exchanger surface variation on motor cooling is developed in subsection 4.4.5.

Zone	Stator	Shaft	Exchanger
Hydraulic diameter D_h (mm)	10.2	5.1	35
Flow rate q ($\text{m}^3\cdot\text{s}^{-1}$)	4×10^{-3}	10^{-4}	4.1×10^{-3}
Channel length l (m)	0.5386	0.5386	10.62
Convection coefficient h ($\text{W}\cdot\text{m}^{-2}\cdot\text{K}^{-1}$)	1500	1000	6700

Table 4.8 : Cooling system parameters in channels according to motor zones and exchanger.

Even if no rigorous optimization process is conducted, those values have been chosen after a comparison of several configurations with numerous values. The weight of the cooling system without the pump is around 19 kg .

With these parameters, the motor temperatures are obtained and the cooling system hydraulic calculations are performed to estimate hydraulic losses and deduce pump power.

4.4.2 Results and Analysis

With these values of the parameters and characteristics and a total flow rate in exchanger of $q_{exch} = 4.1 \times 10^{-3} \text{ m}^3 \cdot \text{s}^{-1}$, the model is simulated and the maximum temperatures are verified according to each critical zone. The rear-end-nodes of the motor have higher temperatures than the front motor side. In *Figure 4.19*, the nodes of extracted temperatures are indicated in red circles in the nodal network. They are as follows:

- $T_{coolant\ outlet}$ is the outlet cooling temperature of the coolant node 53,
- T_{stator} corresponds to node 33,
- T_{teeth} is the temperature at node 35,
- Stator windings hottest point $T_{windings}$ is given at node 34,
- The highest temperature of end-windings $T_{end-windings}$ is given at node 13,
- Rotor temperatures, T_{pm} of permanent magnet and T_{rotor} of iron structure, are given at nodes 14 and 15, and
- Shaft temperature T_{shaft} is given at node 16.

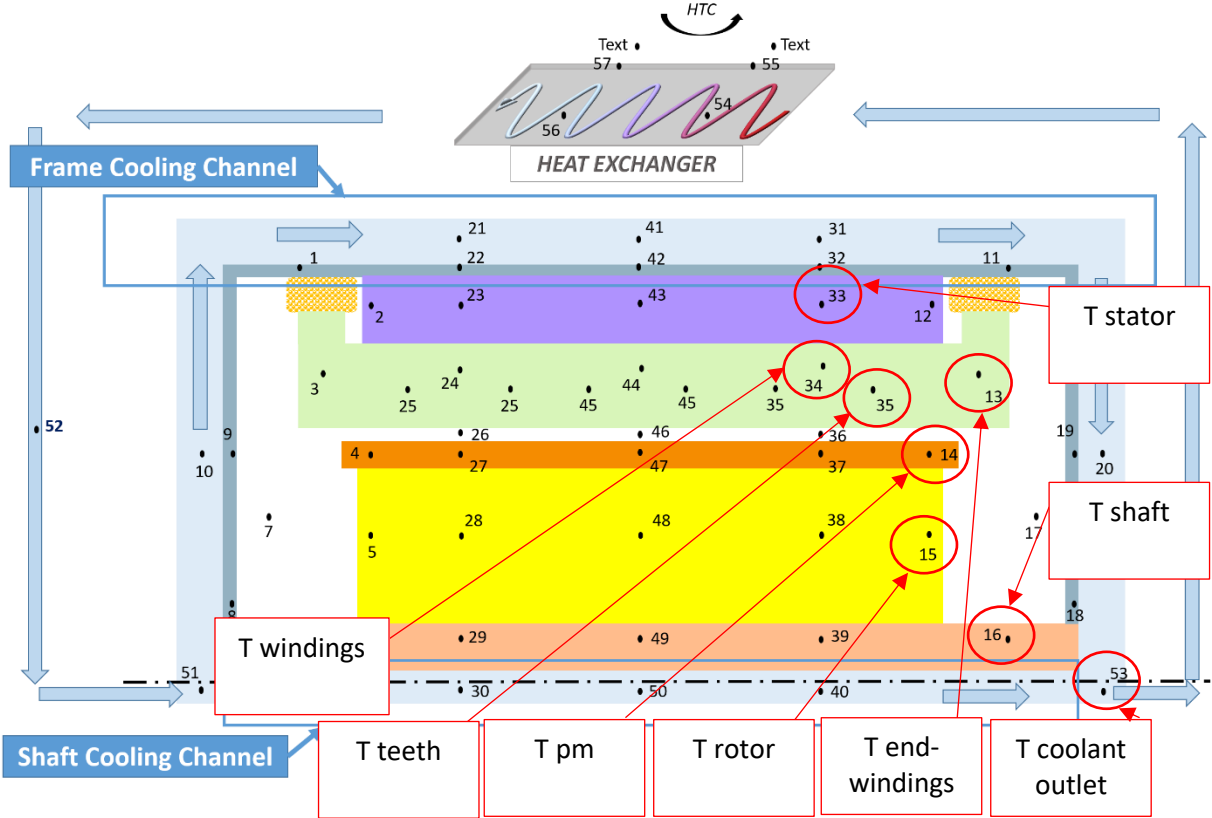


Figure 4.19 : Nodal network with the positions of extracted temperatures.

According to this simulation, the motor will exhibit the temperature profiles depicted in *Figure 4.20*. This figure shows the group of temperature evolution curves at indicated nodes. Separate graphs for stator and rotor temperatures are displayed in *Figure 4.21* and *Figure 4.22*.

The first evidence in this graph is that the temperatures in the stator and rotor have a dynamical evolution all mission long without reaching a definite steady-state. This proves that thermal inertia has an important influence on temperature profiles in the motor.

When analyzing the temperature profiles, it is remarked from the plots that there are two types of thermal behavior. The first set of curves represents the stator parts temperatures evolution and a second set represents rotor lamination and permanent-magnets temperatures response.

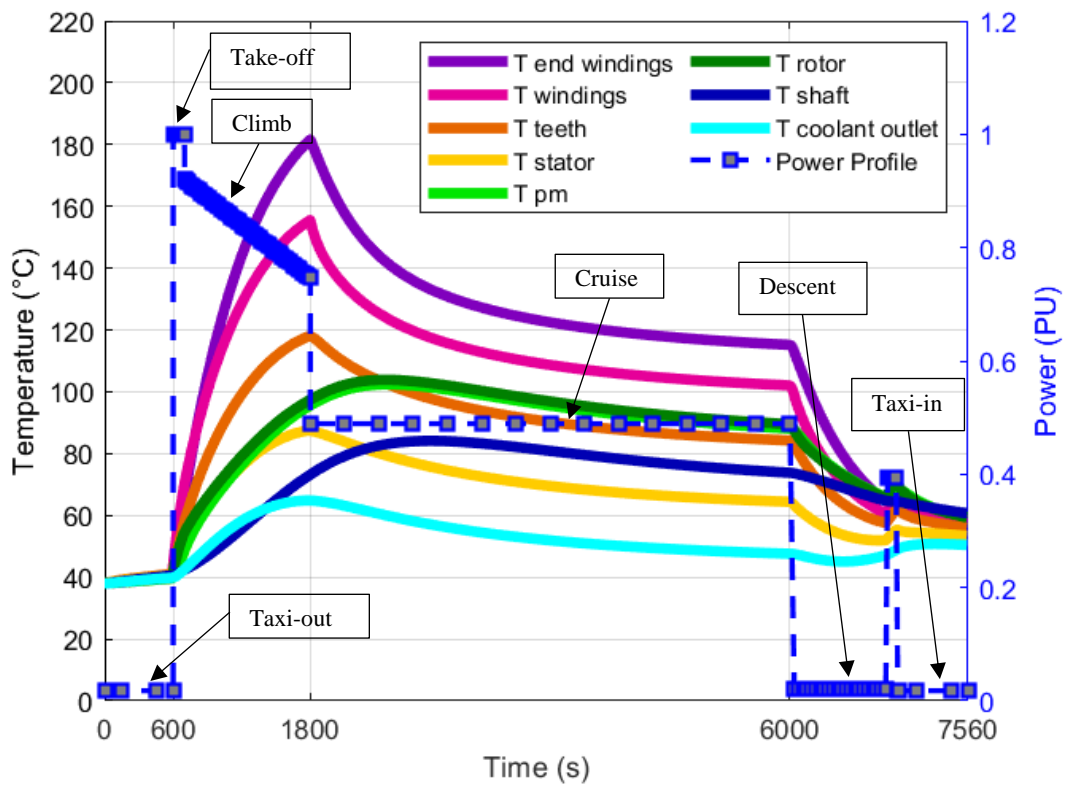


Figure 4.20 : Temperature profile of motor EM2025 parts with corresponding power profile.

4.4.2.1 Stator Behavior

For stator behavior, the temperature rise in the observed parts is very slight during the taxi-out phase, and then a significant increase is exhibited during take-off and climb phases.

Almost all of the stator components reach their maximum temperatures at the end of the climb phase, which is 1800 s after the mission start-off. Actually, the spike observed in these temperature profiles indicates that the steady-state was not reached. Then, a temperature drop follows an exponential decay during the cruise phase where the motor is running at only half of its full power. The losses profiles in this phase record a sharp decrease of Joule and iron losses (see Figure 4.4).

Consequently, the maximum temperature in each stator part would attain significantly higher values if the motor was kept on running at a high power rate for a longer time. In fact, these evolutions in temperature depend strongly on the boundary conditions during the motor functioning. Indeed, the heat profiles and levels influencing this motor part and creating these curves of temperature, are those produced due mainly to Joule losses and also to iron losses.

Another two exponential decays are observed for the power drop after the cruise phase for descent and taxi-in phases. Amidst the last two phases, a brief and moderate shot of 40% power-on pushes the evolution of the temperatures up to a sharp spike before resuming its last decrement from that point. The temperature decrement continues its way down until reaching a low level that is slightly higher than the ground temperature surrounding the nacelle, at the end of the aircraft mission. The significant losses reduction during these two phases acts as the major player in the evolution of the resulting temperatures. Thus, despite the increasing outside temperature, the reduction of the influencing losses has a much higher effect on temperature for these last two phases, as seen in the stator temperature curves of *Figure 4.20*.

Globally, one more evidence is noticed in the graph, which is the peak temperature zones. The end-windings are the hottest points found in the motor all mission long as seen in *Figure 4.20*. This was an expected result according to previous studies. Actually, this is due to high Joule losses in all windings part and the high thermal resistances between the end-windings core and the surrounding environment. While these parts dissipate a great percentage of Joule losses (as much flux density as windings), they are thermally more isolated than the slot part. In fact, the thermal resistance between this part and the frame through the air in the cavity is at least 3 times the one between the winding in the slot and the frame through adjacent teeth. Besides, the thermal resistance connecting the end-windings to the frame through potting (between nodes 1 and 3 for instance) is around 1.3 times higher than the thermal resistance between the winding core in the slot and the frame in the radial direction (between nodes 22 and 24 for instance).

It can be remarked that in this configuration, the temperatures of the hot-spot zone remain below the thermal limit ($180\text{ }^{\circ}\text{C}$) with the adopted cooling techniques for the chosen winding impregnation thermal class.

In *Figure 4.21*, the speed of increase of four temperatures in the stator with respect to time is displayed with their corresponding evolutions. For windings and end-windings, a peak of around $20\text{ }^{\circ}\text{C}/\text{min}$ is noticed for take-off, which is a crucial speed to consider in controlling the evolution of motor temperatures. Moreover, during the climb phase, a significant decrease of this speed is observed.

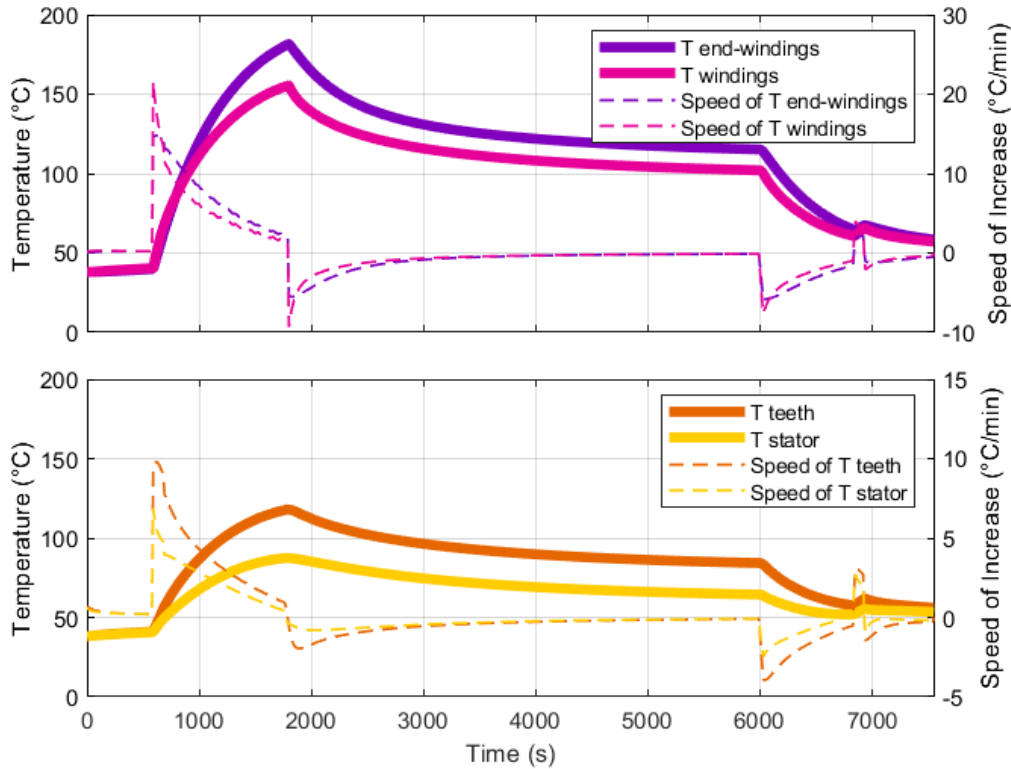


Figure 4.21 : Evolution of four stator temperatures and their speed of increase during the mission.

The breaking point of the slopes of temperature curves between the end of the climb and the beginning of the cruise induces a change in the aspect of the speed curve since the speed becomes negative. Also, the same behavior is noticed between the end of the cruise phase and the beginning of the descent phase.

For stator and teeth temperatures, their speeds of temperature increase follow the same evolution as previous graphs with a ratio of 0.5 and a peak of around $10\text{ }^{\circ}\text{C}/\text{min}$.

4.4.2.2 Rotor Behavior

For the rotor, the upper graph of Figure 4.22 demonstrates that the stator evolution of temperature exhibited during the mission does not apply to the rotor behavior.

Moreover, the graphs show a similar evolution and levels of temperatures in the rotor laminations T_{rotor} and permanent magnets T_{pm} .

For permanent magnets, the maximum is around $100\text{ }^{\circ}\text{C}$, which prevents magnets from overheating. At the beginning of each phase, these elements exhibit a quite different transient

evolution than rotor laminations due to their thermal inertia. However, since the rotor tends to stabilize into a steady-state in the critical phases, the end temperature result is quite similar.

During taxi-out, a similar temperature evolution is observed for all motor parts, due to the low heat dissipations occurring at this level. At the end of this low-power phase, the sudden full power for take-off phase and high-power level for the climb phase afterward, the stator and rotor behaviors are quite different. Actually, the rotor reaches its maximum temperatures at a delayed time relatively to the stator temperatures peak. This delay is justified by a group of parameters that controls the rotor peak time, mainly losses in the rotor environments (end-caps, airgap..) maintaining almost the same level between end of climb and cruise phases. For the stator, the location of the maximum temperature at the end of the climb is due to the losses significantly reduced: Joule losses by more than 50% and Iron losses by around 25%. Other factors lead to this time difference, which are the coolant temperature extremely influenced by the stator temperatures. Besides, rotor temperatures display a smoother peak curvature, specifically in permanent magnets and rotor laminations zones. The maximum for these two latter parts is obtained at 2500 s after the beginning of the mission. A very slight decrease is noticed in the cruise since the losses are constant in this phase while only the drop in outside air temperature affects the temperature evolution.

Afterward, the descent phase starting at 6000 s is marked by a sudden drop of heat sources (losses). The reduction of windage and bearings losses (influencing the rotor) is less pronounced than that of Joule and iron losses (influencing the stator). Therefore, the rotor temperatures in this phase pursue a decrease with a lower slope than that of the stator temperatures curve.

For the last two phases, the temperature evolutions in the stator and rotor are similar due to the same relative heat dissipations in the components.

On the other side, the evolutions of the rotor and coolant speed of temperature increase are depicted in *Figure 4.22*.

As rotor and permanent magnets temperatures have almost the same evolution, the peaks of speed are in phase, with a higher level noticed for rotor (maximum of 12 °C/min) due to its lower thermal capacity.

For the shaft, it is remarked from *Figure 4.22* that the scale of the increased speed is notably reduced by ten times compared to other motor parts with a smoother curve aspect.

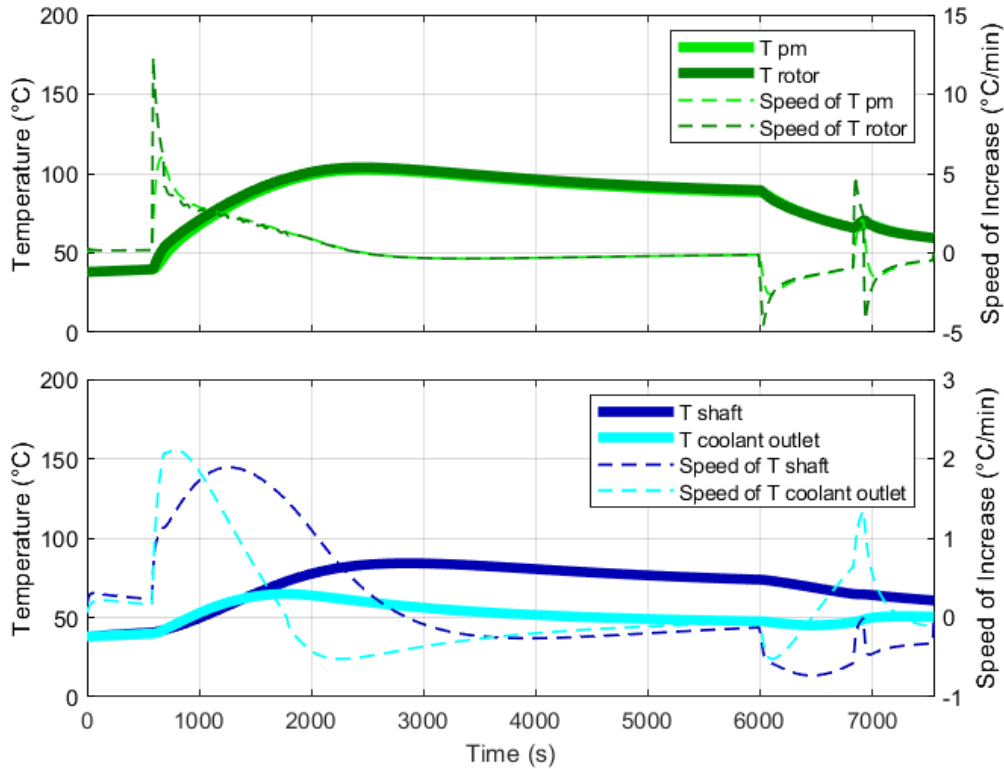


Figure 4.22 : Evolution of rotor and coolant temperatures and their speed of increase during the mission.

Besides the evolution of the speed of increase of the coolant outlet temperature follows the dynamics associated with the adopted cooling system characteristics. Here, with the weight, the mass flow rate, the exchange surface, and the convection coefficients, we notice a maximum speed of increase of around $2\text{ }^{\circ}\text{C}/\text{min}$ during the take-off phase.

4.4.2.3 Influence of Outside Air Temperature

The coolant evolution seems to follow the stator temperature dynamics with a variation between $38\text{ }^{\circ}\text{C}$ and $70\text{ }^{\circ}\text{C}$. The heat is mainly extracted from the stator (around 85% of the total losses at full power) through the coolant medium. High heat dissipations in this motor part influence the coolant outlet temperature considerably. During take-off and climb phases, the water-glycol mixture exhibits a continuous temperature increase. The high heat extracted from the motor is evacuated through the nacelle surface to the outside with a convection coefficient HTC . Since the exchanger surface is limited and the coefficient HTC is relatively low, the process of heat evacuation is limited and the coolant temperature increases.

The convection coefficient of the plate with outside air is a limiting factor since the corresponding thermal resistance is the highest among the three main resistances between coolant and outside air in the heat exchanger (see subsection 4.3.4.1). Finally, the ending phases (descent and taxi-in) of the mission are marked by an outside air temperature that increases significantly, which influences the coolant temperature evolution, in addition to the dynamical profiles of losses during these phases.

The temperature of the outside air during the mission is another influencing factor acting on the stator temperatures. The dynamically changing temperature of external air at the heat exchanger level is critically important to avoid oversizing of the exchanger. If a constant outside air temperature is considered during the mission, the hot spot temperatures would follow the curves depicted in Figure 4.23 and Figure 4.24 for 38 °C and 53 °C constant values respectively.

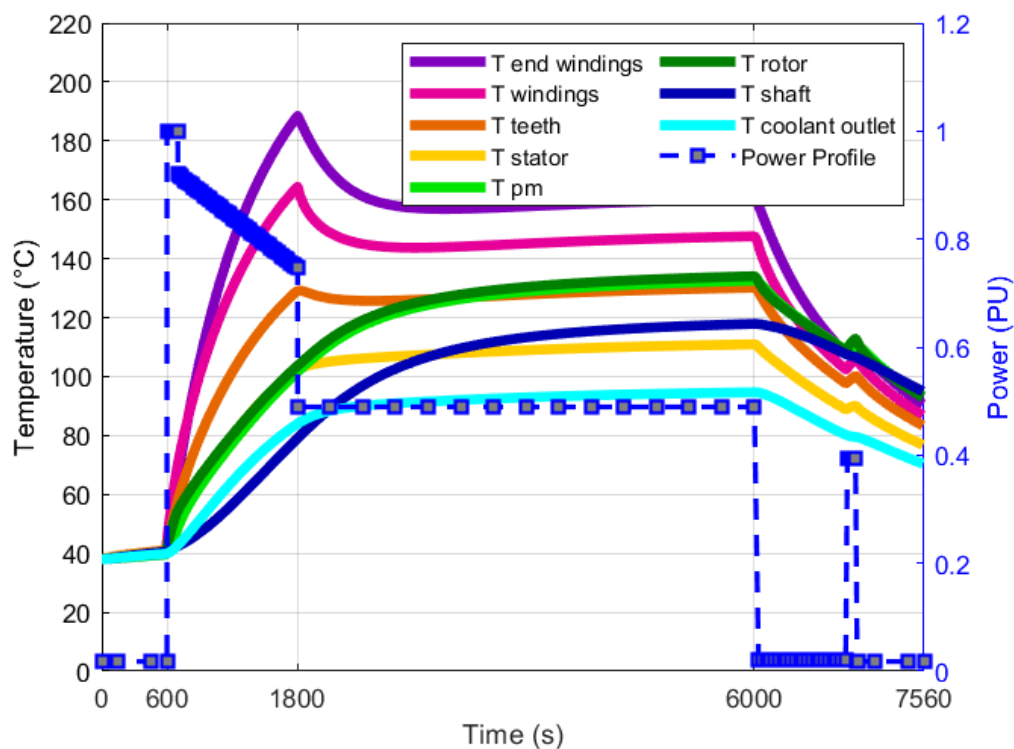


Figure 4.23 : Temperature profile of motor EM2025 parts with a constant outside temperature of 38°C.

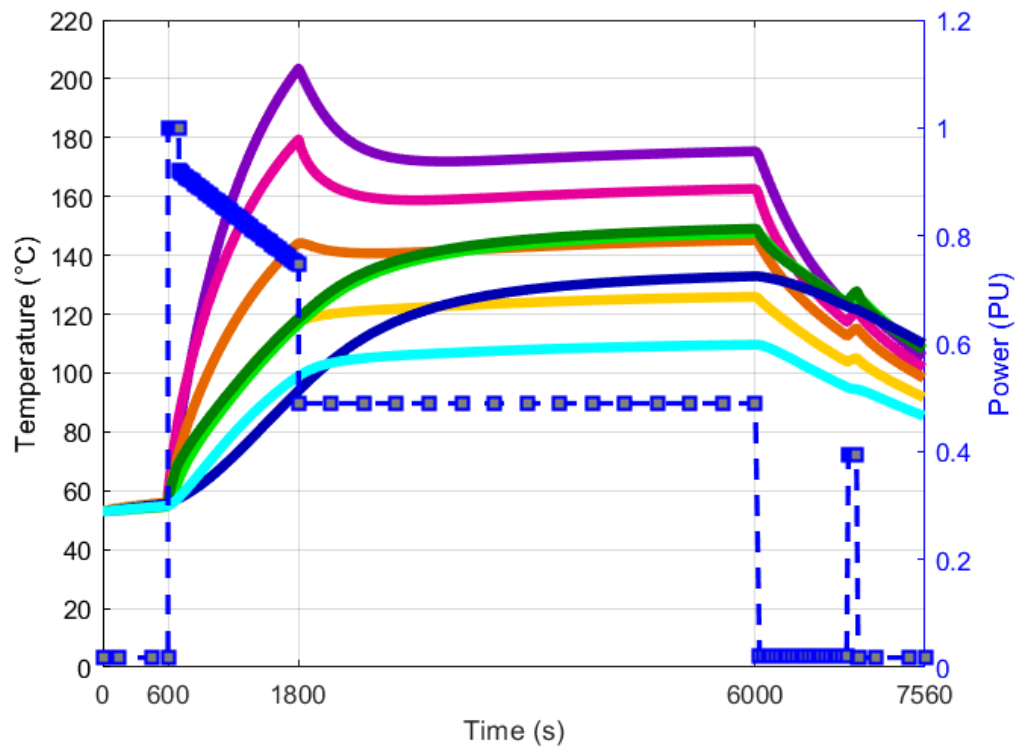


Figure 4.24 : Temperature profile of motor EM2025 parts with a constant outside temperature of 53°C (same legend as Figure 4.23).

In these two cases, the maximum temperatures at end-windings increase by 5 °C and 20 °C respectively. It is noticed that the temperatures rise in the rotor is in the range of 30 °C to 40 °C, which brings the maximum temperatures in laminations and permanent magnets close to (or above) the allowed limits. Besides, in this case, the coolant temperatures increased since they are highly dependent on the heat evacuation rate in the exchanger. Actually, the outside air temperature (which is the fluid in the secondary cooling circuit) controls directly the efficacy of the cooling system by controlling the coolant temperature at the motor inlet.

Moreover, we can notice that the vaporization temperature is not reached. The maximum temperature of the liquid even remains far below 100 °C. Hence, the main reason to use water-glycol instead of water is the lower bound of its temperature for the liquid phase of -33 °C that allows the aircraft traveling in northern countries.

4.4.2.4 Hydraulic Losses and Pump

The resulting hydraulic losses H_L are presented in *Table 4.9*. The pump characteristics (mainly pump head H_{pump} and flow rate q) should allow the identification of the pump weight and properties according to the catalog of hydraulic pumps from Parker Pumps and Motor Division [182]. An adequate pump has the characteristics found in *Table 4.10*.

Zone	Stator	Shaft	Exchanger
Hydraulic major losses $H_L(m)$	0.06	3.89	2.54

Table 4.9 : Resulting hydraulic major losses in channels according to motor zones and exchanger.

Pump		
Characteristic	Unit	Value
Normal Operating Pressure	bar	206
Maximum Speed	RPM	3646
Length	cm	26.16
Height	cm	21.84
Width	cm	17.27
Weight	kg	14

Table 4.10 : Pump characteristics (AP27V) from [182].

4.4.3 Influence of Thermophysical Parameters Variation

Due to the temperature evolution of motor parts, some physical parameters' values might be subject to variation, whereas in the model we have assumed the values of thermophysical properties of motor materials as constant. Therefore, a focused sensitivity study has been conducted to verify that this assumption does not lead to faulty thermal results.

To proceed with this study, we were interested in evaluating the impact of a 10% increase in two thermal properties of each motor part on motor maximum temperatures. The properties are thermal conductivity and specific heat capacity. It is worth mentioning that variation of specific heat capacity in the model is equivalent to that of the density since the product of these two properties is considered in thermal capacity calculation. The material properties of the following motor components were successively changed: the frame, the permanent magnet, the windings (or resin impregnation material), the shaft, and the laminations.

The temperatures of several motor zones are included in this study: end-space (node 17), rotor (node 15), permanent magnets (node 14), stator yoke (node 33), teeth (node34), windings (node 35), and end-windings (node 13). The decrease in temperature for each motor zone is displayed in graphs of *Figure 4.25* and *Figure 4.26* for thermal conductivity and specific heat capacity respectively.

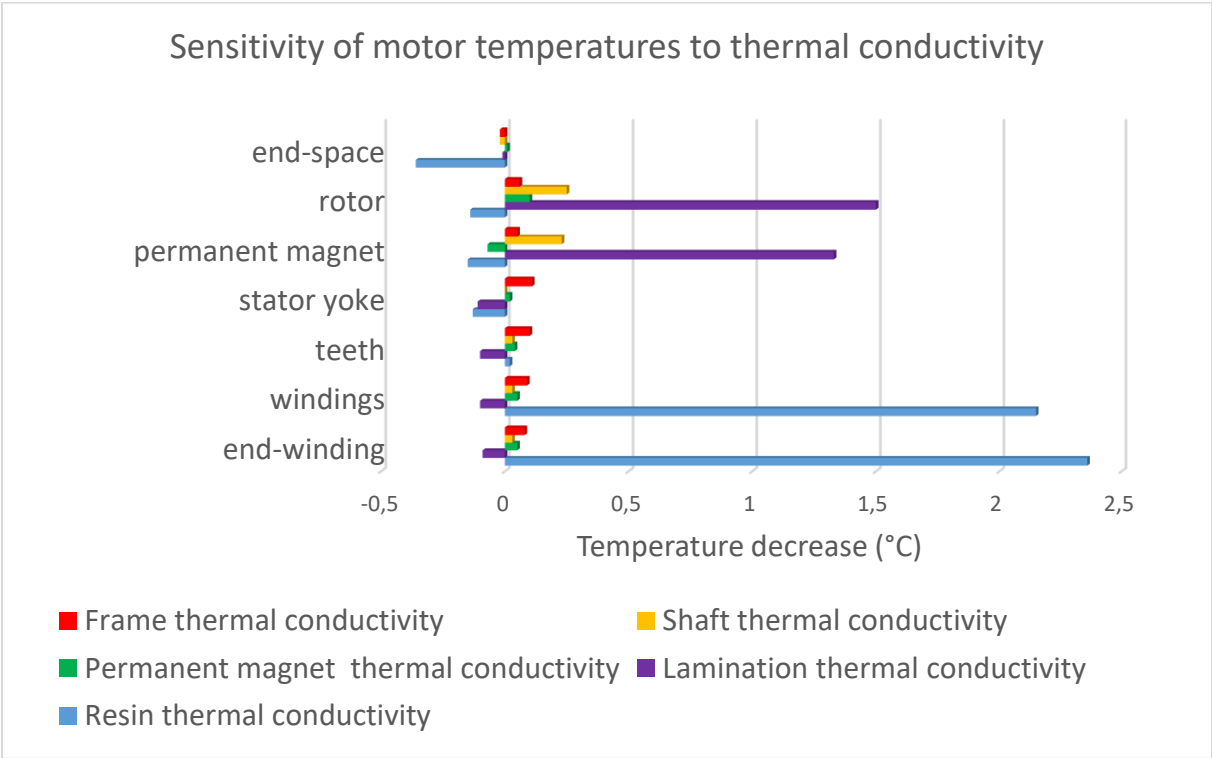


Figure 4.25 : Maximum temperature difference of motor parts with 10% variation in thermal conductivity of motor materials.

As depicted in these figures, the temperature decrease is slight or insignificant. Therefore, only high temperatures' differences will be analyzed hereafter.

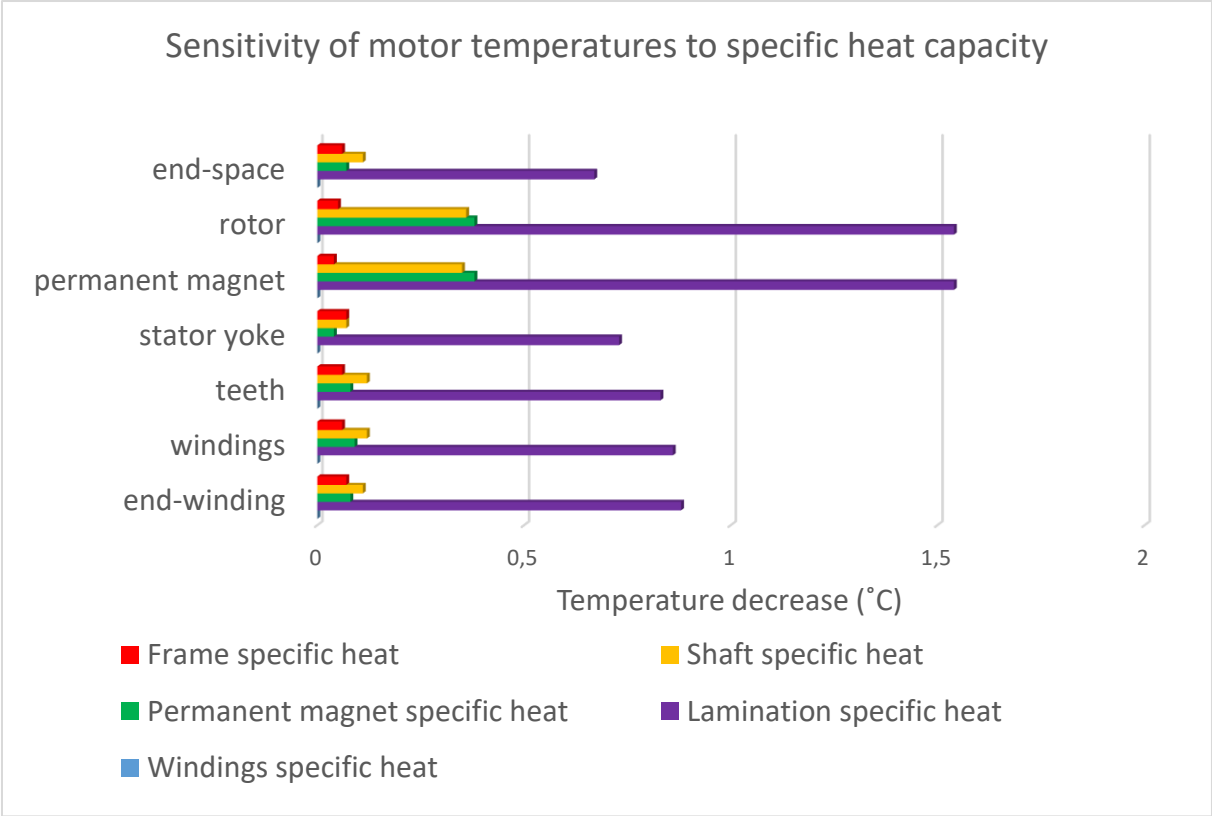


Figure 4.26 : Maximum temperature difference in motor parts with 10% variation in specific heat capacity of different motor materials.

4.4.3.1 Influence of Thermal Conductivity

The thermal conductivity of resin as impregnation material applied in windings influences the windings and end-windings temperatures the most (decrease of 2.2 °C and 2.4 °C respectively) relative to 135 °C and 180 °C of allowed maximum temperatures. A minor effect of this variation is noticed on end-space and rotor temperatures (decrease of 0.4 °C and 0.2 °C respectively). However, this indirect effect is justified by the enhanced heat evacuation path from the stator to the cavity, specifically from the end-windings heat dissipation zones.

For laminations, the variation of thermal conductivity has the most significant impact on the rotor temperatures (1.3-1.5 °C) since the conduction is the main mode of heat transfer to the shaft coolant medium, considering that the convection coefficient is optimized for cooling the rotor.

The thermal conductivity variation of shaft material has around much lower effect (around ten times lower) on temperatures than that of laminations.

4.4.3.2 *Influence of Specific Heat*

The specific heat of stator and rotor laminations dominantly influences all temperatures. In fact, among all other materials, the specific heat property of laminations concerns the larger volumes of motor components. Besides, in the rotor, we observed a temperature difference around twice that in the stator for the same increase in laminations specific heat.

Actually, we notice that the temperature difference relative to the maximum increase in its temperature (i.e. temperature rise with respect to initial temperature condition) for rotor and stator laminations are proportional.

Permanent magnet specific heat has a more significant impact on rotor maximum temperatures than on other motor components (around 5 times the effect on these latter ones). However, the global effect on the motor thermal behavior and temperature evolution in all components is comprehensively explained by the fact that permanent magnets are the point of connection between heat flux paths from rotor and stator. The heat flux is conducted through the thermal conductances with the airgap area, considered in the numerical model.

Finally, these diagrams allow stating a frank conclusion that a variation of 10% of these properties gives a maximum temperature difference (between 1.5 °C and 2.4 °C) is observed for lamination specific heat and thermal conductivity variations, and resin thermal conductivity variation. This remains an acceptable temperature oscillation compared to motor temperature levels.

4.4.4 **Fluid Choice**

The water-glycol mixture was adopted as a coolant in the design of the liquid cooling system. This fluid exhibits interesting thermal properties cited earlier in this chapter. Water, in general, is known to be by far one of the most beneficial and performant coolant in single-phase circuits (purely used or combined with other liquids to improve boiling and/or freezing points). However, other potential candidates can be advantageous in hybrid aircraft motor application for industrial reasons (compatibility, maintenance, cost,..) or for some of their advantages (low dielectric property, phase changing possibility under particular conditions,..). Herein, two fluids will be tested hereafter to verify their efficiency, provided that they demonstrate a pronounced interest.

The coolants tested are namely: industrial oil and pure water. Oil as a coolant in electrical machines is recently being investigated in winding cooling techniques since some types of this fluid are safe to use in the case of direct contact with electrical wires and are more beneficial in convection cooling of end-windings than air convection. While pure water will be tested to compare the temperature results to those with water-glycol. It is known that water temperatures in the circuit should not fluctuate beyond the margins corresponding to the liquid phase state (above 0 °C and below 100 °C).

Properties of the coolants applied in this investigation, oil and water respectively, are grouped in *Table 4.11* and *Table 4.12*.

Coolant Property	Unit	Value for oil
Density ρ	$\text{kg}\cdot\text{m}^{-3}$	835
Thermal conductivity λ_{fluid}	$\text{W}\cdot\text{m}^{-1}\cdot\text{K}^{-1}$	0.133
Specific heat c_p	$\text{J}\cdot\text{kg}^{-1}\cdot\text{K}^{-1}$	1970
Dynamic viscosity μ	$\text{kg}\cdot\text{m}^{-1}\cdot\text{s}^{-1}$	3.17×10^{-2}

Table 4.11 : Oil coolant properties at 40 °C.

Coolant Property	Unit	Value for water
Density ρ	$\text{kg}\cdot\text{m}^{-3}$	995
Thermal conductivity λ_{fluid}	$\text{W}\cdot\text{m}^{-1}\cdot\text{K}^{-1}$	0.628
Specific heat c_p	$\text{J}\cdot\text{kg}^{-1}\cdot\text{K}^{-1}$	4178
Dynamic viscosity μ	$\text{kg}\cdot\text{m}^{-1}\cdot\text{s}^{-1}$	6.51×10^{-4}

Table 4.12 : Water coolant properties at 40 °C [183].

Definitely, the same conditions of flow rate are applied. Therefore, the resulting hydraulic losses are different for every change in coolant type. The objective is to test the heat extraction efficiency of the coolant.

The results are depicted in *Figure 4.27* and *Figure 4.29* respectively for oil and water as coolants.

Figure 4.27 shows that oil, as a coolant, does not act efficiently in cooling the motor with the applied configuration. As seen in the graph, the oil temperatures have an increasing tendency all mission long despite the outside air temperature decrease between take-off moment and the

end of the cruise phase. This continuous increase in coolant temperature proves that the heat exchanger is not sized adequately to evacuate all the heat generated in the motor.

Moreover, the motor temperatures increase with a higher slope – which means more rapidly - than the coolant curve. This is an indicator that the heat transfer in motor channels (stator and rotor) between coolant and motor parts does not occur efficiently due to the lower specific heat of oil compared to water-glycol.

Finally, the convection coefficients are not sufficiently high: $170 \text{ W}\cdot\text{m}^{-2}\cdot\text{K}^{-1}$ for stator channel and $140 \text{ W}\cdot\text{m}^{-2}\cdot\text{K}^{-1}$ for rotor channel (see *Table 4.8* for water-glycol convection coefficients). To obtain these results (even not acceptable for temperature limits), the generated hydraulic losses are more than twice those obtained with water-glycol (23.9 m against 9.6 m), and the pump power is more than twice that required with water-glycol coolant. The use of oil will result in increasing significantly the weight of the pump while not providing efficiency in cooling the motor parts.

Actually, the oil being viscous, either channels' geometries or flow rates or both together, should be adapted to provide the required coefficients of convection and block the temperature rise in the motor. However, the thermally suitable hydraulic and geometrical parameters will lead to much higher hydraulic losses and higher pump head and power.

Another test of oil is conducted with twenty times the old flow rate in the stator channel and fifty times that in the rotor channel. The resulting temperatures' profiles with oil as coolant are presented in *Figure 4.28*. The stabilization of coolant and motor temperatures during the cruise proves that the heat flux extraction from the motor is quite efficient. Whereas, the high flow rates applied require a huge pump head and super-high pump power, which is industrially not applicable. This specificity lowers the efficiency of using oil as a coolant when other performant cooling fluids can be used and are completely safe for the motor application.

Using oil would be interesting only if the flow is directly injected into the critical part (as a way to reduce the thermal resistance).

Water as a coolant in the hydraulic circuit has a positive impact on reducing motor temperatures compared to other liquids since it has higher thermal conductivity and specific heat. However, compared to the water-glycol mixture applied in the reference model, there is no significant variation in temperatures when pure water is utilized.

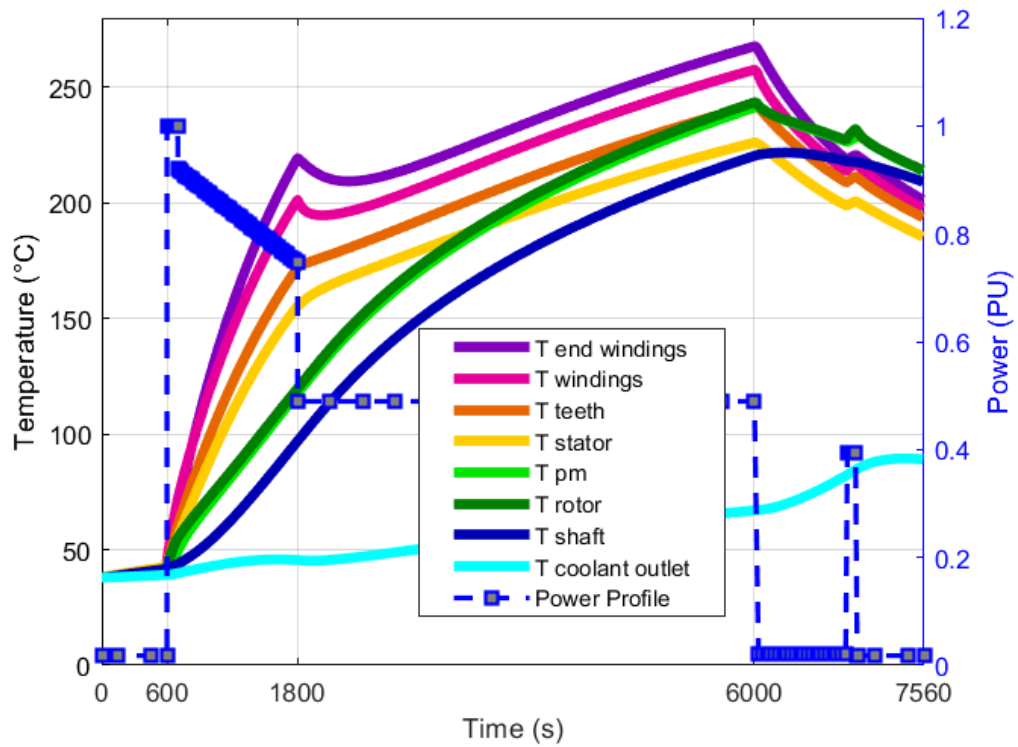


Figure 4.27 : Temperatures profiles in different motor parts with oil as coolant with initial flow rates.

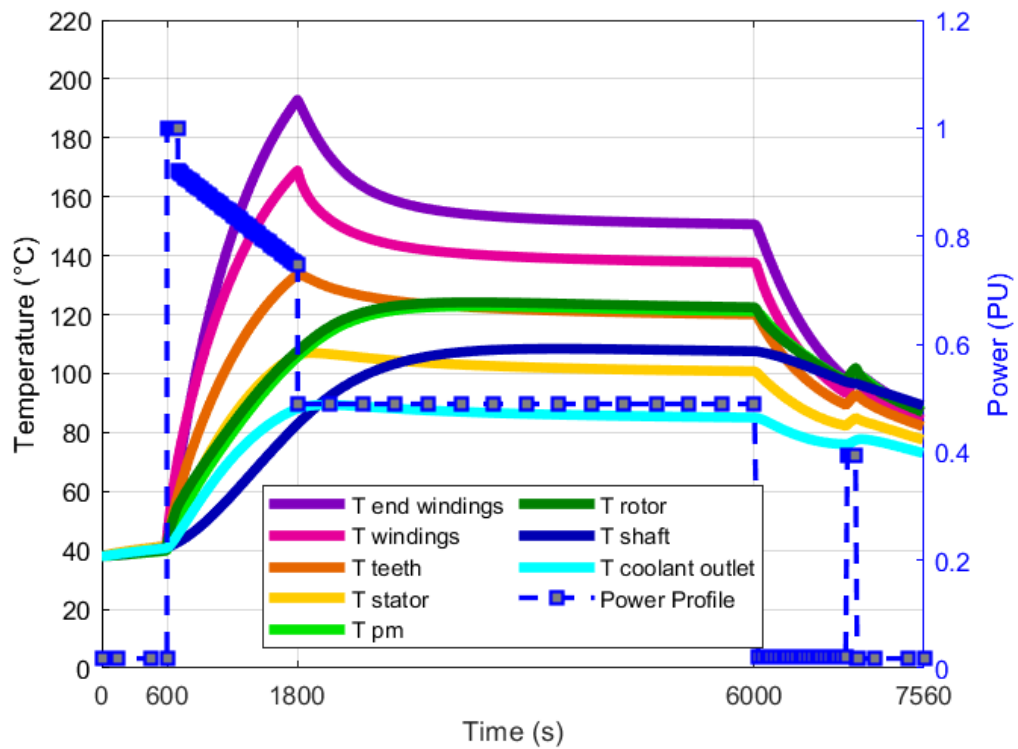


Figure 4.28 : Temperatures profiles in different motor parts with oil as coolant with higher flow rates.

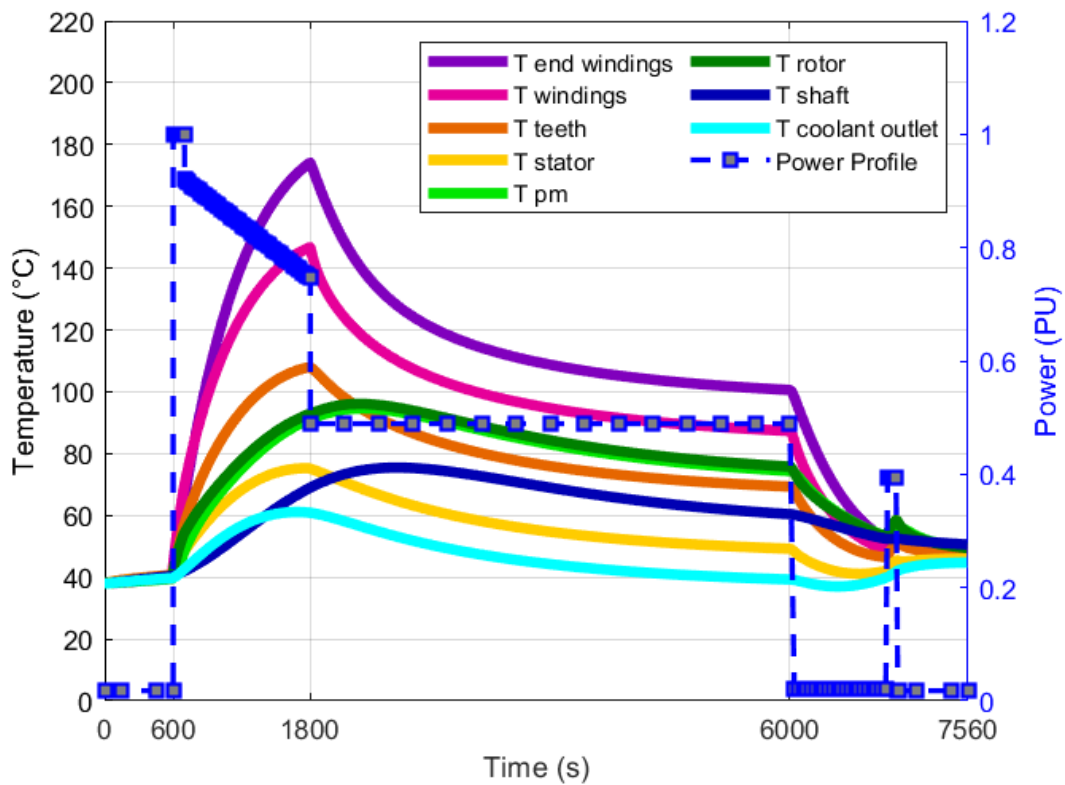


Figure 4.29 : Temperatures profiles of different motor parts with water as a coolant.

In addition to the water-glycol mixture features, this fluid has more advantageous properties than water when system temperatures are strongly changing, i.e. the operating temperature range (freezing to boiling points) are $[0\text{ }^{\circ}\text{C to }100\text{ }^{\circ}\text{C}]$ for water and $[-33\text{ }^{\circ}\text{C to }107\text{ }^{\circ}\text{C}]$ for the water-glycol adopted solution.

Some unpredictable circumstances that might take place during flight operation (for instance an overheated motor due to a lasting full power regime or freezing outside temperature during cruise lower than that considered in the profile) would expose the coolant to different ranges of temperatures. In these cases, the water-glycol mixture has a significant advantage over pure water. Besides, the DOWTHERM SR-1 Fluid solution contains industrial corrosion inhibitors.

4.4.5 Exchanger Surface and Coolant Flows

The exchanger plate involved in the cooling system can be a proportion of the nacelle. A variation in the exchanger surface is proportional to a variation of the exchanger pipe length since the pipe is assigned a plate proportion all-long. The surface of the plate could vary between 35% and 95% of $S_{nacelle}$. Variations of the shaft flow rate and stator flow rate are also

evaluated. The flow rates values that were tested are as follows: for the stator, the flow rates vary from $84 \times 10^{-5} \text{ m}^{-3} \cdot \text{s}^{-1}$ up to $84 \times 10^{-4} \text{ m}^{-3} \cdot \text{s}^{-1}$ and for shaft flow the rate variation is between $2 \times 10^{-5} \text{ m}^{-3} \cdot \text{s}^{-1}$ and $2 \times 10^{-4} \text{ m}^{-3} \cdot \text{s}^{-1}$. The separate cooling of rotor and stator, the low level of losses in the rotor with respect to those in the stator, and the geometry of channels influencing the flow rate of the shaft that is by far lower than stator one are all factors to be kept in mind in analyzing the results of this study.

Note that actually, the shaft channel flow rate variation has no significant impact on T_{max} since the hottest point is in the stator as it can be seen in *Figure 4.30*. Hence only the first two parameters (exchanger surface and stator flow rate) are investigated. The corresponding response surface is depicted in *Figure 4.31*. In the response surface displayed, two discontinuous levels of temperatures corresponding to two sets of points are seen.

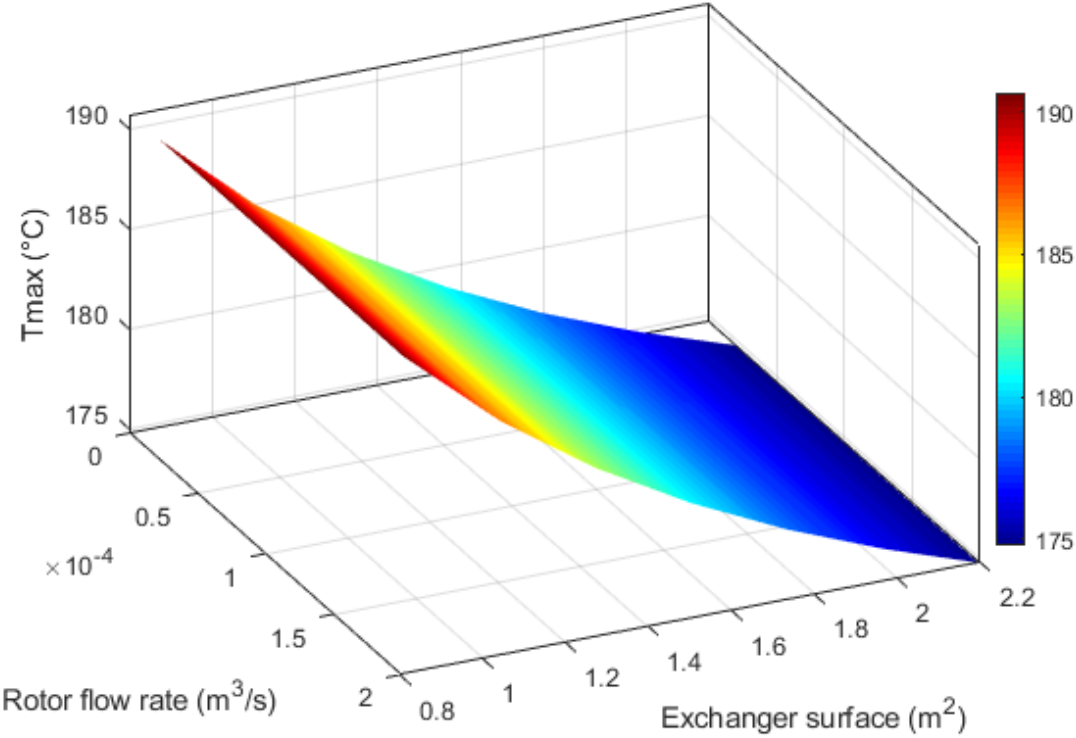


Figure 4.30 : Surface response of temperature to variation of exchanger surface and rotor flow rate

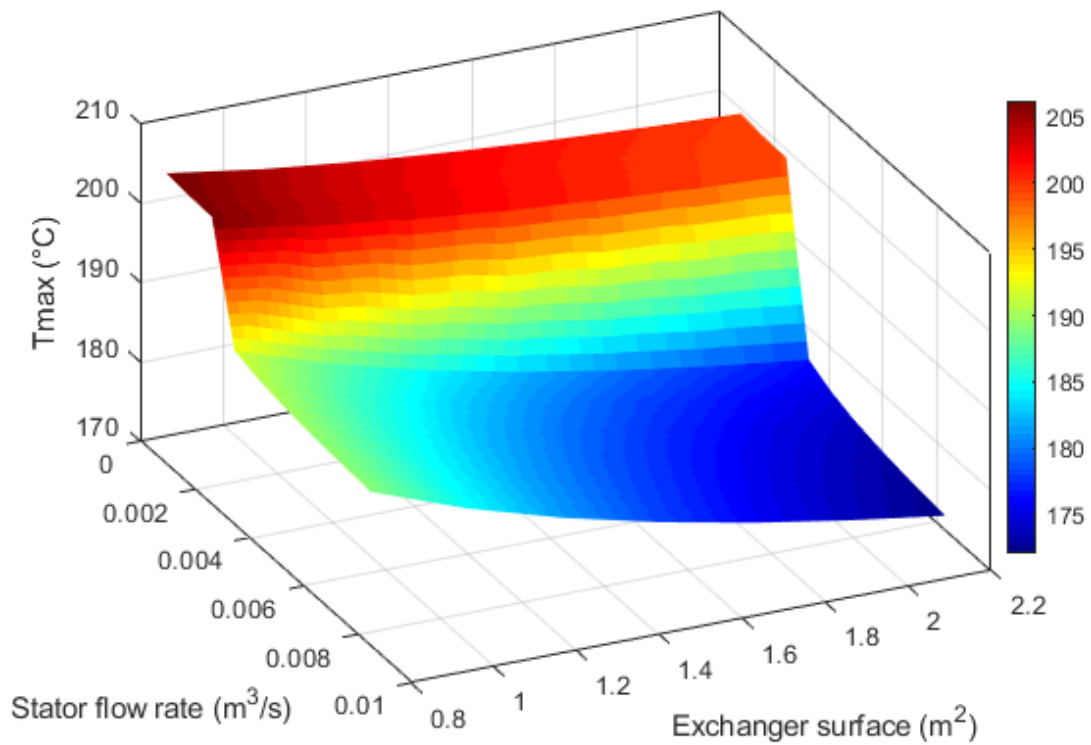


Figure 4.31 : Surface response of temperature to variation of exchanger surface and stator flow rate.

The maximum temperature difference reaches $30\text{ }^{\circ}\text{C}$. This is justified by a switch between laminar and turbulent flows when changing the flow rate value. Turbulent flow provides a higher convection coefficient and helps to extract more efficiently the heat from the motor, and thus lowering temperatures in the critical zone. This flow corresponds to the lower set of points.

Moreover, the effect of exchanger surface reduction is less pronounced in laminar flows (the upper set of points) than turbulent flows. Finally, in this latter flow type, the stator flow rate has a more significant impact on temperature reduction at high exchanger surface (around $5\text{ }^{\circ}\text{C}$) than at reduced surfaces ($2\text{-}3\text{ }^{\circ}\text{C}$).

4.5 Case-studies

4.5.1 Influence of Flight Mission Scenarios

In this same configuration, we have tested the model in an emergency condition that calls the motor to run under continuous full power after the take-off phase. The resulting evolution of temperatures in the motor is depicted in *Figure 4.32*. The simulation shows that the maximum temperature reached is $282\text{ }^{\circ}\text{C}$. The total time before reaching the limit of $180\text{ }^{\circ}\text{C}$ at end-windings after the end of the taxiing phase is 900 s . If we consider the real maximum allowed temperature of winding without considering the safety margin, the time to reach $220\text{ }^{\circ}\text{C}$ is around 1600 s from the same reference point. For the rotor temperatures, the limit with the safety margin is touched in 1400 s after take-off and without this margin in 2100 s .

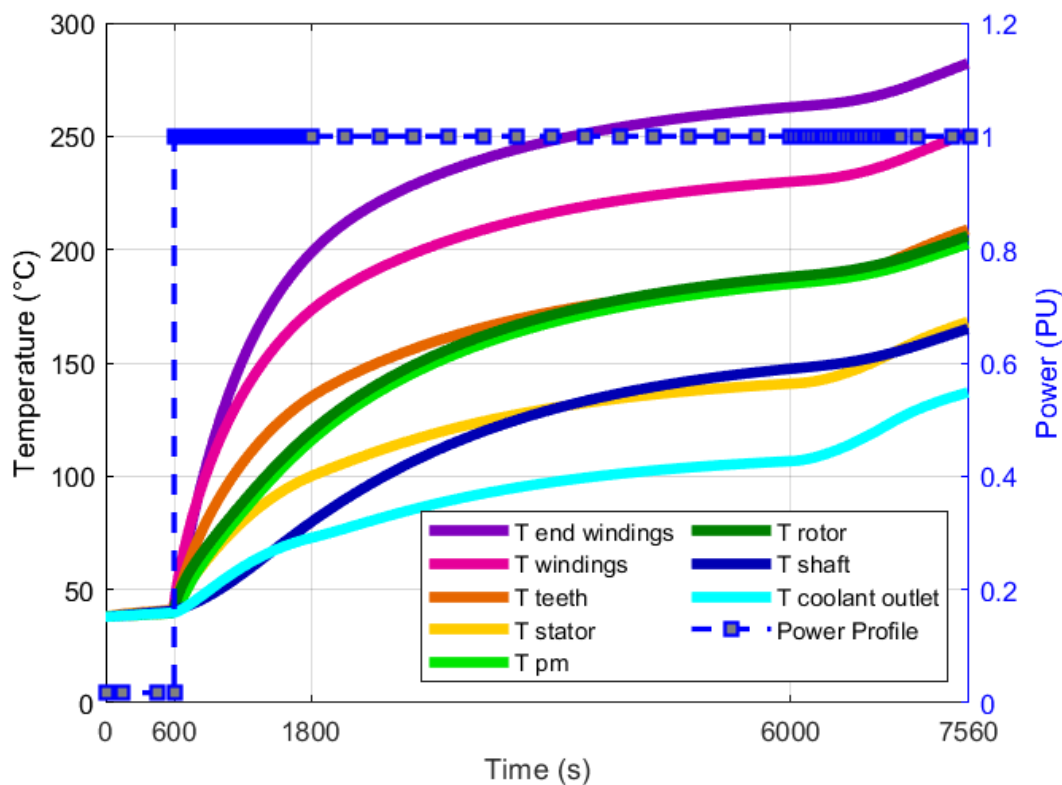


Figure 4.32 : Motor temperatures evolution for a continuous full-power regime after take-off.

The effect of outside temperature decrease during climb and cruise phases and increase during descent and landing phases, prohibit the steady-state to take place. However, the objective of this simulation is not to approve maintaining a flight mission under these severe conditions but to determine the time-to-damage duration of the electric motor and prevent any failure risk.

This duration should be strictly considered in the case of full-power application to keep motor temperatures within the safe margins.

4.6 Electric Motor for 2035

The second objective is to design a motor with higher specific power (10 kW/kg) that could be used for aircraft propulsion in the year 2035.

Actually, for the electric design of this motor, several technological solutions are proposed, investigated, and assessed (such as inorganic insulation materials of class 240°C , carbon fiber sleeves having high permissible stresses, Litz wires to reduce windings losses [176]).

Once more, the electro-magnetic design and data are provided by our project partners at WP1.

Hence, adapted thermal management of this motor design is required. It must include several considerations and modifications in the inputs of the thermal model. The cooling strategy is modified accordingly.

Practically, a preliminary study has been conducted upon estimations of the influence of these modifications (mainly losses) brought to the design of EM2025. Actually, with the same motor power as that of EM2025, the EM2035 has considerably higher total losses, with the same distribution in the machine. The minimum specific power should be 10 kW/kg , which means that the machine must not weigh more than half of the weight of EM2025.

Logically, with the same power and a lower weight, the motor will exhibit higher temperatures due to lower thermal capacities. Besides, the doubled specific power value generates higher motor losses than EM2025, and a different distribution of motor losses.

Hence, we have begun the investigation with increasing losses (specifically Joule losses), with respect to the recommendations of electric machine specialists to obtain first temperatures' results. Based on the resulting profiles and hot spots, we have elaborated a provisional cooling system design guaranteeing its efficiency on the modified EM2025 model. The procedure at this stage implies a brand-new motor design from WP1 for the long-term hybrid aircraft propulsion.

Since many inputs of WP1 design tools can be tuned to optimize the system (specifically loads and material choice), multiple electric motor designs of EM2035 were provided and tested

successively throughout a complementary work process between our Work-Package and WP1. A synthesis study of only two motors is presented hereafter. The second design was adopted and its cooling system was developed accordingly. Nevertheless, the results and issues of the first design are discussed before getting to the final design of EM2035.

4.6.1 Motor Cooling System Choice

Before presenting the possible cooling system of EM2035, a variation in the thermal conductivity of resin applied for the impregnation of windings is made in the model.

The cooling system choice for EM2035 is based on the maximum allowed temperatures set as constraints as for EM2025. However, the values of these temperatures for critical motor parts are quite different. For windings, the insulation class is $240\text{ }^{\circ}\text{C}$, which allows a limit of $200\text{ }^{\circ}\text{C}$ in the numerical model. The magnets limit is similar to that of the EM2025 case, as reminded in *Table 4.13*. The modified temperature is based on the probable use of different techniques of winding.

Component	Temperature limit for Target 2
Windings	200 °C
Permanent magnet	135 °C

Table 4.13 : Temperature limits for EM2035 critical components.

The thermal conductivity of the impregnation material remains the same around $1\text{ W}\cdot\text{m}^{-1}\cdot\text{K}^{-1}$.

To allow the evacuation of the generated heat to the outside, the cooling system of the EM2025 is maintained. It focuses on frame liquid cooling with liquid jackets around the motor core and a possible rotor liquid cooling and end-windings potting. In addition to these solutions, the high heat dissipation in windings and surroundings (due to Joule and iron losses) and based on first results, ‘direct’ cooling of windings through internal channels in slots is a necessity.

The cooling of windings consists of two channels integrated into each slot at the sides as depicted in *Figure 4.33*. A proportion of 25% of the slot is reserved for these channels. Thus, the two channels occupy this proportion in width while their height is only a proportion of 75% of the slot height. Each channel is made of a plastic material electrically insulating with 0.1 mm thickness and thermal conductivity of $0.5\text{ W}\cdot\text{m}^{-1}\cdot\text{K}^{-1}$.

At the end-windings, the channels cover the lateral sides of the geometry (rectangular in the model). Since we consider an ortho-radial section, the corresponding surfaces of contact between channels and end-windings are numerically computed. Practically, at each motor side (front and rear), all of the windings channels will be connected into an annular channel covering the end-winding surface in the parallel plan to motor radial view.

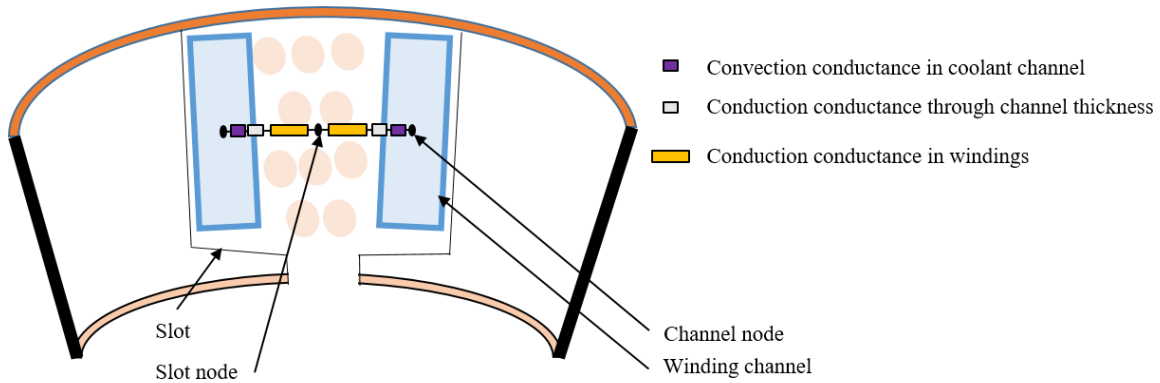


Figure 4.33 : Slot channels illustration with corresponding thermal resistances.

Five nodes are added in the nodal network for EM2035 (nodes 58 to 62). An illustration of the new LPTM with channels location is depicted in *Figure 4.34*, showing half of the axial section of the motor.

With the added nodes, the developed LPTM is a 62-node-base network. The data entry and general composition of discretized volumes follow the same process applied to develop the EM2025 model. The coolant is the same water-glycol mixture (DOWTHERM SR-1 Fluid).

The use of potting at end-windings was maintained for first results, and has been evaluated afterwards.

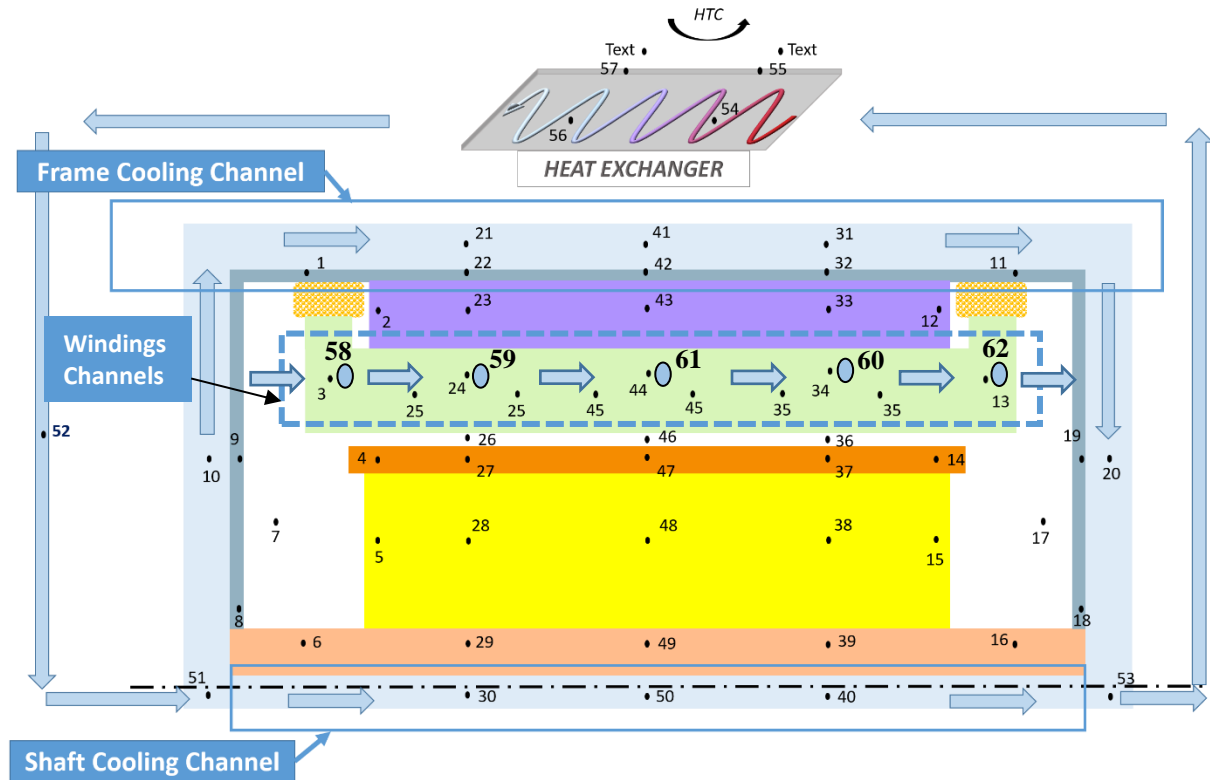


Figure 4.34 : LPTM nodes of the motor EM2035 with windings channels locations and added nodes.

4.6.2 First Motor Design and Results

A first motor design is presented for comparison with the adopted final EM2035 motor.

4.6.2.1 Data and Dimensions

The corresponding data for the first design of the motor with their maximum values are gathered in Table 4.14 (including losses levels). The machine geometrical dimensions are grouped in Table 4.15. For this first design, the corresponding losses profiles are given in Figure 4.35.

Losses data in this first design configuration exhibit a disproportional distribution of Joule and iron losses. The iron losses are more than twice the Joule losses all along the mission.

Characteristic	Unit	Value
Mechanical speed	RPM	29000
Number of phases	-	3
Number of slots	-	24
Winding losses	PU	0.26
Stator iron losses	PU	0.59
Windage losses	PU	0.13
Friction losses	PU	0.02

Table 4.14 : Data of first design of EM2035 from WP1.

The interaction between WP1 and our Work-Package WP3 induced a strategy consisting of reducing Joule losses to a minimum since the windings are confined areas with low thermal conductivity in radial and ortho-radial direction. This has logically been compensated in other losses, mainly iron losses.

Main size	Unit	Value
External stator radius	mm	120.84
Inner stator radius	mm	72.09
Stator yoke height	mm	18.82
Slot height	mm	29.93
Tooth width	mm	11.50
Slot width	mm	7.38
Airgap thickness	mm	3.03
Permanent magnet thickness	mm	7.56
Rotor yoke height	mm	15.92
Shaft radius	mm	45.58
Active length	mm	288.38
Motor length	mm	404.30

Table 4.15 : Main dimensions of the first design of EM2035 from WP1.

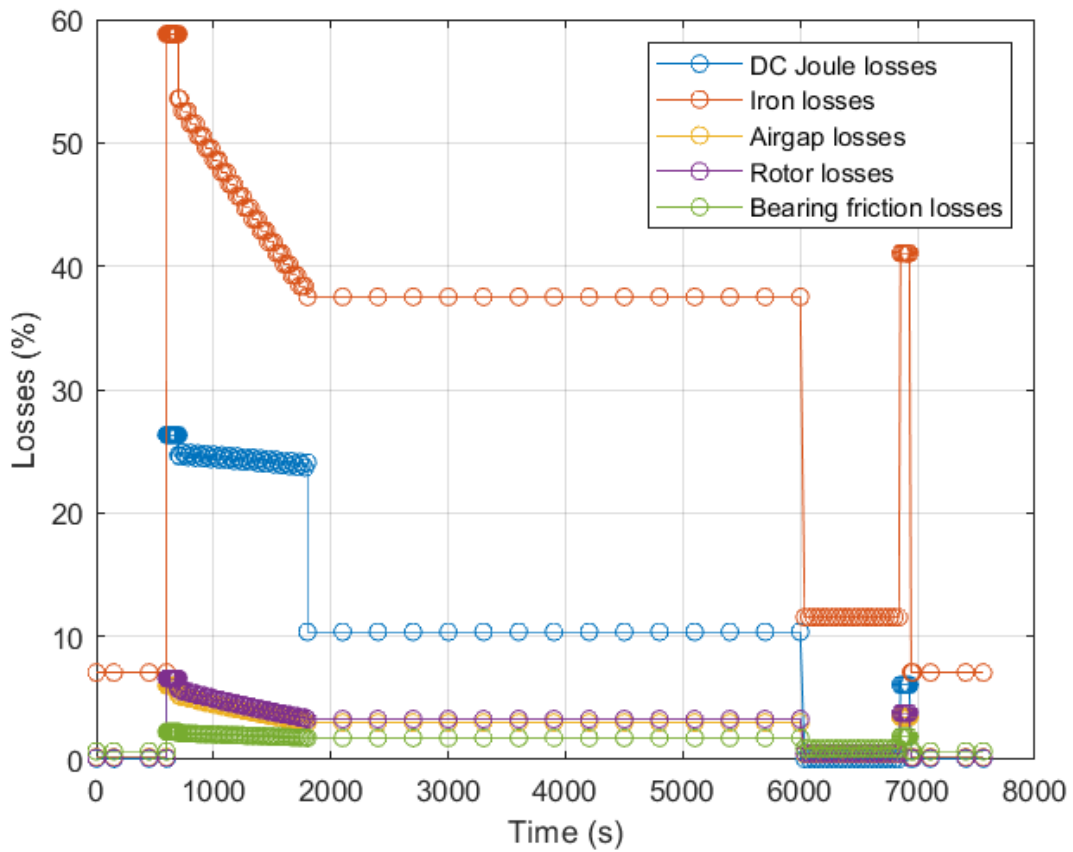


Figure 4.35 : Losses Profiles for the first design of EM2035 from WP1.

This should have a big influence on hot spot temperatures found at windings and end-windings since the reduced Joule losses strongly control these regions. Besides, the cooling focusing on this same region will help further reduction of temperatures.

The distribution of flow rates in the motor is shown in Table 4.16 as well as the corresponding hydraulic diameters and channels' lengths. It is worth to remind that the results of temperatures are obtained considering that the entire nacelle surface is engaged.

Zone	Stator	Shaft	Winding	Exchanger
Hydraulic diameter D_h (mm)	7.1	9.1	1.9	42
Flow rate q ($m^3 \cdot s^{-1}$)	1×10^{-4}	5×10^{-5}	5×10^{-5}	2.55×10^{-3}
Channel length l (m)	4.09×10^{-1}	4.09×10^{-1}	4.09×10^{-1}	17.5
Convection coefficient h ($W \cdot m^{-2} \cdot K^{-1}$)	250	1600	4700	3300

Table 4.16 : Cooling system parameters in channels according to motor zones and exchanger.

4.6.2.2 Results

The simulation results are depicted in *Figure 4.36*. With this first design features, and the marked increase of iron losses, a significant increase of temperatures in rotor and magnets (around $180\text{ }^{\circ}\text{C}$) is noted during the take-off phase, far above the maximum allowed temperature.

The windage losses, affecting mainly the rotor, are estimated to around 13% of total losses, which is a high proportion for this motor configuration and temperature limits (10% in EM2025 configuration). The profile and magnitude of losses at this level have led to high magnets temperatures rapidly after take-off and until the descent phase. Even if the nacelle surface is entirely engaged, temperatures increase drastically.

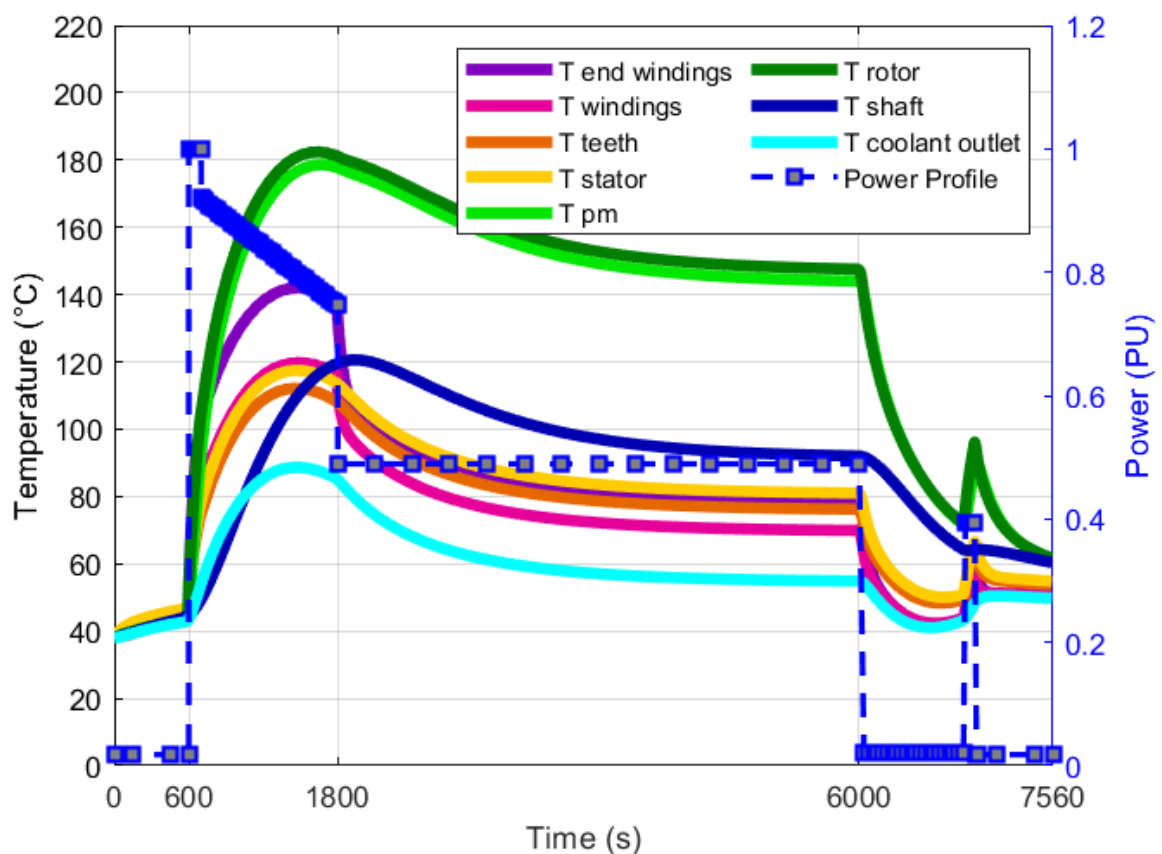


Figure 4.36 : Resulting temperatures profiles for the first design of EM2035.

Whereas other temperatures, specifically end-windings, exhibit low temperatures during the mission and a low peak value ($140\text{ }^{\circ}\text{C}$). This is induced by the low Joule losses in this first design of the motor (26% of total losses compared to 43% in the EM2025).

It is interesting also to mention that the magnets peak value is reached earlier in this case compared to the EM2025 configuration and before the shaft peak.

Even with a significant increase in mass flow rate in the shaft channel or an increase in channel diameter, rotor maximum temperatures cannot be maintained below $135\text{ }^{\circ}\text{C}$ all mission long due to the high thermal resistance between the rotor surface and the channel. Hence, this design configuration is not adapted to our application and is rejected.

Finally, another motor design is therefore proposed. An enhancement is required, mainly in losses profile with a reduction of at least 50% of windage losses, by reducing the rotational speed (variation of windage losses is proportional to ω^3) and providing a new motor geometry.

4.6.3 Second Design for EM2035

A second design of EM2035 is presented herein. The created heat paths in the motor as well as the exchanger characteristics are optimized. The thermal analysis of data and results are briefly exposed since the main issue is to provide a design that answers the specifications and target of electric motor for the time-target (EM2035).

4.6.3.1 Motor Design Data

As for the previous design, the corresponding data of the motor design with their maximum values are gathered in *Table 4.17*. The geometrical dimensions are grouped in *Table 4.18*. Losses profiles are given in *Figure 4.37*.

Characteristic	Unit	Value
Mechanical speed	RPM	20000
Number of phases	-	3
Number of slots	-	24
Winding losses	PU	0.5
Stator iron losses	PU	0.44
Windage losses	PU	0.05
Friction losses	PU	0.01

Table 4.17 : Data of final design of EM2035 from WP1.

Main size	Unit	Value
External stator radius	mm	111.94
Inner stator radius	mm	72.92
Stator yoke height	mm	14.07
Slot height	mm	24.95
Tooth width	mm	9.38
Slot width	mm	9.71
Airgap thickness	mm	3.06
Permanent magnet thickness	mm	7.84
Rotor yoke height	mm	16.66
Shaft radius	mm	45.36
Active length	mm	291.67
Motor length	mm	408.90

Table 4.18 : Main dimensions of the final design of EM2035 [184].

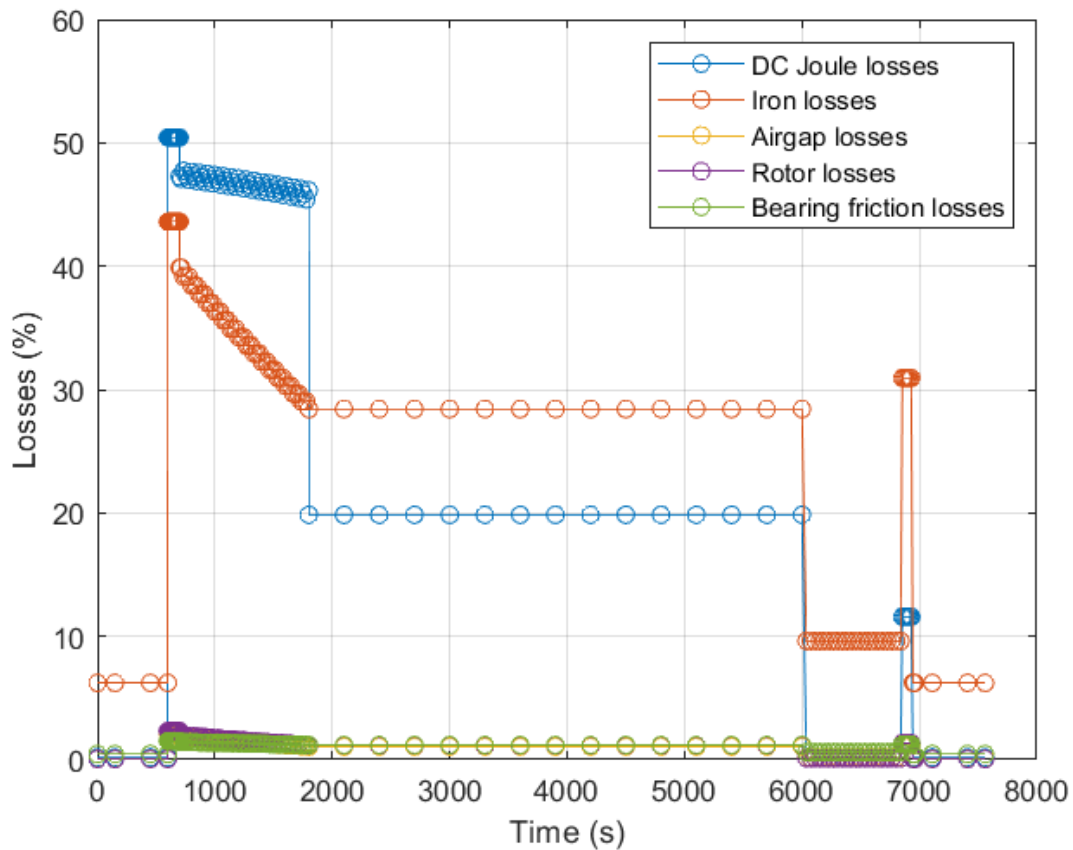


Figure 4.37 : Losses Profiles for the final design of EM2035 [184].

The corresponding profiles of EM2035 losses (resulting from different loads' sets in the design tool of WP1) show a significant reduction of rotor losses with windage losses around 4.5% of total motor losses.

4.6.3.2 Results and Analysis

The resulting profiles of motor temperatures are depicted in *Figure 4.38*. Thanks to the losses distribution, different thermal behavior is exhibited in the machine. As seen in the figure, the thermal response of the motor with this design and these losses profiles is dissimilar from the previous configuration. Unlike the first design, the magnets and windings temperatures retrieved a dynamical evolution similar to that found in EM2025 adopted design, with a maximum temperature of $133\text{ }^{\circ}\text{C}$.

According to the model results, stator behavior is consistent in all parts and the peaks ($188\text{ }^{\circ}\text{C}$ for end-windings and $155\text{ }^{\circ}\text{C}$ for windings) are reached before the end of the climb phase

(1540 s), while the rotor peaks are obtained afterward during the beginning of the cruise phase (1980 s). This time difference corresponds to the difference in the evolution between losses.

Beginning with a slight temperature rise during the taxi-out phase, then a spike increase during take-off and climb phases. The reduction of 50% of power during the cruise phase and the drop in outside air temperature, associated with an efficient cooling system allow reaching a steady-state at the end of this phase. The temperature evolutions during the last two phases are typically similar to that noticed in EM2025 behavior and correspond to the losses profiles according to motor zones. Attention should be paid to coolant temperature, which reaches a maximum of 100 °C.

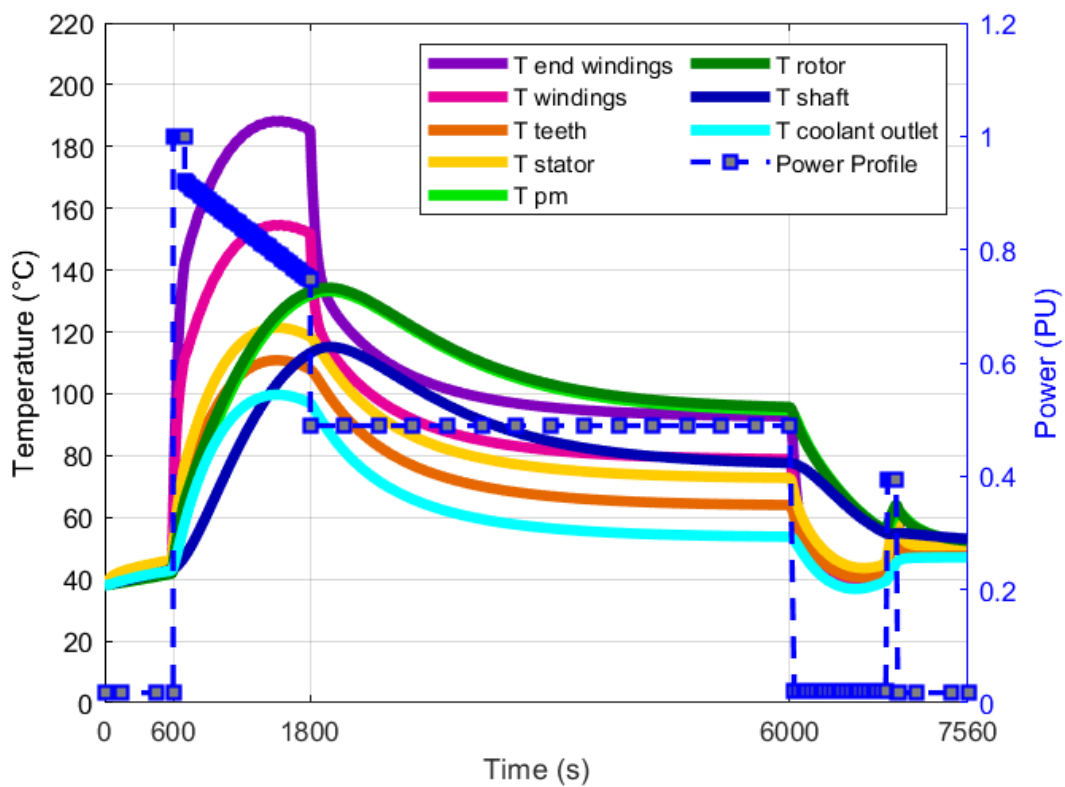


Figure 4.38 : Resulting temperatures profiles for the final design of EM2035 with potting.

Since the resulting end-winding maximum temperature is below the limit of 200 °C, the potting could be useless in this design. A simulation of the model is carried out without end-windings potting to check if this additional technique is required. The resulting graphs of Figure 4.39 depict the temperature evolution in the motor without potting. In both cases, motor behavior is

quite similar. A temperature increase of very few degrees is observed. However, the limit is not reached for end-winding temperature. This result allows choosing to remove the potting option from the EM2035 configuration.

The thermal behavior of the motor in this configuration approves the heat extraction and evacuation techniques. The temperature values are below the maximum limits and are acceptable. Hence, this design is adopted.

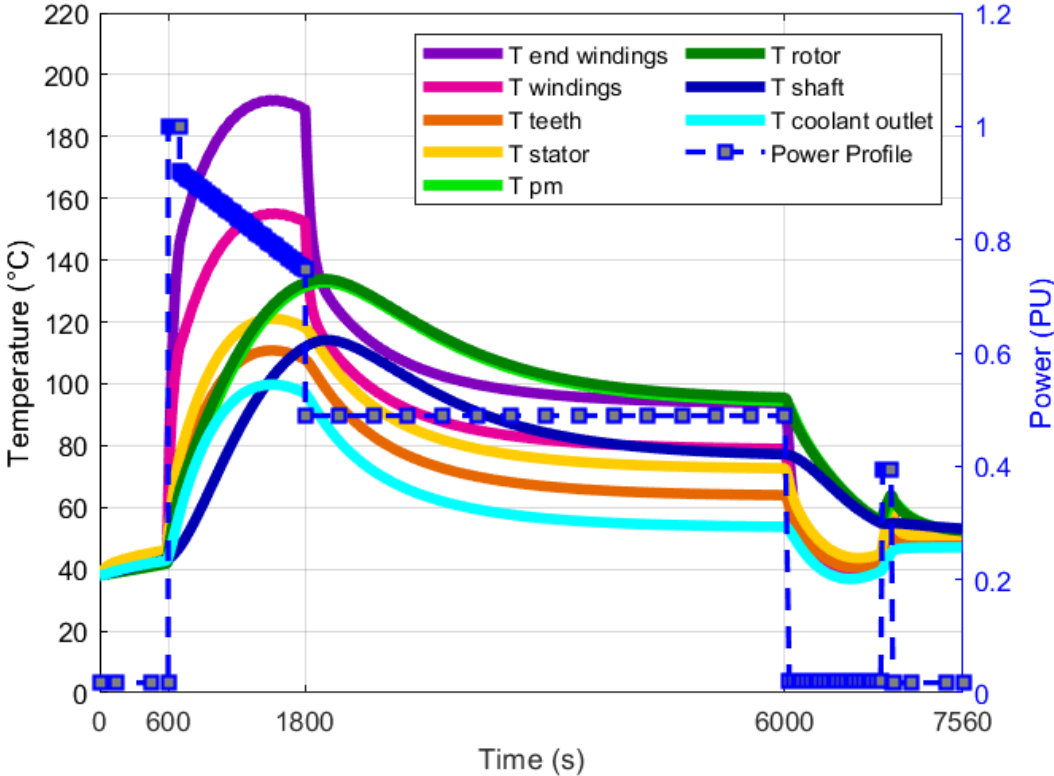


Figure 4.39 : Resulting temperatures profiles for the final design of EM2035 without potting.

4.6.3.3 Cooling System Sizing

In *Table 4.16*, the values of the hydraulic diameters, the flow rates, and the channel lengths are grouped for each corresponding zone. To optimize the pump weight, a convenient total flow rate of $2.55 \times 10^{-3} \text{ m}^3 \cdot \text{s}^{-1}$ has been chosen.

The resulting hydraulic losses H_L in each motor zone and in exchanger are grouped in *Table 4.19*. The pump is selected from the catalog of hydraulic pumps from Parker Pumps and Motor Division [182]. An adequate pump has the characteristics found in *Table 4.20*. The pump weight is integrated into the calculation of the total weight of the motor and its cooling system, and the specific power target is met.

Zone	Stator	Shaft	Winding	Exchanger
Hydraulic major losses H_L (m)	0.021	0.061	3.707	0.493

Table 4.19 : Resulting hydraulic major losses in channels according to motor zones and exchanger for EM2035.

Pump		
Characteristic	Unit	Value
Normal Operating Pressure	bar	206
Maximum Speed	RPM	4420
Length	cm	26.42
Height	cm	19.05
Width	cm	17.78
Weight	kg	11.34

Table 4.20 : Pump characteristics (AP15V) for EM2035 from [182].

The weight of the cooling system without pump is around 30 kg . The overall cumulative weights of the motor and its cooling system - including the coolant weight and the pump - respect the limits to reach 10 kW/kg of motor specific power target.

4.7 Conclusion

Electric motors for the project targets are thermally assessed in this chapter. Two designs of SM-PMSM have been finally adopted for the first and second time-frames respectively.

The design of Electric Motor Target 1 (EM2025) is investigated using the developed numerical tool: *AthEM* model. The cooling system, adequately chosen for the motor configuration, is integrated into this model and the expected temperatures' results are elaborated. Corresponding calculations are presented. A double liquid cooling with water jackets and shaft channel and a potting of end-windings provided satisfactory results. The hot spot levels of temperatures and weight values for the motor and cooling system are obtained allowing reaching 5 kW/kg of specific power for the motor and its cooling system.

For the Electric Motor for 2035 (EM2035), an assessment of many motor designs has been carried out. Based on the thermal studies, a direct liquid cooling of winding is strongly required to maintain motor temperatures below the limits during the mission. Thus, additional cooling channels for windings are integrated into the motor model, covering a part of end-windings. Simulations and analyses have proved that high windage losses (specifically at rotor level) induce overheating of magnets. Among several case-study motor designs, two were presented. The second configuration with corresponding losses distribution is found adequate for EM2035. The resulting temperatures' profiles are presented showing acceptable peak values in hot spot zones.

Consequently, from the studies, it is deduced that in this motor type (high specific power synchronous machine), adapted configurations of geometry, losses distribution, and cooling technique, altogether, should be tuned to reach a reliable and optimized electric motor design.

CHAPTER 5 MODEL INVESTIGATION AND INVERSE METHOD

Synopsis:

Since the developed Lumped Parameter Thermal Model has the advantage of having few degrees of freedom, it will be applied to identify motor losses by solving an inverse problem. Once identified, these losses will be used to monitor temperatures at unreachable critical points.

5.1 Introduction

Our numerical model LPTM is now developed, validated, and adapted to the targeted motor type. In this motor type and in electric motors in general, losses are generally hardly determined. The identification of motor heat sources through an inverse method, based on thermal measurements, is proposed using the same LPTM model; which is an adapted choice because of the small number of degrees of freedom. Beforehand, a sensitivity study to losses has been carried out to distinguish the impact of losses types on motor values.

Finally, based on optimal losses and external measurements, it is possible to predict rapidly low-accessibility temperatures to prevent exceeding critical temperature.

5.2 Sensitivity of Motor Temperature to Losses

Before carrying out the losses determination through the inverse technique, a sensitivity study of motor temperatures to losses has been conducted on EMT1 (Electric Motor Target 1). This study aims to determine which losses are critical, and on which motor parts each type of losses has a significant impact.

Figure 5.1 reminds of the position of each losses type in the nodal network of the motor in a symmetric cut at the middle of the machine scheme.

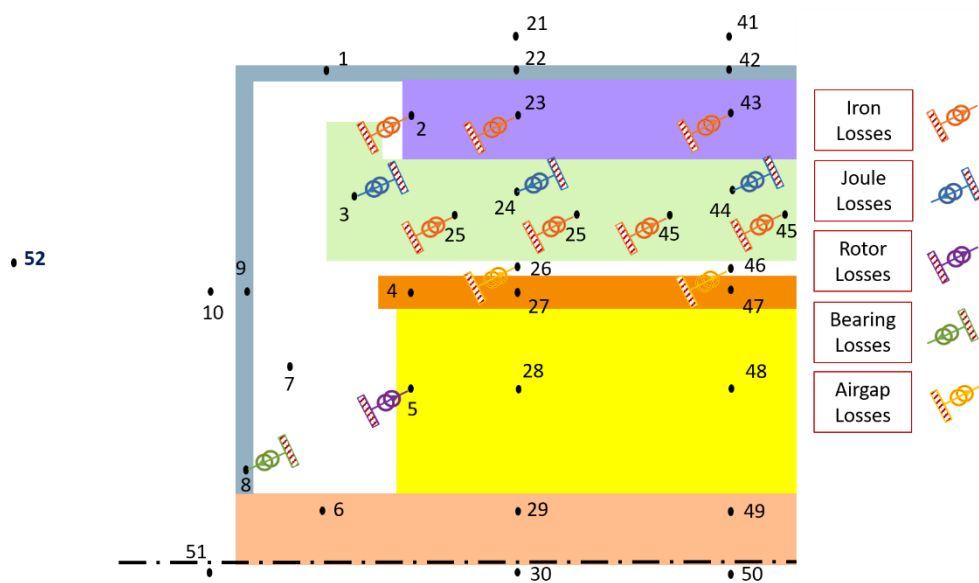


Figure 5.1 : E-motor losses locations in the nodal network symmetric cut according to nodes.

According to zones, the results of a 10% decrease in each type of losses (equivalent to heat sources) are depicted in *Figure 5.2*. Variations of losses in bearings, airgap, rotor, iron/yoke part, iron/teeth part, and windings (Joule losses) are examined.

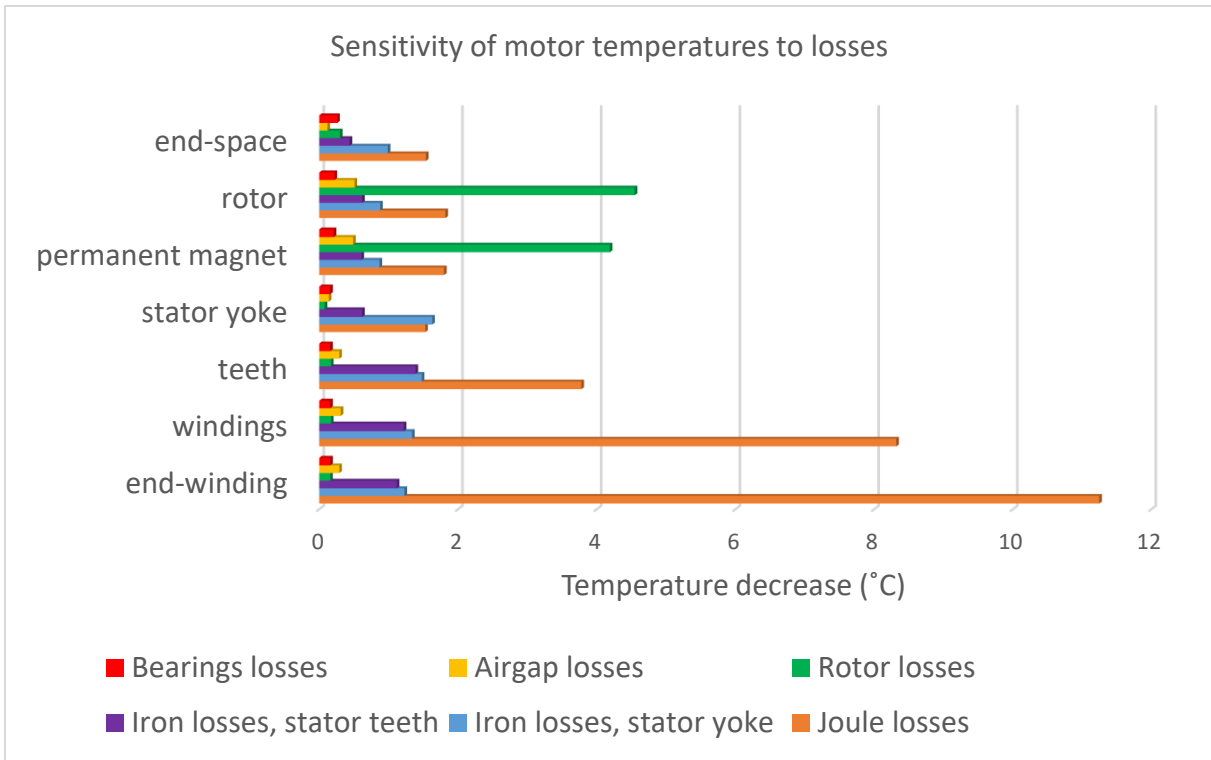
Figure 5.2a represents the temperature decrease ΔT_{sen} resulting from each variation in losses as: $\Delta T_{sen} = T_{initial} - T_{variation}$. In *Figure 5.2b*, the relative temperature decrease ε_T is calculated for each motor zone, and is given by: $\varepsilon_T = 100 \times \Delta T_{sen}/T_{initial}$.

For each zone, the corresponding temperatures in the network are taken according to nodes positions as follows:

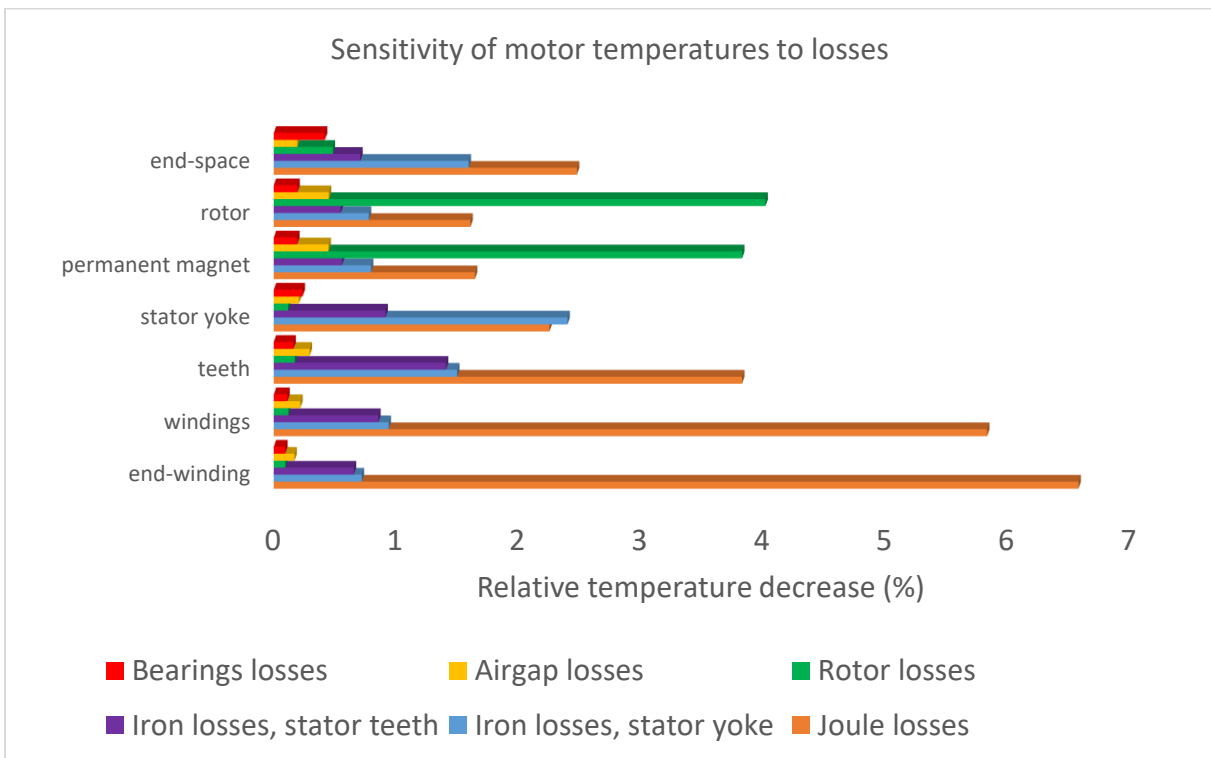
- Node 17 for end-space,
- Node 15 for rotor (laminations),
- Node 14 for permanent magnets,
- Node 33 for stator yoke (laminations),
- Node 34 for teeth,
- Node 35 for windings,
- Node 13 for end-windings.

The temperature decrease depends mainly on the zone to which the losses are injected. The closer the losses are to the zone, the higher is the drop in this zone temperature. Globally, stator losses (iron and Joule losses) are extremely significant in the determination of stator temperatures. The maximum allowed temperatures are $180\text{ }^\circ\text{C}$ and $120\text{ }^\circ\text{C}$ respectively for winding and permanent magnets.

Joule losses in windings and end-windings are highly critical to almost all motor temperatures. Their impact is significant on all stator temperatures but also on rotor temperatures. An average of $10\text{ }^\circ\text{C}$ of reduction in winding and end-winding temperatures (6% of temperature variation) is noticed when decreasing Joule losses by 10%. As a result, the stator teeth temperatures are simultaneously reduced by around $4\text{ }^\circ\text{C}$ in stator teeth temperature (4% of temperature variation) for the same variation in Joule losses. Actually, an interesting heat path for Joule losses is made through the teeth to the stator iron and the cooling medium due to the small slot width compared to its height. The significant effect of Joule losses on windings can be justified by the very high thermal resistance between the slots and the stator laminations, making it more complicated for the generated heat to be extracted from this area. This makes the windings zone ultimately sensitive to the heat resulting from Joule losses.



(a)



(b)

Figure 5.2 : Sensitivity of motor temperature to 10% of losses variation, (a) temperature decrease in (°C), (b) relative temperature decrease in %.

Although these losses are produced in the stator part, the rotor will be indirectly affected by any variation at this level. This results from the coolant arriving at the rotor and the air inside the cavities. Those are the only two fluid media connecting the rotor to the outside heat sink.

The major finding in the rotor sensitivity to losses is that losses injected at the rotor end-caps have the sharpest influence on permanent-magnets and rotor yoke temperatures (up to 4% of temperature variation). Besides, it is noticed that iron and Joule losses variations can have a slightly higher impact on rotor temperatures than bearings and airgap losses: $1\text{ }^{\circ}\text{C}$ to $2\text{ }^{\circ}\text{C}$ (up to 1.6% of temperature variation) for the former two types compared to less than $1\text{ }^{\circ}\text{C}$ (less than 0.5% of temperature variation) for the latter two types. End-space is influenced by the percentage of variation in stator electromagnetic losses rather than the variation of the same percentage in mechanical losses (up to 1.5% of temperature variation). This can be justified by the losses level in windings and their temperatures, which are both higher than those of rotor end-caps and their sensitivity. In fact, this end-space air is contacting both end-motor surfaces.

Finally, rotor losses affect considerably the hot spot in permanent magnets temperature: more than $4\text{ }^{\circ}\text{C}$ of variation is observed for rotor temperatures when reducing these losses by 10%, which corresponds to around 4% of temperature variation.

Decreasing the rotor end-caps losses by 10% has four times more significant impact on decreasing rotor temperatures than the airgap losses reduction by the same percentage (more than 4% of temperature decrease against less than 0.5%). This is due to the nodes connections in airgap where a part of the heat flux has its path towards the stator, which creates less influence on rotor temperatures than the losses injected to end-caps directly. Practically, reducing the rotor or airgap losses by 10% represents a reduction of 2.5% of actual RPM or exactly 345 RPM fewer for the full power regime of EMT1.

The sensitivity of all stator temperatures (teeth and yoke) to iron losses injected to stator yoke is extremely similar. The radial thermal conductivity of laminations is quite high in this direction and the heat injected tends to follow a path towards the outside. This creates a kind of homogenization of temperatures in stator laminations. Moreover, Joule losses and iron losses variations have relatively the same impact on stator yoke thermal behavior (~2.3% of temperature variation).

To sum up, one can conclude that in the case-study motor configuration, efficient distribution of losses should take into account the greater influence of Joule losses reduction compared to decreasing other stator losses. In the rotor, friction losses at the rotor end-caps have the highest impact on permanent-magnets temperature.

5.3 Losses Identification using an Inverse Method

5.3.1 Interest and Background

Besides being hardly evaluated with analytical and some computational methods, it is believed that even with a motor prototype, determination of the different losses and distinguishing their types or origins are quite complicated. Generally, such information can be barely obtained with long iterative methods. A possible solution to identify electric motor losses is to measure temperatures inside the motor and then use an inverse method. Such methods need a thermal model with a quick solving process. The thermal nodal network developed in this thesis could be a good choice because of the few degrees of freedom.

Being mathematically ill-posed, the solution of the inverse problem may be unstable and not unique. Hence, several regularization techniques have been developed by researchers to ensure stable solutions [185]. Some examples of inverse problems for electric machines can be found in the literature. Let us cite hereafter some of these works. In [186], the authors propose an inverse problem in order to identify a set of 9 design parameters (geometric and magnetic parameters) for a permanent magnet brushless motor. The results show that the density of the magnetic flux in the air gap is increased, as well as motor efficiency. A 3D inverse heat conduction problem is presented by [187] to estimate the generated heat fluxes for a high-speed electric motor. An inverse method for the identification of heat convection coefficients on coil end-windings from experimental data is presented in [137]. An interesting algorithm is developed and described for this nonlinear inverse heat conduction problem using a lumped parameter model. In [188], a low-order model is built in the first stage to estimate a set of thermal parameters. In the second stage, this model is used to identify thermal losses in the stator of an axial flux PM machine. A prediction of the strength of the heat source field in an induction motor is also carried out in [189] using a steady-state thermal model.

Considering these studies, it seems possible to determine losses using our low-order model LPTM and specific thermal measurements. To verify this, a numerical study has been conducted, starting with only one unknown source to be determined and then increasing the number of losses to finally calculate all losses. Moreover, as comparison criteria, we have also included the prediction of temperatures at unreachable critical parts. This study can be found in [190].

5.3.2 Heat Transfer Equation

The temperature distribution within the motor is determined by solving the Lumped Parameter Thermal Model (LPTM). The heat equation governing heat diffusion and convection in the domain Ω associated with initial and boundary conditions can be written as a system of N Ordinary Differential Equation (ODE), where N is the total number of nodes. Our system model equation is detailed in *Chapter 3* and can be written as follows:

$$C(M) \frac{dT(M, t)}{dt} = G(M) T(M, t) + \Psi(t) \quad \forall M \in \Omega \quad (5.1)$$

Where $T(M, t)$ is the temperature at a point M in the domain representing a volume, C is the thermal capacity of this volume, G is the thermal conductance connecting M to other points, Ψ is the heat source or heat sink in the corresponding volume.

The initial condition is:

$$T(M, 0) = T_{init} \quad \forall M \in \Omega \quad (5.2)$$

Boundary conditions are determined based on the external temperature T_{ext} and the external coefficient of convection.

5.3.3 State-Space Representation

The developed LPTM, discretizing the domain into N nodes and having a relatively low number of parameters, is used to solve the problem. Matrix C being invertible, equation (5.1) can be written as follows:

$$\dot{T}(t) = C^{-1}GT(t) + C^{-1}\Psi(t) \quad (5.3)$$

To adapt the heat transfer equation to this study, the thermal stress term $C^{-1}\Psi$ is separated into two terms representing respectively the heat sinks due to the convective mode and heat sources generated in the motor: $C^{-1}\Psi = B_c T_{ext} + B_p P$, where B_c and B_p are two command matrices relative to convective boundary conditions and heat sources respectively.

Hence, equation (5.3) can be rewritten as follows:

$$\dot{T}(t) = AT(t) + B_c T_{ext}(t) + B_p P(t) \quad (5.4)$$

Where $T(t)$ (dimension N) is the vector of temperatures, a function of time t , at the N discretization nodes, $\dot{T}(t)$ is its derivative with respect to time ($\frac{dT(t)}{dt}$). Matrix $A = C^{-1}G$ (dimension N,N) is the state matrix that connects temperatures at discretization nodes and contains diffusion and transport terms, as well as terms related to convective boundary conditions. The vector B_c is associated with these latter conditions and links corresponding nodes to environment nodes. Matrix B_p (dimension N,n_p) associated discretization nodes to internal heat sources gathered in vector function $P(t) = [P_{Joule} P_{Iron} P_{Rotor} P_{Airgap} P_{Bearings}]^T$ (dimension n_p).

In what follows, let us separate vector P into two sets: unknown heat sources included in U (dimension n_U) and known heat sources included in K (dimension $(n_p - n_U)$). The command matrix B_p can also be split into two matrices as: $B_p = [B_K B_U]$. By defining a vector V as: $V = B_c T_{ext} + B_K K$, the state space representation takes the following form:

$$\begin{cases} \dot{T}(t) = AT(t) + V(t) + B_U U(t) & (5.5) \\ Y(t) = C_o T(t) & (5.6) \end{cases}$$

Where an observation matrix C_o (dimension n_q, N) allows to select n_q temperatures in the whole temperature field $T(t)$ and to store them in vector function $Y(t)$.

In this study, a maximum of nine temperature locations will be used as outputs. These temperatures are depicted in *Figure 5.3*, and are located in the stator lamination (Ts1, Ts2, and Ts3), in the end-winding (Tw) at the surface of the end-winding (Tsw), on the surface of the stator in the airgap (Ta), in the cavity between the rotor end-cap and the frame (Tc), in the bearings (Tb), and in the magnets (Tm).

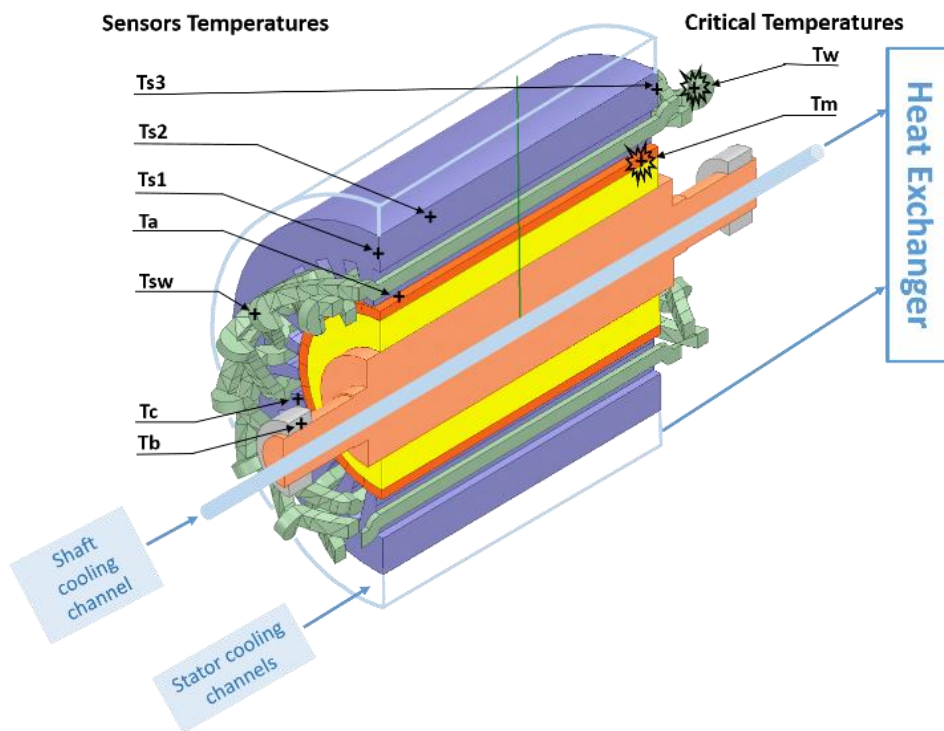


Figure 5.3 : E-motor schematic section with specific locations of temperatures.

These locations have been chosen given the heat sources but also considering plausible experimental measurement system positions. The temperature in the static part of the motor could be obtained using thermocouples (T_{s1} , T_{s2} , T_{s3} , T_{sw} , T_a , T_b , and T_c). The rotor flange temperature could be obtained by infrared measurement. T_m and T_w are the critical temperatures difficult to obtain experimentally due to their locations, i.e. T_w inside the end-windings is confined and thought to be the hottest point and T_m requires a slip ring due to the rotor in rotational motion.

5.3.4 Inverse Problem Solution

The form of the heat transfer model, developed in *subsection 5.3.3*, is convenient to be used now in the inverse procedure. The inverse problem aims at finding an estimation \hat{U} of the input vector U from measured temperatures Y^* . Note that, in this study, real temperature measurements are not available. The temperatures included in the vector Y^* derive from the direct problem with known heat sources. In order to simulate measurement errors, each temperature is altered with an additive Gaussian error, whose standard deviation is given by σ .

Subsequently, to have simplified and clear annotations, we will write U_k for $U(t_k)$, $U(t_k)$, T_k for $T(t_k)$, Y_k for $Y(t_k)$.

A sequential estimation method is adopted. Having the vector of measured temperatures Y_{k+1}^* , and an estimated \hat{U}_k of U_k , an estimation of \hat{U}_{k+1} is then computed.

Using the Euler implicit scheme with a time step Δt , equation (5.5) becomes:

$$\dot{T} = \frac{T_{k+1} - T_k}{\Delta t} = AT_{k+1} + V_{k+1} + B_U U_{k+1} \quad (5.7)$$

Then:

$$T_{k+1} = (I - A\Delta t)^{-1}[T_k + \Delta t V_{k+1} + \Delta t B_U U_{k+1}] \quad (5.8)$$

Hence, according to equation (5.6):

$$Y_{k+1} = C_o(I - A\Delta t)^{-1}[T_k + \Delta t V_{k+1} + \Delta t B_U U_{k+1}] \quad (5.9)$$

Due to the lagging and damping effects of heat diffusion and convection, a variation of heat source strength does not immediately affect the sensors. To take into account these effects, Future Time Steps (FTS) [191]–[194] are used. It means that sensor information at further times t_{k+2} t_{k+3} ... are used to correctly estimate \hat{U}_{k+1} .

If nf is the number of FTS, then:

for $1 \leq f \leq nf$, equation (5.9) is written for $k + 1 + f$ instead of $k + 1$. A temporary approximation of U_{k+1+f} is therefore needed to look for \hat{U}_{k+1} . In this study, a constant value is chosen:

$$U_{k+1+f} = U_{k+1} \text{ for } 1 \leq f \leq nf \quad (5.10)$$

Hence, a global matrix formulation is obtained as in equation (5.11):

$$Y_{k+1}^* = S U_{k+1} + D_k \quad (5.11)$$

With:

$$Y_{k+1}^* = \begin{bmatrix} Y_{k+1}^* \\ Y_{k+2}^* \\ \vdots \\ Y_{k+1+f}^* \\ \vdots \\ Y_{k+1+nf}^* \end{bmatrix} \quad (5.12)$$

$$S = \begin{bmatrix} C_o(I - A\Delta t)^{-1}B_U\Delta t \\ C_o[(I - A\Delta t)^{-1} + (I - A\Delta t)^{-2}]B_U\Delta t \\ \vdots \\ C_o \left[\sum_{j=1}^{f+1} (I - A\Delta t)^{-j} \right] B_U\Delta t \\ \vdots \\ C_o \left[\sum_{j=1}^{nf+1} (I - A\Delta t)^{-j} \right] B_U\Delta t \end{bmatrix} \quad (5.13)$$

And:

$$D_k = \begin{bmatrix} C_o(I - A\Delta t)^{-1}[T_k + V_{k+1}\Delta t] \\ C_o(I - A\Delta t)^{-2}[T_k + V_{k+1}\Delta t] + C_o(I - A\Delta t)^{-1}V_{k+2}\Delta t \\ \vdots \\ C_o(I - A\Delta t)^{-(f+1)}[T_k + V_{k+1}\Delta t] + C_o \left[\sum_{j=1}^f (I - A\Delta t)^{-j} \right] V_{k+2+f-j}\Delta t \\ \vdots \\ C_o(I - A\Delta t)^{-(nf+1)}[T_k + V_{k+1}\Delta t] + C_o \left[\sum_{j=1}^{nf} (I - A\Delta t)^{-j} \right] V_{k+2+nf-j}\Delta t \end{bmatrix} \quad (5.14)$$

The size of vector Y^* is $((nf + 1) \times n_q, 1)$ and matrix S is of size $((nf + 1) \times n_q, n_U)$. The objective is to identify the pseudo-solution \hat{U}_{k+1} of the inverse problem, such that $Y^* - Y \approx 0$, where Y is the temperature vector computed by LPTM. As matrix S is not square due to the addition of future time steps, the least square method is used to solve equation (5.11) and leads to the sequential solution:

$$\hat{U}_{k+1} = (S^T S)^{-1} S^T (Y_{k+1}^* - D_k) \quad (5.15)$$

In order to evaluate the accuracy of the estimations for the different studied cases, a mean quadratic discrepancy between exact heat sources (vector U^{exact}) and estimated ones (vector \hat{U}) is defined as follows:

$$\sigma_U = \left[\frac{1}{n_U \times (nt - nf)} \sum_{i=1}^{n_U} \sum_{k=1}^{nt-nf} (\hat{U}_{i,k} - U_{i,k}^{exact})^2 \right]^{1/2} \quad (5.16)$$

Where nt is the number of time steps in the inverse problem.

It is worth to remind that, in a practical application, this quantity is not reachable. Similarly, for each output Y_i , a mean quadratic error between measured temperatures and those computed with the estimated set of heat sources strengths is defined as follows:

$$\sigma_{Y_i} = \left[\frac{1}{(nt - nf)} \sum_{k=1}^{nt-nf} (\hat{Y}_{i,k} - Y_{i,k+1}^*)^2 \right]^{1/2} \quad (5.17)$$

When the unknown heat sources \hat{U}_{k+1} are identified, they will be used as inputs in the direct problem to predict the temperature in inaccessible parts of the motor, for instance, the critical temperatures T_{crit} in windings or magnets. The complete procedure is illustrated in the block diagram of *Figure 5.4*.

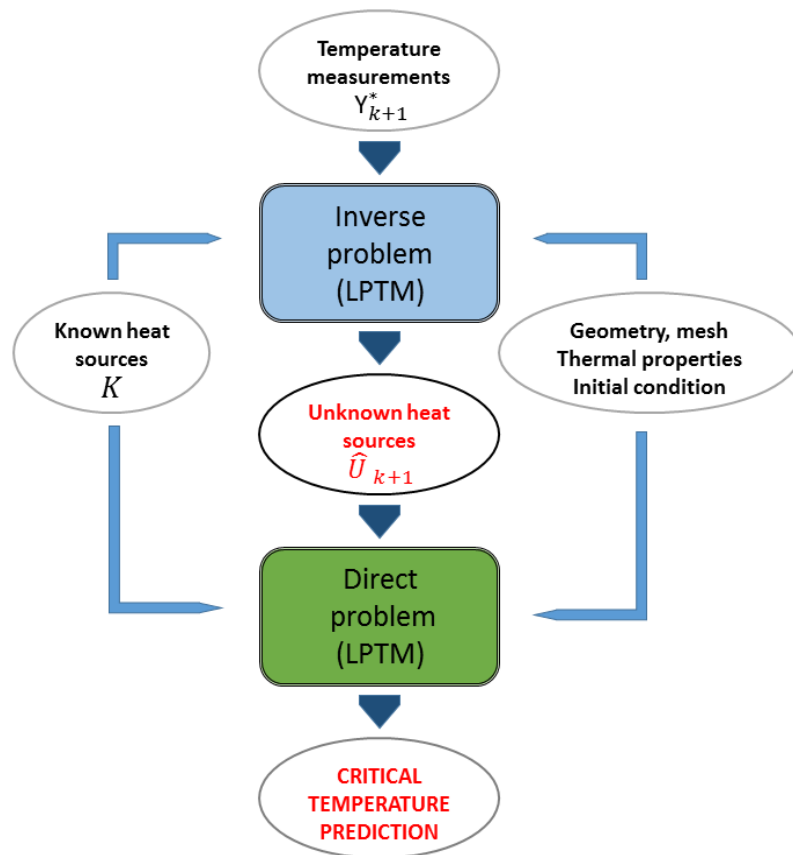


Figure 5.4 : Block diagram: use of LPTM for both inverse and forward problems.

At each time-step, the model is solved in the inverse problem approach to get motor losses. The inputs for inverse LPTM are the temperature measurements equivalent to sensors' output temperatures at accessible points.

Then, forward LPTM is used to determine indicated critical temperatures.

5.3.5 Results and Analysis

A scenario of motor operation is chosen corresponding to a profile mission in an aircraft flight application as in *Figure 5.5*. This profile is different from the proposed mission flight in the project since the objective of this investigation is testing the efficiency of the inverse technique on the motor model independently from the profile used. The flight phases correspond to the taxi-out phase (0 to 450 s), take-off and climb (450 s to 900 s), cruise flight (900 s to 2250 s), descent and landing (2250 s to 2700 s), and taxi-in (2700 s to 3600 s).

Besides, the corresponding outside temperature profile during the flight is an input of the model. It is given by T_{ext} as function of time as in *Figure 5.6*.

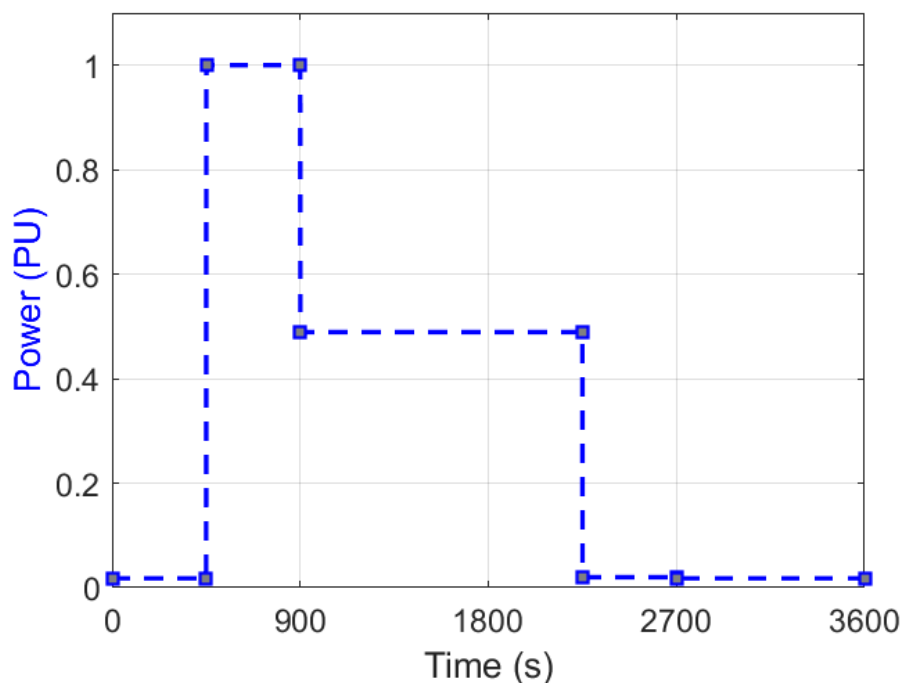


Figure 5.5 : Power profile for losses profile model in the inverse technique.

The corresponding profiles of heat sources generated in the motor (motor losses) are depicted in *Figure 5.7* during the mission profile of 3600s. For confidentiality reasons, all losses (or heat sources) are expressed in Per-Unit (PU) with respect to total losses value.

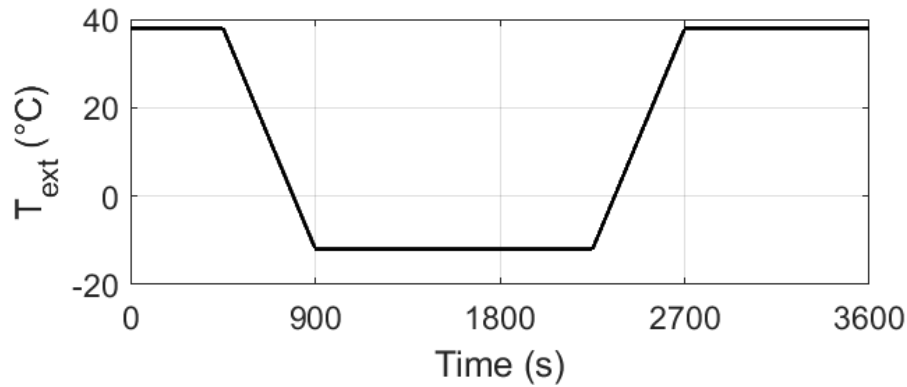


Figure 5.6 : Outside temperature variation as function of time during mission profile corresponding to the current application.

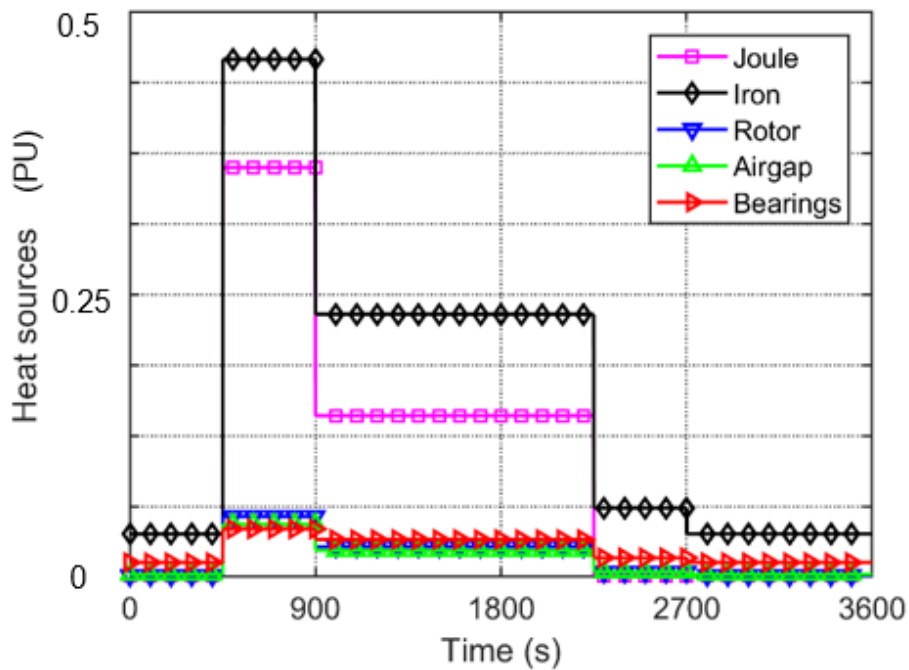


Figure 5.7 : PMSM heat sources evolution as function of time.

Rotor, Airgap, and Bearings losses remain relatively low and are at the same level all mission long, whereas Joule and Iron losses change significantly. Those losses are particularly high during the take-off phase as they are linked to propulsion power. Airgap and Bearings losses

depend principally on the rotor rotation speed, which varies slightly between take-off and cruise, and is very low during taxi phases.

Temperatures are then computed using LPTM and a time step equal to one second. Among these temperatures, a set of observables is chosen depending on the different case studies (see *subsection 5.3.3*). A noise of standard deviation equal to $\sigma = 0.1^\circ\text{C}$ is added to these observables so that they are used as temperature measurements in various inverse problem cases.

5.3.5.1 Identification of Iron Losses

In this first case, among the five heat sources, four are supposed to be known (P_{Joule} P_{Rotor} P_{Airgap} $P_{Bearings}$) and only iron losses ($P_{Iron}(t)$) have to be identified. *Figure 5.8a* shows the evolution of temperature T_{s1} with respect to time.

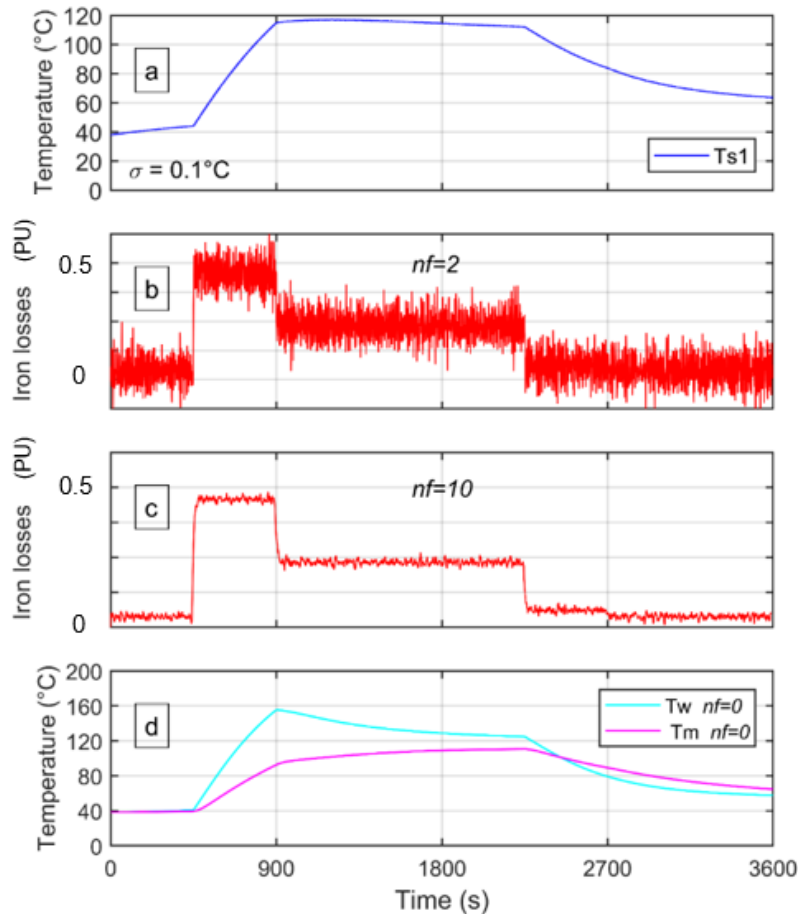


Figure 5.8 : Iron losses identification from sensor T_{s1} with $nf=2$ and $nf=10$ and computation of critical temperatures T_w and T_m .

From this temperature, the inverse problem is solved to identify $P(t) = P_{Iron}(t)$ knowing $K(t) = [P_{Joule} P_{Rotor} P_{Airgap} P_{Bearings}]^T$. Hence, for this case, $n_q = n_U = 1$.

The procedure is sequential, as mentioned before, expressed in equation (5.15), and depends on the number of future time steps. Results of identification are presented in *Figure 5.8b* and *Figure 5.8c* for respectively $nf = 2$ and $nf = 10$. It is remarkable that, without regularization ($nf = 0$), the oscillations of $P_{Iron}(t)$ are huge. Hence, we have chosen to draw $P_{Iron}(t)$ for $nf = 2$ in *Figure 5.8b*.

It appears that the number of future time steps filters the oscillations of P_{Iron} , which is confirmed by the quadratic criterion σ_U in *Table 5.1*. The main criterion, and the only one to be computed in a real case, is σ_Y . Its evolution with respect to nf is quite interesting. For $nf = 0$, even if the problem is ill-posed, large oscillations in \hat{U} allow to follow exactly the evolution of the noisy temperature. Hence, as indicated in *Table 5.1*, $\sigma_Y \approx 0^\circ\text{C}$. When nf increases, regularization tends to damp the time evolution of \hat{U} , leading to a bias in the temperature computation. We choose then the number nf for which $\sigma_Y \geq \sigma$ to “get out” of the noise level. The identification of $P_{Iron}(t)$ for $nf = 10$ is depicted in *Figure 5.8c* and shows a very good agreement with the exact evolution of these losses drawn in *Figure 5.7*.

nf	σ_U (W)	σ_{Ts1} ($^\circ\text{C}$)
0	5303.1	3e-14
2	936.7	0.0871
4	451.3	0.0935
6	304.7	0.0964
8	249.4	0.0988
10	229.2	0.1009
12	224.0	0.1034

Table 5.1 : Inversion results for iron losses identification from Ts1; bold lines correspond to results shown in Figure 5.8.

Once P_{Iron} is identified, the aim is to predict temperatures T_w and T_m in inaccessible parts of the electric motor. They have been computed for the different values of nf and are shown in *Figure 5.8d* for $nf = 0$. Note that for $nf = 0$, temperature prediction occurs without any delay whereas it is executed with a 10 s delay with $nf = 10$ since the time step Δt is equal to 1 s. For any value of nf the temperature evolution in critical zones is the same, since oscillations in \hat{U} are damped by the thermal path and inertia of the system. Same as in equation (5.16), critical temperatures T_w and T_m are compared to the exact temperatures computed with the exact

inputs. For $nf = 0$, a quadratic error $\sigma_{T_{crit}} = 0.003 \text{ }^\circ\text{C}$ is obtained, which gives a very accurate prediction.

Now, a new test is carried out using a second measurement point Ts2 located in the stator. Graphical results are summarized in *Figure 5.9*.

It appears obvious that the oscillations of $P_{Iron}(t)$ decreased compared to *Figure 5.8*, which is confirmed by *Table 5.2* where σ_U goes from 229 W to 200 W for $nf = 10$.

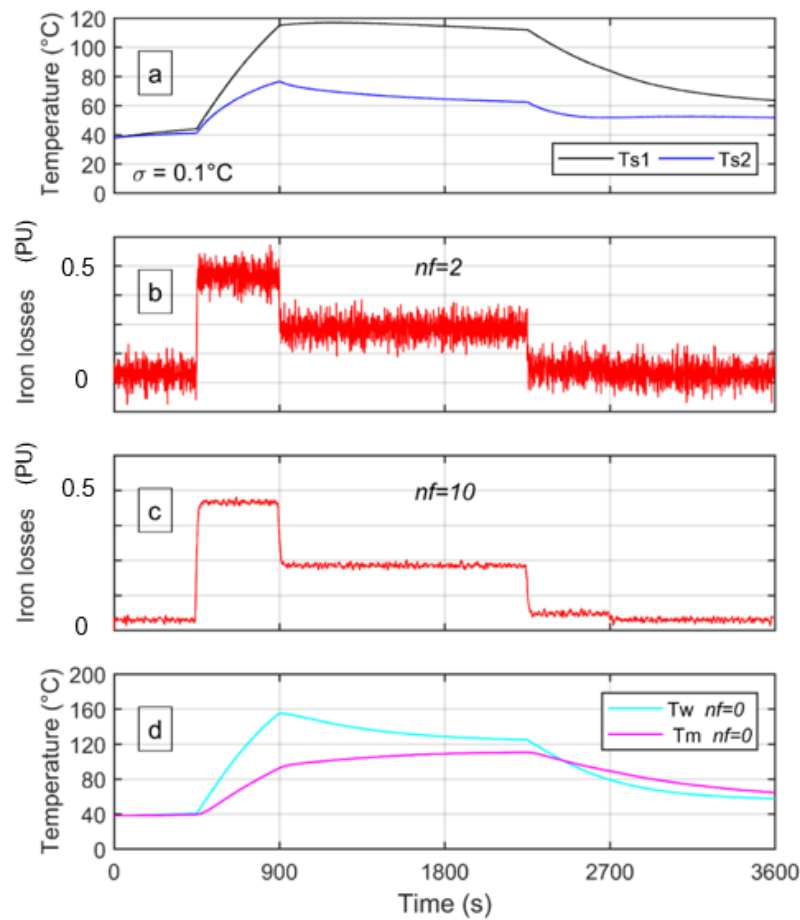


Figure 5.9 : Iron losses identification from sensors Ts1 and Ts2 with $nf=2$ and $nf=10$ and computation of critical temperatures T_w and T_m .

nf	σ_U (W)	σ_{Ts1} ($^{\circ}C$)	σ_{Ts2} ($^{\circ}C$)
0	3713.2	0.0690	0.0700
2	673.8	0.0921	0.0929
4	336.0	0.0957	0.0960
6	237.5	0.0976	0.0975
8	205.1	0.0992	0.0987
10	200.1	0.1011	0.1001
12	205.0	0.1034	0.1020

Table 5.2 : Inversion results for iron losses identification from Ts1 and Ts2; bold lines correspond to results shown in Figure 5.9.

It is interesting to observe that in this case ($n_q = 2$, $n_U = 1$) it is not possible to obtain $\sigma_Y \approx 0^{\circ}C$ for each of the two sensors from only one heat source $P_{Iron}(t)$. The temperature prediction in windings and magnets is also very accurate with an error $\sigma_{Tcrit} = 0.002^{\circ}C$ for $nf = 0$.

5.3.5.2 Identification of Joule and Iron Losses

For the second case, Joule losses (P_{Joule}) are also unknown. The evolutions of $P_{Joule}(t)$ and $P_{Iron}(t)$ have to be identified. Firstly, sensors Ts1 and Tsw located in the stator and at the winding surface are used. It can be remarked in Figure 5.10 and Table 5.3 that both heat sources are well identified when increasing the number of future time steps.

In this case, $nf = 12$ gives $\sigma_Y \geq \sigma$ for each sensor, as calculated in Table 5.3.

The condition number of the matrix $\mathbf{S}^T \mathbf{S}$ to invert is also indicated. It is noteworthy that this last one decreases when the number of future time steps increases, which confirms the regularization effect of the function specification, knowing that in case 1, $\mathbf{S}^T \mathbf{S}$ is a scalar, hence its condition number is equal to 1.

Compared to the first case, the winding temperature is quite sensitive to the oscillations in Joule losses identification, hence the error increases: $\sigma_{Tcrit} = 1.161^{\circ}C$ for $nf = 0$.

On the other hand, by adding two other sensors Ts2 and Ts3, located in the stator, better inversion results are again obtained, as depicted in Figure 5.11 and Table 5.4, since σ_U goes from 200 W to 180 W.

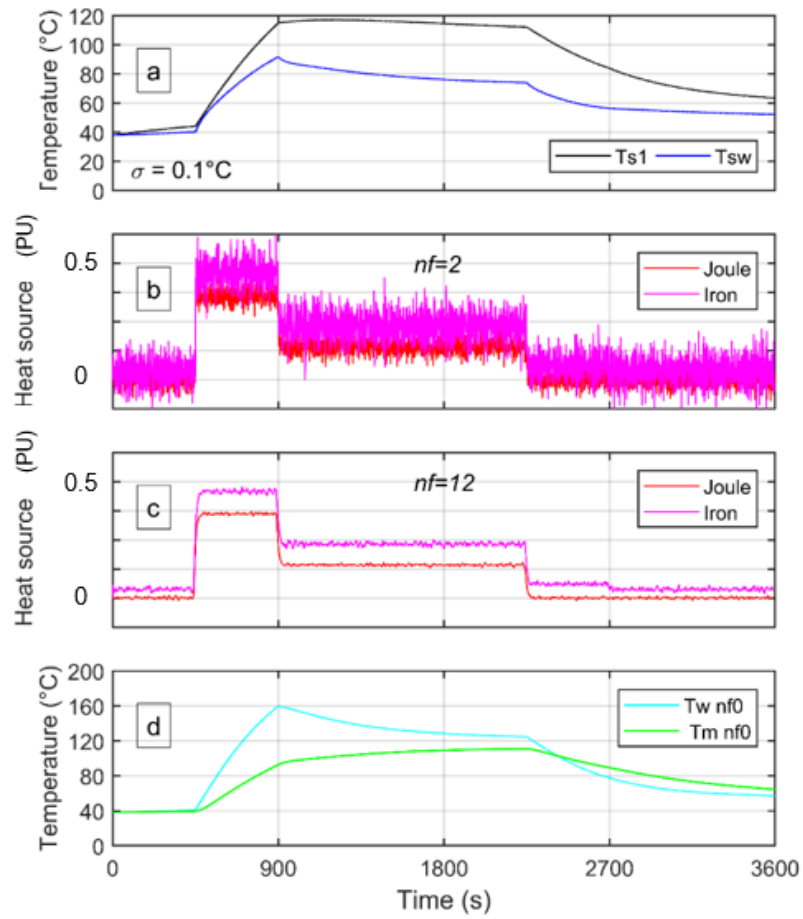


Figure 5.10 : Joule and iron losses identification and computation of critical temperatures from sensors Ts1 and Tsw with $nf=2$ and $nf=12$.

nf	σ_U (W)	σ_{Ts1} (°C)	σ_{Tsw} (°C)	$CN(S^T S)$
0	4125.2	3e-14	6e-15	3.74
2	741.2	0.0859	0.0869	3.64
4	359.2	0.0926	0.0931	3.54
6	246.4	0.0949	0.0971	3.45
8	209.3	0.0970	0.1007	3.36
10	198.9	0.0992	0.1051	3.28
12	200.4	0.1017	0.1104	3.20
14	207.9	0.1047	0.1168	3.12

Table 5.3 : Inversion results for Joule and iron losses identification from Ts1 and Tsw; bold lines correspond to results shown in Figure 5.10.

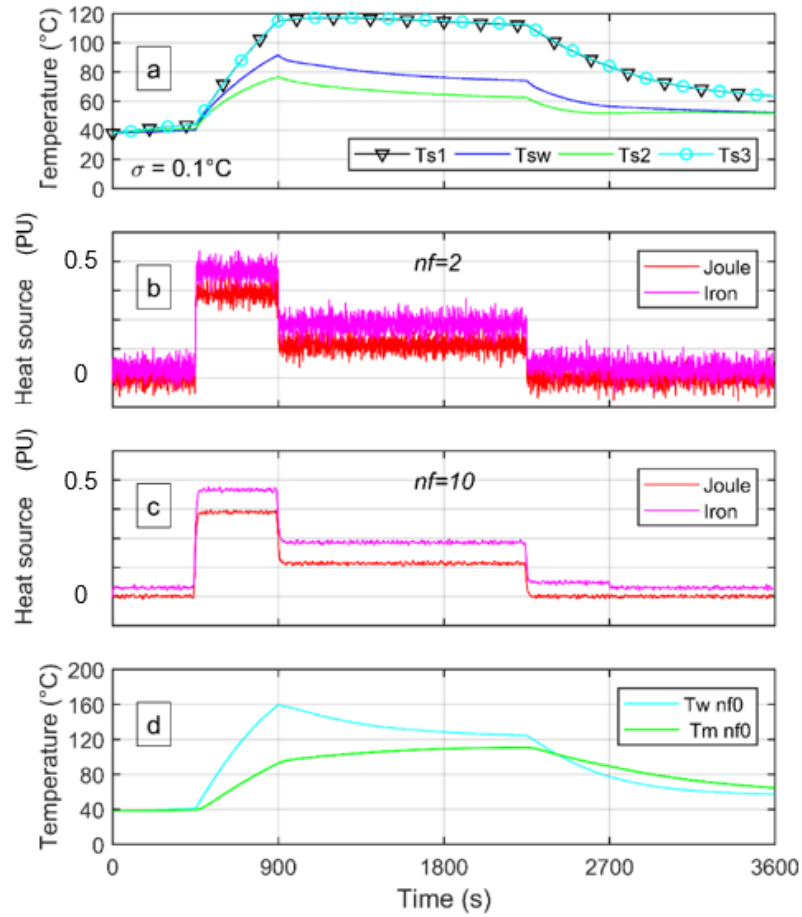


Figure 5.11 : Joule and iron losses identification and computation of critical temperatures from sensors $Ts1$, Tsw , $Ts2$, and $Ts3$ with $nf=2$ and $nf=10$.

nf	σ_U (W)	σ_{Ts1} (°C)	σ_{Tsw} (°C)	σ_{Ts2} (°C)	σ_{Ts3} (°C)	$CN(S^T S)$
0	2849.0	0.0803	3e-5	0.0832	0.0816	1.26
2	518.4	0.0941	0.0867	0.0974	0.0952	1.23
4	262.6	0.0964	0.0937	0.0994	0.0974	1.21
6	194.5	0.0976	0.0975	0.1004	0.0987	1.18
8	179.2	0.0990	0.1012	0.1012	0.0999	1.16
10	180.3	0.1007	0.1055	0.1025	0.1016	1.13
12	188.3	0.1028	0.1109	0.1040	0.1038	1.11

Table 5.4 : Inversion results for Joule and iron losses identification from $Ts1$, Tsw , $Ts2$, and $Ts3$; bold lines correspond to results shown in Figure 5.11.

The addition of sensors acts as a filter in the inversion procedure and the condition number of the matrix $S^T S$ decreases as well. The temperature prediction in windings and magnets remains relatively accurate with an error $\sigma_{Tcrit} = 1.158 \text{ }^\circ\text{C}$ for $nf = 0$.

5.3.5.3 Identification of all Losses

In this third case, the five heat sources altogether are considered unknown and have to be identified simultaneously from five sensors $Ts1$, Tc , Tsw , Ta , and Tb , whose temperature evolutions are given in *Figure 5.12a*.

These sensors are located in the stator, in the cavity, on the surface of the windings, in the airgap, and on the bearings respectively. It can be remarked that the temperature magnitude is very different according to the locations of the sensors.

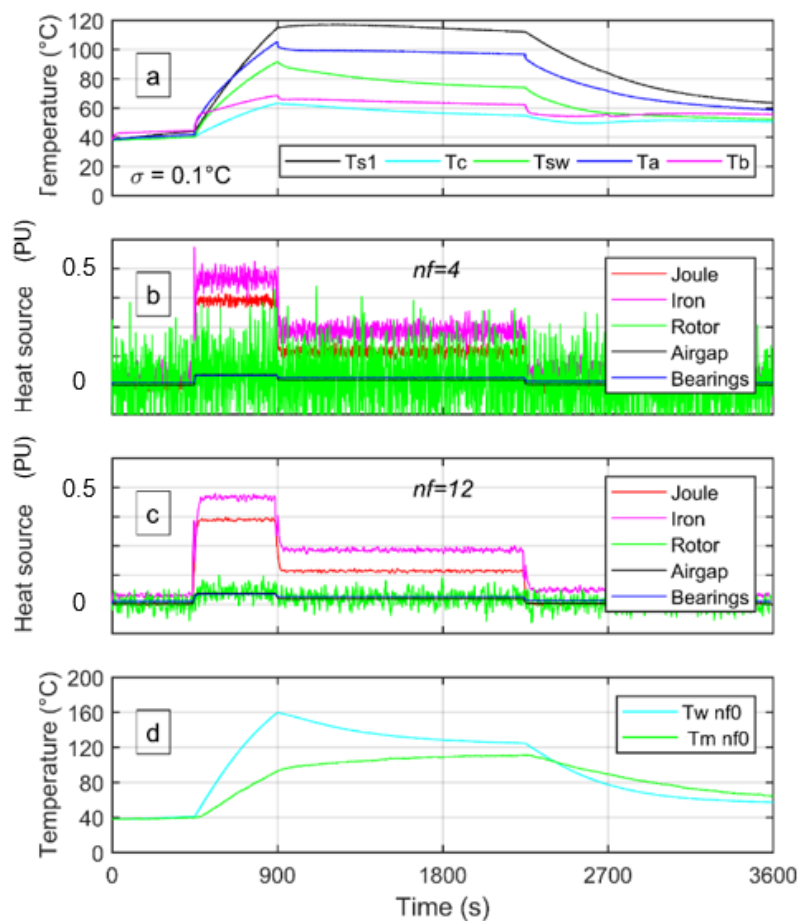


Figure 5.12 : Identification of all the heat sources and computation of critical temperatures from sensors $Ts1$, Tc , Tsw , Ta , and Tb with $nf=4$ and $nf=12$.

As for previous cases, the quadratic errors and the condition number are given in *Table 5.5* with respect to the number of future time steps.

nf	σ_U (W)	σ_{Ts1} ($^{\circ}\text{C}$)	σ_{Tc} ($^{\circ}\text{C}$)	σ_{Tsw} ($^{\circ}\text{C}$)	σ_{Ta} ($^{\circ}\text{C}$)	σ_{Tb} ($^{\circ}\text{C}$)	$CN(S^T S)$
0	11990.5	3e-14	1e-14	6e-15	2e-14	2e-14	2.46e6
2	1859.6	0.0881	0.0861	0.0842	0.1213	0.0876	4.48e5
4	859.3	0.0973	0.0930	0.0913	0.1639	0.0996	1.82e5
6	529.7	0.1038	0.0959	0.0952	0.1982	0.1129	9.90e4
8	382.1	0.1100	0.0975	0.0990	0.2282	0.1295	6.23e4
10	305.8	0.1169	0.0987	0.1037	0.2557	0.1490	4.85e4
12	263.9	0.1243	0.1000	0.1096	0.2816	0.1712	4.29e4
14	240.1	0.1326	0.1014	0.1167	0.3061	0.1950	3.82e4

*Table 5.5 : Inversion results for all losses identification from T_{s1} , T_c , T_{sw} , T_a , and T_b ; bold lines correspond to results shown in *Figure 5.12*.*

In this case, the condition number of the matrix $S^T S$ is very high, hence, the noise in temperature measurements may be greatly amplified by the inverse problem. As in previous cases, $nf = 0$ corresponds to a square case ($n_q = n_U = 5$), thus, even if the problem is ill-posed, large oscillations in \hat{U} allow to follow exactly the noisy temperature evolutions.

Hence, as indicated in *Table 5.5*, $\sigma_Y \approx 0^{\circ}\text{C}$. An increase of nf leads to $\sigma_Y > \sigma$ for all sensors for $nf = 12$. *Figure 5.12c* shows large oscillations in P_{Rotor} due to the fact that the sensors are located far from this heat source. But, these oscillations are damped when increasing nf , as depicted in *Figure 5.12c*.

Concerning the temperature prediction in windings and magnets (*Figure 5.12d*), the error is reasonably acceptable with $\sigma_{T_{crit}} = 1.178^{\circ}\text{C}$ for $nf = 0$.

5.4 Conclusion

In this chapter, the numerical model developed earlier in this work is applied to assess the losses identification in high specific power electric motors design.

Being a critical problem in electric machinery, electric motor losses are major players in temperature evolution. An inverse method has been developed to enable determining these losses based on easily accessed temperatures. Firstly, a sensitivity study of temperatures to losses has been carried out to determine the influence of each losses type on motor thermal behavior to adapt the losses identification procedure.

Then, the low-order Lumped Parameter Thermal Model (LPTM) has been used to solve both inverse and direct problems. The method is sequential and includes regularization with the function specification technique. Different configurations have been tested according to the number of heat sources to be identified. For each case, the influence of the required number of sensors to be used to solve the inverse problem, and the number of future time steps were analyzed.

The technique gives also an accurate prediction of the temperature in unreachable critical parts of the motor and is computationally efficient: only $10^{-3}s$ at each time step is needed for identification of the heat sources and prediction of the motor temperatures.

CHAPTER 6 CONCLUSIONS AND PERSPECTIVES

Synopsis:

*General conclusions are given hereafter, in addition to some perspectives from
academic and industrial points of view.*

6.1 Conclusions

Electric Motors are nowadays crucial systems for different applications in multiple domains. In the recent era of electrification of vehicles, these components have a major role to play. Indeed, to meet the requirements of reaching the aimed reduction in gas emissions and noise, solutions of electrification and hybridization in the transportation sector are proposed.

In the domain of aeronautics, many industries, institutes, and researchers are moving forward on working on a hybrid aircraft with electric motors as a step towards less polluting air transportation means. However, such transition in propulsive power requires detailed and specific studies on electrical and thermal issues. Actually, the aircraft targets in terms of weight are almost not reachable with the existing technologies. On the other hand, electric motor high targets of specific powers and efficiencies are limited by, among other factors, the thermal constraints. Those constraints result from super-high losses induced by such motors and the relatively low allowed maximum temperatures of specific components. In fact, these components' lifetimes are subject to variations at each cycle of overshooting of temperature, leading to a drastic reduction of motor operational time or even a total motor failure. Pushing the technological limits suggests advancements in the motor design and cooling solutions so that the temperatures do not exceed the allowed maximum values.

The framework of this thesis is a CleanSky II project aiming to design propulsive electrical architectures for aircraft with specific targets and multiple Work-Packages. The objective of our Work-Package is the thermal assessment of high specific power electric motors, with high efficiencies, designed in the same framework. These motors are Surface Mounted-Permanent Magnet Synchronous Machines with issues in thermal behavior, in addition to their temperature limits.

First, a state of the art, reviewing thermal characteristics and cooling techniques applied to electric motors, has been elaborated to comprehend the cooling issue and solutions. Based on this review, some methods were selected for their feasibility and adaptability to the motor type and geometry.

A thermal modeling approach based on the nodal network method is adopted to design the motors with their cooling systems. The developed numerical model consisting of a nodal network, of a relatively low number of nodes, allows a rapid assessment of the temperatures and fluxes in the motor. It takes into account the motor electromagnetic and mechanical losses

(Joule losses, iron losses, bearings losses, and windage losses of two types) that generate the heat. The proposed designs of the targeted motors have been tested. The exchanger and the cooling circuit are integrated into the model. Actually, the nacelle surface is used as a cold plate in the heat exchanger. Hence, the boundary conditions in terms of outside temperature at the nacelle external surface are implemented in the model. Besides, the heat sources' dynamic profiles are injected to corresponding nodes where losses occur.

Strong interaction with the Work-Package working on the electromagnetic design of the motor was required to get an optimized distribution of losses in the motor. This interaction has been the topic of several synergies and public contributions.

Motors for two time-target (5 kW/kg then 10 kW/kg of specific powers) were investigated using the developed model, and cooling solutions consisting mainly of a liquid cooling jacket and motor channels were proposed. These investigations allowed reaching relatively optimal designs for the two target motors.

❖ Studies on Electric Motor of 5 kW/kg

For this intermediate specific power value, the motor cooling consists of a liquid shaft channel for rotor heat extraction, a liquid jacket cooling of the stator in the frame structure, and a potting of the end-windings with high thermal conductivity impregnation material. The liquid coolant used is a mixture of Water-Ethylene-Glycol. The resulting temperatures, taking into account the mission dynamical profile, for heat sources injected, and the outside air-temperatures show two different behaviors for rotor and stator components. Other fluids are tested and compared, whereas the first adopted mixture seems to be the most convenient. A scenario of full power application after the aircraft take-off is tested to show the limits of the design and cooling efficiency. Then, a parametric investigation on the heat exchanger's main parameters (coolant flow rates and plate surface) is carried out to verify the optimum operating point. Moreover, a sensitivity study of thermophysical properties to temperatures is performed.

❖ Studies on Electric Motor of 10 kW/kg

For this high specific power motor, simulations show that winding direct cooling is inevitable given the current density (producing high Joule losses) in this confined area. Two motor designs were investigated in *Chapter 4*, one with relatively low Joule losses and high iron and rotor

losses, and the other with comparable levels of Joule and iron losses. The results suggested that the second design is more suitable for the specific power target in terms of cooling system weight since the first design exhibited a serious issue.

❖ Losses Identification through an Inverse Method

Finally, using the elaborated motor thermal model, an inverse method has been developed to enable determining the motor losses based on temperature data at relatively easy-accessed points. First, a sensitivity study of temperatures to losses has been carried out to determine the influence of each losses type on motor thermal behavior to adapt the losses identification procedure. Then, a sequential technique, that uses Beck's function specification for regularization, was developed. Different configurations, with increasing complexity in unknown losses, have been tested. For each of these configurations, the influence of the required number of sensors to be used to solve the inverse problem, and the number of future time steps were analyzed. The method seems efficient in identifying the losses and in predicting temperatures in poorly accessible critical parts.

6.2 Perspectives

Industrial Aspects

❖ Multiphysics model for optimization

The LPTM technique offers a great ability to be adapted to other models since the tool is built by coding concepts and can be combined with the electromagnetic tools and specific environment models. Optimization of the design of the motor or the overall aircraft propulsion architecture can be enabled by such multiphysics models.

❖ Current density product

In collaboration with WP1, the equivalent current density product has been introduced as a constraint for the design of high-specific power electric motors. It takes into account the electromagnetic and thermal issues. A further investigation of this constraint can allow

designing motors of different specific power values or different types (for example the induction motor, or the synchronous motor with wound rotor).

❖ Larger integration of the thermal system

The cooling system could be better integrated into the plane at several levels. For instance, the extracted heat could be used for specific applications such as anti-icing or air-conditioning. Moreover, a single thermal system could be used to cool different systems.

Academic Research Aspects

❖ Validation of the inverse method on an experimental bench

The concept of the technique allowing identifying losses through thermal measurements has been only tested numerically. This first step must be followed by an experimental validation that would take into account issues related to measuring process and uncertainties.

❖ Testing the method on other motor types

The inverse method has been developed for the identification of losses in a Surface Mounted-Permanent Magnet Synchronous Machine. It is possible to test the method on other topologies. However, the method can be adapted to other motor types. With the new field of research on electric motors thermal aspects, the proposed technique interests the electrical machines specialists and motor designers, especially with the lack of other methods that allow the determination of losses or poorly accessed temperatures.

❖ Other regularization technique (drawbacks of the proposed one)

The regularization technique used in this thesis to solve the inverse problem of the identification of heat sources is the Future Time Step (FTS) method. Its only drawback in real-time consists of requiring temperature measurements at subsequent times, which causes a slight delay (depending on the number of FTS) in the identification of unknowns. Hence, it would be very interesting to find other real-time identification methods that allow however minimizing the propagation of the noise in the inversion process.

FUNDING ACKNOWLEDGMENT

This project has received funding from the European Union's Horizon 2020 (Cleansky 2 JTI) research and innovation program, 2014-2024 under grant agreement No 715483.

CHAPTERS' SUMMARIES IN FRENCH

Chapitre 1

La propulsion électrique des moyens de transport connaît récemment un progrès inédit lié à l'intérêt sérieux que portent les acteurs du secteur du transport à réduire les émissions de gaz nocifs et les nuisances sonores. Maintenant que le développement de voitures électriques et hybrides prend une place importante dans le transport terrestre afin de réduire la consommation d'énergie fossiles, vient le tour des avions hybrides électriques.

Outre le défi de passer à une architecture différente de propulsion, les aspects contraignants de l'électrification du secteur du transport aéronautique sont multiples. Effectivement, du fait des limites de poids et de volume des aéronefs, une puissance élevée de moteurs, suffisamment compacts et légers, est exigée. Ces moteurs électriques de propulsion d'avions doivent vérifier alors un cahier des charges contraignant de densités de puissance.

Grâce aux avancées technologiques réalisées sur les matériaux, qui sont de plus en plus adaptés à ces applications, une remarquable nouvelle génération de ces moteurs est en cours de développement.

Pourtant, au vu des forts flux de chaleur dissipés dans ces machines ainsi que des limites de température pour certains de leurs composants, de nouvelles contraintes thermiques apparaissent dans la phase de dimensionnement de machines, et la mise en place d'un système d'extraction de chaleur efficace et optimisé devient inévitable. En effet, au-delà de certaines valeurs critiques de température, le fonctionnement nominal du moteur ne peut plus être assuré.

Le présent travail fait partie d'un projet européen de Clean Sky 2 décomposé en plusieurs Work-Packages (WP) et impliquant de nombreux partenaires des milieux académique et industriel (tels que le laboratoire Laplace et Airbus). Notre partie constitue le WP3 visant en particulier à étudier le comportement thermique de moteurs électriques pour la propulsion d'avions hybrides.

En plus de la performance et du poids, d'autres aspects contraignants des machines électriques apparaissent dans la propulsion aéronautique, que l'on devrait considérer dans ce genre d'étude multiphysique. On peut citer notamment l'altitude, les conditions externes de l'environnement, la sécurité de fonctionnement, les matériaux à proscrire, etc.

Le travail consiste à modéliser le moteur, trouver des techniques de refroidissement adaptées et à optimiser le moteur et son système de refroidissement pour répondre aux cahiers des charges respectivement pour les années 2025 et 2035. Dans cette étude, les conditions de vol en termes de profil de puissance ainsi que de conditions extérieures de température sont considérées.

Chapitre 2

Dans la conception de moteurs électriques à forte densité de puissance, du fait de l'existence de points chauds critiques, le choix de techniques de refroidissement adaptées est incontournable. Ce choix est fait en se basant sur l'étude des aspects thermiques dans la machine ainsi que sur les méthodes d'extraction de chaleur possibles, ce que l'on va appeler management thermique du moteur.

Une étude bibliographique est détaillée dans le *Chapitre 2* portant sur la thermique du moteur électrique. Cette étude a été développée de la manière la plus exhaustive possible pour la création d'un rapport complet sur le management thermique de ces machines. Pour cela, une partie du chapitre est dédiée au transfert de chaleur ayant lieu à l'intérieur, comme autour de la machine par différents modes. Ensuite, les approches classiques de refroidissement de moteurs électriques à haute densité de puissance ainsi que les dernières innovations sur ce sujet sont présentées.

Les études concernent parfois des moteurs de densités de puissance relativement faibles, mais qui présentent suffisamment de similarités avec les moteurs de plus fortes densités de puissance pour que leurs études restent intéressantes.

Cet état de l'art a notamment permis de classer les méthodes de refroidissement en deux catégories : le refroidissement global de toute la machine et le refroidissement spécifique de certains composants.

Une attention particulière a été accordée aux parties du moteur qui sont sensibles à la température, et où un refroidissement global ne serait pas suffisamment efficace.

L'état de l'art sur la thermique du moteur électrique est divisé en 3 grands paragraphes :

- i. Le transfert par conduction dans les composants du moteur ;

- ii. Le transfert par convection, particulièrement dans l'entrefer entre le rotor et le stator et sur les têtes de bobines ;
- iii. Les méthodes de refroidissement connues et classiquement utilisées dans ces machines ainsi que celle considérées prometteuses et qui sont en cours d'évaluation pour des applications futures.

Ce chapitre a permis de trouver les technologies de refroidissement les plus prometteuses pour notre application. Un point important à signaler est que le refroidissement doit être adapté au design du moteur. Enfin, le refroidissement liquide, assurant une extraction de chaleur significativement plus importante que le refroidissement par air, est fortement suggéré pour refroidir des points chauds internes du moteur notamment les têtes de bobines et les aimants afin de pouvoir atteindre des densités de puissances élevées.

Chapitre 3

Le Chapitre 3 présente la méthode de travail choisie pour l'étude des moteurs électriques des objectifs 2025 et 2035 du projet.

Parmi les différentes techniques de modélisation thermique, la méthode nodale ou LPTM (pour Lumped Parameter Thermal Model) a été considérée comme la plus adaptée à la modélisation et à l'étude du comportement thermique de nos moteurs électriques et de leurs systèmes de refroidissement. Cette méthode permet de résoudre l'équation de la chaleur en régimes transitoire et permanent en discrétisant spatialement le système à étudier. Elle se base sur l'analogie entre les quantités électriques et thermiques et permet une représentation de la thermique par des composants électrique (conductances, condensateurs...).

Dans la pratique, cette méthode consiste à définir des nœuds correspondants à chaque volume discrétisé du moteur. Chacun de ses nœuds est affecté une capacité thermique et, le cas échéant, une source ou un puits de chaleur. Les nœuds sont connectés les uns aux autres par des conductances thermiques représentant les échanges de chaleur entre nœuds adjacents. Un réseau nodal peut être désormais créé.

La structure des moteurs à étudier est du type synchrone à aimants permanents. Dans ce cadre, les entrées thermiques sont de plusieurs natures : les pertes dans le moteur (Joule, fer, roulements, entrefer, flasques du rotor) fonction du profil de puissance, ainsi que la température

et les échanges avec l'extérieur. Ces entrées thermiques variant dans le temps seront considérées afin d'étudier le comportement en régime transitoire du moteur durant un vol type.

Partant de certaines hypothèses et considérations relatives à la géométrie et aux spécificités du moteur électrique en question (comme l'axisymétrie au niveau du rotor du fait de l'homogénéité des matériaux dans la direction azimutale, la périodicité au niveau du stator, etc.), un nombre réduit de nœuds (57 à 62 nœuds) est utilisé pour modéliser le moteur et son système de refroidissement.

Une fois les matrices de capacités thermiques et de conductances thermiques, et le vecteur des sollicitations thermiques assemblés, le modèle devient un système de N équations différentielles ordinaires en temps, où N est le nombre de nœuds de la discrétisation spatiale.

La méthode de résolution par Euler implicite est utilisée pour trouver la distribution de températures dans la machine. La modélisation est effectuée sous le logiciel Matlab, et un modèle appelé *AThEM* se basant sur le LPTM est développé.

Afin de valider le code, les résultats de simulation du modèle sont comparés à des résultats expérimentaux issues d'essais sur un moteur similaire à ceux envisagées pour la propulsion aéronautique avec un refroidissement liquide autour du moteur. Pour le point de fonctionnement du moteur considéré, le maximum d'écart entre les températures simulées et les températures expérimentales est de 3,2% ($\sim 1,8$ °C) au niveau des têtes de bobines et dans le bobinage, ce qui permet de valider les hypothèses faites lors de la modélisation.

Des modèles similaires vont être utilisés dans le chapitre suivant pour simuler le comportement thermique des moteurs propulsifs envisagés pour l'avion hybride (à échéance 2025 et 2035).

Chapitre 4

Une procédure itérative a été mise en place avec le Work-Package 1 (WP1), qui s'occupe de l'électrotechnique du moteur, du fait du fort couplage électrotechnique/thermique nécessaire à l'optimisation des moteur notamment en terme de densité de puissance (kW/kg).

Au modèle précédemment validé de moteur synchrone à aimants permanents (type choisi pour nos moteurs), une extension comprenant tout le circuit de refroidissement et notamment l'échangeur permettant au liquide de refroidissement d'évacuer vers l'air extérieur la chaleur prise au moteur a été développée. En effet, d'une part, le poids du système de refroidissement

doit être pris en compte dans la densité de puissance. D'autre part, du fait de notre modélisation en régime transitoire, son inertie doit être prise en compte. Un vol complet fourni par Airbus est simulé, allant du taxi-out au taxi-in avec une phase de décollage de quelques minutes où la puissance requise du moteur est à 100% de la valeur nominale. Cette phase est suivie d'une phase de montée durant laquelle on observe une décroissance de la puissance jusqu'à environ 78% de la puissance maximale requise, et à la fin de laquelle une chute de puissance aux alentours de 50% correspond à la phase de croisière.

Pour le premier objectif du projet (pour l'année 2025), le moteur a une densité de puissance de 5 kW/kg . Après plusieurs itérations avec le WP1, un design optimal et des stratégies de refroidissement adéquates sont considérés pour le moteur électrique. Un double refroidissement par canaux d'eau glycolée au niveau de la carcasse du stator et dans l'arbre du rotor, ainsi qu'un encapsulant sur les têtes de bobines ont donné des résultats satisfaisants pour maintenir les températures du moteur en dessous des valeurs seuils critiques. La température maximale durant ce vol est atteinte à la fin de la phase de montée, et est obtenue aux têtes de bobines et aux bobinages. Les températures maximales au rotor sont décalées par rapport à celle du stator. Nous avons pu maintenir les températures en-dessous des valeurs seuils critiques en jouant sur l'inertie du moteur et sa variation de puissance ainsi que sur la baisse de température extérieure durant la montée.

Une optimisation du poids du système de refroidissement a permis également d'atteindre la densité de puissance demandée dans le cahier des charges. Des études de sensibilité sont menées sur ce modèle pour évaluer l'influence de certains paramètres thermophysiques et électriques sur le maximum de températures à l'intérieur de la machine.

Plusieurs designs de moteurs ont été également étudiés pour le second objectif du projet pour 2035 afin de trouver un dimensionnement adapté permettant d'avoir une densité de puissance doublée de 10 kW/kg . La machine choisie est assez similaire au moteur précédent (celui de l'année 2025) en termes de pertes et de caractéristiques physiques. Cette machine a une densité de pertes plus importante que la précédente et alors présente des températures plus élevées si on utilise le même refroidissement. Nous avons donc adapté notre système de refroidissement de façon à compenser cette augmentation, en rapprochant l'écoulement liquide d'une source principale de pertes localisées au niveau du bobinage et des têtes de bobines. Ainsi, un troisième circuit de refroidissement en contact avec le bobinage a été choisi constitué par des canaux dans les encoches du stator. En conséquence, le système de refroidissement choisi est formé par le double refroidissement du stator (externe) et du rotor (dans l'arbre) précédemment considéré,

et d'un circuit de refroidissement avec du liquide dans le bobinage. Nous avons alors été amenés à modifier notre modèle LPTM au travers de nœuds supplémentaires pour intégrer les canaux du bobinage. D'autre part, ce système a rendu inefficace la présence d'encapsulant qui ne sera plus considéré pour ce moteur. Les températures trouvées à partir du modèle numérique sont parfaitement acceptables, surtout au niveau des zones critiques. Finalement, la cible de 10 kW/kg en densité de puissance pour ce design de moteur a pu être satisfaite.

Chapitre 5

Après avoir développé le code du modèle numérique du moteur en adaptant et intégrant le refroidissement et après avoir obtenu les résultats en termes de températures du moteur en simulation directe, nous allons nous intéresser dans ce dernier chapitre à une extension de l'utilisation du LPTM. Il s'agit d'estimer les puissances dissipées dans le système à partir de quelques observables en températures par résolution d'un problème inverse. Dans un second temps, ces pertes estimées serviront à calculer les températures à des endroits inaccessibles à la mesure.

Il s'agit ici de profiter du faible nombre de degrés de liberté du LPTM afin de résoudre le problème inverse en temps réel.

A partir du vecteur de température complet, quelques observables vont être choisis convenablement et ensuite bruités pour reproduire une mesure expérimentale. Ces températures seront utilisées à travers le LPTM pour identifier les entrées inconnues qui sont les pertes dans ce cas. Mathématiquement, ce problème inverse est délicat à résoudre. Il est dit mal posé car sa solution n'est pas unique, ni stable en particulier avec un bruit de mesure.

Par conséquent, il a été nécessaire eu nécessité d'adjoindre une méthode de régularisation. Pour cela, parmi les techniques existantes, la méthode des pas de temps futurs de Beck très bien adaptée à la résolution séquentielle a été choisie. Trois cas de configurations, de complexité croissante allant jusqu'à chercher toutes les pertes simultanément, sont étudiés et montrent la fiabilité de la méthode pour l'identification des pertes du moteur. Cela permet de remonter aux températures inaccessibles dans le moteur, via le LPTM. Dans chaque cas, l'influence des pas de temps futurs est étudiée.

Finalement, les résultats trouvés sont très satisfaisants et la procédure d'identification est très rapide à chaque itération, ce qui rend la technique « temps réel ». Le temps nécessaire pour chaque itération est de 10^{-3} s.

Chapitre 6

Cette thèse s'intéresse à la gestion thermique de moteurs électriques de fortes densités de puissance, appliqués à la motorisation électrique des avions hybrides. Elle s'inscrit dans le projet européen de Clean Sky2 appelé HASTECS, qui porte sur l'hybridation d'avions futurs à travers le développement d'outils électrothermiques et l'étude de différentes architectures hybrides avec des objectifs respectifs pour les années 2025 et 2035.

Etant donné les densités de puissance très élevées des moteurs électriques de propulsion, ces derniers dissipent de fortes densités de puissance qu'il faut évacuer efficacement. Ce travail concerne alors la conception de moteurs avec leurs systèmes de refroidissement. La gestion thermique comprend alors une étape de création du modèle du moteur pour simuler son comportement thermique et une étape de choix de solutions et techniques de refroidissement adaptées ainsi que leur intégration au modèle.

La thèse est composée de 5 chapitres comme suit :

Premièrement, le sujet et ses contours sont présentés afin de créer une base scientifique pour le travail et permettre de comprendre les problématiques à résoudre.

Ensuite, une recherche bibliographique a permis de construire un état de l'art sur le transfert de chaleur et les techniques de refroidissement, ainsi que d'évaluer les solutions prometteuses pour extraire la chaleur des moteurs.

La modélisation du moteur est présentée dans le troisième chapitre. Elle a permis d'obtenir des températures dans le moteur en fonction des conditions initiales et des conditions aux limites à partir de la simulation du modèle de base.

Les moteurs des deux objectifs d'avions hybrides sont maintenant modélisés et un design optimal pour chacun est déterminé après échange avec les spécialistes de moteurs électriques. Les cahiers des charges contraignants sont respectés en termes de densité de puissance.

Enfin, une méthode inverse a été développée pour l'identification des pertes dans le moteur et pour la supervision de températures inaccessibles à la mesure, surtout aux points chauds critiques du moteur.

BIBLIOGRAPHY

- [1] “Average temperature anomaly,” *Our World in Data*. <https://ourworldindata.org/grapher/temperature-anomaly> (accessed Oct. 24, 2019).
- [2] “Scientific Consensus: Earth’s Climate is Warming,” *Climate Change: Vital Signs of the Planet*. <https://climate.nasa.gov/scientific-consensus> (accessed Jul. 20, 2020).
- [3] “Global Warming,” Jun. 03, 2010. <https://earthobservatory.nasa.gov/features/GlobalWarming/page5.php> (accessed Jan. 22, 2020).
- [4] “Global Energy & CO2 Status Report 2019 – Analysis,” *IEA*. <https://www.iea.org/reports/global-energy-and-co2-status-report-2019> (accessed Jan. 22, 2020).
- [5] “Environment,” *Airbus*. <https://www.airbus.com/company/sustainability/environment.html> (accessed Jul. 20, 2020).
- [6] “SUNSEEKER II,” *Solar Flight*. <https://www.solar-flight.com/sunseeker-ii/> (accessed Oct. 24, 2019).
- [7] “Taurus Electro – Pipistrel.” <https://www.pipistrel-aircraft.com/aircraft/electric-flight/taurus-electro/> (accessed Oct. 24, 2019).
- [8] Siemens, “Electric propulsion components with high power densities for aviation,” presented at the Transformative Vertical Flight Workshop, Mar. 08, 2015.
- [9] “Rolls-Royce unveils all-electric YASA powered plane targeting the record books | YASA Limited.” https://www.yasa.com/news/rolls-royce_accel_unveiling/ (accessed Dec. 30, 2019).
- [10] “magniX and AeroTEC Announce Successful First Flight of the World’s Largest All-Electric Aircraft,” *AeroTEC*, May 28, 2020. <https://www.aerotec.com/magnix-and-aerotec-announce-successful-first-flight-of-the-worlds-largest-all-electric-aircraft/> (accessed Jul. 19, 2020).
- [11] “ZUNUM Aero – JetBlue Technology Ventures.” <https://www.jetblueventures.com/portfolio/zunum-aero/> (accessed Oct. 24, 2019).
- [12] J. Welstead and J. L. Felder, “Conceptual Design of a Single-Aisle Turboelectric Commercial Transport with Fuselage Boundary Layer Ingestion,” presented at the 54th AIAA Aerospace Sciences Meeting, San Diego, California, USA, Jan. 2016, doi: 10.2514/6.2016-1027.
- [13] K. R. Antcliff and F. M. Capristan, “Conceptual Design of the Parallel Electric-Gas Architecture with Synergistic Utilization Scheme (PEGASUS) Concept,” in *18th AIAA/ISSMO Multidisciplinary Analysis and Optimization Conference*, American Institute of Aeronautics and Astronautics.
- [14] “Airbus Group Electrical Aircraft Program, The E-Fan Project | AIAA Propulsion and Energy Forum.” <https://arc.aiaa.org/doi/abs/10.2514/6.2016-4613> (accessed Oct. 23, 2019).
- [15] “E-Fan X,” *Airbus*. <https://www.airbus.com/innovation/future-technology/electric-flight/e-fan-x.html> (accessed Dec. 11, 2019).
- [16] S. Beganovic, “Comparison of Dynamic Characteristics of Electric and Conventional Road Vehicles,” Sep. 2012, pp. 149–155, Accessed: Feb. 04, 2020. [Online]. Available: https://www.academia.edu/3401454/Comparison_of_Dynamic_Characteristics_of_Electric_and_Conventional_Road_Vehicles.
- [17] Environmental Potentials, “Reducing Slip Losses in Motors,” 2009. http://ep2000.com/uploads/EP_WhitePaper-SlipLosses.pdf (accessed Jan. 03, 2020).

- [18] B. R. Teare, "Theory of hysteresis-motor torque," *Electrical Engineering*, vol. 59, no. 12, pp. 907–912, Dec. 1940, doi: 10.1109/EE.1940.6435257.
- [19] F. Un-Noor, S. Padmanaban, L. Mihet-Popa, M. N. Mollah, and E. Hossain, "A Comprehensive Study of Key Electric Vehicle (EV) Components, Technologies, Challenges, Impacts, and Future Direction of Development," *Energies*, vol. 10, no. 8, p. 1217, Aug. 2017, doi: 10.3390/en10081217.
- [20] J. de Santiago *et al.*, "Electrical Motor Drivelines in Commercial All-Electric Vehicles: A Review," *IEEE Transactions on Vehicular Technology*, vol. 61, no. 2, pp. 475–484, Feb. 2012, doi: 10.1109/TVT.2011.2177873.
- [21] A. M. Bazzi, "Electric machines and energy storage technologies in EVs and HEVs for over a century," in *2013 International Electric Machines Drives Conference*, May 2013, pp. 212–219, doi: 10.1109/IEMDC.2013.6556255.
- [22] A. M. Bazzi, Y. Liu, and D. S. Fay, "Electric Machines and Energy Storage: Over a Century of Technologies in Electric and Hybrid Electric Vehicles," *IEEE Electrification Magazine*, vol. 6, no. 3, pp. 49–53, Sep. 2018, doi: 10.1109/MELE.2018.2849900.
- [23] B. Sarlioglu, C. T. Morris, D. Han, and S. Li, "Benchmarking of electric and hybrid vehicle electric machines, power electronics, and batteries," in *2015 Intl Aegean Conference on Electrical Machines Power Electronics (ACEMP), 2015 Intl Conference on Optimization of Electrical Electronic Equipment (OPTIM) 2015 Intl Symposium on Advanced Electromechanical Motion Systems (ELECTROMOTION)*, Sep. 2015, pp. 519–526, doi: 10.1109/OPTIM.2015.7426993.
- [24] T. Burress and S. Campbell, "Benchmarking EV and HEV power electronics and electric machines," in *2013 IEEE Transportation Electrification Conference and Expo (ITEC)*, Jun. 2013, pp. 1–6, doi: 10.1109/ITEC.2013.6574498.
- [25] B. Bilgin *et al.*, "Making the Case for Electrified Transportation," *IEEE Transactions on Transportation Electrification*, vol. 1, no. 1, pp. 4–17, Jun. 2015, doi: 10.1109/TTE.2015.2437338.
- [26] N. Zabihi and R. Gouws, "A review on switched reluctance machines for electric vehicles," in *2016 IEEE 25th International Symposium on Industrial Electronics (ISIE)*, Jun. 2016, pp. 799–804, doi: 10.1109/ISIE.2016.7744992.
- [27] A. Cassidy, *English: Cutaway view of the electric motor which powers the Tesla Model S*. 2013.
- [28] R. Benlamine, F. Dubas, C. Espanet, S. A. Randi, and D. Lhotellier, "Design of an Axial-Flux Interior Permanent-Magnet Synchronous Motor for Automotive Application: Performance Comparison with Electric Motors Used in EVs and HEVs," in *2014 IEEE Vehicle Power and Propulsion Conference (VPPC)*, Oct. 2014, pp. 1–6, doi: 10.1109/VPPC.2014.7007043.
- [29] J. M. Miller, "Oak Ridge National Laboratory Annual Progress Report for the Power Electronics and Electric Motors Program," 2013. [Online]. Available: <https://info.ornl.gov/sites/publications/files/Pub46377.pdf>.
- [30] T. de Paula Machado Bazzo, J. F. Kölzer, R. Carlson, F. Wurtz, and L. Gerbaud, "Multiphysics Design Optimization of a Permanent Magnet Synchronous Generator," *IEEE Transactions on Industrial Electronics*, vol. 64, no. 12, pp. 9815–9823, Dec. 2017, doi: 10.1109/TIE.2017.2726983.
- [31] K. Farsane, P. Desevaux, and P. K. Panday, "Experimental study of the cooling of a closed type electric motor," *Applied Thermal Engineering*, vol. 20, no. 14, pp. 1321–1334, Oct. 2000, doi: 10.1016/S1359-4311(99)00094-0.
- [32] A. F. Mills, *Heat Transfer*. Englewood Cliffs, NJ: Prentice-Hall, 1999.
- [33] Incropera and De Witt, *Fundamentals of heat and mass transfer*. Johny Wiley Sons, 1985.

- [34] C. Cezário, M. Verardi, S. Borges, J. Silva, A. Antônio, and M. Oliveira, “Transient thermal analysis of an induction electric motor,” presented at the 18th International Congress of Mechanical Engineering, Ouro Preto, MG, Nov. 2005.
- [35] S. Nategh, A. Krings, O. Wallmark, and M. Leksell, “Evaluation of Impregnation Materials for Thermal Management of Liquid-Cooled Electric Machines,” *IEEE Transactions on Industrial Electronics*, vol. 61, no. 11, pp. 5956–5965, Nov. 2014, doi: 10.1109/TIE.2014.2308151.
- [36] S. Nategh, Z. Huang, A. Krings, O. Wallmark, and M. Leksell, “Thermal Modeling of Directly Cooled Electric Machines Using Lumped Parameter and Limited CFD Analysis,” *IEEE Transactions on Energy Conversion*, vol. 28, no. 4, pp. 979–990, Dec. 2013, doi: 10.1109/TEC.2013.2283089.
- [37] M. rabie Guéchi, “Etude numérique et expérimentale du refroidissement de moteurs de traction électriques,” 2014.
- [38] “SIMOTICS Motors,” *siemens.com Global Website*. <https://new.siemens.com/global/en/products/drives/electric-motors.html> (accessed May 05, 2020).
- [39] M. Popescu, D. Staton, A. Boglietti, A. Cavagnino, D. Hawkins, and J. Goss, “Modern heat extraction systems for electrical machines - A review,” in *2015 IEEE Workshop on Electrical Machines Design, Control and Diagnosis (WEMDCD)*, Mar. 2015, pp. 289–296, doi: 10.1109/WEMDCD.2015.7194542.
- [40] Y. Alhassoun, “Étude et mise en oeuvre de machines à aimantation induite fonctionnant à haute vitesse,” thesis, Toulouse, INPT, 2005.
- [41] C. Henaux, B. Nogarede, and D. Harribey, “A New Concept of Modular Permanent Magnet and Soft Magnetic Compound Motor Dedicated to Widespread Application,” *IEEE Transactions on Magnetics*, vol. 48, no. 6, pp. 2035–2043, Jun. 2012, doi: 10.1109/TMAG.2011.2181530.
- [42] J. D. Widmer, R. Martin, and M. Kimiabeigi, “Electric vehicle traction motors without rare earth magnets,” *Sustainable Materials and Technologies*, vol. 3, pp. 7–13, Apr. 2015, doi: 10.1016/j.susmat.2015.02.001.
- [43] A. Fasquelle, “Contribution à la modélisation multi-physique : électro-vibro-acoustique et aérothermique de machines de traction,” Nov. 2007, Accessed: Oct. 16, 2019. [Online]. Available: <https://tel.archives-ouvertes.fr/tel-00196574>.
- [44] F. Kreith, R. M. Manglik, and M. S. Bohn, *Principles of heat transfer, 7th edition*, Cengage Learning, Inc. 2011.
- [45] D. A. Staton and A. Cavagnino, “Convection Heat Transfer and Flow Calculations Suitable for Electric Machines Thermal Models,” *IEEE Transactions on Industrial Electronics*, vol. 55, no. 10, pp. 3509–3516, Oct. 2008, doi: 10.1109/TIE.2008.922604.
- [46] D. A. Howey, A. S. Holmes, and K. R. Pullen, “Measurement and CFD Prediction of Heat Transfer in Air-Cooled Disc-Type Electrical Machines,” *IEEE Transactions on Industry Applications*, vol. 47, no. 4, pp. 1716–1723, Jul. 2011, doi: 10.1109/TIA.2011.2156371.
- [47] Y. Bertin, “Refroidissement des machines électriques tournantes,” *Techniques de l'ingénieur Généralités sur les machines électriques tournantes*, vol. base documentaire : TIB250DUO., no. ref. article : d3460, 1999, [Online]. Available: <https://www.techniques-ingenieur.fr/base-documentaire/energies-th4/generalites-sur-les-machines-electriques-tournantes-42250210/refroidissement-des-machines-electriques-tournantes-d3460/>.
- [48] M. Nili-Ahmadabadi and H. Karrabi, “Heat transfer and flow region characteristics study in a non-annular channel between rotor and stator,” *Thermal Science*, vol. 16, no. 2, pp. 593–603, 2012.
- [49] M. Fénot, Y. Bertin, E. Dorignac, and G. Lalizel, “A review of heat transfer between concentric rotating cylinders with or without axial flow,” *International Journal of Thermal*

- Sciences*, vol. 50, no. 7, pp. 1138–1155, Jul. 2011, doi: 10.1016/j.ijthermalsci.2011.02.013.
- [50] B. Assaad, “Contribution à la prise en compte des aspects thermiques des machines électriques dans un environnement mécatronique,” Ph.D. Thesis, UTC, 2015.
- [51] G. I. Taylor, “Stability of a viscous liquid contained between two rotating cylinders,” *Philosophical Transactions of the Royal Society of London. Series A, Containing Papers of a Mathematical or Physical Character*, vol. 223, no. 605–615, pp. 289–343, Jan. 1923, doi: 10.1098/rsta.1923.0008.
- [52] D. Coles, “Transition in circular Couette flow,” *Journal of Fluid Mechanics*, vol. 21, no. 3, pp. 385–425, Mar. 1965, doi: 10.1017/S0022112065000241.
- [53] C. Gazley, “Heat-Transfer Characteristics of the Rotational and Axial Flow Between Concentric Rotating Cylinders,” *Transactions ASME*, vol. 80, pp. 79–90, 1958.
- [54] F. Tachibana and S. Fukui, “Convective Heat Transfer of the Rotational and Axial Flow between Two Concentric Cylinders,” *Bulletin of JSME*, vol. 7, no. 26, pp. 385–391, 1964, doi: 10.1299/jsme1958.7.385.
- [55] K. M. Becker and J. Kaye, “The Influence of a Radial Temperature Gradient on the Instability of Fluid Flow in an Annulus With an Inner Rotating Cylinder,” *J. Heat Transfer*, vol. 84, no. 2, pp. 106–110, May 1962, doi: 10.1115/1.3684306.
- [56] I. S. Bjorklund and W. M. Kays, “Heat Transfer Between Concentric Rotating Cylinders,” *J. Heat Transfer*, vol. 81, no. 3, pp. 175–183, Aug. 1959, doi: 10.1115/1.4008173.
- [57] B. T. Nijaguna and B. Mathiprakasam, “HEAT TRANSFER IN AN ANNULUS WITH SPIRAL FLOWS,” presented at the International Heat Transfer Conference 7, 1982, doi: 10.1615/IHTC7.1540.
- [58] M. Bouafia, Y. Bertin, J. B. Saulnier, and P. Ropert, “Analyse expérimentale des transferts de chaleur en espace annulaire étroit et rainuré avec cylindre intérieur tournant,” *International Journal of Heat and Mass Transfer*, vol. 41, no. 10, pp. 1279–1291, May 1998, doi: 10.1016/S0017-9310(97)00317-7.
- [59] M. Bouafia, A. Ziouchi, Y. Bertin, and J.-B. Saulnier, “Étude expérimentale et numérique des transferts de chaleur en espace annulaire sans débit axial et avec cylindre intérieur tournant,” *International Journal of Thermal Sciences*, vol. 38, no. 7, pp. 547–559, Jul. 1999, doi: 10.1016/S0035-3159(99)80035-X.
- [60] F. Tachibana, S. Fukui, and H. Mitsumura, “Heat Transfer in an Annulus with an Inner Rotating Cylinder,” *Bulletin of JSME*, vol. 3, no. 9, pp. 119–123, 1960, doi: 10.1299/jsme1958.3.119.
- [61] G. I. Taylor, “Statistical Theory of Turbulence,” *Proceedings of the Royal Society of London. Series A, Mathematical and Physical Sciences*, vol. 151, no. 873, pp. 421–444, 1935.
- [62] S. Harmand, J. Pellé, S. Poncet, and I. V. Shevchuk, “Review of fluid flow and convective heat transfer within rotating disk cavities with impinging jet,” *International Journal of Thermal Sciences*, vol. 67, pp. 1–30, May 2013, doi: 10.1016/j.ijthermalsci.2012.11.009.
- [63] I. V. Shevchuk, “Convective heat and mass transfer in rotating disk systems,” *Springer Verlag*, Berlin, Heidelberg, pp. 1–239, 2009.
- [64] Cz. O. Popiel and L. Bogusławski, “Local heat-transfer coefficients on the rotating disk in still air,” *International Journal of Heat and Mass Transfer*, vol. 18, no. 1, pp. 167–170, Jan. 1975, doi: 10.1016/0017-9310(75)90020-4.
- [65] C. J. Elkins and J. K. Eaton, “Heat transfer in the rotating disk boundary layer,” Stanford University, Department of Mechanical Engineering, Thermosciences Division Report TSD-103, 1997.
- [66] G. Cardone, T. Astarita, and G. M. Carlomagno, “Infrared heat transfer measurements on rotating disk,” *Optical Diagnostics in Engineering 1*, pp. 1–7, 1996.

- [67] F. Kreith, "Convection Heat Transfer in Rotating Systems," in *Advances in Heat Transfer*, vol. 5, T. F. Irvine and J. P. Hartnett, Eds. Elsevier, 1969, pp. 129–251.
- [68] J. W. Daily and R. E. Nece, "Chamber Dimension Effects on Induced Flow and Frictional Resistance of Enclosed Rotating Disks," *J. Basic Eng*, vol. 82, no. 1, pp. 217–230, Mar. 1960, doi: 10.1115/1.3662532.
- [69] C. Vasilescu, "Modélisation du transfert de chaleur au sein des machines électriques tournantes: dimensionnement et optimisation de leur système de refroidissement," Université Paris 6, 2003.
- [70] E. Schubert, "Heat transfer coefficients at end winding and bearing covers of enclosed asynchronous machines," *Elektrie*, vol. 22, pp. 160–162, 1968.
- [71] D. Staton, A. Boglietti, and A. Cavagnino, "Solving the More Difficult Aspects of Electric Motor Thermal Analysis in Small and Medium Size Industrial Induction Motors," *IEEE Transactions on Energy Conversion*, vol. 20, no. 3, pp. 620–628, Sep. 2005, doi: 10.1109/TEC.2005.847979.
- [72] A. Di Gerlando and I. Vistoli, "Improved thermal modelling of induction motors for design purposes," in *1993 Sixth International Conference on Electrical Machines and Drives (Conf. Publ. No. 376)*, Sep. 1993, pp. 381–386.
- [73] O. Oslejsek, "The cooling of the endwindings of small enclosed electric machines," *Elektrotech*, vol. 61, no. 10, 1972.
- [74] C. Micallef, "End winding cooling in electric machines," 2006. <http://eprints.nottingham.ac.uk/10260/> (accessed Jun. 05, 2018).
- [75] S. J. Pickering, D. Lampard, N. Hay, and T. F. Roylance, "Heat transfer from the stator end-windings of a low voltage concentric-wound induction motor," in *1995 Seventh International Conference on Electrical Machines and Drives (Conf. Publ. No. 412)*, Sep. 1995, pp. 477–481, doi: 10.1049/cp:19950918.
- [76] S. J. Pickering, D. Lampard, N. Hay, and T. F. Roylance, "Heat transfer in a high voltage, through-ventilated 4-pole induction motor," in *1997 Eighth International Conference on Electrical Machines and Drives (Conf. Publ. No. 444)*, Sep. 1997, pp. 11–15, doi: 10.1049/cp:19971028.
- [77] J. Mugglestone, S. J. Pickering, and D. Lampard, "Prediction of the heat transfer from the end winding of a TEFC strip-wound induction motor," in *IEEE International Electric Machines and Drives Conference. IEMDC'99. Proceedings (Cat. No.99EX272)*, May 1999, pp. 484–486, doi: 10.1109/IEMDC.1999.769153.
- [78] J. Mugglestone, S. J. Pickering, and D. Lampard, "Effect of geometric changes on the flow and heat transfer in the end region of a TEFC induction motor," in *1999. Ninth International Conference on Electrical Machines and Drives (Conf. Publ. No. 468)*, Sep. 1999, pp. 40–44, doi: 10.1049/cp:19990987.
- [79] S. J. Pickering, D. Lampard, N. Hay, and T. F. Roylance, "Heat transfer in a through-ventilated induction motor," *IEE Proceedings - Electric Power Applications*, vol. 145, no. 5, pp. 429–433, Sep. 1998, doi: 10.1049/ip-epa:19982169.
- [80] B. Zhang, R. Qu, W. Xu, J. Wang, and Y. Chen, "Thermal model of totally enclosed water-cooled permanent magnet synchronous machines for electric vehicle applications," in *2014 International Conference on Electrical Machines (ICEM)*, Sep. 2014, pp. 2205–2211, doi: 10.1109/ICELMACH.2014.6960490.
- [81] J. R. Hendershot and T. J. E. Miller, *Design of Brushless Permanent-magnet Motors*. Magna Physics Pub., 1994.
- [82] Y. Bertin, "Refroidissement des machines tournantes. Études paramétriques," *Techniques de l'ingénieur Généralités sur les machines électriques tournantes*, vol. base documentaire: TIB250DUO., no. ref. article: d3462, 2006, [Online]. Available: <https://www.techniques-ingenieur.fr/base-documentaire/energies-th4/generalites-sur-les>

- machines-electriques-tournantes-42250210/refroidissement-des-machines-tournantes-etudes-parametriques-d3462/.
- [83] Y. Gai *et al.*, “Cooling of Automotive Traction Motors: Schemes, Examples, and Computation Methods,” *IEEE Transactions on Industrial Electronics*, vol. 66, no. 3, pp. 1681–1692, Mar. 2019, doi: 10.1109/TIE.2018.2835397.
- [84] M. Grabowski, K. Urbaniec, J. Wernik, and K. J. Wołosz, “Numerical simulation and experimental verification of heat transfer from a finned housing of an electric motor,” *Energy Conversion and Management*, vol. 125, pp. 91–96, Oct. 2016, doi: 10.1016/j.enconman.2016.05.038.
- [85] S. Ulbrich, J. Kopte, and J. Proske, “Cooling Fin Optimization on a TEFC Electrical Machine Housing Using a 2-D Conjugate Heat Transfer Model,” *IEEE Transactions on Industrial Electronics*, vol. 65, no. 2, pp. 1711–1718, Feb. 2018, doi: 10.1109/TIE.2017.2748051.
- [86] H. Nemati, M. A. Moghimi, P. Sapin, and C. N. Markides, “Shape optimisation of air-cooled finned-tube heat exchangers,” *International Journal of Thermal Sciences*, vol. 150, p. 106233, Apr. 2020, doi: 10.1016/j.ijthermalsci.2019.106233.
- [87] F. Heiles, “Design and arrangement of cooling fins,” *Elektrotechnik und Maschinenbau*, vol. 69, no. 14, 1952.
- [88] A. Giret, “Transferts thermiques convectifs dans le cadre de machines tournantes,” thesis, Chasseneuil-du-Poitou, Ecole nationale supérieure de mécanique et d’aéronautique, 2009.
- [89] M. M. Baggu, H. L. Hess, and K. Rink, “Thermal modeling of ‘direct lamination cooling (DLC)’ induction motor for hybrid electric vehicle applications,” in *2005 IEEE Vehicle Power and Propulsion Conference*, Sep. 2005, pp. 468–472, doi: 10.1109/VPPC.2005.1554564.
- [90] A. Nollau and D. Gerling, “A new cooling approach for traction motors in hybrid drives,” in *2013 International Electric Machines Drives Conference*, May 2013, pp. 456–461, doi: 10.1109/IEMDC.2013.6556136.
- [91] Z. Huang, S. Nategh, V. Lassila, M. Alaküla, and J. Yuan, “Direct oil cooling of traction motors in hybrid drives,” in *2012 IEEE International Electric Vehicle Conference*, Mar. 2012, pp. 1–8, doi: 10.1109/IEVC.2012.6183163.
- [92] T. A. Burrell *et al.*, “Evaluation of the 2008 Lexus LS 600H Hybrid Synergy Drive System,” 2009, doi: 10.2172/947393.
- [93] P. H. Mellor, D. Roberts, and D. R. Turner, “Lumped parameter thermal model for electrical machines of TEFC design,” *IEE Proceedings B Electric Power Applications*, vol. 138, no. 5, p. 205, 1991, doi: 10.1049/ip-b.1991.0025.
- [94] J. HUETZ and J.-P. PETIT, “Notions de transfert thermique par convection,” *Ref: TIP100WEB - “Plastiques et composites,”* Aug. 10, 1990. <https://www.techniques-ingenieur.fr/base-documentaire/archives-th12/archives-plastiques-et-composites-tiaam/archive-1/notions-de-transfert-thermique-par-convection-a1540a/> (accessed May 11, 2020).
- [95] E. N. Sieder and G. E. Tate, “Heat Transfer and Pressure Drop of Liquids in Tubes,” *Ind. Eng. Chem.*, vol. 28, no. 12, pp. 1429–1435, Dec. 1936, doi: 10.1021/ie50324a027.
- [96] W. H. McAdams and National Research Council. Committee on Heat Transmission, *Heat Transmission*. London: McGraw-Hill, 1942.
- [97] A.-M. Ebrahim Momin, J. S. Saini, and S. C. Solanki, “Heat transfer and friction in solar air heater duct with V-shaped rib roughness on absorber plate,” *International Journal of Heat and Mass Transfer*, vol. 45, no. 16, pp. 3383–3396, Jul. 2002, doi: 10.1016/S0017-9310(02)00046-7.
- [98] A. Chaube, P. K. Sahoo, and S. C. Solanki, “Analysis of heat transfer augmentation and flow characteristics due to rib roughness over absorber plate of a solar air heater,”

- Renewable Energy*, vol. 31, no. 3, pp. 317–331, Mar. 2006, doi: 10.1016/j.renene.2005.01.012.
- [99] A. R. Jaurker, J. S. Saini, and B. K. Gandhi, “Heat transfer and friction characteristics of rectangular solar air heater duct using rib-grooved artificial roughness,” *Solar Energy*, vol. 80, no. 8, pp. 895–907, Aug. 2006, doi: 10.1016/j.solener.2005.08.006.
- [100] J. L. Bhagoria, J. S. Saini, and S. C. Solanki, “Heat transfer coefficient and friction factor correlations for rectangular solar air heater duct having transverse wedge shaped rib roughness on the absorber plate,” *Renewable Energy*, vol. 25, no. 3, pp. 341–369, Mar. 2002, doi: 10.1016/S0960-1481(01)00057-X.
- [101] R. Karwa, S. C. Solanki, and J. S. Saini, “Heat transfer coefficient and friction factor correlations for the transitional flow regime in rib-roughened rectangular ducts,” *International Journal of Heat and Mass Transfer*, vol. 42, no. 9, pp. 1597–1615, May 1999, doi: 10.1016/S0017-9310(98)00252-X.
- [102] G. Tanda, “Heat transfer in rectangular channels with transverse and V-shaped broken ribs,” *International Journal of Heat and Mass Transfer*, vol. 47, no. 2, pp. 229–243, Jan. 2004, doi: 10.1016/S0017-9310(03)00414-9.
- [103] X. Chen, H. Ye, X. Fan, T. Ren, and G. Zhang, “A review of small heat pipes for electronics,” *Applied Thermal Engineering*, vol. 96, pp. 1–17, Mar. 2016, doi: 10.1016/j.applthermaleng.2015.11.048.
- [104] T. Hassett and M. Hodowanec, “Electric motor with heat pipes,” US7569955B2, Aug. 04, 2009.
- [105] R.-J. Owng, C.-W. Ruan, Y.-T. Wei, and M.-C. Liao, “Electric motor having heat pipes,” US8368265B2, Feb. 05, 2013.
- [106] S. Ruby and J.-P. L. Lagadec, “Cooling of an electric motor via heat pipes,” US9561716B2, Feb. 07, 2017.
- [107] L. Fedoseyev and E. M. P. JR, “Rotor Assembly with Heat Pipe Cooling System,” US20140368064A1, Dec. 18, 2014.
- [108] N. Putra and B. Ariantara, “Electric motor thermal management system using L-shaped flat heat pipes,” *Applied Thermal Engineering*, vol. 126, pp. 1156–1163, Nov. 2017, doi: 10.1016/j.applthermaleng.2017.01.090.
- [109] A. Faghri, “Review and Advances in Heat Pipe Science and Technology,” *J. Heat Transfer*, vol. 134, no. 12, Dec. 2012, doi: 10.1115/1.4007407.
- [110] D. Bugby, C. Stouffer, J. Garzon, M. Beres, and A. Gilchrist, “Advanced Devices for Cryogenic Thermal Management,” *AIP Conference Proceedings*, vol. 823, no. 1, pp. 1790–1798, Apr. 2006, doi: 10.1063/1.2202608.
- [111] Yu. F. Maydanik, “Loop heat pipes,” *Applied Thermal Engineering*, vol. 25, no. 5, pp. 635–657, Apr. 2005, doi: 10.1016/j.applthermaleng.2004.07.010.
- [112] F. Mena, W. Supper, and C. Puillet, “Design and Development of Loop Heat Pipes,” SAE International, Warrendale, PA, SAE Technical Paper 2000-01-2315, Jul. 2000. doi: 10.4271/2000-01-2315.
- [113] A. A. M. Delil, V. Baturkin, G. Gorbenko, P. Gakal, and V. Ruzaykin, “Modeling of a Miniature Loop Heat Pipe with a Flat Evaporator,” *SAE Transactions*, vol. 111, pp. 315–322, 2002.
- [114] T. Kaya and J. Ku, “Experimental Investigation of Performance Characteristics of Small Loop Heat Pipes,” in *41st Aerospace Sciences Meeting and Exhibit*, American Institute of Aeronautics and Astronautics.
- [115] H. Jouhara, A. Chauhan, T. Nannou, S. Almahmoud, B. Delpech, and L. C. Wrobel, “Heat pipe based systems - Advances and applications,” *Energy*, vol. 128, pp. 729–754, Jun. 2017, doi: 10.1016/j.energy.2017.04.028.

- [116] S. Nategh, D. Barber, A. Boglietti, D. Lindberg, O. Aglen, and R. Brammer, "A Study on Thermal Effects of Different Potting Strategies in Traction Motors," in *2018 IEEE International Conference on Electrical Systems for Aircraft, Railway, Ship Propulsion and Road Vehicles & International Transportation Electrification Conference (ESARS-ITEC)*, Nottingham, Nov. 2018, pp. 1–6, doi: 10.1109/ESARS-ITEC.2018.8607600.
- [117] J. Pyrhönen, P. Lindh, M. Polikarpova, E. Kurvinen, and V. Naumanen, "Heat-transfer improvements in an axial-flux permanent-magnet synchronous machine," *Applied Thermal Engineering*, vol. 76, pp. 245–251, Feb. 2015, doi: 10.1016/j.applthermaleng.2014.11.003.
- [118] J. Belletre, V. Sartre, F. Biais, and A. Lallemand, "Transient state study of electric motor heating and phase change solid-liquid cooling," *Applied Thermal Engineering*, vol. 17, no. 1, pp. 17–31, Jan. 1997, doi: 10.1016/1359-4311(96)00026-9.
- [119] H. Martin, "Heat and Mass Transfer between Impinging Gas Jets and Solid Surfaces," in *Advances in Heat Transfer*, vol. 13, J. P. Hartnett and T. F. Irvine, Eds. Elsevier, 1977, pp. 1–60.
- [120] S. Kakaç, "Introduction to ASI on Cooling of Electronic Systems," in *Cooling of Electronic Systems*, S. Kakaç, H. Yüncü, and K. Hijikata, Eds. Dordrecht: Springer Netherlands, 1994, pp. 1–15.
- [121] J. Pellé and S. Harmand, "Heat transfer study in a rotor–stator system air-gap with an axial inflow," *Applied Thermal Engineering*, vol. 29, no. 8, pp. 1532–1543, Jun. 2009, doi: 10.1016/j.applthermaleng.2008.07.014.
- [122] M. Fénot, J.-J. Vullierme, and E. Dorignac, "A heat transfer measurement of jet impingement with high injection temperature," *Comptes Rendus Mécanique*, vol. 333, no. 10, pp. 778–782, Oct. 2005, doi: 10.1016/j.crme.2005.08.002.
- [123] J. P. Yu, E. M. Sparrow, and E. R. G. Eckert, "Experiments on a shrouded, parallel disk system with rotation and coolant throughflow," *International Journal of Heat and Mass Transfer*, vol. 16, no. 2, pp. 311–314, Feb. 1973, doi: 10.1016/0017-9310(73)90060-4.
- [124] C. M. Haynes and J. M. Owen, "Heat Transfer From a Shrouded Disk System With a Radial Outflow of Coolant," *J. Eng. Power*, vol. 97, no. 1, pp. 28–35, Jan. 1975, doi: 10.1115/1.3445907.
- [125] J. C. Lallave, M. M. Rahman, and A. Kumar, "Numerical analysis of heat transfer on a rotating disk surface under confined liquid jet impingement," *International Journal of Heat and Fluid Flow*, vol. 28, no. 4, pp. 720–734, Aug. 2007, doi: 10.1016/j.ijheatfluidflow.2006.09.005.
- [126] A. Tüysüz, F. Meyer, M. Steichen, C. Zwysig, and J. W. Kolar, "Advanced Cooling Methods for High-Speed Electrical Machines," *IEEE Transactions on Industry Applications*, vol. 53, no. 3, pp. 2077–2087, May 2017, doi: 10.1109/TIA.2017.2672921.
- [127] T. Woolmer, "Wheel-hub motor cooling," US20130187492A1, Jul. 25, 2013.
- [128] H. Fujita, A. Itoh, and T. Urano, "Newly Developed Motor Cooling Method Using Refrigerant," *World Electric Vehicle Journal*, vol. 10, no. 2, p. 38, Jun. 2019, doi: 10.3390/wevj10020038.
- [129] P. Zhou, N. R. Kalayjian, G. D. Cutler, and P. K. Augenbergs, "Liquid cooled rotor assembly," US7489057B2, Feb. 10, 2009.
- [130] T. Miyamoto and K. NAGATA, "Rotating electrical machine cooling system," US8912691B2, Dec. 16, 2014.
- [131] T. Miyamoto, S. Matsusaka, and K. Kato, "Cooling structure of rotary electric machine," US9729027B2, Aug. 08, 2017.
- [132] S. H. Swales, P. F. Turnbull, B. Schulze, F. R. Poskie, W. J. Omell, and W. C. Deneszczuk, "Oil cooled motor/generator for an automotive powertrain," US8169110B2, May 01, 2012.

- [133] B. Assaad, K. Mikati, T. V. Tran, and E. Negre, "Experimental Study of Oil Cooled Induction Motor for Hybrid and Electric Vehicles," in *2018 XIII International Conference on Electrical Machines (ICEM)*, Sep. 2018, pp. 1195–1200, doi: 10.1109/ICELMACH.2018.8507058.
- [134] K. Oliphant, B. W. Webb, and M. Q. McQuay, "An experimental comparison of liquid jet array and spray impingement cooling in the non-boiling regime," *Experimental Thermal and Fluid Science*, vol. 18, no. 1, pp. 1–10, Sep. 1998, doi: 10.1016/S0894-1777(98)10013-4.
- [135] N. Karwa, S. R. Kale, and P. M. V. Subbarao, "Experimental study of non-boiling heat transfer from a horizontal surface by water sprays," *Experimental Thermal and Fluid Science*, vol. 32, no. 2, pp. 571–579, Nov. 2007, doi: 10.1016/j.expthermflusci.2007.06.007.
- [136] T. Davin, J. Pellé, S. Harmand, and R. Yu, "Experimental study of oil cooling systems for electric motors," *Applied Thermal Engineering*, vol. 75, pp. 1–13, Jan. 2015, doi: 10.1016/j.applthermaleng.2014.10.060.
- [137] T. Davin, J. Pellé, S. Harmand, and R. Yu, "Motor Cooling Modeling: An Inverse Method for the Identification of Convection Coefficients," *Journal of Thermal Science and Engineering Applications*, vol. 9, no. 4, pp. 041009–041009–13, Apr. 2017, doi: 10.1115/1.4036303.
- [138] K. Bennion, E. Cousineau, X. Feng, C. King, and G. Moreno, "Electric Motor Thermal Management R&D," presented at the IEEE Power & Energy Society General Meeting, Denver, CO, USA, Jul. 2015, [Online]. Available: <https://www.ieee-pes.org/presentations/gm2015/PESGM2015P-002837.pdf>.
- [139] G. R. G. Guemo, "Modélisation et caractérisation thermique de machines électriques synchrones à aimants permanents," phdthesis, INSA de Lyon, 2014.
- [140] T. Kikuchi, S. Kitada, and Y. Kaneko, "Motor/generator with equalized coolant distribution," US6515384B1, Feb. 04, 2003.
- [141] K. Chen, A. Masrur, S. Ahmed, and V. K. Garg, "Jet impingement cooling of electric motor end-windings," US6639334B2, Oct. 28, 2003.
- [142] S. J. Slayzak, R. Viskanta, and F. P. Incropera, "Effects of interaction between adjacent free surface planar jets on local heat transfer from the impingement surface," *International Journal of Heat and Mass Transfer*, vol. 37, no. 2, pp. 269–282, Jan. 1994, doi: 10.1016/0017-9310(94)90098-1.
- [143] X. C. Lee, C. F. Ma, Q. Zheng, Y. Zhuang, and Y. Q. Tian, "Numerical study of recovery effect and impingement heat transfer with submerged circular jets of large Prandtl number liquid," *International Journal of Heat and Mass Transfer*, vol. 40, no. 11, pp. 2647–2653, Jul. 1997, doi: 10.1016/S0017-9310(96)00263-3.
- [144] C. F. Ma, Q. Zheng, S. C. Lee, and T. Gomi, "Impingement heat transfer and recovery effect with submerged jets of large Prandtl number liquid—I. Unconfined circular jets," *International Journal of Heat and Mass Transfer*, vol. 40, no. 6, pp. 1481–1490, Apr. 1997, doi: 10.1016/S0017-9310(96)00069-5.
- [145] C. F. Ma, Q. Zheng, and S. Y. Ko, "Local heat transfer and recovery factor with impinging free-surface circular jets of transformer oil," *International Journal of Heat and Mass Transfer*, vol. 40, no. 18, pp. 4295–4308, Nov. 1997, doi: 10.1016/S0017-9310(97)00054-9.
- [146] D. H. Wolf, F. P. Incropera, and R. Viskanta, "Jet Impingement Boiling," in *Advances in Heat Transfer*, vol. 23, J. P. Hartnett and T. F. Irvine, Eds. Elsevier, 1993, pp. 1–132.
- [147] D. E. Metzger, K. N. Cummings, and W. A. Ruby, "Effects of Prandtl Number on Heat Transfer Characteristics of impinging Liquid Jets," presented at the International Heat Transfer Conference 5, 1974, doi: 10.1615/IHTC5.1680.

- [148] J. Kim, "Spray cooling heat transfer: The state of the art," *International Journal of Heat and Fluid Flow*, vol. 28, no. 4, pp. 753–767, Aug. 2007, doi: 10.1016/j.ijheatfluidflow.2006.09.003.
- [149] K. A. Estes and I. Mudawar, "Comparison of Two-Phase Electronic Cooling Using Free Jets and Sprays," *J. Electron. Packag.*, vol. 117, no. 4, pp. 323–332, Dec. 1995, doi: 10.1115/1.2792112.
- [150] I. Mudawar and K. A. Estes, "Optimizing and Predicting CHF in Spray Cooling of a Square Surface," *J. Heat Transfer*, vol. 118, no. 3, pp. 672–679, Aug. 1996, doi: 10.1115/1.2822685.
- [151] M. Visaria and I. Mudawar, "Theoretical and experimental study of the effects of spray inclination on two-phase spray cooling and critical heat flux," *International Journal of Heat and Mass Transfer*, vol. 51, no. 9, pp. 2398–2410, May 2008, doi: 10.1016/j.ijheatmasstransfer.2007.08.010.
- [152] I. Mudawar, D. Bharathan, K. Kelly, and S. Narumanchi, "Two-Phase Spray Cooling of Hybrid Vehicle Electronics," *IEEE Transactions on Components and Packaging Technologies*, vol. 32, no. 2, pp. 501–512, Jun. 2009, doi: 10.1109/TCAPT.2008.2006907.
- [153] I. Mudawar and W. S. Valentine, "Determination of the local quench curve for spray-cooled metallic surfaces," *J. Heat Treating*, vol. 7, no. 2, pp. 107–121, Sep. 1989, doi: 10.1007/BF02833195.
- [154] Y. Wang, M. Liu, D. Liu, K. Xu, and Y. Chen, "Experimental study on the effects of spray inclination on water spray cooling performance in non-boiling regime," *Experimental Thermal and Fluid Science*, vol. 34, no. 7, pp. 933–942, Oct. 2010, doi: 10.1016/j.expthermflusci.2010.02.010.
- [155] Y. Wang, M. Liu, D. Liu, and K. Xu, "Heat Flux Correlation for Spray Cooling in the Nonboiling Regime," *Heat Transfer Engineering*, vol. 32, no. 11–12, pp. 1075–1081, Oct. 2011, doi: 10.1080/01457632.2011.556505.
- [156] M. Liu, Y. Wang, D. Liu, K. Xu, and Y. Chen, "Experimental study of the effects of structured surface geometry on water spray cooling performance in non-boiling regime," *Front. Energy*, vol. 5, no. 1, pp. 75–82, Mar. 2011, doi: 10.1007/s11708-010-0014-0.
- [157] J. R. Rybicki and I. Mudawar, "Single-phase and two-phase cooling characteristics of upward-facing and downward-facing sprays," *International Journal of Heat and Mass Transfer*, vol. 49, no. 1, pp. 5–16, Jan. 2006, doi: 10.1016/j.ijheatmasstransfer.2005.07.040.
- [158] D. H. Lim and S. C. Kim, "Thermal performance of oil spray cooling system for in-wheel motor in electric vehicles," *Applied Thermal Engineering*, vol. 63, no. 2, pp. 577–587, Feb. 2014, doi: 10.1016/j.applthermaleng.2013.11.057.
- [159] A. Boglietti, A. Cavagnino, D. Staton, M. Shanel, M. Mueller, and C. Mejuto, "Evolution and Modern Approaches for Thermal Analysis of Electrical Machines," *IEEE Transactions on Industrial Electronics*, vol. 56, no. 3, pp. 871–882, Mar. 2009, doi: 10.1109/TIE.2008.2011622.
- [160] Y. Bertin, "Analyse des transferts de chaleur dans un moteur électrique asynchrone : développement d'un environnement CAO et modélisations thermoaérauliques," thesis, Poitiers, 1987.
- [161] A. Boglietti, A. Cavagnino, M. Parvis, and A. Vallan, "Evaluation of radiation thermal resistances in industrial motors," *IEEE Transactions on Industry Applications*, vol. 42, no. 3, pp. 688–693, May 2006, doi: 10.1109/TIA.2006.873655.
- [162] G. Bertotti, "Physical interpretation of eddy current losses in ferromagnetic materials. I. Theoretical considerations," *Journal of Applied Physics*, vol. 57, no. 6, pp. 2110–2117, Mar. 1985, doi: 10.1063/1.334404.

- [163] J. Saari, *Thermal analysis of high-speed induction machines*. Helsinki University of Technology, 1998.
- [164] J. E. Vrancik, *Prediction of windage power loss in alternators*. Washington, DC: National Aeronautics and Space Administration, 1968.
- [165] G. W. Milton, “Concerning bounds on the transport and mechanical properties of multicomponent composite materials,” *Appl. Phys. A*, vol. 26, no. 2, pp. 125–130, Oct. 1981, doi: 10.1007/BF00616659.
- [166] K. Mori *et al.*, “Thermal transport and magnetic properties of GdBa₂Cu₃O_{7-y} superconductor,” *Physica C: Superconductivity*, vol. 153–155, pp. 1515–1516, Jun. 1988, doi: 10.1016/0921-4534(88)90398-X.
- [167] J. Lutun, “Modélisation thermique des alternateurs automobiles,” Jan. 2012, Accessed: Oct. 16, 2019. [Online]. Available: <https://tel.archives-ouvertes.fr/tel-00742950>.
- [168] General Electric, *Heat transfer and fluid flow data book*. 1981.
- [169] W. M. Rohsenow, J. P. Hartnett, and E. N. Ganic, “Handbook of heat transfer fundamentals (2nd edition),” Jan. 1985, Accessed: Oct. 15, 2019. [Online]. Available: <https://www.osti.gov/biblio/5892601>.
- [170] B. Renard, “Etude expérimentale et modélisation du comportement thermique d’une machine électrique multi-fonctions : application à un alerno-démarrateur intégré,” Poitiers, 2003.
- [171] A. Zeaiter and M. Fénot, “Thermal Sensitivity Analysis of a High Power Density Electric Motor for Aeronautical Application,” in *2018 IEEE International Conference on Electrical Systems for Aircraft, Railway, Ship Propulsion and Road Vehicles International Transportation Electrification Conference (ESARS-ITEC)*, Nov. 2018, pp. 1–6, doi: 10.1109/ESARS-ITEC.2018.8607393.
- [172] A. Zeaiter, M. Fénot, and D. Saury, “Numerical Approach to Determining Windings’ Thermal Conductivity,” in *2018 XIII International Conference on Electrical Machines (ICEM)*, Alexandroupoli, Sep. 2018, pp. 1291–1296, doi: 10.1109/ICELMACH.2018.8506692.
- [173] S. Thieblin, “Analyse et modélisation du comportement thermique d’un moteur électrique soumis à des régimes de charge et de vitesse variables - application au moteur de traction d’un véhicule électrique,” Ph. D. Thesis, Université de Poitiers, 1997.
- [174] J. Lindström, “Thermal Model of a Permanent-Magnet Motor for a Hybrid Electric Vehicle,” Department of Electric Power Engineering Chalmers University of Technology, Göteborg, Sweden, 1999.
- [175] K. Bennion and J. Cousineau, “Sensitivity analysis of traction drive motor cooling,” in *2012 IEEE Transportation Electrification Conference and Expo (ITEC)*, Jun. 2012, pp. 1–6, doi: 10.1109/ITEC.2012.6243512.
- [176] S. Touhami, A. Zeaiter, M. Fénot, Y. Lefèvre, J.-F. Llibre, and E. Videcoq, “Electro-thermal Models and Design Approach for High Specific Power Electric Motor for Hybrid Aircraft,” presented at the Aerospace Europe Conference, Bordeaux, France, Feb. 2020, Accessed: Apr. 22, 2020. [Online]. Available: <https://aerospace-europe2020.eu/>.
- [177] J. Pyrhönen, T. Jokinen, and V. Hrabovcová, *Design of rotating electrical machines*. John Wiley & Sons, Ltd, 2008.
- [178] “Liquid cooled rotor assembly - US 7,579,725 B2 - PatentSwarm.” <https://patentswarm.com/patents/US7579725B2> (accessed May 28, 2020).
- [179] K.-H. Lee, H.-R. Cha, and Y.-B. Kim, “Development of an interior permanent magnet motor through rotor cooling for electric vehicles,” *Applied Thermal Engineering*, vol. 95, pp. 348–356, Feb. 2016, doi: 10.1016/j.applthermaleng.2015.11.022.
- [180] R. Christie, A. Dubois, and J. Derlaga, “Cooling of Electric Motors Used for Propulsion on SCEPTOR,” presented at the AIAA Aviation and Aeronautics Forum and Exposition;

- 13-17 Jun. 2016, Washington, DC; United States, Jun. 13, 2016, [Online]. Available: <https://ntrs.nasa.gov/archive/nasa/casi.ntrs.nasa.gov/20170001724.pdf>.
- [181] I. E. Idelchik, *Handbook of Hydraulic Resistance*, 3rd ed. New York: Begell House Inc., 1996.
- [182] “Catalog of hydraulic pumps,” *Parker Hannifin Corporation*. <https://www.parker.com/> (accessed Jun. 03, 2020).
- [183] E. R. G. Eckert, E. R. G. Eckert, and R. M. Drake, *Analysis Of Heat And Mass Transfer*. Taylor & Francis, 1986.
- [184] S. Touhami, “Analytical Sizing Models to Assess the Performances of High Specific Power Electric Motors for Hybrid Aircraft,” These en préparation, Toulouse, INPT, 2016.
- [185] K. A. Woodbury, *Inverse Engineering Handbook*. CRC Press, 2002.
- [186] M. Khelifa, M. Mordjaoui, and A. Medoued, “An inverse problem methodology for design and optimization of an interior permanent magnetic BLDC motor,” *International Journal of Hydrogen Energy*, vol. 42, no. 28, pp. 17733–17740, Jul. 2017, doi: 10.1016/j.ijhydene.2017.02.017.
- [187] C.-H. Huang and H.-C. Lo, “A three-dimensional inverse problem in estimating the internal heat flux of housing for high speed motors,” *Applied Thermal Engineering*, vol. 26, no. 14, pp. 1515–1529, Oct. 2006, doi: 10.1016/j.applthermaleng.2005.12.009.
- [188] H. Vansompel, A. Yarrantseva, P. Sergeant, and G. Crevecoeur, “An Inverse Thermal Modeling Approach for Thermal Parameter and Loss Identification in an Axial Flux Permanent Magnet Machine,” *IEEE Transactions on Industrial Electronics*, vol. 66, no. 3, pp. 1727–1735, Mar. 2019, doi: 10.1109/TIE.2018.2838089.
- [189] D. G. Nair and A. Arkkio, “Inverse Thermal Modeling to Determine Power Losses in Induction Motor,” *IEEE Transactions on Magnetics*, vol. 53, no. 6, pp. 1–4, Jun. 2017, doi: 10.1109/TMAG.2017.2661381.
- [190] A. Zeaiter, E. Videcoq, and M. Fénot, “Determination of electric motor losses and critical temperatures through an inverse approach,” *Electr Eng*, Sep. 2020, doi: 10.1007/s00202-020-01098-0.
- [191] J. V. Beck, B. Blackwell, and C. R. St. Clair, *Inverse heat conduction: ill-posed problems*. New York: Wiley, 1985.
- [192] E. Videcoq, D. Petit, and A. Piteau, “Experimental modelling and estimation of time varying thermal sources,” *International Journal of Thermal Sciences*, vol. 42, no. 3, pp. 255–265, Mar. 2003, doi: 10.1016/S1290-0729(02)00025-X.
- [193] J. V. Beck, B. Blackwell, and A. Haji-Sheikh, “Comparison of some inverse heat conduction methods using experimental data,” *International Journal of Heat and Mass Transfer*, vol. 39, no. 17, pp. 3649–3657, Nov. 1996, doi: 10.1016/0017-9310(96)00034-8.
- [194] G. Blanc, M. Raynaud, and T. H. Chau, “A guide for the use of the function specification method for 2D inverse heat conduction problems,” *Revue Générale de Thermique*, vol. 37, no. 1, pp. 17–30, Jan. 1998, doi: 10.1016/S0035-3159(97)82463-4.

MODELISATION THERMIQUE ET REFROIDISSEMENT DE MOTEURS ELECTRIQUES. APPLICATION A LA PROPULSION D'UN AVION HYBRIDE

Résumé :

Le travail présenté dans ce mémoire concerne la modélisation thermique de moteurs électriques de forte densité de puissance. Le but est de trouver les techniques de refroidissement efficaces et adaptées aux moteurs conçus pour application à la propulsion de l'avion hybride du futur. Deux cibles de densité de puissance, 5 kW/kg pour le court terme (année 2025) et 10 kW/kg pour le long terme (année 2035), sont abordées avec leurs propres exigences. Les moteurs électriques étudiés sont de type synchrone à aimants permanents montés en surface du rotor. Ce type de moteur est caractérisé par un rendement élevé et contraint par les températures maximales admissibles relativement faibles de son bobinage et de ses aimants. Une fois atteintes, ces valeurs de température entraînent le dysfonctionnement du moteur ou la limitation de sa durée de vie. En outre, avec un design fermé imposé et des densités élevées de flux de chaleur dissipées dans la machine, une optimisation du refroidissement est incontournable.

Pour se familiariser avec le problème, un état de l'art détaillé sur le refroidissement des machines électriques est réalisé. En conséquence, les différentes techniques utilisées et les avancements technologiques récents sont analysés vis-à-vis de notre cas d'application. Ensuite, afin de prédire le comportement thermique du moteur et d'assurer le suivi des températures critiques (surtout au bobinage et aux aimants), un modèle nodal transitoire est mis en place et résolu sous Matlab. Ce dernier est construit en considérant l'intégralité du système moteur avec son circuit de refroidissement. Les conditions externes liées à l'environnement sont prises en compte, en particulier la variation de la température d'air extérieur en fonction de l'altitude et le profil de mission de vol de l'avion. En effet, les pertes dans le moteur, qui constituent les sources de chaleur, varient en fonction de la puissance pendant le vol. Afin d'identifier précisément les paramètres intrinsèques du modèle, une étude par éléments finis a été menée et des corrélations permettant l'estimation de la conductivité thermique du bobinage en sont déduites par interpolation polynomiale. Plusieurs études ont ensuite été menées concernant l'influence des propriétés thermophysiques, de la température extérieure, de la nature du liquide de refroidissement, de son débit ainsi que la surface extérieure de l'échangeur sur les réponses en température du modèle. Plusieurs designs du moteur sont étudiés grâce à ce modèle afin de proposer des solutions de refroidissement adaptées. Pour chacune des cibles, une configuration optimale du moteur avec son système de refroidissement a été adoptée.

Par ailleurs, les pertes électromagnétiques et mécaniques étant difficiles à estimer dans ces machines, un chapitre est consacré à leur identification par résolution d'un problème inverse. La technique est séquentielle et utilise la spécification de fonction de Beck comme méthode de régularisation. Trois cas, de complexité croissante, sont étudiés et montrent la fiabilité de la méthode qui permet également d'estimer les températures inaccessibles dans le moteur. C'est finalement ce modèle nodal à faible nombre de degré de liberté qui nous permet d'assurer, en temps réel, le suivi des points chauds.

Mots clés : Avions--Moteurs, Conductivité thermique, Moteurs électriques--Construction et conception, Moteurs électriques--Refroidissement, Problèmes inverses, Moteur synchrone à aimants permanents, Modélisation thermique méthode nodale, Pertes moteur.

THERMAL MODELING AND COOLING OF ELECTRIC MOTORS. APPLICATION TO THE PROPULSION OF HYBRID AIRCRAFT

Abstract :

The concern of this thesis is the thermal modeling of high-specific power electric motors. The aim is to allow finding the efficient and adequate cooling solutions of the motors designed for hybrid aircraft propulsion application. Two specific power values, 5 kW/kg for the short-term (year 2025) and 10 kW/kg for the long-term (year 2035), are targeted, each with specific requirements. The investigated type of electric motors is the synchronous machine with surface-mounted permanent magnets. This motor type is constrained by relatively low values of maximum allowed temperatures in windings and magnets. Once reached, these temperature values lead to a failure in motor operation or at least to shortening its lifetime. Moreover, with a closed motor design and high heat fluxes generated, the optimization of the cooling is essential.

To become acquainted with the issue, a detailed state of the art on electric machine cooling is elaborated. Then, the commonly used techniques and the recent technological advancements are analyzed with respect to our case study. Afterward, in order to predict motor thermal behavior and ensure the monitoring of critical temperatures (windings and magnets), a nodal transient model is implemented and solved on Matlab software. This latter is built for the whole system of the motor and cooling circuit. Specific conditions of the flight are taken into account, particularly the outside air temperature variation in terms of altitude and the flight mission profile. Actually, the motor losses, generating the heat in the machine, vary depending on the motor power during the mission. For the identification of crucial parameters, a Finite-Element study was conducted and corresponding correlations were elaborated to estimate the windings thermal conductivity through polynomial interpolation.

Several studies were carried out involving the influence of the thermo-physical properties, the outside temperature, the coolant nature, its flow rate as well as the exchanger surface, on the temperature response of the model. This model has allowed studying several motor designs and proposing adequate cooling solutions. For each target, a final optimal configuration of the motor with its cooling system was adopted.

Besides, since the electromagnetic and mechanical losses are hardly estimated in this machine type, a chapter was dedicated to identifying them through an inverse approach. A sequential technique, that uses Beck's function specification for regularization, was developed. Three cases of unknown losses, with increasing complexity, were studied, proving the method's reliability. Finally, using the same developed low-order model, the real-time procedure also allows monitoring low-accessibility motor temperatures (specifically hot spots).

Keywords : Airplanes--Motors, Thermal conductivity, Electric motors--Design and construction, Electric motors--Cooling, Inverse problems, Permanent-magnet synchronous motor, Nodal network thermal modeling, Motor losses.